

<b>REPORT DOCUMENTATION PAGE</b>				Form Approved OMB No. 0704-0188	
The public reporting burden for this collection of information is estimated to average 1 hour per response, including the time for reviewing instructions, searching existing data sources, gathering and maintaining the data needed, and completing and reviewing the collection of information. Send comments regarding this burden estimate or any other aspect of this collection of information, including suggestions for reducing the burden, to Department of Defense, Washington Headquarters Services, Directorate for Information Operations and Reports (0704-0188), 1215 Jefferson Davis Highway, Suite 1204, Arlington, VA 22202-4302. Respondents should be aware that notwithstanding any other provision of law, no person shall be subject to any penalty for failing to comply with a collection of information if it does not display a currently valid OMB control number.					
1. REPORT DATE (DD-MM-YYYY) 25/Jun/2001		2. REPORT TYPE DISSERTATION		3. DATES COVERED (From - To)	
4. TITLE AND SUBTITLE FOURIER TRANSFORM ION CYCLOTRON RESONANCE MASS SPECTROMETRY INVESTIGATION OF THE PHOTOLYSIS OF PLOCYCLIC AROMATIC HYDROCARBONS				5a. CONTRACT NUMBER	
				5b. GRANT NUMBER	
				5c. PROGRAM ELEMENT NUMBER	
6. AUTHOR(S) MAJ DIBBEN MARK J				5d. PROJECT NUMBER	
				5e. TASK NUMBER	
				5f. WORK UNIT NUMBER	
7. PERFORMING ORGANIZATION NAME(S) AND ADDRESS(ES) UNIVERSITY OF FLORIDA				8. PERFORMING ORGANIZATION REPORT NUMBER CI01-113	
9. SPONSORING/MONITORING AGENCY NAME(S) AND ADDRESS(ES) THE DEPARTMENT OF THE AIR FORCE AFIT/CIA, BLDG 125 2950 P STREET WPAFB OH 45433				10. SPONSOR/MONITOR'S ACRONYM(S)	
				11. SPONSOR/MONITOR'S REPORT NUMBER(S)	
12. DISTRIBUTION/AVAILABILITY STATEMENT Unlimited distribution In Accordance With AFI 35-205/AFIT Sup 1					
13. SUPPLEMENTARY NOTES					
20010720 027					
14. ABSTRACT					
15. SUBJECT TERMS					
16. SECURITY CLASSIFICATION OF:			17. LIMITATION OF ABSTRACT	18. NUMBER OF PAGES 141	19a. NAME OF RESPONSIBLE PERSON
a. REPORT	b. ABSTRACT	c. THIS PAGE			19b. TELEPHONE NUMBER (Include area code)

FOURIER TRANSFORM ION CYCLOTRON RESONANCE MASS  
SPECTROMETRY INVESTIGATION OF THE PHOTOLYSIS OF POLYCYCLIC  
AROMATIC HYDROCARBONS

By

MARK J. DIBBEN

A DISSERTATION PRESENTED TO THE GRADUATE SCHOOL  
OF THE UNIVERSITY OF FLORIDA IN PARTIAL FULFILLMENT  
OF THE REQUIREMENTS FOR THE DEGREE OF  
DOCTOR OF PHILOSOPHY

UNIVERSITY OF FLORIDA

2001

This dissertation is dedicated to my wife, Lynn.

## ACKNOWLEDGMENTS

There are many individuals I would like to thank who have given me the opportunity to be where I am today. My parents taught me responsibility and determination at an early age. Two of my high school teachers were very inspirational to me: B. R. Wells in mathematics and Jay Schweitzer in chemistry and physics.

Dr. Vala has been phenomenal. Not only has he helped me write papers and this dissertation, he has also been very available to discuss the projects I have worked on. It has been great to work with someone that is so dedicated.

Dr. Eyler has been wonderful as well. I used his instruments for this entire project and would never have been able to operate the laser without his electronics skills.

The members of my group have always been helpful, both in Dr. Vala's group and Dr. Eyler's. The top of this list is Dr. Jan Szczepanski who always had an answer for whatever question I came up with. He was especially patient in teaching me instrumentation my first year here.

My children, Jason, Luis and Amanda, have always been an inspiration to me. I hope they can be half as proud of me as I am of them. Annette and Angela have been very patient with me the last three years, and understanding when I have not always been there to help them with their math and science homework. I really appreciate their tolerance.



Thanks also go to Colonel Mueh and the Air Force Academy for sponsoring my Ph.D. Nowhere else could I have gotten an opportunity like the one they have given me. I am going to enjoy teaching there for the next five years (or longer!).

I would also like to thank the employees at the Gate convenience store, especially Clara and Linda. I saw them every morning when I got my 44 ounce Diet Coke and they always had a friendly word for me and helped me to not take things so seriously.

Most especially, I thank my wife, Lynn. She has taken care of all those little things to make my life easier while I have been in school. She has been understanding, sympathetic and, above all, very supportive and proud of the work I have accomplished.

## TABLE OF CONTENTS

	<u>page</u>
ACKNOWLEDGMENTS .....	iii
LIST OF TABLES .....	viii
LIST OF FIGURES .....	ix
ABSTRACT .....	xvii
 CHAPTERS	
1 POLYCYCLIC AROMATIC HYDROCARBONS IN SPACE .....	1
Introduction .....	1
Chemistry of PAHs in Space .....	4
Unidentified Infrared Bands .....	7
Diffuse Interstellar Bands .....	9
Related Efforts .....	10
2 FUNDAMENTALS OF FOURIER TRANSFORM ION CYCLOTRON RESONANCE MASS SPECTROMETRY .....	14
Historical Perspective .....	14
Motion of Trapped Ions .....	16
Instrument Overview .....	21
Magnet .....	21
Vacuum System .....	22
Analyzer Cell .....	22
Data Acquisition .....	23
Experimental Procedures .....	23
Experimental Parameters Used in this Study .....	29
3 PHOTODISSOCIATION OF FLUORENE CATION .....	33
Introduction .....	33
Hydrogen Loss .....	33
Fragmentation .....	39
m/z 166 .....	40
m/z 165: .....	42

m/z 164:	42
m/z 163:	42
m/z 162:	42
m/z 161:	45
Kinetics	51
Fragmentation Pathways	53
Computational Procedures	54
Sequential Hydrogen Loss	54
Loss of first hydrogen	57
Loss of second hydrogen	58
Loss of the third hydrogen	58
Loss of fourth hydrogen	59
Loss of fifth hydrogen	60
Loss of sixth hydrogen	60
Structural Integrity vs Ring Opening	60
Further Fragmentation	62
Photoproducts from the m/z 165 ion	63
Photoproducts from the m/z 163 ion	63
Photoproducts from the m/z 161 ion	64
4 ABSORPTION SPECTRA OF FLUORENE CATION	70
Action Spectrum of Fluorene Cation	71
Laser Induced Action Spectrum	73
5 ION-MOLECULE REACTION PRODUCTS OF FLUORENE	78
Aggregate Formation	78
Source Of Photoaggregates	80
C <sub>5</sub> H <sub>n</sub> <sup>+</sup> Ions (m/z 62-68)	82
C <sub>7</sub> H <sub>n</sub> <sup>+</sup> (m/z 84-92)	84
C <sub>9</sub> H <sub>n</sub> <sup>+</sup> (m/z 108-115)	87
C <sub>11</sub> H <sub>n</sub> <sup>+</sup> (m/z 132-141)	89
C <sub>13</sub> H <sub>n</sub> <sup>+</sup> (m/z 161-166)	89
6 PHOTOLYSIS OF NAPHTHALENE AND 1,2-BENZANTHRACENE	96
Naphthalene	97
C <sub>10</sub> H <sub>n</sub> <sup>+</sup> (m/z 126-129)	99
C <sub>8</sub> H <sub>6</sub> <sup>+</sup> (m/z 102)	104
C <sub>6</sub> H <sub>4</sub> <sup>+</sup> (m/z 76)	104
C <sub>20</sub> H <sub>n</sub> <sup>+</sup> (m/z 250-255)	107
C <sub>19</sub> H <sub>n</sub> <sup>+</sup> (m/z 231-243)	107
C <sub>18</sub> H <sub>n</sub> <sup>+</sup> (m/z 224-228)	109
C <sub>16</sub> H <sub>n</sub> <sup>+</sup> (m/z 198-204)	110
Naphthalene Summary	111
1,2-Benzanthracene	113

Hydrogen Loss .....	113
$C_{18}H_n^+$ (m/z 226-228) .....	119
$C_{17}H_n^+$ (m/z 209-218) .....	119
$C_{16}H_n^+$ (m/z 197-204) .....	119
$C_{15}H_n^+$ (m/z 184-191) .....	123
Ion-molecule reactions .....	123
1,2-Benzanthracene Summary .....	125
7 CONCLUSIONS.....	127
REFERENCES .....	131
BIOGRAPHICAL SKETCH .....	140

## LIST OF TABLES

<u>Table</u>	<u>Page</u>
1. Assignments of IR emission components within the PAH hypothesis.....	8
2. Fragment ion yields and rate constants for photodissociation of the fluorene cation and its dehydrogenated partners . ....	47
3. C-H bond energies (in kcal/mol (eV)) and energies of precursors (in Hartrees) calculated at B3LYP/4-31G level of theory for sequential hydrogen loss in photodissociation reactions of fluorene cation ( $C_{13}H_{10}^+$ , m/z 166). Energies are ZPE x 0.957 corrected. Hydrogen numbering is defined in Fig. 37. Energetically favorable reactions are given in bold type. Reactions proceed sequentially based on the previous reaction given in parentheses. ....	56
4. Laser dyes and their useful ranges. ....	75
5. Summary of the aggregates formed during a four second delay time (column 3) with their formulas. The last column lists the photolysis products of the isolated aggregates after four seconds of irradiation. ....	95

## LIST OF FIGURES

<u>Figure</u>	<u>Page</u>
1. The Unidentified Infrared bands in BD +30°3639. Prominent bands are present at 3.29, 6.2, 7.7, 8.6, and 11.2 $\mu\text{m}$ . Adapted from Allamandola et al.....	2
2. The Diffuse Interstellar Band spectrum. The graph is a composite of gaussian profiles fitted to all certain and probable DIBs. This spectrum is thought to be characteristic of diffuse medium matter.....	3
3. Schematic of the Omegatron in which ions are accelerated continuously to larger cyclotron radius until they strike a collector electrode. Adapted from Mashall.....	15
4. Power absorption measurement (with a marginal oscillator) during simultaneous resonant excitation. A mass spectrum is obtained by slowly varying the magnetic field at fixed excitation/detection frequency. Adapted from Marshall.....	16
5. Origin of ion cyclotron motion. The path of an ion moving in the plane of the paper is bent into a circle by the inward-directed Lorentz magnetic force produced by a magnetic field directed perpendicular to the plane of the paper. Adapted from Marshall and Verdun.....	17
6. ICR orbital frequency, $\nu_c = \omega_c/2\pi$ , in Hz, as a function of ionic mass-to-charge ratio, $m/z$ , in Daltons per multiple ( $z$ ) of the elementary electron charge, at each of five magnetic field strengths: 1.0, 3.0, 4.7, 7.0, and 11.5 tesla. Note that ICR frequencies for ions in the usual "chemical" mass-to-charge ratio ( $\sim 15 < m/z < 10,000$ ) typically lie between a few kHz and a few MHz. Adapted from Marshall et al.....	18
7. ICR orbital radius, $r$ , vs. ionic mass-to-charge ratios, $m/z$ , (in $u$ per multiple of elementary electronic charge) at each of five representative magnetic field strengths: 1.0, 3.0, 4.7, 7.0, and 11.5 tesla at 298 K. Note that even relatively heavy ions are confined to conveniently small-radius orbits by such magnetic fields. Adapted from Marshall et al.....	19
8. Ion translational (kinetic) energy (Eq. 7) as a function of ICR orbital radius, at five different magnetic field strengths: 1.0, 3.0, 4.7, 7.0, and 11.5 tesla, for an ion of $m/z=100$ . Ions may be accelerated to relatively high energy while still confined to relatively small orbital radii. Adapted from Leger et al.....	20

9. A cubic analyzer cell and a cylindrical, open-ended cell. The arrow shows the orientation of the magnetic field lines. ....	20
10. The basic steps in an experimental sequence using FTMS.....	24
11. Excitation corresponding to selected mass ranges ( $m/z$ 112-116 and 165-168) in the lower panel is converted into a SWIFT excitation waveform (upper panel) by inverse Fourier transform.....	27
12. Transformation of the time domain spectrum (upper panel) to the frequency domain spectrum (lower panel). Since frequency is inversely related to the mass, the masses appear in reverse order. ....	28
13. Schematic of the 2 tesla FT-ICR instrument. Vapor from liquid or high volatility solids can be inlet through the sample tubes and controlled with the leak valves. The solids probe is used for low volatility solids. The electronically controlled shutter allows the lamp to illuminate the cell through a window. Adapted from Kage.....	29
14. Schematic of the MIDAS hardware. Adapted from Senko et al.....	31
15. Typical pulse sequence. This includes SWIFT isolation of the parent ion, irradiation by the Xe arc lamp, isolation of one or more of the photofragments, further irradiation and finally chirp excitation and detection.....	32
16. Fluorene Molecule, $C_{13}H_{10}$ , mass 166. ....	33
17. FTICR mass spectrum of photolysis products after a four second irradiation period of the $m/z$ 166 ion. ....	34
18. Relative abundance of photolysis products and fluorene cation parent as a function of irradiation time. ....	35
19. FTICR mass spectrum of photolysis products after a one second irradiation of the $m/z$ 166 ion while simultaneously ejecting $m/z$ 165. ....	36
20. FTICR mass spectrum of photolysis products after three seconds of irradiation of the $m/z$ 166 ion while simultaneously ejecting $m/z$ 163. ....	36
21. FTICR mass spectrum of the photolysis products after three seconds of irradiation of the $m/z$ 166 ion while simultaneously ejecting $m/z$ 164. ....	38
22. FTICR mass spectrum of the photolysis products after seven seconds of irradiation of the $m/z$ 166 ion while simultaneously ejecting $m/z$ 162. ....	38
23. FTICR mass spectrum of the photolysis products after four seconds of irradiation of the $m/z$ 166 ion showing full fragmentation of the parent fluorene ion. ....	40

24. FTICR mass spectrum of photolysis products after one second of irradiation of the m/z 166 ion. Masses m/z 161-165 were ejected during lamp exposure.....	41
25. Time dependence of the photoproducts of the m/z 166 ion.....	41
26. FTICR mass spectrum of photolysis products after three seconds of irradiation of the isolated m/z 165 ion. Masses m/z 161-164 and m/z 166 were ejected during lamp exposure. M/z 166 is present due to incomplete ejection.....	43
27. Time dependence of the abundance of photoproducts of the m/z 165 ion. ....	43
28. FTICR mass spectrum of photolysis products after five seconds of irradiation of the isolated m/z 163 ion. The abundance of the m/z 163 ion is very large compared to that of the photoproducts and is not shown.....	44
29. Time dependence of the abundance of photoproducts of the m/z 163 ion. ....	44
30. FTICR mass spectrum of photolysis products after three seconds of irradiation of the isolated m/z 161 ion. ....	46
31. Time dependence of the abundance of photoproducts of the m/z 161 ion. ....	46
32. Photodecomposition pathways and products from the m/z 166 fluorene parent ion. Bold lines indicate yields of 50% or greater, thin lines indicate yields between 15 and 49%, and dashed lines indicate yields less than 15%. ....	48
33. Ten seconds of irradiation while ejecting m/z 91-162 and m/z 164-168.....	49
34. Four seconds of irradiation of the m/z 87 while ejecting 88-168. Slight dehydrogenation to m/z 86 and 85 occurs but no m/z 63 is present.....	50
35. Four seconds of irradiation of the m/z 89 ion while ejecting m/z 90-168. No dehydrogenation occurs but m/z 63 is present due to fragmentation. ....	50
36. Example of the calculated rate constants versus experimental values. Experimental values are solid lines while the corresponding calculated values are dashed. The m/z 161 and m/z 162 ions have been omitted for clarity. ....	53
37. Energetically favorable photoreaction pathways for sequential hydrogen loss (up to five hydrogens) for parent fluorene cation, $C_{13}H_{10}^+$ , m/z 166, calculated at B3LYP/4-31G level. The C-H bond energies (in eV, ZPE x 0.957 scale factor) for particular hydrogen losses are indicated. This represents the experimentally observed route for m/z 166 $\rightarrow$ 161 sketched in Fig. 32.....	55
38. Formation of cyclic m/z 163 ( $C_{13}H_7^+$ ) and m/z 161 ( $C_{13}H_5^+$ ) ions by rupture of the $C_a-C_b$ and $C_c-C_d$ bonds in the proposed ring-opening mechanism. The final lowest energy photoproducts are formed via the opening of the specific bonds marked. ....	61



39. Formation of m/z 87 ( $C_7H_3^+$ ) and m/z 85 ( $C_7H^+$ ) from the m/z 163 (Table 3, form 163d, $C_{13}H_7^+$ ) isomer.....	65
40. Formation of m/z 89 ( $C_7H_5^+$ ) directly from m/z 163 (Table 3, form 163c, $C_{13}H_7^+$ ) isomer. ....	66
41. Optimized geometries for: (a) fluorene cation ( $C_{13}H_{10}^+$ , m/z 166), (b) fluorene cation fragment with H9' loss ( $C_{13}H_9^+$ , m/z 165), (c) fluorene cation fragment with 5 H (H9', H8, H7, H6 and H5) loss ( $C_{13}H_5^+$ , m/z 161).....	68
42. Optimized structures (B3LYP/6-31G(d, p) level) for the m/z 63, 85, 87, 89, and two different m/z 161 cations proposed as photolysis products of the fluorene cation. The bond lengths are in angstroms and angles in degrees. These are the lowest energy isomers found on the potential surface. The calculated energy of the m/z 161 cyclic isomer is 0.698 eV above the chain-triangle-ring structure.....	69
43. FTICR "action" spectrum obtained by monitoring the m/z 165 ion mass peak and scanning the irradiation wavelength with a monochromator / Xe lamp combination....	72
44. Absorption spectrum of the fluorene cation in a sec-butylchloride solid matrix at 77K. Adapted from Shida.....	72
45. Calibration curve (% dissociation vs number of laser pulses) obtained at 600 nm at a pressure of $3 \times 10^{-8}$ torr. ....	74
46. Calibration curve (% dissociation vs number of laser pulses) obtained at 600 nm at a pressure of $1.5 \times 10^{-8}$ torr. ....	74
47. FTICR action spectrum obtained by monitoring the m/z 165 ion mass peak and scanning the irradiation wavelength with the dye laser.....	76
48. FTICR mass spectrum of photolysis products after a four second irradiation of the m/z 166 ion and four second reaction delay.....	79
49. Expansion of Figure 48 showing aggregate products only.....	79
50. FTICR mass spectrum of the ion-molecule reaction products of isolated m/z 161-166 after a four second reaction delay.....	81
51. FTICR mass spectrum of photolysis products after four seconds of irradiation of isolated m/z 316-328. ....	81
52. FTICR mass spectrum of the ion-molecule reaction products of isolated m/z 50-159 after a four second reaction delay.....	82
53. FTICR mass spectrum of the ion-molecule reaction products of isolated m/z 52-68 after a four second reaction delay.....	83

54. FTICR mass spectrum of photolysis products after four seconds of irradiation of isolated m/z 219-230. ....	83
55. FTICR mass spectrum of the ion-molecule reaction products of isolated m/z 82-92 after a four second reaction delay.....	85
56. FTICR mass spectrum of photolysis products after four seconds of irradiation of isolated m/z 244-253. ....	85
57. FTICR mass spectrum of the ion-molecule reaction products of isolated m/z 87 after a four second reaction delay.....	86
58. FTICR mass spectrum of the ion-molecule reaction products of isolated m/z 89 after a four second reaction delay. ....	86
59. FTICR mass spectrum of the ion-molecule reaction products of isolated m/z 108-115 after a four second reaction delay.....	88
60. FTICR mass spectrum of photolysis products after four seconds of irradiation of isolated m/z 267-277. ....	88
61. FTICR mass spectrum of the ion-molecule reaction products of isolated m/z 131-141 after a four second reaction delay.....	90
62. FTICR mass spectrum of photolysis products after four seconds of irradiation of isolated m/z 286-302. ....	90
63. FTICR mass spectrum of the ion-molecule reaction products of isolated m/z 161 after a four second reaction delay.....	91
64. FTICR mass spectrum of the ion-molecule reaction products of isolated m/z 162 after a four second reaction delay.....	91
65. FTICR mass spectrum of the ion-molecule reaction products of isolated m/z 163 after a four second reaction delay.....	93
66. FTICR mass spectrum of the ion-molecule reaction products of isolated m/z 164 after a four second reaction delay.....	93
67. FTICR mass spectrum of the ion-molecule reaction products of isolated m/z 165 after a four second reaction delay.....	94
68. FTICR mass spectrum of the ion-molecule reaction products of isolated m/z 166 after a four second reaction delay.....	94
69. Molecular structures of naphthalene and 1,2-benzanthracene. ....	96
70. FTICR mass spectrum of photolysis products and ion-molecule reaction products after a seven second irradiation period of the m/z 128 ion.....	97

71. Expansion of the lower mass range of Figure 70 showing fragmentation products only.....	98
72. Expansion of the upper mass range of Figure 70 showing the aggregate products only.....	98
73. FTICR mass spectrum of photolysis products of m/z 128 after seven seconds of irradiation, showing a maximum dehydrogenation of two.....	100
74. FTICR mass spectrum of photolysis products after three seconds of irradiation of the isolated m/z 128 ion. ....	100
75. FTICR mass spectrum of the ion-molecule reaction products of isolated m/z 128 after a four second reaction delay.....	101
76. FTICR mass spectrum of photolysis products after a three second irradiation of the m/z 127 ion. ....	101
77. FTICR mass spectrum of the ion-molecule reaction products of isolated m/z 127 after a two second reaction delay. ....	102
78. FTICR mass spectrum of photolysis products after a three second irradiation of the m/z 126 ion. ....	103
79. FTICR mass spectrum of the ion-molecule reaction products of isolated m/z 126 after a four second reaction delay.....	103
80. FTICR mass spectrum of photolysis products after a three second irradiation of the m/z 102 ion. ....	105
81. FTICR mass spectrum of the ion-molecule reaction products of isolated m/z 102 after a four second reaction delay.....	105
82. FTICR mass spectrum of photolysis products after a two second irradiation of the m/z 102 ion while ejecting m/z 76-78. ....	106
83. FTICR mass spectrum of photolysis products and ion-molecule reaction products after a three second irradiation of the m/z 102 ion. ....	106
84. Proposed mechanism for the ion-molecule reaction of the m/z 76 ion to form m/z 202. ....	107
85. FTICR mass spectrum of photolysis products after two seconds of irradiation of isolated m/z 249-256 ions.....	108
86. FTICR mass spectrum of photolysis products after three seconds of irradiation of the isolated m/z 231-241 ions.....	108

87. FTICR mass spectrum of photolysis products after three seconds of irradiation of the isolated m/z 224-230 ions.....	109
88. FTICR mass spectrum of photolysis products after four seconds of irradiation of the isolated m/z 198-206 ions.....	110
89. Proposed fragmentation and ion-molecule reaction pathways for naphthalene. ....	112
90. FTICR mass spectrum of the photolysis products after irradiation of the m/z 228 ion (9s.).....	114
91. Expansion of the lower mass range of Figure 90 showing photolysis products only.....	114
92. Time dependence of the abundance of photoproducts of the m/z 228 ion, grouped by number of carbons. ....	115
93. Expansion of Figure 92 without the parent group, C <sub>18</sub> . ....	115
94. FTICR mass spectrum of photolysis products after 10 seconds of irradiation of the m/z 228 ion. ....	116
95. FTICR mass spectrum of photolysis products after 0.5 seconds of irradiation. ....	117
96. FTICR mass spectrum of photolysis products after 0.5 seconds of irradiation while m/z 227 was ejected. ....	117
97. FTICR mass spectrum of photolysis products after three seconds of irradiation of the m/z 228 ion. ....	118
98. FTICR mass spectrum of photolysis products after three seconds of irradiation of the m/z 228 ion while ejecting m/z 226. ....	118
99. FTICR mass spectrum of photolysis products after five seconds of irradiation of the m/z 228 ion. ....	120
100. FTICR mass spectrum of photolysis products after five seconds of irradiation of the m/z 228 ion while ejecting m/z 225. ....	120
101. FTICR mass spectrum of photolysis products after two seconds of irradiation of the isolated m/z 228 ion. ....	121
102. FTICR mass spectrum of photolysis products after 0.25 seconds of irradiation of the isolated m/z 227 ion. ....	121
103. FTICR mass spectrum of photolysis products after four seconds of irradiation of the isolated m/z 226 ion. ....	122
104. FTICR mass spectrum of photolysis products after three seconds of irradiation of the isolated m/z 209-218 ions. ....	122

105. FTICR mass spectrum of photolysis products after five seconds of irradiation of the isolated m/z 197-204 ions. ....	123
106. FTICR mass spectrum of photolysis products after irradiation (3 s.) of the isolated m/z 184-191 ions.....	124
107. FTICR mass spectrum of the ion-molecule reaction products of isolated m/z 220-228 ions after a five second delay.....	124
108. FTICR mass spectrum of possible ion-molecule reaction products formed after 9 seconds of irradiation. ....	125

Abstract of Dissertation Presented to the Graduate School  
of the University of Florida in Partial Fulfillment of the  
Requirements for the Degree of Doctor of Philosophy

FOURIER TRANSFORM ION CYCLOTRON RESONANCE MASS  
SPECTROMETRY INVESTIGATION OF THE PHOTOLYSIS OF POLYCYCLIC  
AROMATIC HYDROCARBONS

By

Mark J. Dibben

August 2001

Chairman: Dr. Martin Vala  
Major Department: Chemistry

Of the many problems currently being tackled by astrophysicists, two are of particular interest to spectroscopists and molecular physicists. These are emission observed from numerous objects in the infrared region in the interstellar medium and the absorption seen in the near infrared and visible regions. It is generally accepted that the species giving rise to these spectral features are gaseous molecules (or radical or ions), and not dust particles or grains. Polycyclic aromatic hydrocarbons (PAHs) are one class of molecules which have been proposed as carriers of these features.

In this dissertation, the effect of visible/UV irradiation on several PAHs is studied in detail. FT-ICR mass spectrometry was used to determine the photolysis products of the ionized PAHs fluorene, naphthalene and 1,2-benzanthracene in the vapor phase by irradiation with a xenon arc lamp. Products of ion-molecule reactions were also characterized for all three PAHs.

Broad-band visible and ultraviolet irradiation of ionized fluorene for relatively short times ( $\sim 0.5$ s) is shown to lead predominantly to sequential hydrogen atom loss, with one to five hydrogens lost. Rate constants and branching ratios for the photodecomposition of the fluorene parent ion and its dehydrogenated partners have been determined. Longer irradiation times lead to various products resulting from multiple C-C bond cleavages.

Density functional calculations are used to show dehydrogenation first occurs from the  $sp^3$  carbon on the five-membered ring and then from only one of the six-membered rings. Possible geometries have been calculated for all of the photoproducts.

Aggregates are shown to form from the fluorene fragments reacting with neutral molecules. These aggregates are fairly stable except for dehydrogenation and slight acetylene fragmentation.

Irradiation of the naphthalene ion for short times resulted in a maximum loss of two hydrogens. CH loss was evident as well as the sequential loss of acetylene. Aggregation of the fragmented ions was also common, including the possible formation of fluoranthene. The aggregate products of naphthalene were not as stable as those of fluorene, with many of them losing acetylene, as well as hydrogen, when irradiated.

The 1,2-benzanthracene ion was more resistant to photofragmentation than fluorene or naphthalene. Although it was capable of losing eight of its twelve hydrogens, the relative abundance of the photoproducts was only 20% after two seconds of irradiation. Sequential fragmentation of carbon atoms as well as acetylene loss was observed. The primary photoproducts did not form aggregates.

## CHAPTER 1 POLYCYCLIC AROMATIC HYDROCARBONS IN SPACE

### Introduction

There has always been an interest to discover what lies “out there” in the interstellar medium (ISM). To date, 121 molecules have been identified, including simple diatomics such as  $\text{H}_2$  and  $\text{CO}$  and extending up to the largest molecule identified so far,  $\text{HC}_{11}\text{N}$ , with 13 atoms.<sup>1</sup> However, much larger molecules are hypothesized to exist, including polycyclic aromatic hydrocarbons (PAHs). PAH-like molecules are presumed to tie up 10%-20% of the cosmic carbon budget.<sup>2</sup>

PAHs are a large and diverse group of organic compounds that are generated from fused benzene rings. Compact arrangements of the rings are known as “catacondensed” and have the highest ratio of carbon to hydrogen. A familiar example is coronene, with a central benzene ring surrounded by six more rings and the molecular formula  $\text{C}_{24}\text{H}_{12}$ . Elongated structures with a linear arrangement of benzene rings also exist and have a lower ratio of carbon to hydrogen. Examples include the smallest PAH with only two benzene rings, naphthalene ( $\text{C}_{10}\text{H}_8$ ), and pentacene ( $\text{C}_{22}\text{H}_{14}$ ), with five benzene rings.

One of the reasons for the interest in PAHs in space is they have been proposed<sup>3, 4</sup> as the species responsible for the so-called “unidentified interstellar infrared” (UIR) emission bands,<sup>5</sup> a series of bands now observed from a wide variety of objects in space. The most prominent of these bands appear at 3.3, 6.2, 7.8, 8.6 and 11.3  $\mu\text{m}$  (cf. Figure 1). Shortly after the original proposal that neutral and ionized PAHs might be responsible for



the UIRs, it was suggested that dehydrogenated PAHs might also contribute to the nearly ubiquitous UIR bands.<sup>6-14</sup> This suggestion was an attempt to rationalize the discrepancy between the intensity distributions of the observed UIR bands and laboratory infrared absorption bands of neutral PAHs. This proposal has since proven unnecessary because of the discovery that the intensity distributions of ionized PAHs more closely mimic the UIR distribution than do those of the neutral PAHs. However, the idea still retains merit because of the high photon fluxes emitted from various stellar sources that could lead to dehydrogenation. Indeed, the fluxes from some of these sources may induce even greater fragmentation of the PAHs.

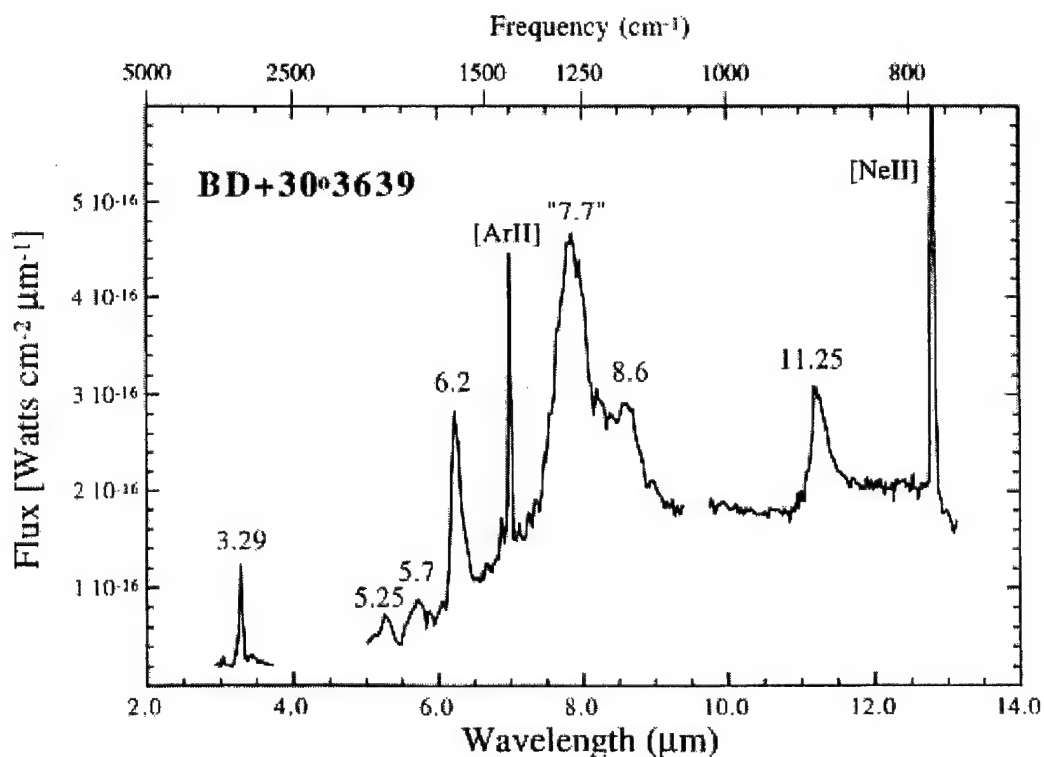


Figure 1. The Unidentified Infrared bands in BD +30°3639. Prominent bands are present at 3.29, 6.2, 7.7, 8.6, and 11.2  $\mu\text{m}$ . Adapted from Allamandola et al.<sup>15</sup>

A second reason for studying PAHs is that ionized PAHs have also been proposed as the carriers of the diffuse interstellar bands (DIB).<sup>4,5,16,17</sup> The DIB spectrum consists of more than 220 confirmed interstellar bands<sup>18</sup> spanning from the near-UV (400 nm) to the near IR (1.2  $\mu\text{m}$ ),<sup>19</sup> as shown in Figure 2. Experimental investigations have suggested that small, positively charged PAHs in matrices have absorption features that bear some resemblance to DIBs,<sup>20-22</sup> but no clear identification of a DIB with any specific PAH cation has yet been made.

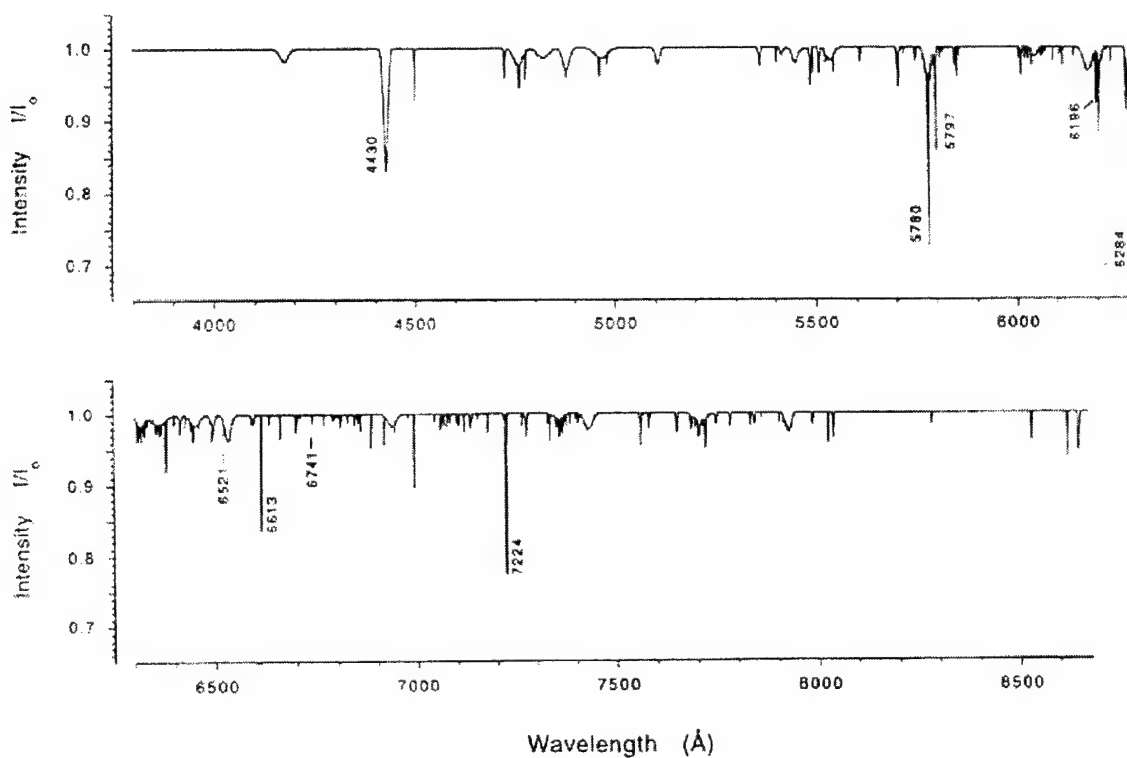


Figure 2. The Diffuse Interstellar Band spectrum. The graph is a composite of gaussian profiles fitted to all certain and probable DIBs. This spectrum is thought to be characteristic of diffuse medium matter.<sup>23</sup>

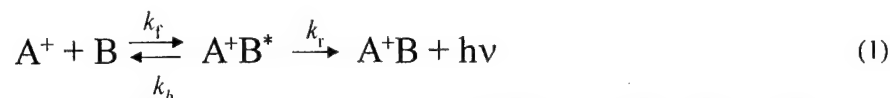
Interest in the fate of photolyzed PAHs has remained strong for many years not only because of astrophysical processes<sup>3-5, 24-26</sup> but also due to the involvement of these species in combustion.<sup>27</sup> The formation process of PAHs in space may be similar to soot formation.

### Chemistry of PAHs in Space

The mechanisms for the formation of PAHs are a very interesting topic and have been studied extensively. Formation in flames, with methane, acetylene, ethylene and other sources as fuels, has been studied both experimentally and theoretically.<sup>28-38</sup> However, because of the unique conditions in space, low temperature and low density, applicable experiments are rare, although a wealth of theories abound.<sup>39-46</sup> Temperatures are typically 10-100 K, while the density is around 50 H atoms cm<sup>-3</sup>. For dense molecular clouds this may increase up to 10<sup>6</sup> molecules cm<sup>-3</sup>.<sup>47</sup> Hydrogen is by far the most abundant element in the ISM. Carbon, nitrogen and oxygen are present at only 0.01% - 0.1% of the hydrogen abundance.<sup>48</sup> Possible formation mechanisms of PAHs include ion-molecule gas-phase chemistry, dust-grain surface chemistry, shock-induced chemistry, and fragmentation from hydrogenated amorphous carbon (HAC). The method of formation depends on the specific conditions in the ISM.<sup>49-51</sup>

Radiative association reactions between positive ions and neutral molecules play a significant role in the chemistry of dense interstellar clouds.<sup>52-54</sup> Two reactants collide to form a "collision complex" which then reverts to the reactants unless it is stabilized by the emission of radiation.<sup>39</sup> Increasing bond energy and size of the collision complex result in larger radiative association rate coefficients, especially at low temperatures.

In general, the kinetics of radiative association can be modeled by



where  $k_f$  is the (bimolecular) collision or encounter rate constant for formation of the metastable  $A^+B^*$  complex,  $k_b$  is the (unimolecular) rate constant for dissociation of  $A^+B^*$  and  $k_r$  is the rate constant for stabilization of  $A^+B^*$  by emission of an infrared photon.<sup>55</sup>

The photosphere of carbon stars is another likely place for PAH formation where the density is much higher than in the ISM. The chemical composition of C-rich giants is similar to that of acetylenic sooting flames. All the oxygen is locked up in carbon monoxide, CO, and the remainder of the carbon is found largely in  $C_2H_2$ .<sup>56</sup> The number density of hydrogen is  $10^{13} \text{ cm}^{-3}$ , the  $C_2H_2$  number density is  $10^9 \text{ cm}^{-3}$  and the temperature range is 500 to 1000 K. These conditions are ideal, since it has been shown that at temperatures less than 850 K,  $C_2H_2$  can be transformed into large PAH molecules.<sup>57</sup>

Allain et al. determined that PAHs can form rapidly and grow in the circumstellar envelope (CSE) of carbon stars.<sup>58</sup> The processes that convert  $C_2H_2$  into larger molecules and eventually carbon soot in the outflow from C-rich red giants are probably very similar to those occurring during the gas phase pyrolysis of hydrocarbon molecules.<sup>59</sup> Several different chemical pathways to soot formation have been proposed based on neutral radicals, ions, PAHs, polyacetylenic chains, or Buckminsterfullerene as intermediaries and each of these may dominate under certain conditions.<sup>60-63</sup> The formation of the first aromatic ring is the rate limiting step. Rapid chemical growth of this ring then forms larger PAHs.

The second method of PAH formation involves grain surfaces. Solid particles provide the surface where reactants can be trapped and retained until they undergo a reaction, and the solid grain itself can be one of the reactants. As an example of this process, Starukhina and Shkuratov have been able to form PAHs by irradiating graphite with accelerated  $H^+$  in conditions that are present in space.<sup>64</sup> Neither high temperature nor high pressure were required.

The third method of PAH formation is in carbon-rich asymptotic giant branch (AGB) stars through periodic shocks. These shocks travel through the inner layers of the envelope altering the temperature and density of the gas. Not only can PAHs form in this environment, but Cherchneff<sup>65</sup> discusses the formation of PAH dimers up to bi-coronene. However, the yields found in this study were quite low and indicate this method is probably not a major route of PAH formation.

Experiments by Mimura<sup>66</sup> suggest that the shock synthesis of PAHs from benzene involves the concerted cycloaddition reaction. Mimura reaches much different conclusions than Cherchneff. His experiments produced a wide variety of PAHs in a low temperature environment simulating interstellar space and suggest that shock synthesis plays an important role in chemical reactions of astrophysical processes.

The last method of PAH formation involves the release of molecules and molecular clusters from a material such as HAC during sputtering or in grain-grain collisions and is expected to lead to a variety of species whose composition and structure mimic that of the parent solid. The experimental observation that aromatic clusters with dimensions of up to several nanometers are present in HAC prior to thermal decomposition<sup>67</sup> suggests that such PAH-like fragments may be released from dust

during dissolution in photodissociation zones or in interstellar shocks. In an intense UV radiation field, HAC material will be reduced to a variety of PAHs. The smaller molecules will be destroyed while the larger will survive.<sup>68</sup> Using low-fluence pulses from a UV (308 nm) laser, Scott and Duley<sup>67</sup> have simulated the decomposition of HAC in interstellar shocks. Mass spectra of the ejecta from HAC under these conditions show the presence of a wide range of large aromatic carbon clusters including fullerenes such as C<sub>50</sub>, C<sub>60</sub>, and C<sub>70</sub>. Molecules with up to 20 C atoms are released during the initial stages of decomposition. After exposure to several UV laser pulses, molecules containing ~40 C atoms are observed.

### Unidentified Infrared Bands

In 1973 Gillett et al. was the first to observe a band in the infrared at 11.3  $\mu\text{m}$  emanating from a number of different astronomical objects.<sup>69</sup> Additional strong bands have since been discovered<sup>70-73</sup> at 3.29 and 6.2  $\mu\text{m}$  as well as a broader peak at 7.6  $\mu\text{m}$  with a shoulder at 8.6  $\mu\text{m}$  (Figure 1). The UIR bands generally cover wavelengths between 3 and 15  $\mu\text{m}$ . The emission spectra also typically exhibit several substantially weaker features and underlying continua. Early observations indicated the spectra from different objects were indistinguishable from one another. Important differences in the details have since been found.<sup>74-79</sup>

The UIR spectra are seen primarily in regions where a high UV radiation field exists: reflection nebulae, planetary nebulae, bipolar nebulae, active galaxy centers, ionization from just outside H I-H II interfaces.<sup>10</sup> However, within H II regions, the UIR emission is either very weak or absent. This is presumed to indicate the UIR carriers are

Table 1. Assignments of IR emission components within the PAH hypothesis.<sup>80</sup>

$\lambda$ ( $\mu\text{m}$ )	Assignment
3.29	Aromatic C—H stretching
6.2	Aromatic C—C stretching
7.6-8.0	Blending of aromatic C—C—C in-plane deformations
8.7	Aromatic C—H in-plane bending
11.3	Aromatic C—H out-of-plane bending (non-adjacent H)
11.9	Aromatic C—H out-of-plane bending (doubly adjacent H)
12.7	Aromatic C—H out-of-plane bending (triply adjacent H)
13.5	Aromatic C—H out-of-plane bending (quadruply adjacent H)

destroyed under these conditions.<sup>81-82</sup> It is also interesting to note that UIR bands do not occur in dust produced by oxygen-rich objects. They are present only in carbon-rich or interstellar-dust environments.

It has been proposed that the bands are the result of fluorescence of very small particles upon the absorption of a single UV photon.<sup>83</sup> The energetics require that the emitting molecules contain on the order of 20-60 carbon atoms. When one of these large molecules absorbs a UV photon, the energy is distributed over all of the vibrational modes of the molecules. The molecule relaxes by emission from C—H and C—C vibrations.<sup>79</sup> These assignments are summarized in Table 1. The 3.29 and 6.2  $\mu\text{m}$  bands correspond to aromatic C—H stretching modes. The 7.6  $\mu\text{m}$  band is a little more complex. It is a blending of aromatic C—C—C in-plane deformations. The 8.7  $\mu\text{m}$  band is due to an aromatic C—H in-plane bend while the 11.3  $\mu\text{m}$  band corresponds to the aromatic C—H out-of-plane bending. This last band is more complex as well. The

11.3  $\mu\text{m}$  band is observed if only one hydrogen is present. If hydrogens are present on the neighboring carbons, this frequency shifts to a longer wavelength, for example, 13.5  $\mu\text{m}$  for the quadruply adjacent hydrogen.

### Diffuse Interstellar Bands

While an emission process produces the UIR bands, the diffuse interstellar bands (DIBs) are due to an absorption process. They were first observed in 1922 by Heger<sup>80</sup> although they were not clearly recognized as interstellar until the work of Merrill and coworkers in the 1930's.<sup>84-86</sup> As late as 1975, only 38 DIBs had been identified.<sup>87</sup> With the advent of digital detectors, not only was the signal-to-noise ratio enhanced, but the range was extended further into the IR. Over 220 distinct bands have now been identified in the spectral range of near-UV (400 nm) to the near-infrared (1.2  $\mu\text{m}$ ), as shown in Figure 2. This number may grow even further as Weselak et al.<sup>88</sup> suggest there may be hundreds of very weak features.

The DIBs are superposed on the interstellar extinction curve and are observed toward stars of low to only moderate extinction<sup>89</sup> with strength varying as the total H I column density. The bands are characterized as diffuse because they are broad and shallow in comparison to the well-known narrow interstellar atomic lines. The full width at half-maximum (FWHM) values for the DIBs range from about 0.4 to 40  $\text{\AA}$ .<sup>18</sup>

Obviously, due to the sheer number of DIBs, more than one carrier is involved. Recent observations<sup>90-91</sup> have demonstrated that all of the strongest DIBs are of different origins because of fluctuations in individual band strengths from one line of sight to another.<sup>89</sup> However, it has been found that the newly discovered weak features may be related to the strong ones.<sup>92</sup>



It is interesting to note that DIBs are not unique to our galaxy. Heckman and Lehnert have presented evidence of DIBs in the spectra of far-IR-bright (dusty) starbursts.<sup>93</sup> Looking at seven different sources, they have found the strong features are remarkably similar to those detected in our galaxy.

Based on high-resolution astronomical observations, the present consensus is that the DIBs arise from free, gas-phase, molecular species (neutrals and/or ions) which are ubiquitous in diffuse ISM clouds.<sup>94</sup> The identification of the actual carriers of the DIBs is far from certain and is complicated in that the spectra of many of them overlap.<sup>87</sup>

The leading candidates for the DIBs are PAHs. This proposal was put forward more than a decade ago on the basis of the expected abundance of PAHs in the interstellar medium and their stability against UV photodissociation.<sup>6,7,16</sup> They are expected to be present as a mixture of free, neutral, and ionized molecules following a large-sized distribution that may range from small, gas-phase molecules to large graphitic platelets.<sup>10,95</sup> Ionized or radical PAH species have transitions in the visual (visible) part of the spectrum with considerable oscillator strength.<sup>6,7,16</sup> Abundant carbon supply in the interstellar gas can provide the PAH column densities required to explain DIB strengths.<sup>89</sup>

Ongoing laboratory investigations have revealed that small, positively charged PAHs in matrices have absorption features that bear some resemblance to DIBs,<sup>20-22</sup> but no clear identification of any DIB with any specific PAH cation has yet been made.

#### Related Efforts

Allamandola and coworkers have pointed out<sup>96</sup> that the PAHs can be expected to be extensively cycled throughout their lives. Possibly originating in asymptotic giant

branch (AGB) stars, the PAHs and other ejecta will be exposed to relatively cool photon sources. But in the course of their travels, the PAHs may also come in the vicinity of planetary nebula where they will be harshly irradiated by extremely hot stellar cores. Only those PAHs able to withstand these different radiation fields can be expected to survive in the long term. Leach and coworkers have remarked<sup>97</sup> that the existence of a limited number of PAHs is consistent with the requirements of the interstellar carbon budget, as recently revised by Snow and Witt.<sup>98</sup>

It is thus important to study the photodissociation products and pathways of the PAHs in order to understand the critical factors leading to PAH or PAH fragment structures which will retain stability over periods long on an astrophysical time scale. There have been a number of important previous studies on this topic. Cooks and coworkers used a variety of techniques including photodissociation to probe the unusual mass spectrometric decomposition behavior of PAHs and concluded that rearrangement of the carbon frameworks was probable after excitation and just prior to fragmentation.<sup>99</sup> Leger, Boissel, Desert and d'Hendecourt presented a model calculation of the "photo-thermo-dissociation" process, in which energy absorbed from a UV photon is transferred to a molecule's internal vibrations and thence induces the ejection of a hydrogen or carbon fragment.<sup>12</sup> Boissel and coworkers showed that PAH cations held in an ion trap could be photodissociated (and lose hydrogens or acetylenes) after the absorption of several low energy photons.<sup>100</sup> A theoretical model involving sequential multi-photon absorption was proposed to explain their results.<sup>101</sup> Allain, Leach and Sedlmayr developed a model for the photodestruction of PAHs in the interstellar medium and concluded that to survive the different radiation fields the PAH had to contain 50 or more

carbons.<sup>102</sup> They have also found that cations and partially dehydrogenated PAHs are less stable than their parent molecules. Photodissociation rate constants of cations may be 5 times larger than the neutral parent. For a totally dehydrogenated coronene molecule there are two orders of magnitude difference. PAHs with less than 50 carbon atoms probably do not survive more than a year in the regions of high UV radiation where the UIR are seen.<sup>102</sup>

The photoionization and photofragmentation processes in naphthalene and azulene cations were thoroughly studied by Leach and coworkers.<sup>103</sup> Jochims, Baumgartel and Leach extended earlier work on the photostability of PAHs to include irregularly-shaped PAHs, methyl-substituted PAHs and related compounds and devised a photostability index, a measure of the propensity for hydrogen loss in PAH cations.<sup>97</sup> Lifshitz and coworkers have reported numerous studies of PAHs using time-resolved photoionization mass spectrometry.<sup>104</sup> Dunbar et al. have published a series of studies on the time-resolved photodissociation (TRPD) mass spectrometry (MS) of PAH ions.<sup>105</sup> An elegant study by Dunbar and coworkers on the TRPD/MS of naphthalene cation and its infrared radiative cooling showed that this approach may be used as an independent confirmation of absolute infrared intensities obtained from matrix studies or theoretical calculations.<sup>106</sup> Guo, Sievers and Grutzmacher used the SORI -CID (sustained off-resonance irradiation collision induced dissociation) method<sup>107</sup> to study sequential hydrogen loss from a series of PAHs.<sup>108</sup> Structural rearrangements were invoked to explain their results. Theoretical work on the probable stable fragments after acetylene loss from photoexcited naphthalene, anthracene and phenanthrene cations has been reported by Granucci et al.<sup>109</sup> and Ling et al.<sup>110</sup> Schwartz and coworkers, using a

combination of mass-spectrometric experiments, found that the loss of acetylene upon dissociative ionization of naphthalene did not lead to phenylacetylene, but probably to benzocyclobutadiene,<sup>111</sup> as predicted by Ling et al.<sup>110</sup> Other acyclic structures could not be excluded and are still possibilities. Joblin and coworkers laser-ablated pyrolyzed coronene into a Fourier transform ion cyclotron resonance mass spectrometer (FTICR/MS) and found evidence for larger, highly dehydrogenated oligomer species.<sup>112</sup> Ekern and coworkers reported the complete dehydrogenation of coronene ( $C_{24}H_{12}^+$ ) and naphthopyrene ( $C_{24}H_{14}^+$ ) using FTICR/MS with brief (500ms) UV/visible photolysis exposures.<sup>113</sup> In a later report, these workers investigated a wide variety of PAH cations using FTICR and found evidence for dehydrogenation and fragmentation using broadband photoexcitation.<sup>114</sup>

## CHAPTER 2

### FUNDAMENTALS OF FOURIER TRANSFORM ION CYCLOTRON RESONANCE MASS SPECTROMETRY

Fourier transform ion cyclotron resonance (FT-ICR) mass spectrometry has grown exponentially since its development in 1973. Over 325 instruments have been installed worldwide.<sup>115</sup> One of the major reasons for the popularity and the rise in the use of FT-ICR is that it offers 10-100 times higher mass resolution and mass accuracy than any other mass analysis technique.

#### Historical Perspective

Although FT-ICR instrumentation is less than 30 years old, its roots can be traced back to experiments performed by Lawrence and Livingston in the 1930's. In 1932 they demonstrated that a charged particle moving perpendicular to a uniform magnetic field is constrained to a circular orbit in which the angular frequency of the particle's motion is independent of the particle's orbital radius.<sup>116</sup> This motion is given in the cyclotron equation:

$$\omega = \frac{qB}{m} \quad (2)$$

where  $\omega$  is the angular frequency,  $q$  is the particle charge,  $B$  is the magnetic field strength and  $m$  is the particle mass. This equation shows that particles with different mass-to-charge ratios have unique cyclotron frequencies. Such behavior is central to the detection of ions in the FT-ICR technique.

The “Omegatron,” developed by Sommer and Hipple in 1951,<sup>117</sup> was the first mass spectrometer to use the cyclotron motion to detect ions according to their mass-to-charge ratio. Resonant excitation was produced by applying a continuous spatially uniform differential rf voltage between two opposed flat electrodes to excite ions in an orbit of increasing radius.<sup>118</sup> The ions increased in radius along an Archimedes spiral until they were detected by the current produced when they hit a collector plate as shown in Figure 3. A  $m/z$  spectrum was acquired by slowly scanning the field of an electromagnet to bring ions of different  $m/z$  into resonance.

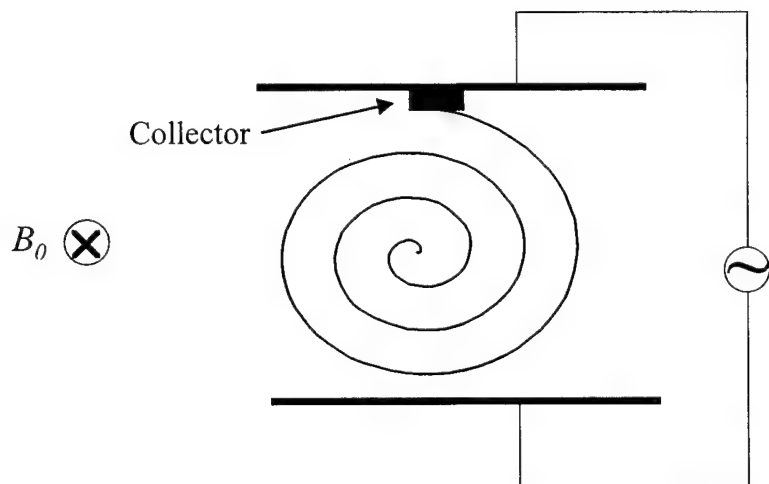


Figure 3. Schematic of the Omegatron in which ions are accelerated continuously to larger cyclotron radius until they strike a collector electrode. Adapted from Mashall<sup>118</sup>.

A method to detect ion resonant power absorption was the next step in the development of the FT-ICR, shown in Figure 4. The idea was introduced by Wobschall at Cornell<sup>119</sup> and developed by Llewellyn at Varian<sup>120</sup> and Baldeschwieler’s group at

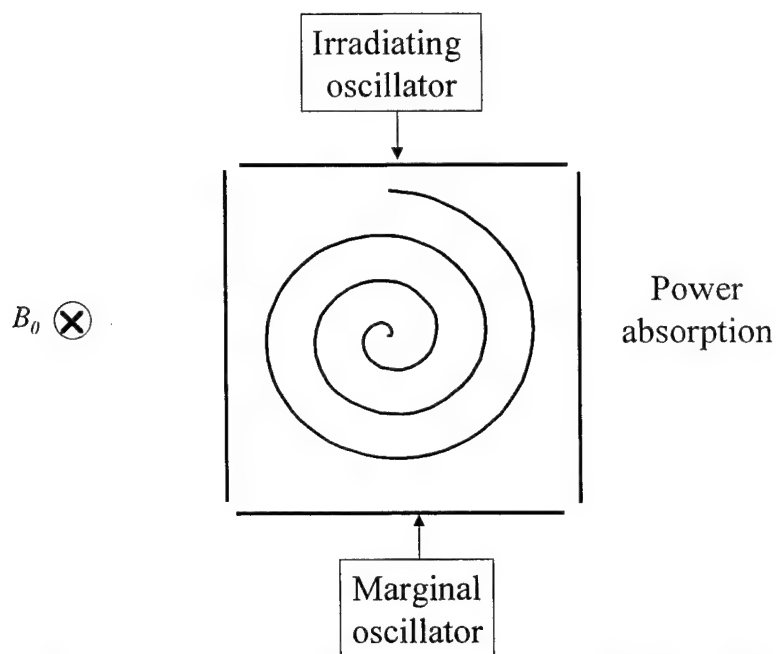


Figure 4. Power absorption measurement (with a marginal oscillator) during simultaneous resonant excitation. A mass spectrum is obtained by slowly varying the magnetic field at fixed excitation/detection frequency. Adapted from Marshall<sup>118</sup>.

Stanford.<sup>121, 122</sup> Ion counting was no longer performed but mass spectrometry was still performed at a fixed rf frequency by scanning the magnetic field.

In 1974 Comisarow and Marshall<sup>123, 124</sup> demonstrated the first application of FT methods to ICR mass spectrometry. Their background in NMR spectroscopy was evident in the crossover of many of the ideas in NMR to ICR. Using a Fourier transform method, all ions could be excited and detected at the same time.

### Motion of Trapped Ions

Because an ion is a charged particle, when it is moving in the presence of spatially uniform electric and magnetic fields,  $\mathbf{E}$  and  $\mathbf{B}$ , it is subjected to the “Lorentz” force given by<sup>125</sup>

$$\text{Force} = \text{mass} \times \text{acceleration} = m \frac{d\mathbf{v}}{dt} = q\mathbf{E} + q\mathbf{v} \otimes \mathbf{B} \quad (3)$$

where  $m$  is the ionic mass,  $q$  is the charge, and  $\mathbf{v}$  is the velocity. The vector cross product term means that the direction of the magnetic component of the Lorentz force is perpendicular to the plane determined by  $\mathbf{v}$  and  $\mathbf{B}$  as shown in Figure 5.

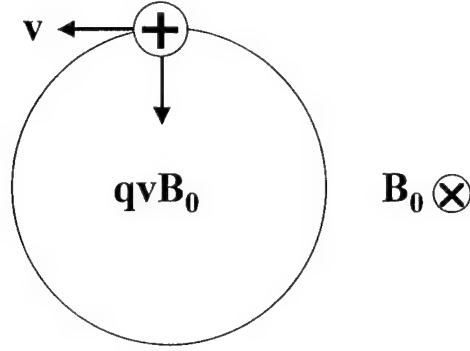


Figure 5. Origin of ion cyclotron motion. The path of an ion moving in the plane of the paper is bent into a circle by the inward-directed Lorentz magnetic force produced by a magnetic field directed perpendicular to the plane of the paper. Adapted from Marshall and Verdun<sup>125</sup>.

In the absence of an electric field, equation 3 becomes:

$$F_L = q\mathbf{v} \otimes \mathbf{B} \quad (4)$$

Likewise, the centrifugal force experienced by an ion is given by:

$$F_c = m\mathbf{v}^2 / r \quad (5)$$

When the Lorentz force and the centrifugal force are equal to each other, the ion will be in a stable orbit given by:

$$m\mathbf{v} / r = qB \quad (6)$$

$\mathbf{v}/r$  is equal to the angular frequency,  $\omega$ . Substituting this into equation 6 and rearranging yields the celebrated “cyclotron” equation.<sup>126</sup>



$$\nu_c = \frac{qB}{2\pi m}, \text{ where the substitution } \omega_c = 2\pi\nu_c \text{ has been made.} \quad (7)$$

This equation is graphed in Figure 6 for various magnetic field strengths. Clearly, the orbital frequency increases with increasing magnetic field strength and decreases with increasing  $m/z$ .

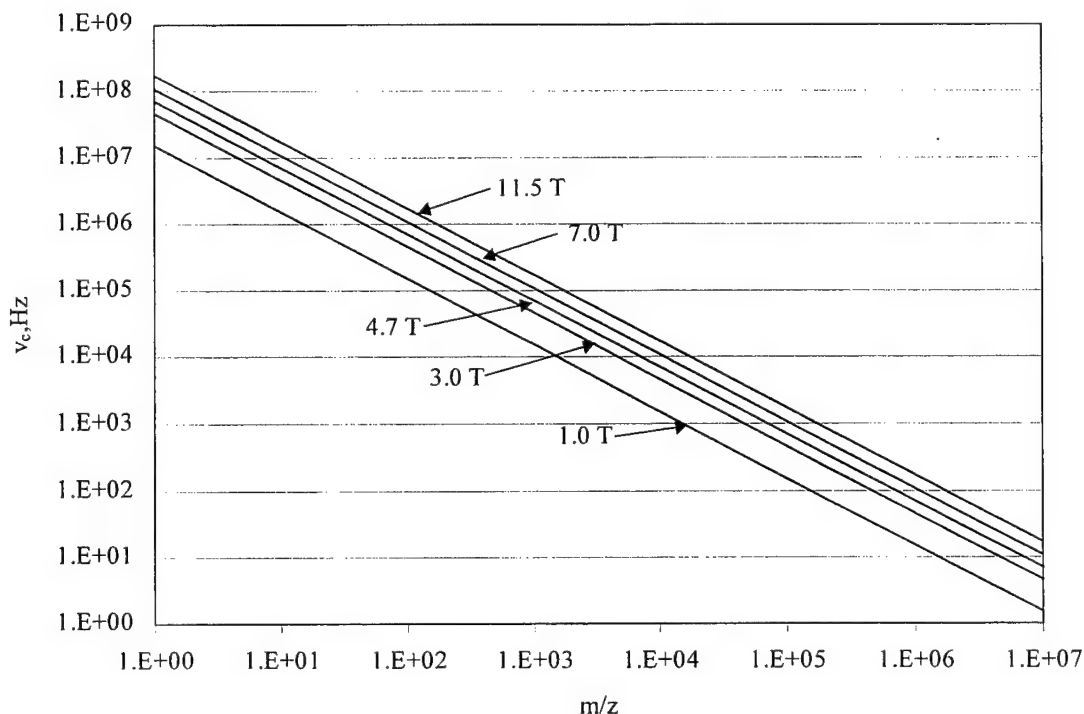


Figure 6. ICR orbital frequency,  $\nu_c = \omega_c/2\pi$ , in Hz, as a function of ionic mass-to-charge ratio,  $m/z$ , in Daltons per multiple ( $z$ ) of the elementary electron charge, at each of five magnetic field strengths: 1.0, 3.0, 4.7, 7.0, and 11.5 tesla. Note that ICR frequencies for ions in the usual “chemical” mass-to-charge ratio ( $\sim 15 < m/z < 10,000$ ) typically lie between a few kHz and a few MHz. Adapted from Marshall et al.<sup>126</sup>.

Another important figure of merit for ICR instruments is the orbital radius. This is graphed by rearranging equation 6 and is shown in Figure 7 for various magnetic field strengths. Even rather large ions are conveniently confined in small orbits.

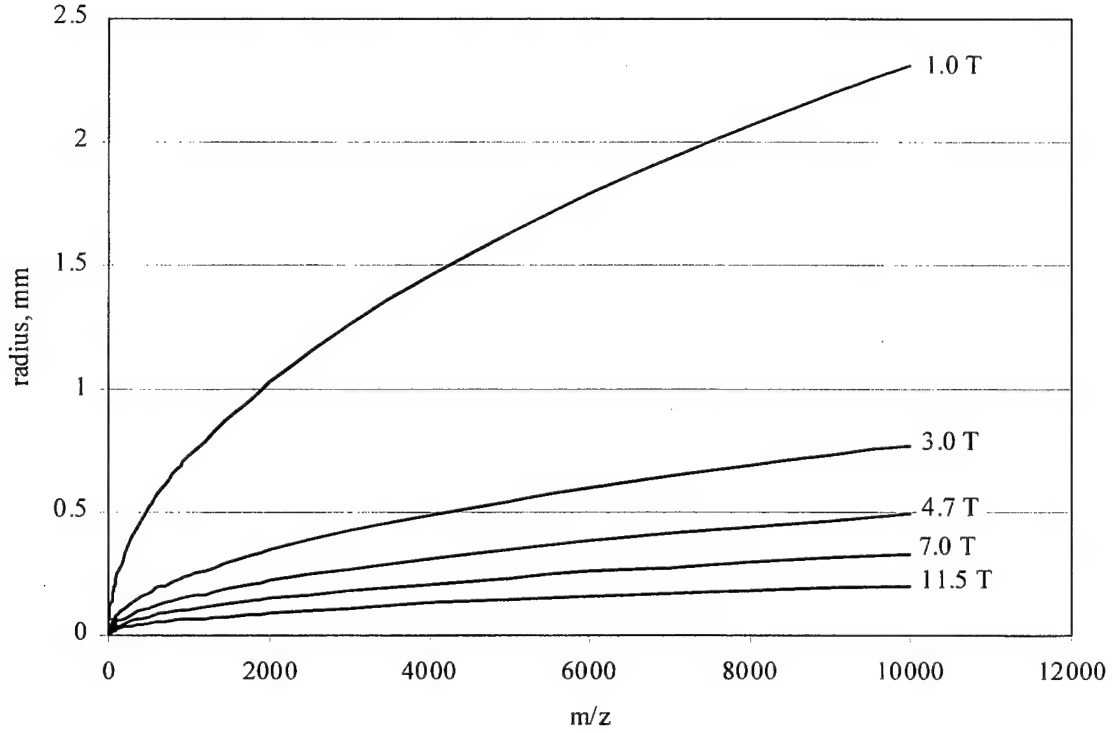


Figure 7. ICR orbital radius,  $r$ , vs. ionic mass-to-charge ratios,  $m/z$ , (in  $u$  per multiple of elementary electronic charge) at each of five representative magnetic field strengths: 1.0, 3.0, 4.7, 7.0, and 11.5 tesla at 298 K. Note that even relatively heavy ions are confined to conveniently small-radius orbits by such magnetic fields. Adapted from Marshall et al.<sup>126</sup>.

As will be shown later, the normal radius of ions in a cyclotron orbit is too small to be detected. However, since ion kinetic energy is equal to  $\frac{1}{2}mv^2$ , this can be substituted into equation 6 and yields the following equation:

$$\text{K.E.} = \frac{q^2 B_0^2 r^2}{2m} \quad (8)$$

This equation for kinetic energy is plotted against radius in Figure 8. By adding energy to an ion, the cyclotron frequency does not change but the radius of orbit increases.

Ions in a magnetic field are subject to two other motions besides the ion cyclotron motion. These are the trapping oscillation and magnetron motion. Although ions are

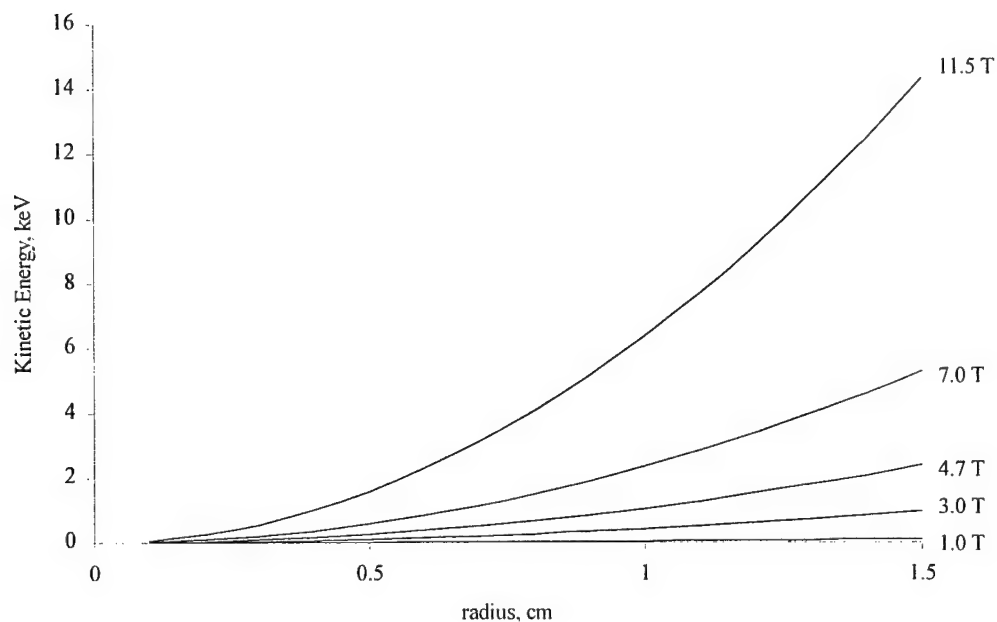


Figure 8. Ion translational (kinetic) energy (Eq. 7) as a function of ICR orbital radius, at five different magnetic field strengths: 1.0, 3.0, 4.7, 7.0, and 11.5 tesla, for an ion of  $m/z=100$ . Ions may be accelerated to relatively high energy while still confined to relatively small orbital radii. Adapted from Leger et al.<sup>12</sup>.

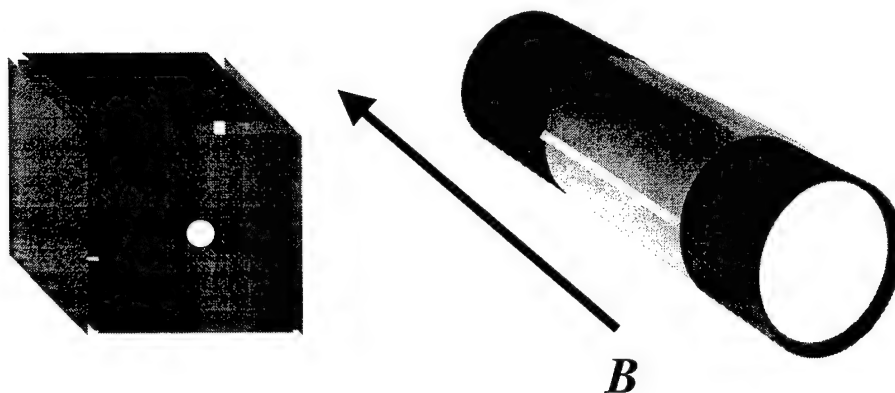


Figure 9. A cubic analyzer cell and a cylindrical, open-ended cell. The arrow shows the orientation of the magnetic field lines.

constrained in the x-y plane by the magnetic field operating in the z-direction, they are free to travel parallel to the field. In 1970, McIver<sup>127</sup> introduced the cubic trapped cell (Figure 9). The two plates perpendicular to the magnetic field are the trapping plates. Ionizing electrons are introduced into the cell through a small hole in one trapping plate.

A small positive voltage applied to the two trapping plates confines ions inside the cell to a simple harmonic oscillation. Likewise, a small negative voltage will trap negative ions.

The third fundamental motion of ions in a magnetic field is called “magnetron” motion. This motion arises from the presence of an electric field inside the cell. Ions precess about lines of constant electrostatic potential. This frequency, which is mass independent, is normally much less than the cyclotron frequency, on the order of a few hundred hertz compared to kHz-MHz for the cyclotron motion. Therefore the magnetron motion is normally ignored.

### Instrument Overview

There are four basic parts to every ICR mass spectrometer. These are the magnet, vacuum system, analyzer cell and data acquisition system. Each subsystem will be discussed briefly while specifics of the instrumentation used in this study will be discussed later in this chapter.

#### Magnet

As shown in Figures 6-8, as well as in the equations relating to ion motion, magnetic field strength is very important. The earliest magnets were simply permanent magnets. Because of their intrinsically low field strengths, they have been used very little. Electromagnets were used on early systems, however, they are limited to field

strengths on the order of 2T or less. Hence, they are seldom used in modern instrumentation.

By far the most common type of magnet is the superconducting magnet. These are solenoidal magnets that are cooled with liquid nitrogen (boiling point 78 K) and liquid helium (boiling point 4 K). The highest magnetic field strength currently being used is 11.5 T at Pacific Northwest National Laboratory.

### Vacuum System

The next important part of an ICR system is the vacuum system. Mass spectrometers of all types require reduced pressure for efficient formation, transportation, and detection of ions. The pressure requirements for a magnetic sector instrument are around  $10^{-6}$  torr while FT-ICR analysis requires a background pressure on the order of  $10^{-9}$  to  $10^{-10}$  torr and an operating pressure only slightly higher. This constraint necessitates the use of cryogenic or turbomolecular pumps as opposed to diffusion pumps. The low pressure is actually only needed for the excitation and detection of the ions. Many experiments, such as collision induced dissociation, take place at much higher pressures.

### Analyzer Cell

The third part of the FT-ICR system is the analyzer cell, which is responsible for trapping, exciting and detecting the ions. As opposed to normal mass spectrometers, which analyze and detect in “space” (i.e. ions interact with and move along the magnetic fields), FT-ICR mass spectrometers analyze and detect in “time.” This allows an operator to not only do MS-MS experiments, but theoretically to do  $MS^n$  experiments, as long as a sufficient number of ions are present.

The earliest type of cell was the cubic cell as shown in Figure 9. The trapping plates are perpendicular to the magnetic field (front and rear). One plate has a hole that allows ionizing electrons to enter along the magnetic field lines. The four plates parallel to the magnetic field work as pairs. Two opposing plates are used for excitation while the remaining pair is used for detection. These functions will be described in greater detail later.

Figure 9 also pictures a more common type of cell, the cylindrical cell. It functions in a similar way to the cubic cell, but is easily adaptable to the round bore of FT-ICR superconducting magnets. The two end cylinders act as trapping plates, while the middle cylinder, which is divided into four electrically isolated sections, is used for excitation and detection. As in the cubic cell, opposite pairs of plates are used for excitation and detection.

#### Data Acquisition

The last major part of the FT-ICR system is data acquisition. Important components include a frequency synthesizer, delay pulse generator, broadband radio frequency amplifier and pre-amplifier, and a fast transient digitizer.<sup>128</sup> Large amounts of data are collected in very short times. Current computers are able to handle this data flow as well as process and analyze the data in “real-time.”

#### Experimental Procedures

A basic FT-ICR experiment consists of quench, ionization, excitation and detection events (Figure 10). The quench event is used to clear the analyzer cell of any ions remaining from a previous experiment and is accomplished by applying positive

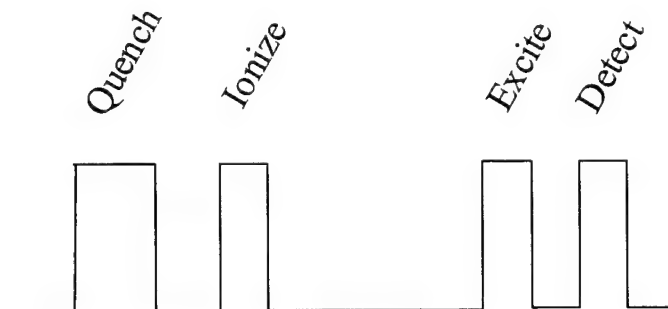


Figure 10. The basic steps in an experimental sequence using FTMS.

(+10 V) and negative (-10 V) voltages to the opposing trapping plates. Ions are then ejected axially from the cell.

The ionization event can be applied either in or near the analyzer cell or completely outside the magnetic field. One of the earliest methods was electron ionization (EI).<sup>129</sup> Electrons, formed from a rhenium or tungsten filament, are accelerated at voltages of 10 – 70 eV, and directed at the neutral gas phase sample. The electron impact on the sample gas provides sufficient energy to form positive ions. This method works especially well with samples that have a relatively high vapor pressure. Alternatively, low vapor pressure samples can be brought into the gas phase through use of a solids probe. The sample is brought close to the cell and then heated. Although EI can be performed external to the magnetic field, it is normally an internal method of ionization. This is advantageous because ion trapping efficiency is greater due to magnetic field focusing, ion loss in directions transverse to the magnetic field is minimized and ions do not have to cross the fringe field of the magnet to enter the trap.<sup>115</sup> Chemical ionization is another method that is normally performed internally.<sup>130</sup>

Even with all of the advantages of internal ionization listed above, most methods rely on external ionization. This is because external sample introduction and/or ionization devices can be attached to an existing FT-ICR MS without extensive modifications. These include gas chromatography,<sup>131</sup> pulsed valves,<sup>132</sup> supercritical fluid chromatography,<sup>133</sup> liquid chromatography<sup>134, 135</sup> and electrospray ionization.<sup>136, 137</sup> Another reason for external ionization is that many methods require high pressure, which is incompatible with FT-ICR mass analysis. Multiple pumping stages are used to decrease the pressure between external sources and the analyzer cell in FT-ICR MS.

After ionization, the sample ions are subjected to an excitation pulse (cf. Fig. 10). Normally, after ions are formed and trapped, their kinetic energy is relatively small. Thus, their orbital radius is small compared to the dimensions of the cell. Increasing the radius will assist in the detection of the ions. Applying a sinusoidal voltage to the excitation plates will increase the kinetic energy and radius of the sample ion. Only ions in resonance with the applied r.f. voltage absorb energy. The ions are excited coherently and undergo cyclotron motion as a packet. If the voltage is applied for too long a period, the ions will continue to spiral outward until they hit the cell walls. This can be done intentionally to neutralize ions of certain masses and thus isolate others.

The first time-domain excitation pulses for FT-ICR MS used single-frequency pulses.<sup>123</sup> Also called an impulse, this waveform excited one specific mass-to-charge ion coherently. A more usable waveform is the frequency-sweep or chirped pulse.<sup>138</sup> All masses with a cyclotron frequency between the starting and ending frequencies are sequentially excited. The time scale, a few milliseconds, is short compared to other parameters so that the time differences in the excitation of different  $m/z$  ions are



insignificant. Although chirps are frequently used today, Marshall has developed a more exact waveform to be used in excitation. SWIFT, Stored Waveform Inverse Fourier Transform, is the optimal ICR excitation waveform.<sup>139, 140</sup> Nearly any combination of mass-to-charge ions can be excited. Figure 11 illustrates the versatility of SWIFT. In this example, ions with a mass of  $m/z$  112-116 and  $m/z$  165-168 have been selected. The cyclotron frequencies are calculated from the masses. By applying an inverse Fourier transform, the appropriate time-domain waveform is generated. By applying a high enough voltage, selected ions are excited and ejected from the cell while all other masses remain unexcited.

The last step is detection of the ions. Detection plates, like excitation plates, are set up opposite one another. As the excited ions pass near a detection plate they attract electrons. As they orbit within the cell a sinusoidal image current is generated from the cyclotron motion of the ions. This image current can then be amplified, digitized and stored on a computer. This method of detection is different from other mass spectrometers such as magnetic sector instruments. In FT-ICR MS, ions are analyzed non-destructively. After analysis, they are still present and can be acted upon again. On the other hand, magnetic sector instruments analyze destructively, since ions are neutralized on a detection surface. Figure 12 is an illustration of the conversion of an image current into a usable mass spectrum. The time domain spectrum, shown in the upper panel, consists of 64k data points. The mathematical technique of Fourier transformation converts this into a usable frequency domain spectrum. Using equation 7, presented earlier, this spectrum is easily modified into a mass spectrum.

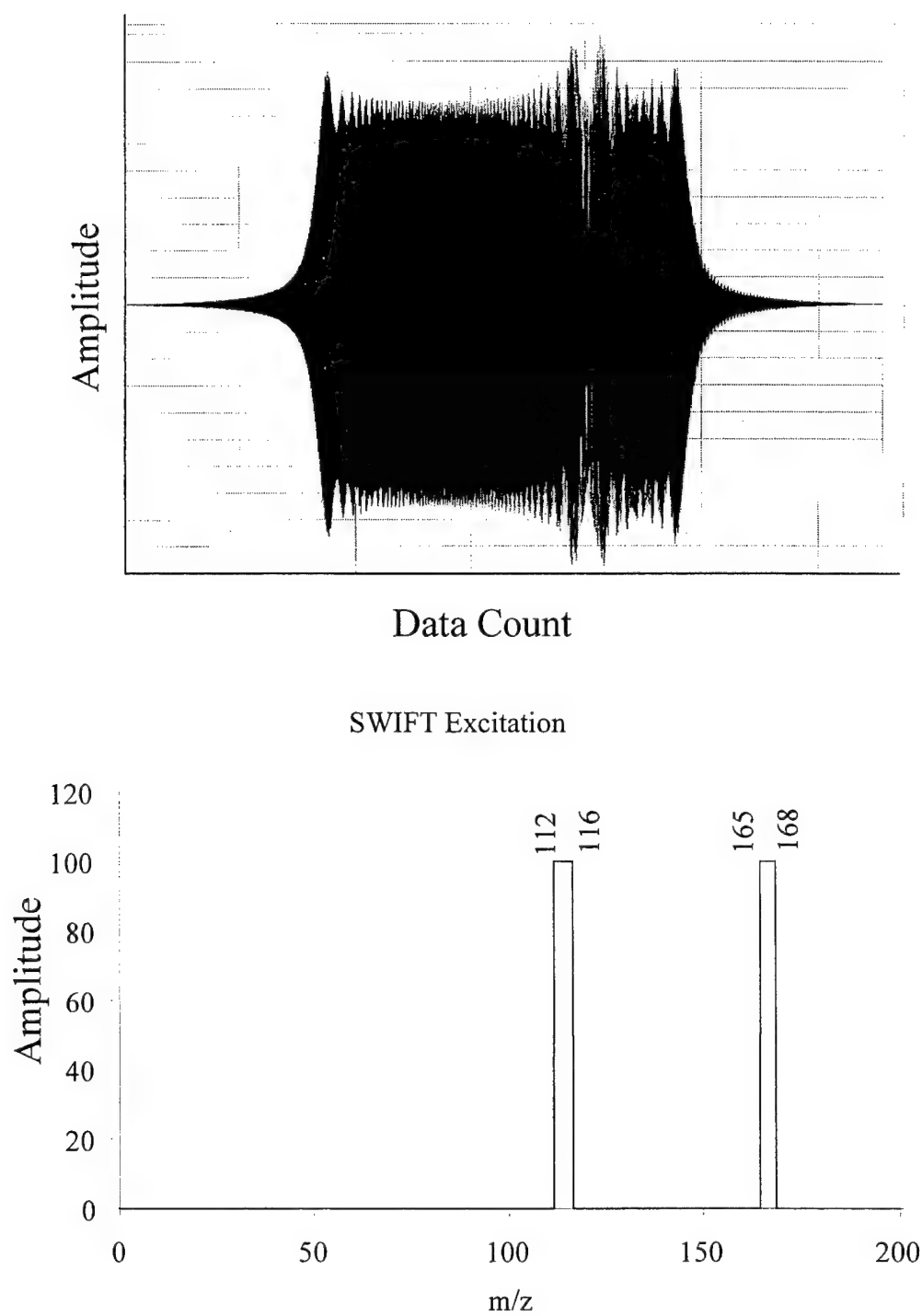


Figure 11. Excitation corresponding to selected mass ranges ( $m/z$  112-116 and 165-168) in the lower panel is converted into a SWIFT excitation waveform (upper panel) by inverse Fourier transform.

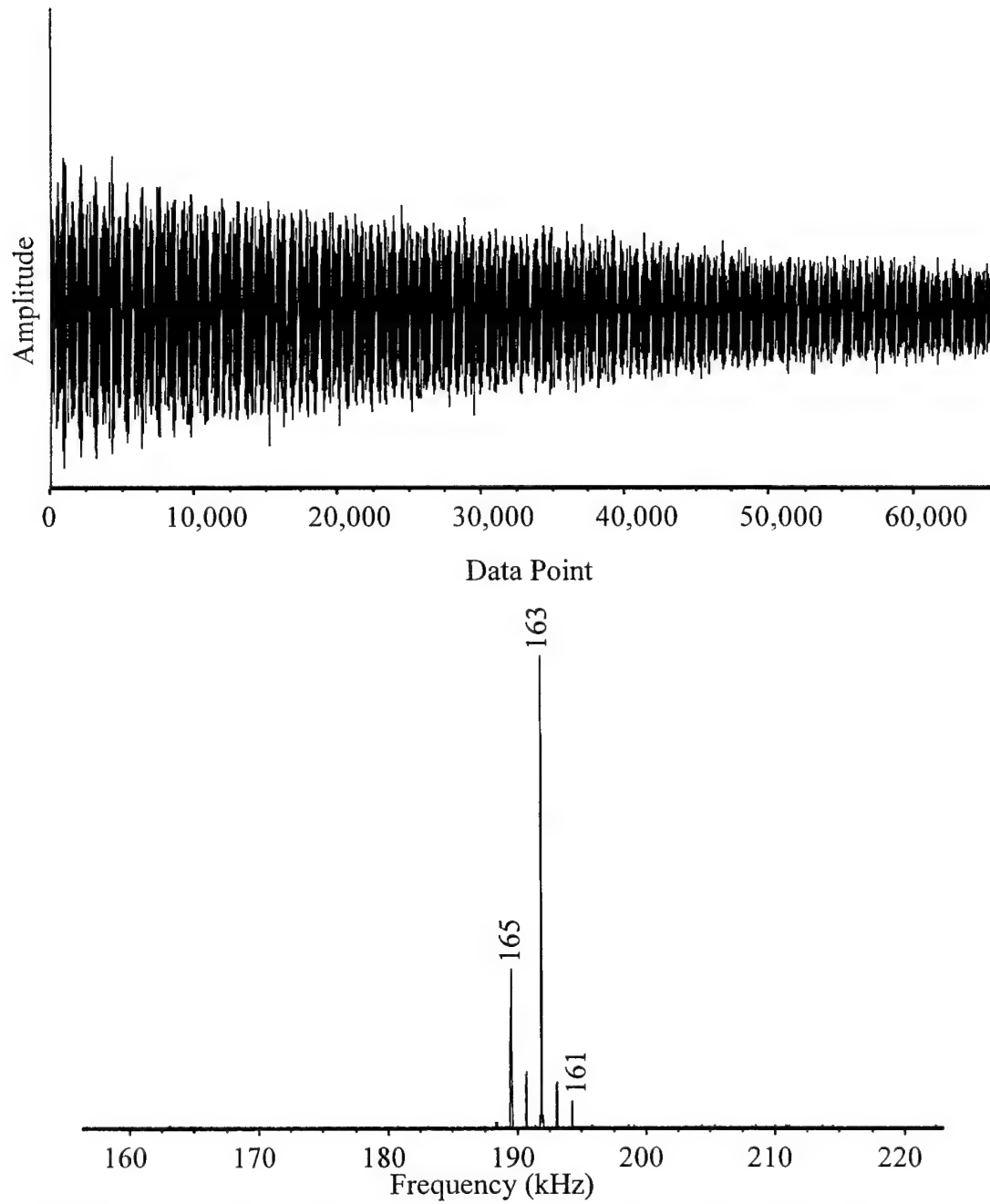


Figure 12. Transformation of the time domain spectrum (upper panel) to the frequency domain spectrum (lower panel). Since frequency is inversely related to the mass, the masses appear in reverse order.

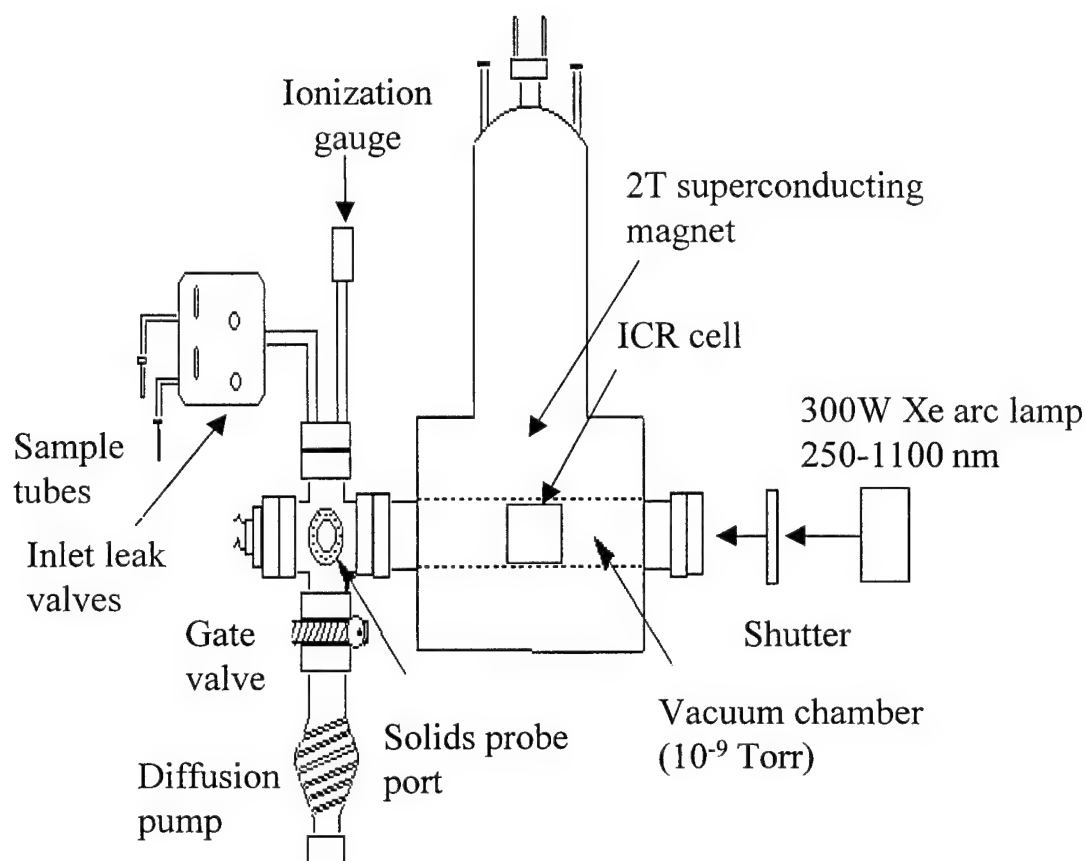


Figure 13. Schematic of the 2 tesla FT-ICR instrument. Vapor from liquid or high volatility solids can be inlet through the sample tubes and controlled with the leak valves. The solids probe is used for low volatility solids. The electronically controlled shutter allows the lamp to illuminate the cell through a window. Adapted from Kage<sup>142</sup>.

#### Experimental Parameters Used in this Study

All experiments were performed using a home-built 2 Tesla FT-ICR mass spectrometer (Figure 13). The magnetic field was calibrated to be 2.038 T. The vacuum system consisted of a  $700 \text{ L s}^{-1}$  oil diffusion pump (Alcatel Vacuum Products, Hingham, MA) that was backed by a mechanical pump (Alcatel Vacuum Products, Hingham, MA). Background pressures were typically  $1\text{-}2 \times 10^{-9}$  torr while the operating pressure was

normally  $4 \times 10^{-8}$  torr. A cylindrical cell 2.7 inches in diameter and 4.5 inches in length was used.

The heart of the ICR is its data acquisition system. In the FT-ICR mass spectrometer used in this work, a new data system called MIDAS (Modular ICR Data Acquisition System) was acquired. The system was developed in the National High Field FTICR Facility at the National High Magnetic Field Laboratory (NHMFL) in Tallahassee, FL.<sup>141</sup> Figure 14 illustrates the MIDAS system. An ISA-MXI bus interface connects a PC to a five-slot VXI chassis. Pulse timing is initiated in a digital pattern generator (DG600VXI, Interface Technology) and expansion card (DG605VXI), both of which are interfaced to an instrument control module (ICM) that controls four 12-bit DC voltage outputs, four 8-bit DC voltage outputs and sixteen TTL triggers. The electron gun is also under the control of the ICM. An arbitrary waveform generator (Tektronix VX4790A) is used to generate the excitation waveforms. Up to sixteen unique waveforms may be used in a single experiment. The waveforms are amplified via an RF power amplifier (ENI 2100L M2). A digitizer (Hewlett-Packard E1437A) collects the time domain signals generated by excited ions after amplification.

A 300-watt xenon arc lamp (ILC Technology, Model LX300UV) was the illumination source. It provided continuous output between 250 and 1100 nm. The lamp was focused by a fused silica lens and illuminated the ions through a quartz window in the end of the ICR vacuum chamber. An electronically operated shutter (Vincent Associates, Uniblitz VS35S2ZM1R1) was used to control the length of the irradiation pulses. The shutter diameter was 35mm and it required approximately 13 msec to open and 12 msec to completely close.

### Modular ICR Data Acquisition System

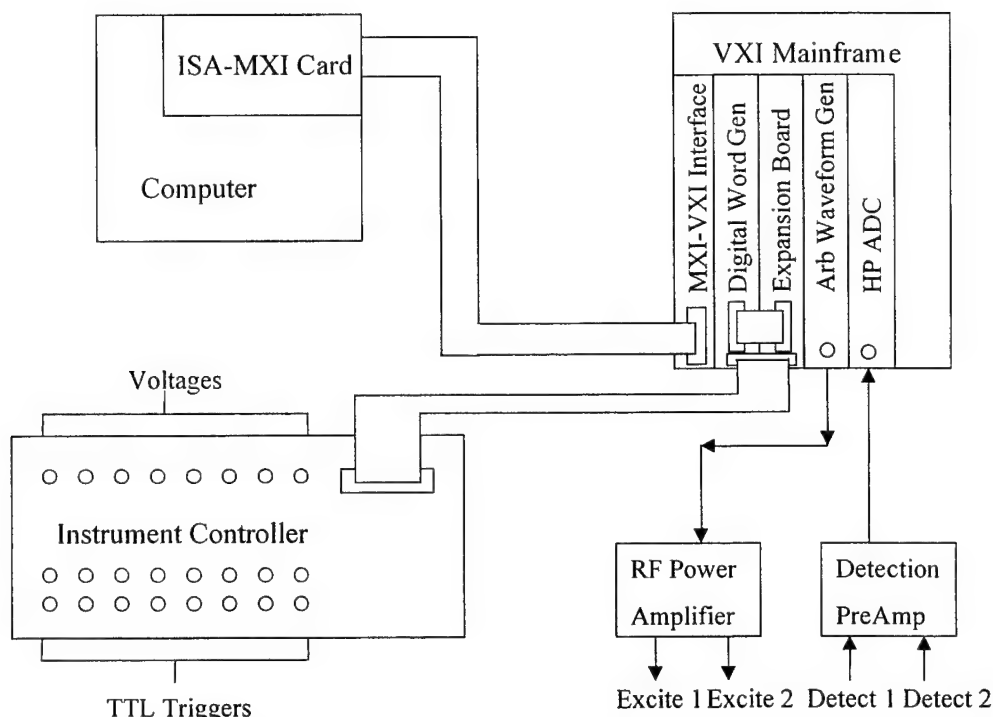


Figure 14. Schematic of the MIDAS hardware. Adapted from Senko et al.<sup>141</sup>.

A typical timing sequence is shown in Figure 15. Following a quench pulse, to clear the cell of ions from previous experiments, the sample was ionized by electron impact. To minimize fragmentation, the ionizing voltage was set as low as possible ( $\sim 14$  eV) while still producing a usable signal. Higher voltages created many fragments while lower voltages did not provide enough ions. An isolation step using a SWIFT pulse retained the fluorene parent ion while ejecting any fragments, as well as  $^{13}\text{C}$  isotopes. The Xe arc lamp then irradiated the sample for a period of 1-4 seconds. After illumination, the photofragments could be isolated for further experimentation, again by using a SWIFT waveform, and irradiated. The final step was excitation using a standard chirp pulse followed by detection.

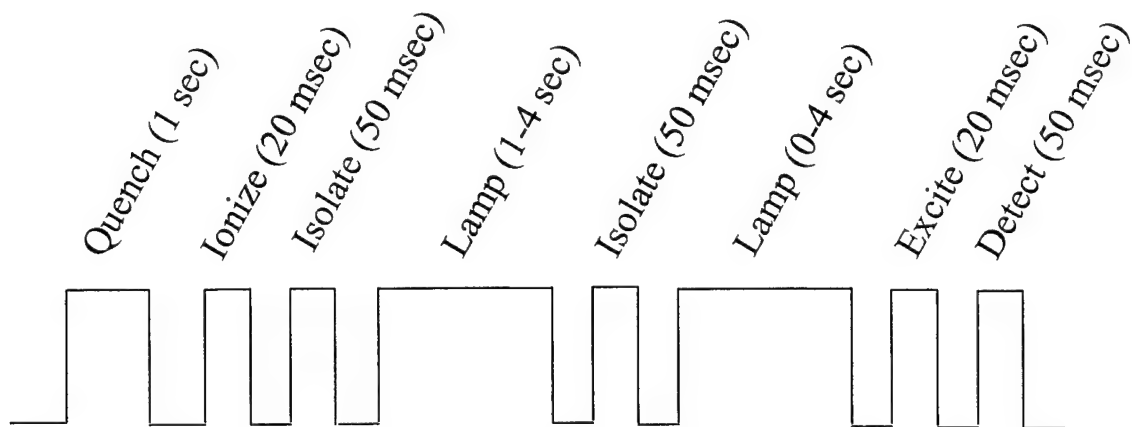


Figure 15. Typical pulse sequence. This includes SWIFT isolation of the parent ion, irradiation by the Xe arc lamp, isolation of one or more of the photofragments, further irradiation and finally chirp excitation and detection.

The PAH sample (Aldrich) was inlet to the system through a leak valve (Varian, Model 951-5100) for the samples with relatively high volatility such as fluorene, naphthalene and anthracene. The solids probe was used for the samples with a lower volatility such as tetracene and 1,2 benzanthracene.

## CHAPTER 3 PHOTODISSOCIATION OF FLUORENE CATION

### Introduction

The fluorene molecule,  $C_{13}H_{10}$ , was the primary PAH (polycyclic aromatic hydrocarbon) studied. Its structure is shown in Figure 16. Photodissociation of the fluorene cation using a xenon arc lamp resulted in sequential hydrogen loss, and further fragmentation. Rate constants and fragmentation pathways were determined.

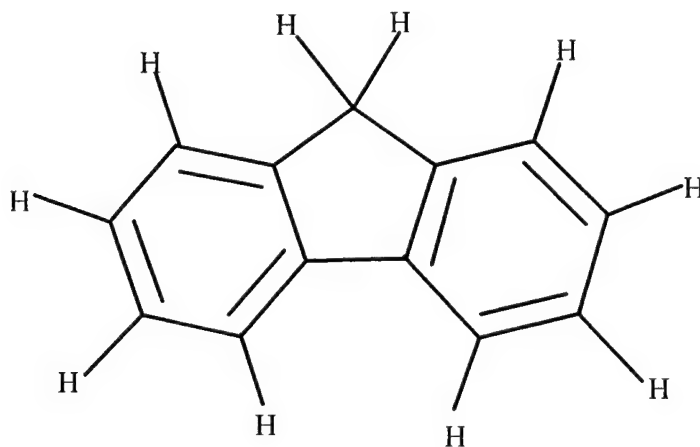


Figure 16. Fluorene Molecule,  $C_{13}H_{10}$ , mass 166.

### Hydrogen Loss

It has previously been shown that when irradiated for brief periods (500 ms), the fluorene cation loses up to five hydrogens.<sup>114</sup> Figure 17 clearly shows this. Information on the mechanism of this loss was not reported, however. Questions that remain include:



1) Are the hydrogens lost sequentially or simultaneously? 2) Are they lost as atoms (or molecules)? 3) From which positions are the hydrogens stripped?

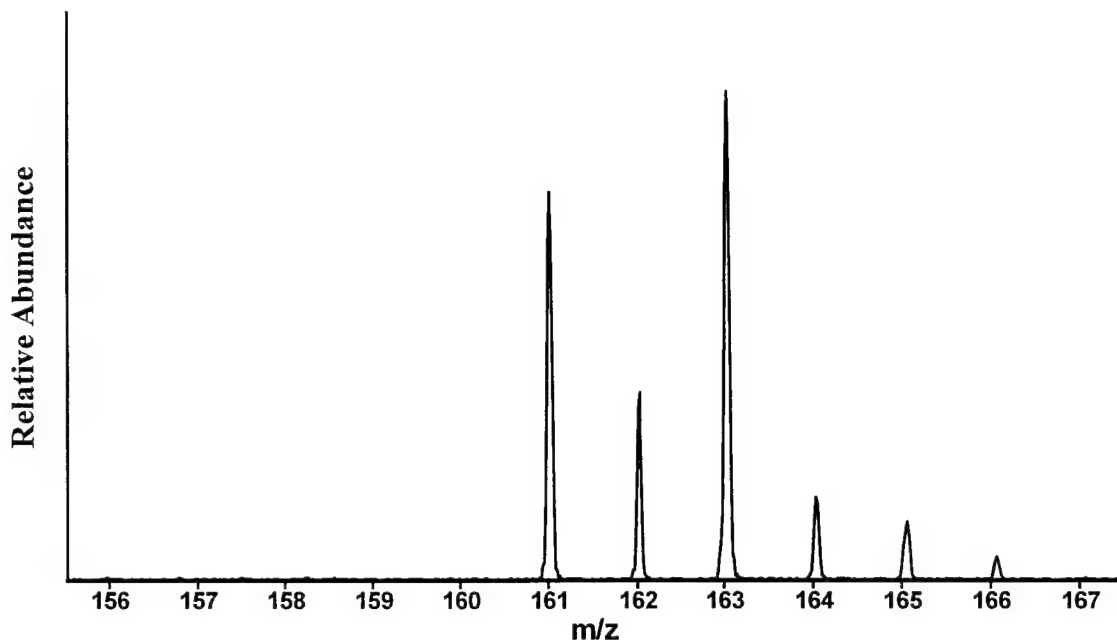


Figure 17. FTICR mass spectrum of photolysis products after a four second irradiation period of the  $m/z$  166 ion.

Figure 18 shows a plot of the time-dependence of the photolysis of the parent and its five dehydrogenated products. Irradiation was effected with the broadband output of a Xe arc lamp as described in Chapter 2. Shortly after commencement of irradiation, the  $m/z$  166 parent ion abundance has decreased precipitously, while the  $m/z$  165 product abundance has grown rapidly and is the dominant species after ca. 200 ms. After 1.5s of photolysis, the  $m/z$  163 product has increased substantially and is now the predominant product. Fragments at  $m/z$  161, 162, 164 and 165 also become visible, but never rise above ca. 15% abundance.

Although the intensity vs. time plot in Figure 18 suggests sequential hydrogen loss, the following procedure was used to prove this mechanism. After ionization, each of

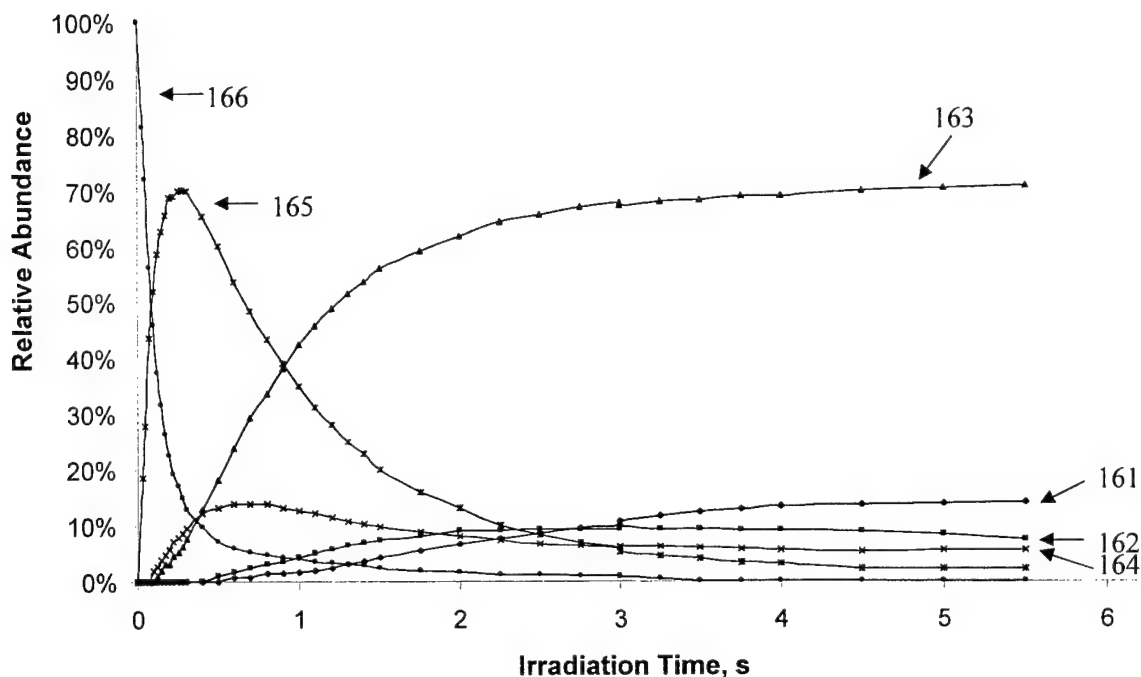


Figure 18. Relative abundance of photolysis products and fluorene cation parent as a function of irradiation time.

the fragment peaks was isolated in turn, and irradiated briefly ( $\sim 1$ s). (Brief photolysis times were essential since longer times resulted in the development of one or more lower mass peak(s), i.e., down two or more amu). The next lower  $m/z$  mass peak was formed in all cases, showing conclusively that the primary dehydrogenation channel is sequential loss of single hydrogen atoms. It follows from this mechanism that, if a particular dehydrogenated product is ejected from the ICR cell, its successor, one amu lower, should then be absent. Figure 19 shows the irradiation of the parent ion while the  $m/z$  165 ion is ejected simultaneously. This is accomplished by using a single frequency ejection (SFE) while the lamp is shining on the cell. It is clear that no  $m/z$  164 product is formed so only single hydrogen loss is possible for the  $m/z$  166 ion. Similar results are shown in Figure 20 for the ejection of the  $m/z$  163 ion. No  $m/z$  162 product is formed.

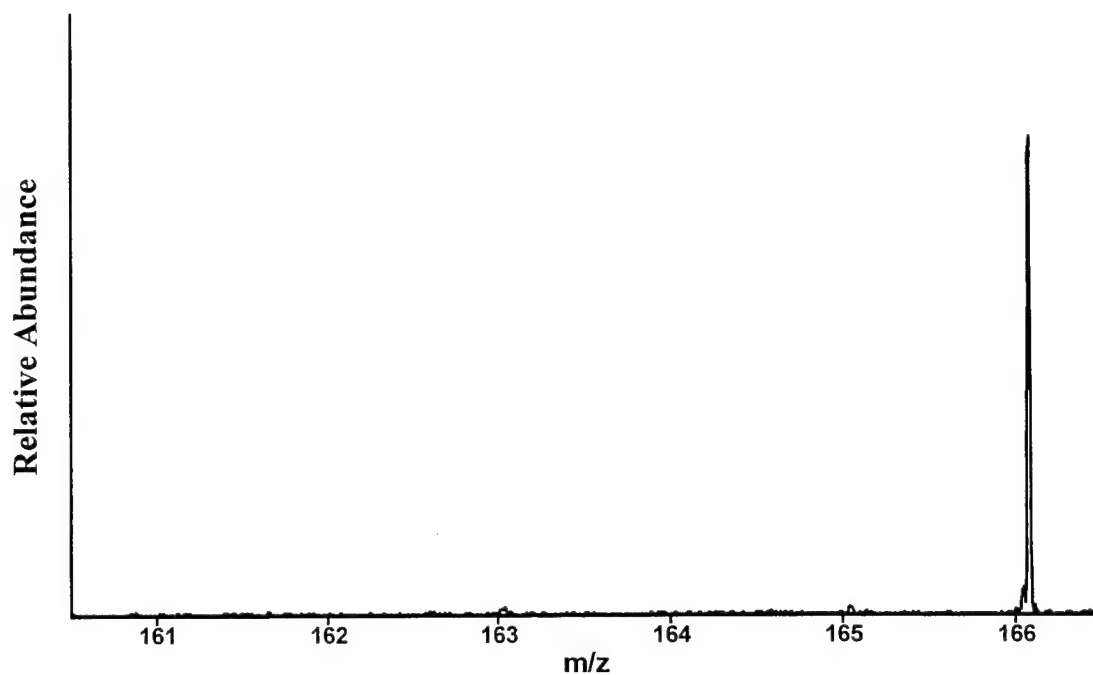


Figure 19. FTICR mass spectrum of photolysis products after a one second irradiation of the  $m/z$  166 ion while simultaneously ejecting  $m/z$  165.

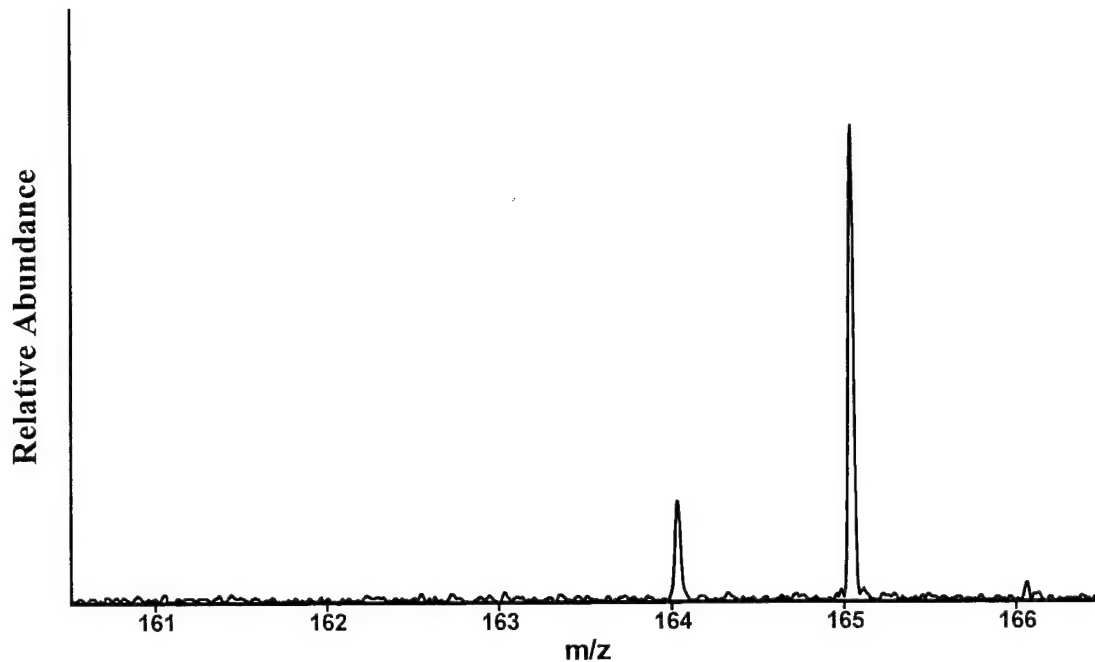


Figure 20. FTICR mass spectrum of photolysis products after three seconds of irradiation of the  $m/z$  166 ion while simultaneously ejecting  $m/z$  163.

A different situation arises for the  $m/z$  165 ion. Figure 21 is similar to the previous figures, except that only the  $m/z$  164 ion is now being ejected. A substantial  $m/z$  163 peak is formed while no  $m/z$  164 is present, indicating the simultaneous loss of two hydrogens from the  $m/z$  165 ion. Figure 22 shows a similar result for the ejection of  $m/z$  162. A substantial amount of  $m/z$  161 is formed, also indicating the simultaneous loss of two hydrogens from the  $m/z$  163 ion.

The branching ratio for  $m/z$  165 dehydrogenation is  $\sim 13\%$  dual H loss and  $87\%$  single H loss, while for the  $m/z$  163 dehydrogenation it is  $\sim 34\%$  dual hydrogen loss and  $66\%$  single hydrogen loss (*vide infra*). The even species ( $m/z$  162, 164 and 166) only lose single hydrogens.

Contrary to previous results, both dehydrogenation and further fragmentation are shown to occur with broad band UV and visible irradiation. In the original report<sup>114</sup> on fluorene ion photolysis it was stated that between one and five hydrogens were lost with no other products observed. This observation is understandable now in light of the present results. The primary decomposition route, i.e., the one possessing the largest rate constants, is sequential H atom loss. The appearance of a large  $m/z$  163 peak results from its slow further decomposition. A detectable quantity of smaller fragmentation products requires longer irradiation times. The original exploratory experiments<sup>113, 114</sup> used only 500ms irradiation periods, clearly insufficient to produce the lower mass fragments observed here.

Experimental work, which will be discussed in Chapter 4, has shown that the parent fluorene ion absorbs UV and visible radiation in the 360 nm as well as the 580-630 nm wavelength range. These wavelengths correspond to photon energies of 4.2 eV for

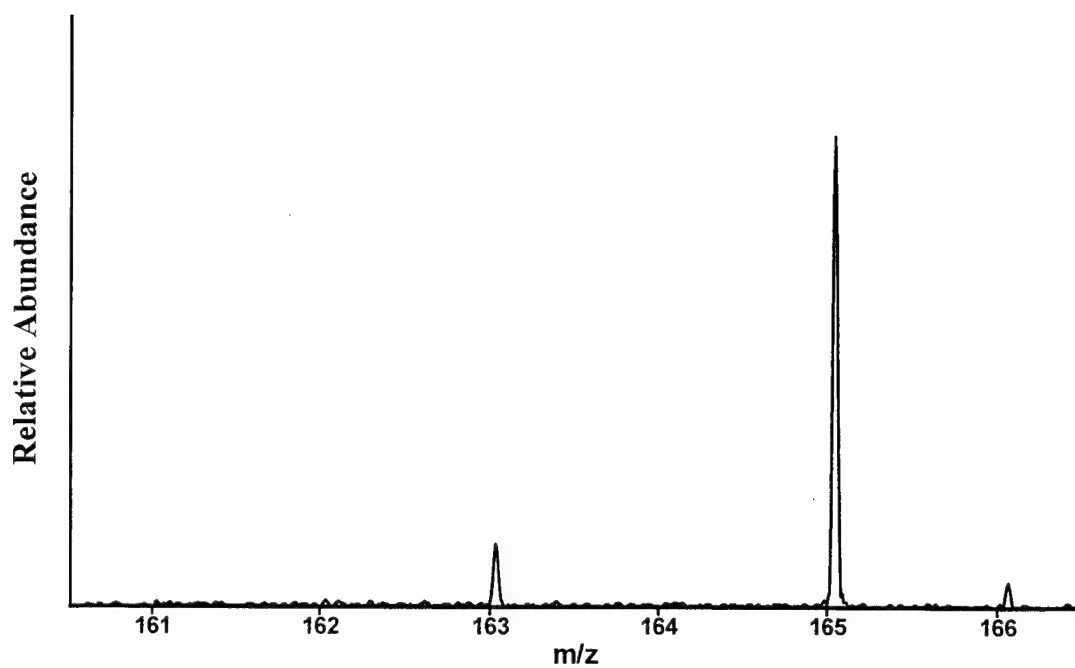


Figure 21. FTICR mass spectrum of the photolysis products after three seconds of irradiation of the  $m/z$  166 ion while simultaneously ejecting  $m/z$  164.

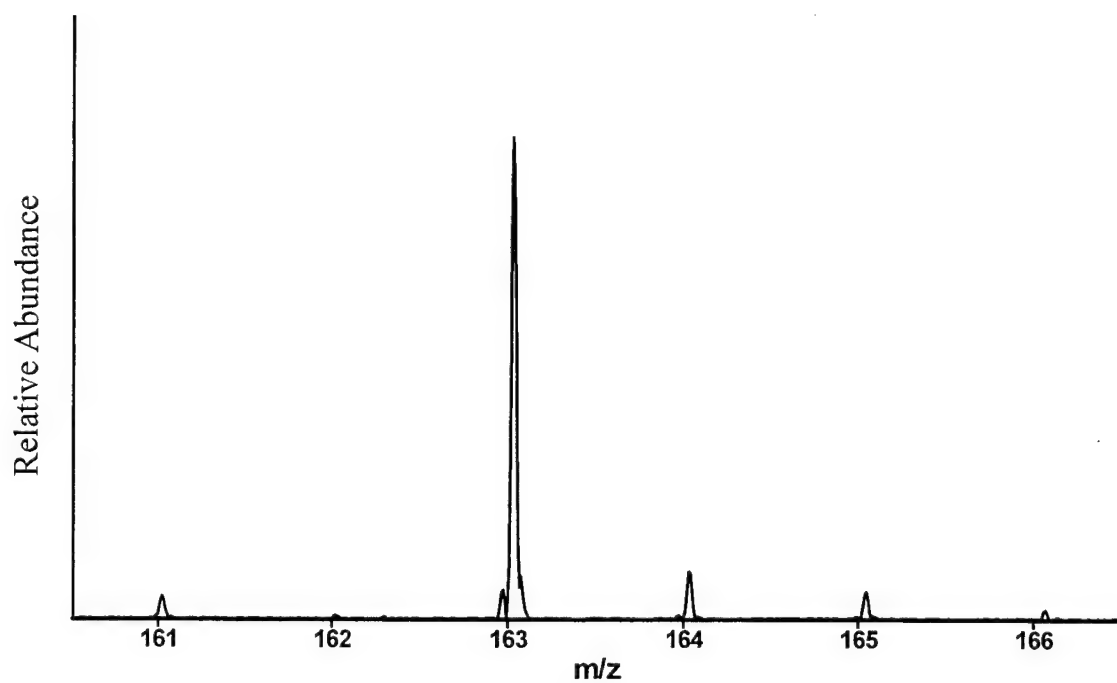


Figure 22. FTICR mass spectrum of the photolysis products after seven seconds of irradiation of the  $m/z$  166 ion while simultaneously ejecting  $m/z$  162.

the former and 2.4-2.6 eV for the latter wavelengths. Theoretical calculations have also shown the energy required to remove the first hydrogen is 2.6 eV while further dehydrogenation requires a much higher energy, 4.0 – 4.9 eV. This would seem to indicate that it is possible to induce the loss of the first hydrogen with only one photon but further dissociation would have to occur via multi-photon processes. Boissel and coworkers have outlined<sup>101, 143</sup> the probable mechanism in operation here, a sequential absorption of visible and UV photons which increase the internal energy of the precursor ion stepwise until the dissociation limit is reached.

### Fragmentation

Longer irradiation times (>ca. 2s) lead to other photofragments with smaller  $m/z$  values than those corresponding to H atom loss only. Figure 23 shows the spectrum of the lower mass products in the  $m/z$  50-166 range. Major products appear at  $m/z$  63, 87, 89, 108-111, 115, 132 and 139. The photodissociation pathways by which these fragments are produced will be discussed in this section.

The precursors of these product ions were determined using the following irradiation-isolation-ejection sequences. After ionization, the cell contents were irradiated for a fixed time, and the  $m/z$  161-165 ions isolated, each in turn. Each isolated ion was subjected to further photolysis and followed as a function of irradiation time. During this procedure the other  $m/z$  16x peaks were ejected. The first photolysis created a detectable population of the  $m/z$  161-165 ions and the buildup of photoproducts was scrutinized during the second irradiation. The first photolysis step was omitted for the  $m/z$  166 ion since a large population of the parent ion was already present due to the ionization process. The photolysis of each of the isolated 16x peaks will be discussed in turn.

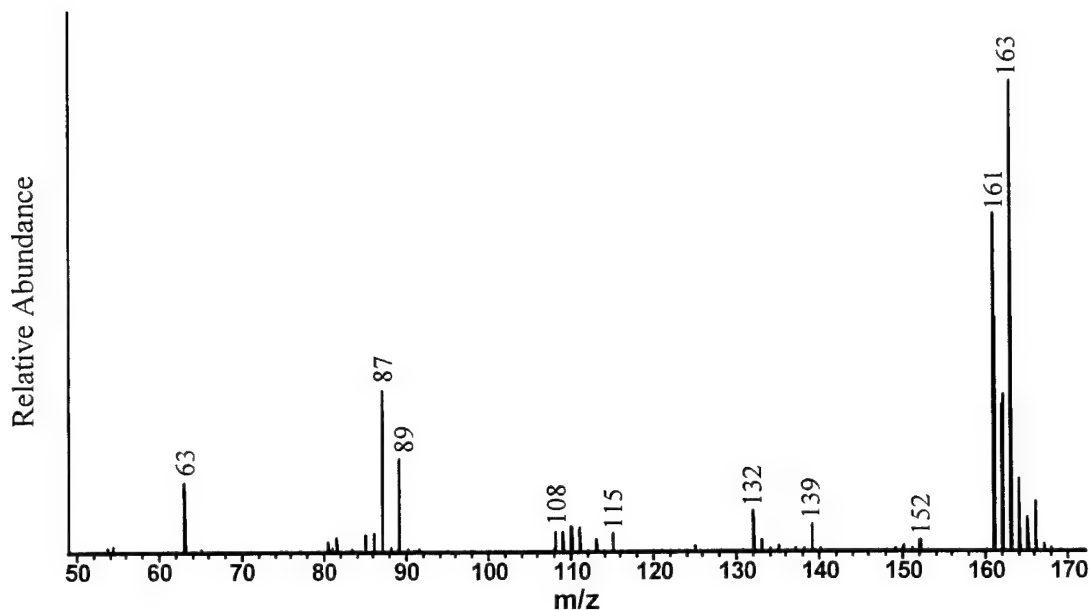


Figure 23. FTICR mass spectrum of the photolysis products after four seconds of irradiation of the  $m/z$  166 ion showing full fragmentation of the parent fluorene ion.

#### $m/z$ 166

The primary fragments produced by irradiation of the  $m/z$  166 parent ion are shown in Figure 24 while a study of their time dependence is shown in Figure 25. The major photoproducts include:  $m/z$  140 ( $C_{11}H_8^+$ ) and 139( $C_{11}H_7^+$ ), 116 ( $C_9H_8^+$ ) and 115 ( $C_9H_7^+$ ), and 89( $C_7H_5^+$ ). The last fragment,  $m/z$  89, is not visible in Figure 24. The difference between the  $m/z$  139 and  $m/z$  140 peaks is thought to be the retention of one of the  $sp^3$  hydrogens located on the central ring of the fluorene ion as shown in Figure 16. The same thing applies to the  $m/z$  115 and  $m/z$  116 peaks. Secondary products appear from some, but not all, of these primary products. For example, photodissociation of  $m/z$  139 produces both  $m/z$  89( $C_7H_5^+$ ) and  $m/z$  87( $C_7H_3^+$ ), while  $m/z$  115( $C_9H_7^+$ ) dissociates to form  $m/z$  89( $C_7H_5^+$ ) and  $m/z$  63( $C_5H_3^+$ ), but not  $m/z$  87( $C_7H_3^+$ ). The  $m/z$  87( $C_7H_3^+$ ) species is found to dehydrogenate sequentially to  $m/z$  85( $C_7H^+$ ).

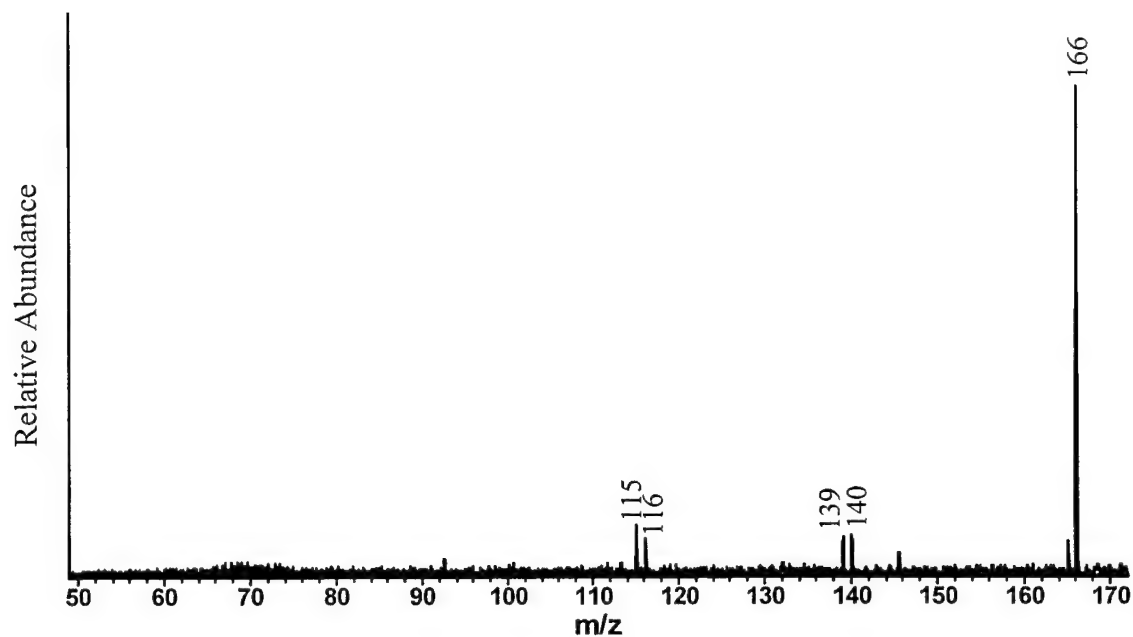


Figure 24. FTICR mass spectrum of photolysis products after one second of irradiation of the  $m/z$  166 ion. Masses  $m/z$  161-165 were ejected during lamp exposure.

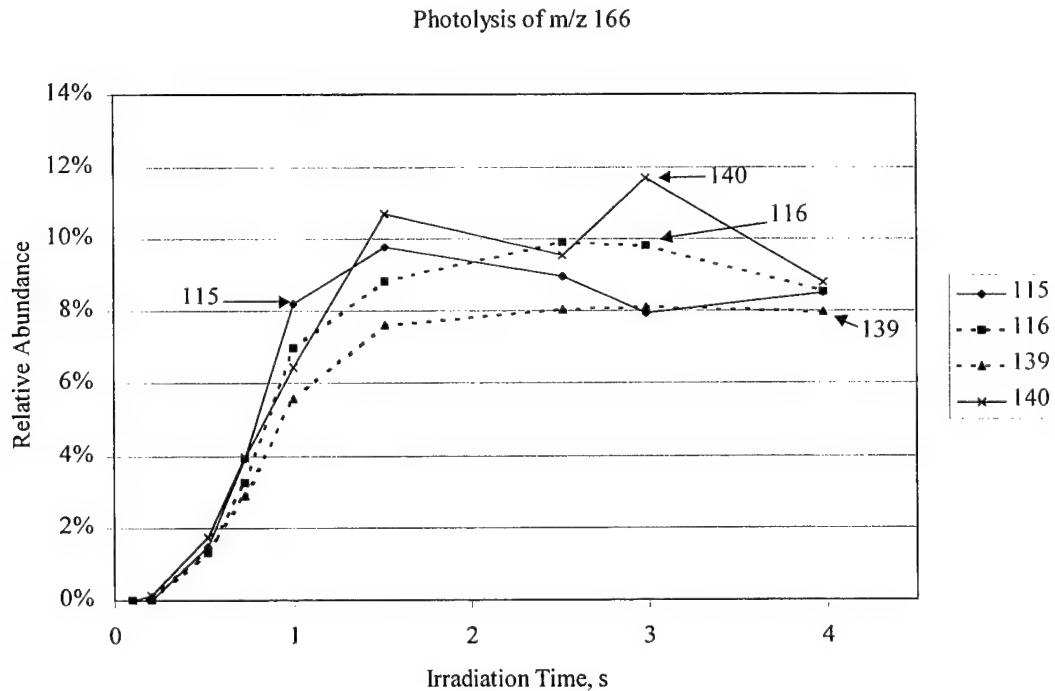


Figure 25. Time dependence of the photoproducts of the  $m/z$  166 ion.



m/z 165:

The primary photo-fragments of the m/z 165 ion are shown in Figure 26 while their time dependence is shown in Figure 27. The decomposition of the m/z 165 product leads to m/z 139( $C_{11}H_7^+$ ) and m/z 115( $C_9H_7^+$ ). These ions are similar to the decay products of m/z 166. The absence of the m/z 116 and m/z 140 peaks is confirmation of the earlier assumption that both  $sp^3$  hydrogens are still bound on the m/z 166 ion. The m/z 139 further decays to m/z 89( $C_7H_5^+$ ) and 87( $C_7H_3^+$ ) while m/z 115 decays to m/z 89( $C_7H_5^+$ ) and m/z 63( $C_5H_3^+$ ). A small percentage of the m/z 165 species loses two hydrogens.

m/z 164:

This species loses only one hydrogen. No other fragments were observed.

m/z 163:

An example of the photolysis of the m/z 163 ion is shown in Figure 28. Lamp exposure was for five seconds. The photofragmentation of this species leads to m/z 89( $C_7H_5^+$ ) and 87( $C_7H_3^+$ ) products, as well as to further dehydrogenation to m/z 162 and 161. The rate of photodecay is very slow for the m/z 163 ion compared to the other ions. Even after four seconds, the total products are only four percent of the m/z 163 signal as seen in Figure 29. Two other products are also seen in this spectrum, m/z 113 and 137. These are thought to be relatively unstable intermediates. Attempts to isolate and photolyze them were unsuccessful. Obviously, the loss of a neutral acetylene from the m/z 163 ion yields the m/z 137 ion and further loss of a  $C_2$  neutral fragment will yield the m/z 113 ion.

m/z 162:

This species only loses one hydrogen.

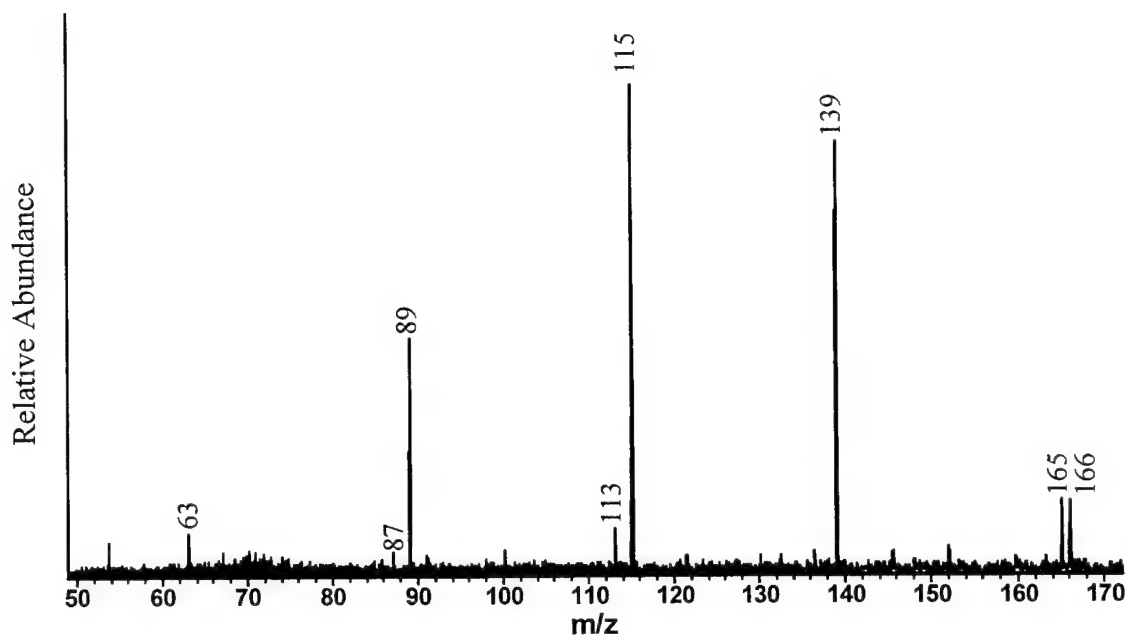


Figure 26. FTICR mass spectrum of photolysis products after three seconds of irradiation of the isolated  $m/z$  165 ion. Masses  $m/z$  161-164 and  $m/z$  166 were ejected during lamp exposure.  $M/z$  166 is present due to incomplete ejection.

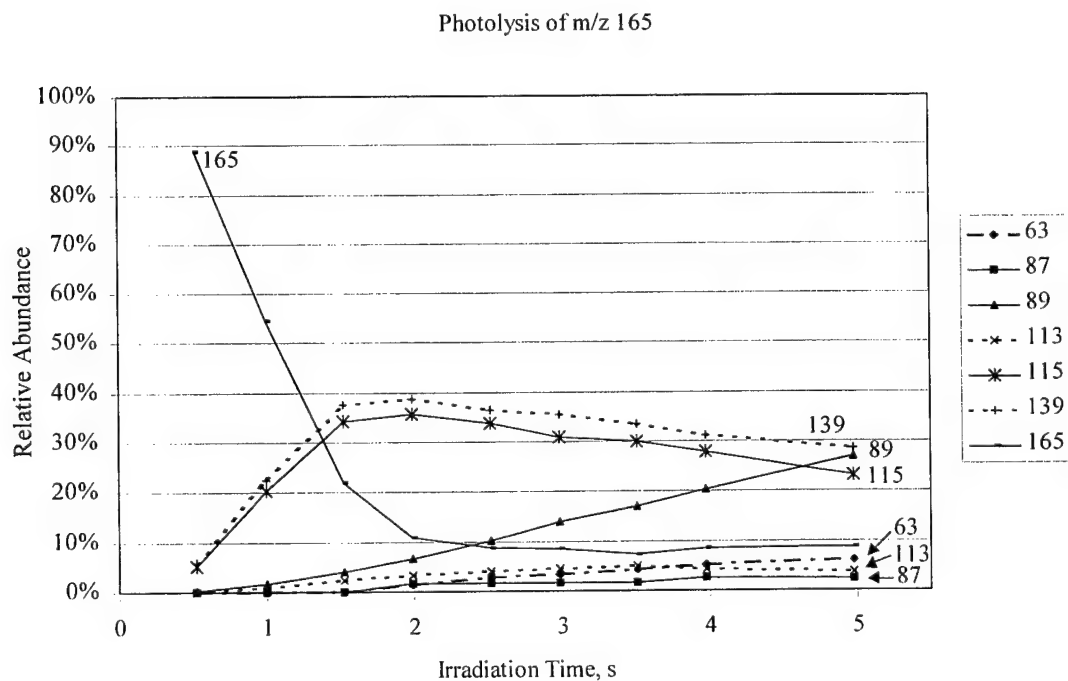


Figure 27. Time dependence of the abundance of photoproducts of the  $m/z$  165 ion.

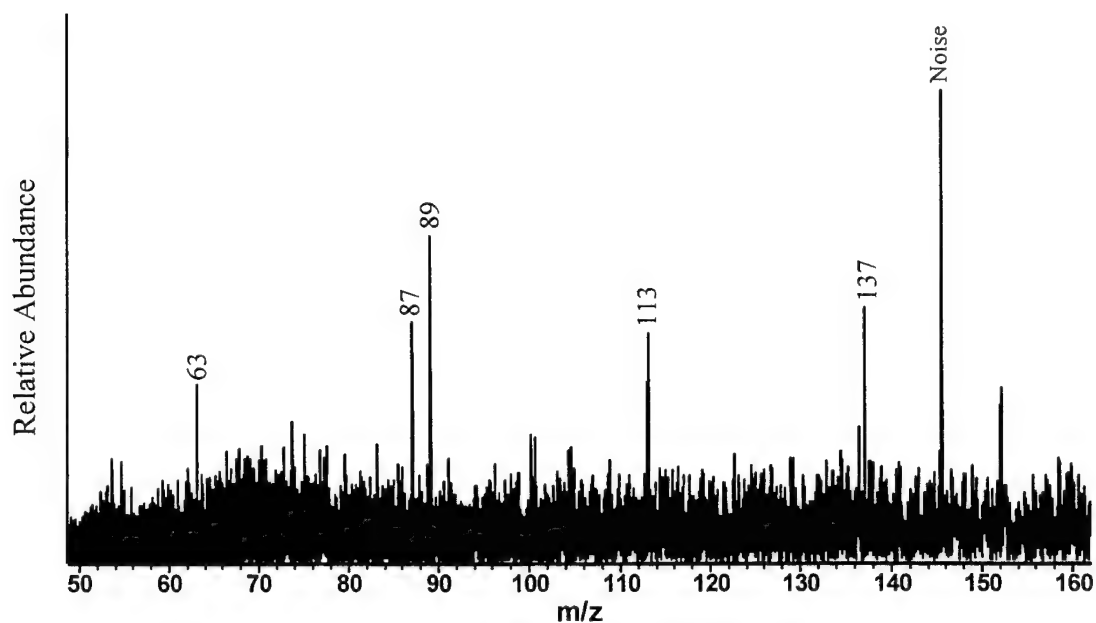


Figure 28. FTICR mass spectrum of photolysis products after five seconds of irradiation of the isolated  $m/z$  163 ion. The abundance of the  $m/z$  163 ion is very large compared to that of the photoproducts and is not shown.

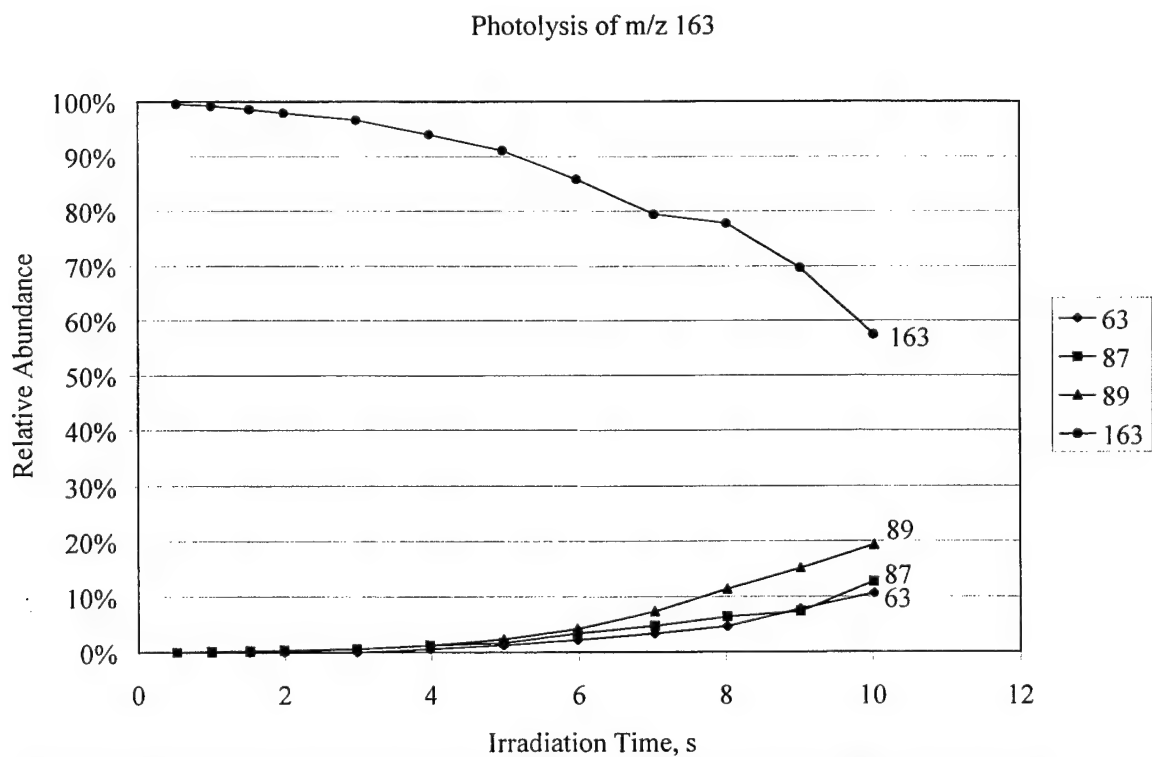


Figure 29. Time dependence of the abundance of photoproducts of the  $m/z$  163 ion.

m/z 161:

For the m/z 161 ion ( $C_{13}H_5^+$ ), fragments containing more than 5 hydrogens are not possible. Figure 30 shows that the major fragment peaks are m/z 63 ( $C_5H_3^+$ ), m/z 87 ( $C_7H_3^+$ , now a major peak), m/z 135 ( $C_{11}H_3^+$ ) and m/z 111 ( $C_9H_3^+$ ). The latter three species lose their hydrogens sequentially, m/z 135 dehydrogenates to form m/z 132 ( $C_{11}^+$ ), which is the product visible in Figure 30, and m/z 111 to form m/z 108 ( $C_9^+$ ). The m/z 87 product only forms m/z 85 ( $C_7H^+$ ).

A slight amount of the m/z 115 ion also appears. The m/z 161 ion has a formula of  $C_{13}H_5^+$ , while the m/z 115 ion is  $C_9H_7^+$ . It is unlikely that m/z 115 is able to attach two extra hydrogens during photolysis. Its source must be from higher 16X masses that were incompletely ejected. A small amount of m/z 165 and m/z 166 are present in this spectrum and are assumed to be the precursors of the m/z 115 product. Other experiments were done to confirm this result by increasing the ejection voltage. However, because of the higher voltage and the nature of SWIFT ejections, there was some bleedover of the ejection excitation, greatly reducing the amount of m/z 161 precursor. This made it nearly impossible to do time-dependent studies because of a low signal-to-noise ratio.

An example of a time-dependent study of m/z 161 ion photo-fragmentation is shown in Figure 31. The m/z 161 population drops off with increasing lamp time while the m/z 63 and m/z 87 products rapidly grow in. The m/z 108 and 132 ions rise to a maximum and then start to fall off. As explained above, although m/z 108 and 132 ions are shown, the actual photoproducts of m/z 161 are their precursors, m/z 111 and 135, respectively.

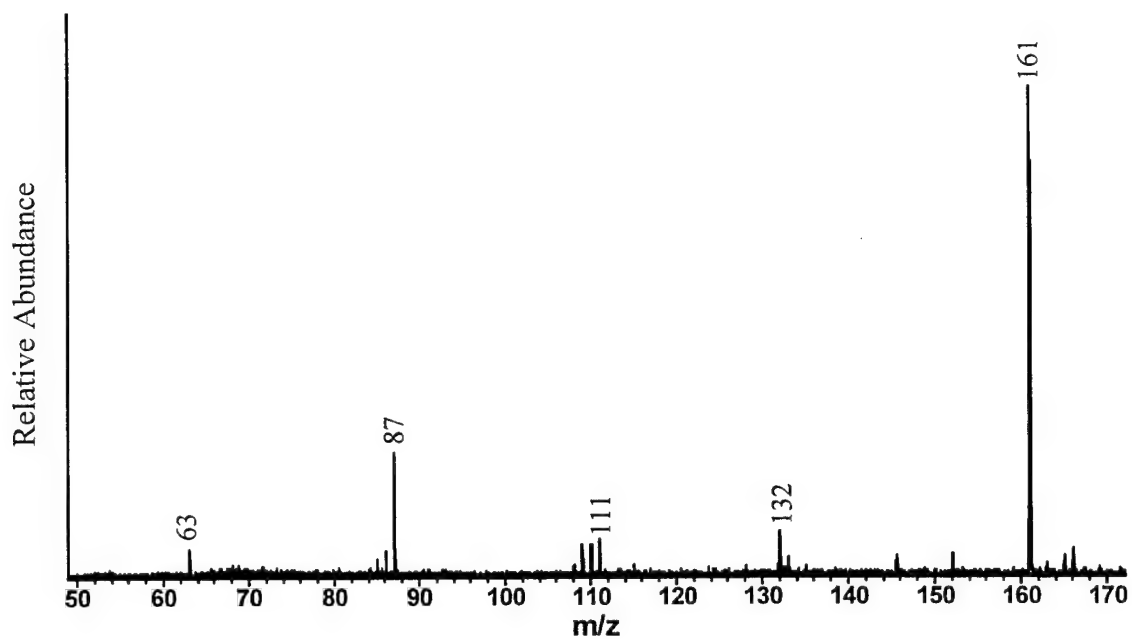


Figure 30. FTICR mass spectrum of photolysis products after three seconds of irradiation of the isolated  $m/z$  161 ion.

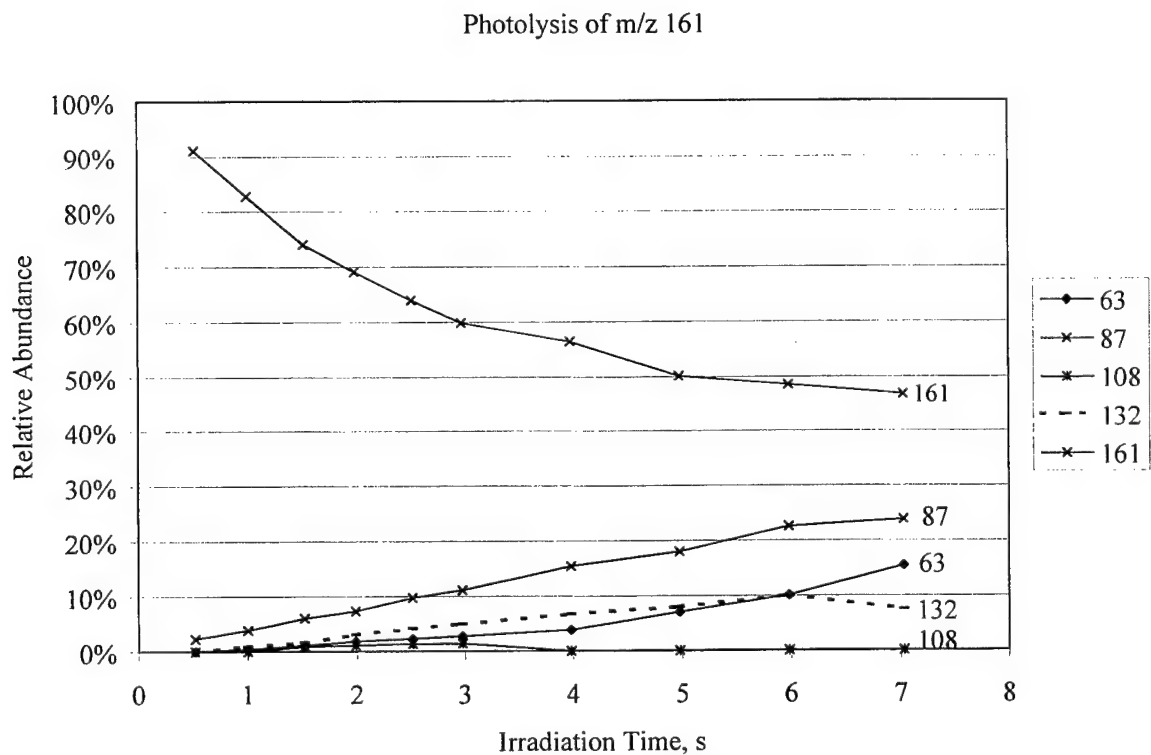


Figure 31. Time dependence of the abundance of photoproducts of the  $m/z$  161 ion.

Table 2. Fragment ion yields and rate constants for photodissociation of the fluorene cation and its dehydrogenated partners .

Precursor ion	Precursor ion (m/z)	Fragment ion	Fragment ion (m/z)	Percent yield (%)	Rate constant	
					<i>i</i>	$k_i$ ( $\times 10^1 \text{ s}^{-1}$ ) <sup>a,b</sup>
$\text{C}_{13}\text{H}_{10}^+$	166	$\text{C}_{13}\text{H}_9^+$	165	92.2	1	32.2
		$\text{C}_{11}\text{H}_8^+$	140	2.0	2	0.71
		$\text{C}_{11}\text{H}_7^+$	139	1.6	3	0.57
		$\text{C}_9\text{H}_8^+$	116	1.6	4	0.57
		$\text{C}_9\text{H}_7^+$	115	2.1	5	0.74
		$\text{C}_7\text{H}_5^+$	89	0.4	6	0.13
$\text{C}_{13}\text{H}_9^+$	165	$\text{C}_{13}\text{H}_8^+$	164	42	8	5.5
		$\text{C}_{13}\text{H}_7^+$	163	2	7	0.3
		$\text{C}_{11}\text{H}_7^+$	139	25	10	3.3
		$\text{C}_9\text{H}_7^+$	115	31	9	4.2
$\text{C}_{13}\text{H}_8^+$	164	$\text{C}_{13}\text{H}_7^+$	163	100	19	27
$\text{C}_{13}\text{H}_7^+$	163	$\text{C}_{13}\text{H}_6^+$	162	50	21	0.51
		$\text{C}_{13}\text{H}_5^+$	161	22	20	0.23
		$\text{C}_7\text{H}_5^+$	89	17	15	0.18
		$\text{C}_7\text{H}_3^+$	87	11	22	0.11
$\text{C}_{13}\text{H}_6^+$	162	$\text{C}_{13}\text{H}_5^+$	161	100	23	19.2
$\text{C}_{13}\text{H}_5^+$	161	$\text{C}_{11}\text{H}_3^+$	135	22	24	0.26
		$\text{C}_9\text{H}_3^+$	111	4	27	0.05
		$\text{C}_7\text{H}_3^+$	87	53	25	0.62
		$\text{C}_5\text{H}_3^+$	63	21	26	0.25

<sup>a</sup>Rate constants valid for the photon fluxes used in this study.

<sup>b</sup>Rate constants are for the processes shown in Figure 32.

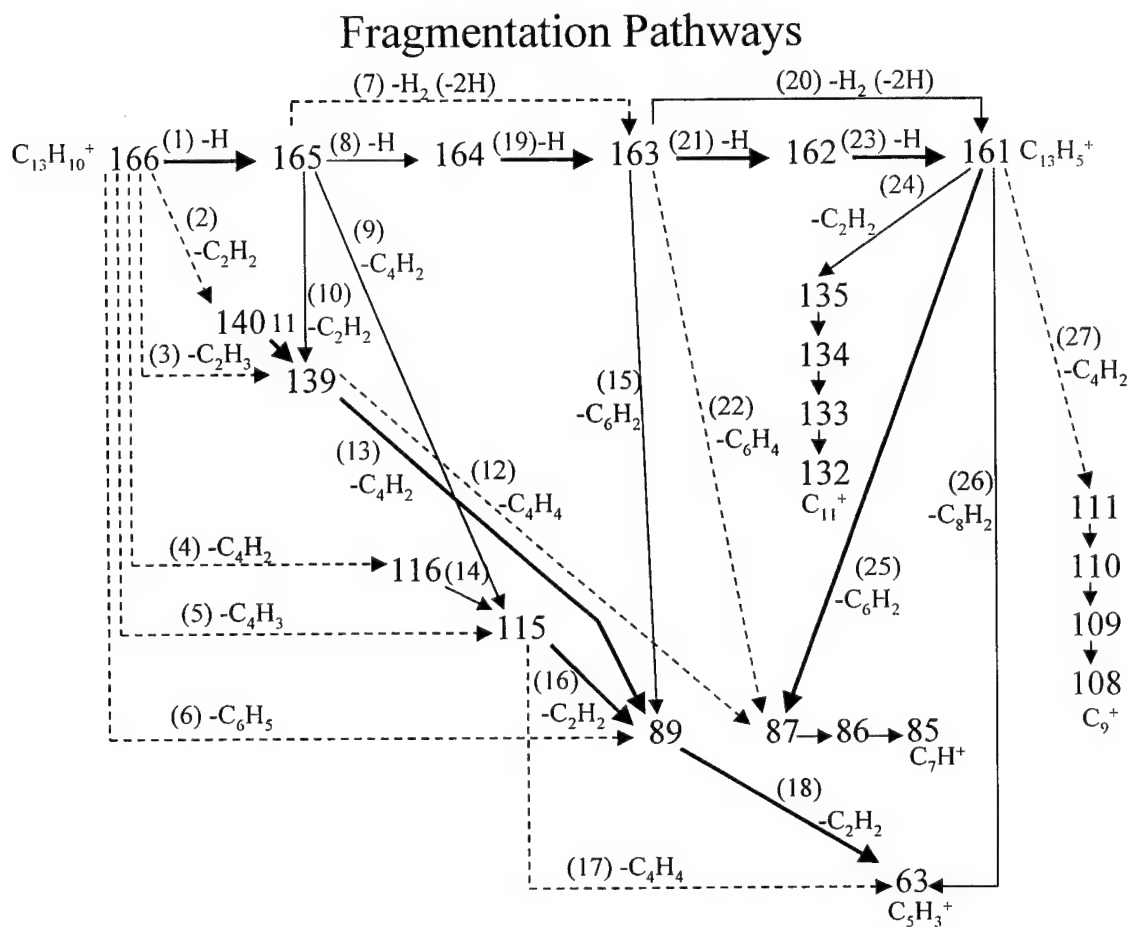


Figure 32. Photodecomposition pathways and products from the  $m/z$  166 fluorene parent ion. Bold lines indicate yields of 50% or greater, thin lines indicate yields between 15 and 49%, and dashed lines indicate yields less than 15%.

Table 2 gives the main photodecomposition products for fluorene and its dehydrogenated partners while Figure 32 gives a visual overview of the fragmentation pathways. The fragmentation pathways followed by the parent and each dehydrogenated product contain clues to the structural identities of their precursors and are discussed later in this chapter. The fragments observed from the parent and its dehydrogenated successor ions are discussed in turn below. The rate constants indicated in this table will be discussed in the next section.

Figure 32 also shows that there are multiple paths of formation for several of the ions, such as  $m/z$  89. Although its primary formation paths are photolysis of the  $m/z$  139 and  $m/z$  115 ions, it can also be formed directly from  $m/z$  166 and  $m/z$  163. Indirect evidence would also suggest  $m/z$  165 as a source, but, if so, it would be a very minor route. These pathways were determined by using multiple “notches” in a SWIFT waveform excitation. For example, Figure 33 shows the direct formation of  $m/z$  89 from  $m/z$  163. The sample was irradiated for 10 seconds while  $m/z$  91-162 and  $m/z$  164-168 were ejected. The  $m/z$  89 is still present as well as  $m/z$  63, which is formed from the  $m/z$  89. This same procedure was used to verify the formation of all ions in the figure.

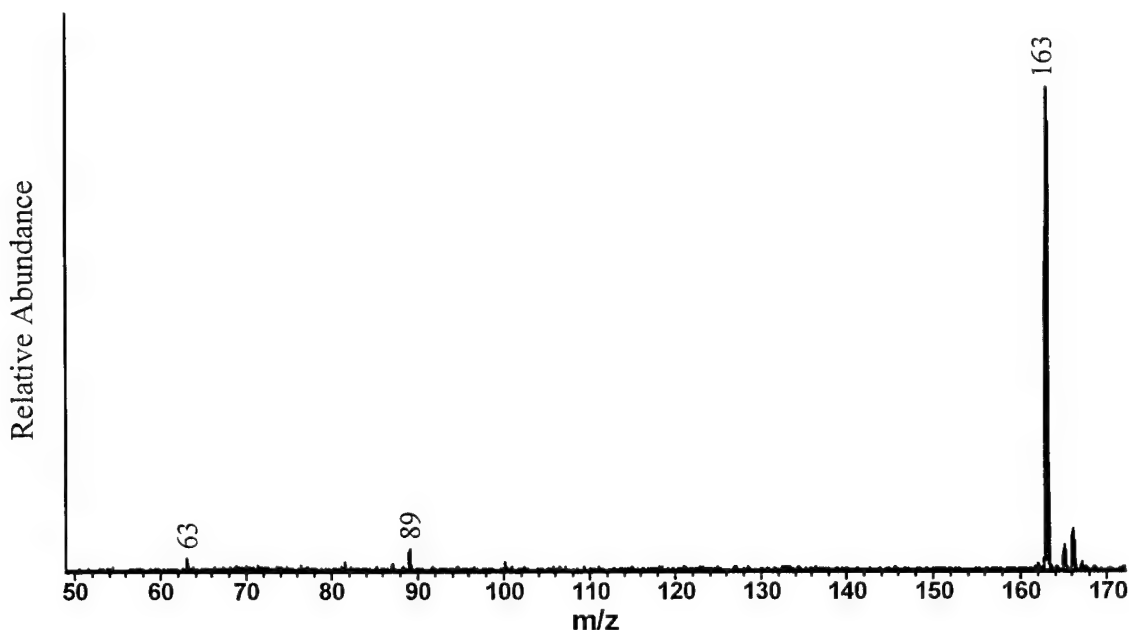


Figure 33. Ten seconds of irradiation while ejecting  $m/z$  91-162 and  $m/z$  164-168.

Figure 23 clearly shows there are mass groupings between  $m/z$  50 and  $m/z$  166 representing increasing numbers of carbons: five carbons for  $m/z$  65 to 13 carbons for  $m/z$  166. Only the odd numbers of carbons are represented except for the small peak around  $m/z$  152, which has twelve carbons. Since the  $^{13}\text{C}$  isotopes have been ejected, the



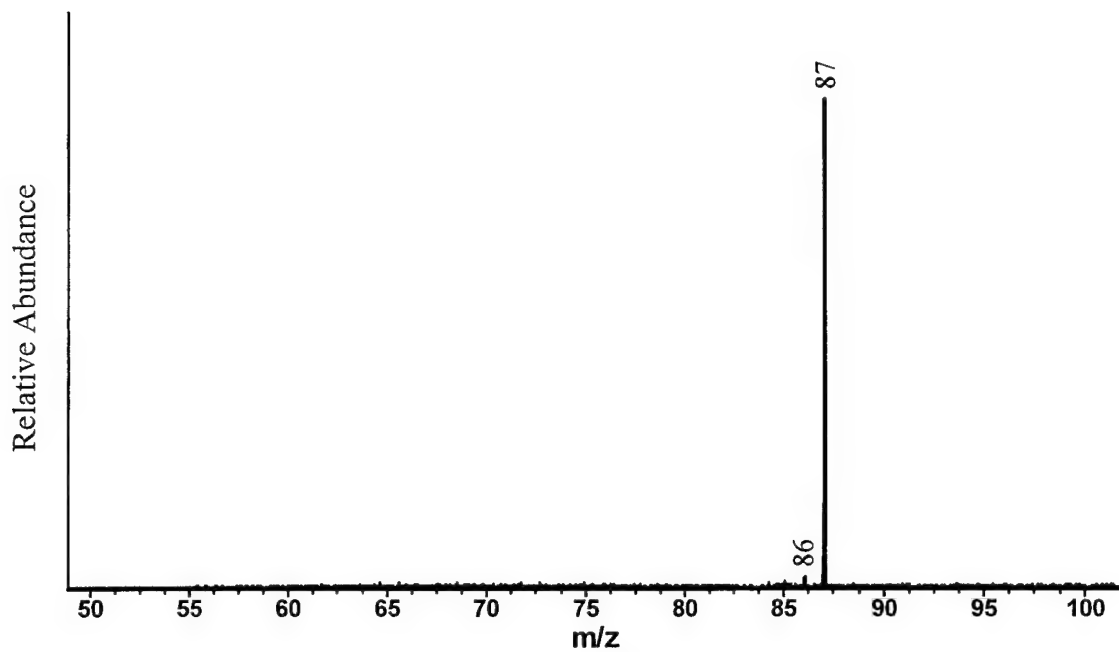


Figure 34. Four seconds of irradiation of the  $m/z$  87 while ejecting 88-168. Slight dehydrogenation to  $m/z$  86 and 85 occurs but no  $m/z$  63 is present.

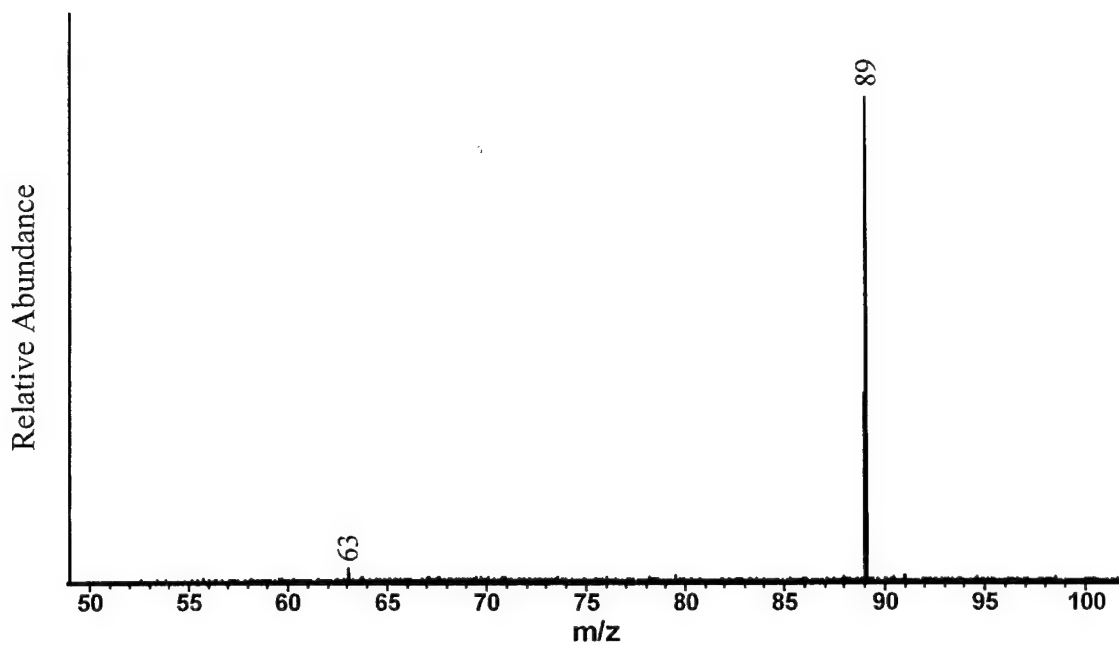


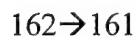
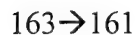
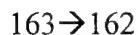
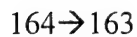
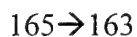
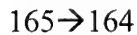
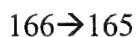
Figure 35. Four seconds of irradiation of the  $m/z$  89 ion while ejecting  $m/z$  90-168. No dehydrogenation occurs but  $m/z$  63 is present due to fragmentation.

masses around these carbon groupings represent losses of hydrogen. Each of these groupings, as well as individual masses, was isolated to determine what action photolysis had on them.

One of the more interesting examples is the difference between  $m/z$  87 and 89. Figure 34 shows the irradiation of the isolated  $m/z$  87 ion while Figure 35 is the irradiation of the  $m/z$  89 ion. The former ion loses a maximum of two hydrogens while the latter dissociates to  $m/z$  63. This would indicate that, although similar in mass, the two ions have different structures.

### Kinetics

To determine the branching ratios and rate constants for photodecomposition of the fluorene cation and its dehydrogenated partners, the time-mass abundance plots were fit by solving the appropriate set of coupled differential equations. Each set describes the kinetics of one of the precursor ions. For example, for the hydrogen loss set of experiments, the following reactions take place:



The formation of the m/z 165 ion is given by the differential equation:

$$\frac{d[165]}{dt} = k_1[166] - (k_8 + k_7)[165] \quad (9)$$

where  $k_1$  is the rate constant for the formation of m/z 165 from m/z 166 (cf. Fig. 32 for decomposition pathways) while  $k_8$  and  $k_7$  are the rate constants for the loss of m/z 165 to form m/z 164 and m/z 163, respectively. Relatively short irradiation times were used so that smaller fragments such as m/z 139 and m/z 115 were not observed.

Experimental data at thirty different times were obtained. The normalized percent of each ion was input to a computer program (KINFIT)<sup>144</sup> and used to solve the equations and fit the experimental curves. Rate constants ( $k_i$ ) and initial (percent) yields were obtained from the fits. An example of the results is shown in Figure 36. In this figure the experimental data for hydrogen loss from ions 162-166 is plotted against the calculated yields. Note that although the data for m/z 161 and 162 were used in the calculations, they have been omitted for clarity in the graph. The fit is excellent. Similar results were obtained for all the time dependent runs. The results for the  $C_{13}H^{+}_{10-n}$  ( $n=0-5$ ) ions are given in Table 2.

Several interesting observations are evident from the table. First, the primary photodecomposition route for the m/z 166 parent ion is single H atom loss with a greater than 90% yield. The five other routes contribute 2% or less each. Second, the rates of dehydrogenation of the even mass species (m/z 166, 164, 162) are relatively fast compared to the other decomposition routes. They are 5 to 10 times faster than the other pathways. Third, the bottleneck in the sequential dehydrogenation from m/z 166 to the m/z 161 species is the m/z 163  $\rightarrow$  m/z 162 step which is  $\sim 10$  times slower ( $0.051 \text{ s}^{-1}$ ) than its closest competitor (m/z 165  $\rightarrow$  m/z 164,  $0.55 \text{ s}^{-1}$ ). Fourth, the odd mass species

( $m/z$  165, 163, 161) are more prone to lose larger neutral fragments (than hydrogen) compared with the even mass species. For example, the  $m/z$  165 ion decomposes  $\sim 40\%$  to  $m/z$  164,  $\sim 30\%$  to  $m/z$  115 and  $\sim 25\%$  to  $m/z$  139, all comparable percentages, while the  $m/z$  162 and 164 precursor ions decompose 100% via single H atom loss.

#### Hydrogen Loss

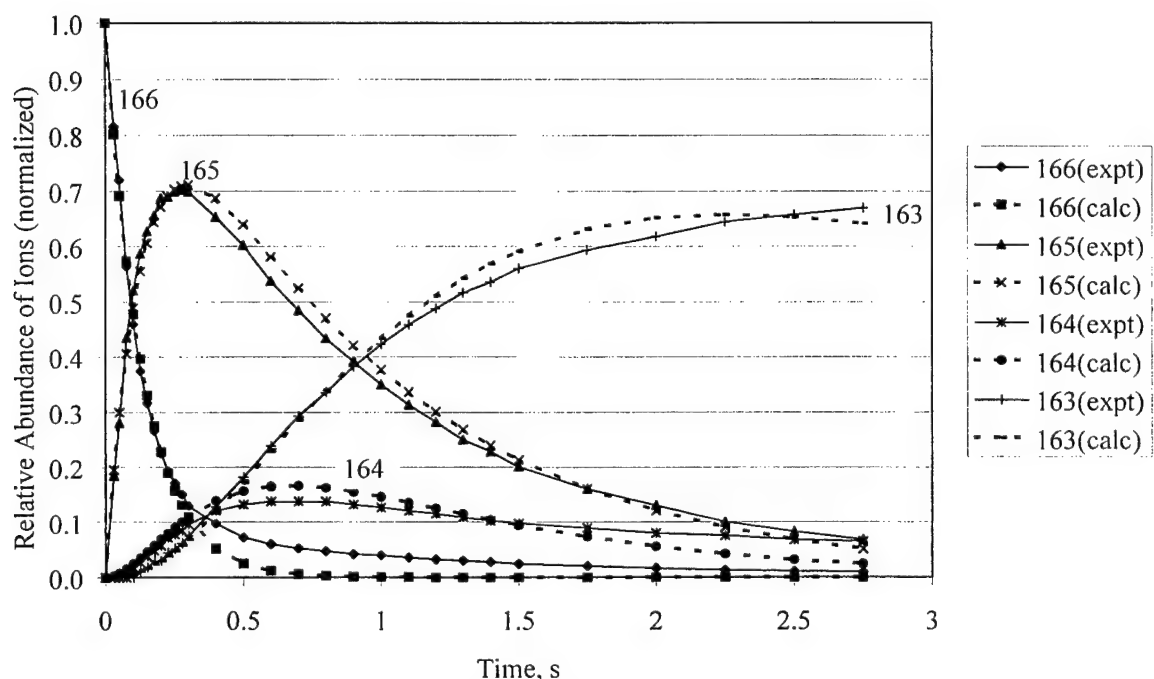


Figure 36. Example of the calculated rate constants versus experimental values. Experimental values are solid lines while the corresponding calculated values are dashed. The  $m/z$  161 and  $m/z$  162 ions have been omitted for clarity.

#### Fragmentation Pathways

This section will use theoretical calculations to attempt to explain the photodecomposition of the fluorene cation. It is shown that density functional theory calculations can be used to determine energetically plausible photofragmentation pathways, which explain the observed decomposition products.

### Computational Procedures

Geometries were optimized and harmonic frequencies calculated using hybrid density functional theory (B3LYP method) with 4-31G or 6-31G(d, p) basis sets using the Gaussian 98 platform.<sup>145</sup> The B3LYP/4-31G level of theory was used for most bond energy calculations, since Bauschlicher has shown that this approach is relatively accurate in predicting H-H and C-H bond energies in H<sub>2</sub> and C<sub>6</sub>H<sub>6</sub>, respectively.<sup>146</sup> Use of the 6-31G(d, p) basis set results in only small improvements in the computed harmonic frequencies (scaled) for neutral and cationic fluorene when compared to matrix band frequencies. All calculated energies have been zero-point energy corrected (ZPE) and scaled by a factor of 0.957 (4-31G) and 0.978 (6-31G(d,p)) to match experimental observations. The bond energies for H<sub>2</sub> and C<sub>6</sub>H<sub>6</sub> (C-H) computed using 4-31G (6-31G(d, p)) basis sets are 103.67 kcal/mol (105.58 kcal/mol) and 110.31 kcal/mol (110.37 kcal/mol), respectively. The corresponding experimental bond energies are 103.27 kcal/mol and 109.8/109.4 kcal/mol.<sup>146</sup> Thus, the choice of the 4-31G basis for the present work is justified from the point of view of accuracy and cost. Over sixty molecular systems, each with between 8 and 25 atoms, were calculated.

Dr. Jan Szczepanski and Mr. Wright Pearson did most of the Gaussian calculations used in this section, the results of which are collected in Table 3. The analysis of the results was a collaborative effort of the Vala group.

### Sequential Hydrogen Loss

The primary photodissociation route for the fluorene cation is the sequential loss of five hydrogens.<sup>114</sup> Figure 32 shows the experimentally determined photodecomposition pathways and products, and emphasizes that the primary fragmentation route is the loss of hydrogen atoms. It is of interest to determine the most

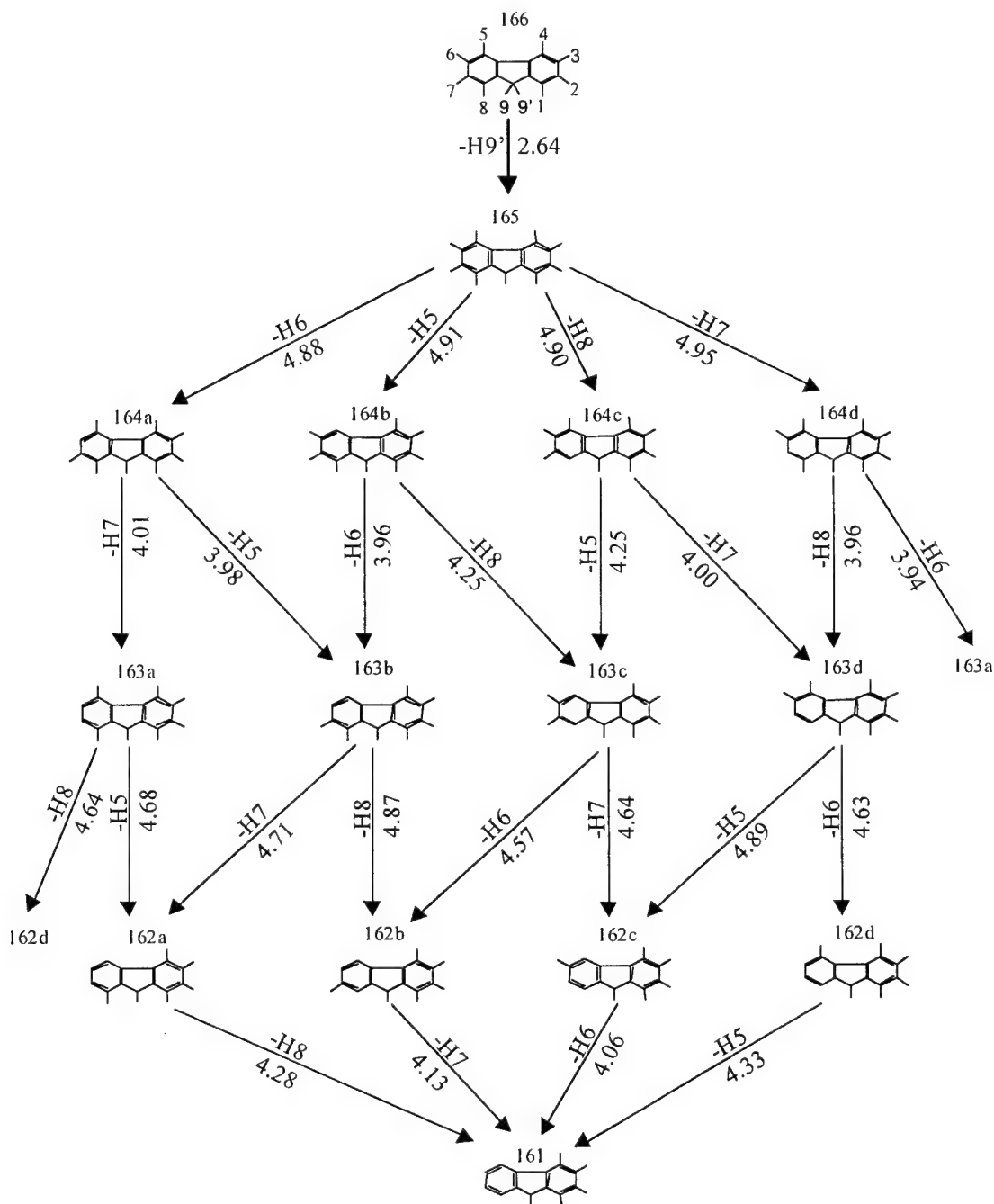


Figure 37. Energetically favorable photoreaction pathways for sequential hydrogen loss (up to five hydrogens) for parent fluorene cation,  $\text{C}_{13}\text{H}_{10}^+$ ,  $m/z$  166, calculated at B3LYP/4-31G level. The C-H bond energies (in eV, ZPE  $\times$  0.957 scale factor) for particular hydrogen losses are indicated. This represents the experimentally observed route for  $m/z$  166  $\rightarrow$  161 sketched in Fig. 32.

Table 3. C-H bond energies (in kcal/mol (eV)) and energies of precursors (in Hartrees) calculated at B3LYP/4-31G level of theory for sequential hydrogen loss in photodissociation reactions of fluorene cation ( $C_{13}H_{10}^+$ , m/z 166). Energies are ZPE  $\times$  0.957 corrected. Hydrogen numbering is defined in Fig. 37. Energetically favorable reactions are given in bold type. Reactions proceed sequentially based on the previous reaction given in parentheses.

	Reaction	Bond Energy (kcal/mol (eV))	Energy of Precursor (Hartrees)
First H loss (m/z 166 $\rightarrow$ 165)			
(1)	<b><math>C_{13}H_{10}^+ \rightarrow C_{13}H_9^+ + H_9</math></b>	<b>60.8 (2.64)</b>	-500.32
(2)	$C_{13}H_{10}^+ \rightarrow C_{13}H_9^+ + H_8$	115.6 (5.01)	
(3)	$C_{13}H_{10}^+ \rightarrow C_{13}H_9^+ + H_7$	120.6 (5.23)	
(4)	$C_{13}H_{10}^+ \rightarrow C_{13}H_9^+ + H_6$	117.7 (5.10)	
(5)	$C_{13}H_{10}^+ \rightarrow C_{13}H_9^+ + H_5$	116.1 (5.04)	
Second H loss (m/z 165 $\rightarrow$ 164)			
(6)	$C_{13}H_9^+ (1) \rightarrow C_{13}H_8^+ + H_9$	116.1 (5.03)	-499.72
(7)	<b><math>C_{13}H_9^+ (1) \rightarrow C_{13}H_8^+ + H_8</math></b>	<b>113.0 (4.90)</b>	
(8)	<b><math>C_{13}H_9^+ (1) \rightarrow C_{13}H_8^+ + H_7</math></b>	<b>114.1 (4.95)</b>	
(9)	<b><math>C_{13}H_9^+ (1) \rightarrow C_{13}H_8^+ + H_6</math></b>	<b>112.6 (4.88)</b>	
(10)	<b><math>C_{13}H_9^+ (1) \rightarrow C_{13}H_8^+ + H_5</math></b>	<b>113.1 (4.91)</b>	
Third H loss (m/z 164 $\rightarrow$ 163)			
(11)	$C_{13}H_8^+ (7) \rightarrow C_{13}H_7^+ + H_9$	133.8 (5.80)	-499.04
(12)	<b><math>C_{13}H_8^+ (7) \rightarrow C_{13}H_7^+ + H_7</math></b>	<b>92.2 (4.00)</b>	
(13)	$C_{13}H_8^+ (7) \rightarrow C_{13}H_7^+ + H_6$	103.0 (4.46)	
(14)	<b><math>C_{13}H_8^+ (7) \rightarrow C_{13}H_7^+ + H_5</math></b>	<b>98.1 (4.25)</b>	
(15)	$C_{13}H_8^+ (7) \rightarrow C_{13}H_7^+ + H_4$	158.9 (6.89)	
(16)	$C_{13}H_8^+ (7) \rightarrow C_{13}H_7^+ + H_3$	149.8 (6.50) <sup>a</sup>	
(17)	$C_{13}H_8^+ (7) \rightarrow C_{13}H_7^+ + H_2$	158.8 (6.89)	
(18)	$C_{13}H_8^+ (7) \rightarrow C_{13}H_7^+ + H_1$	153.8 (6.67) <sup>a</sup>	
(19)	$C_{13}H_8^+ (6) \rightarrow C_{13}H_7^+ + H_5$	120.5 (5.22)	
(21)	$C_{13}H_8^+ (6) \rightarrow C_{13}H_7^+ + H_6$	146.9 (6.37)	
(22)	$C_{13}H_8^+ (6) \rightarrow C_{13}H_7^+ + H_7$	143.6 (6.23) <sup>a</sup>	
(22)	$C_{13}H_8^+ (6) \rightarrow C_{13}H_7^+ + H_8$	130.7 (5.67)	
Fourth H loss (m/z 163 $\rightarrow$ 162)			
(23)	<b><math>C_{13}H_7^+ (12) \rightarrow C_{13}H_6^+ + H_6</math></b>	<b>106.7 (4.63)</b>	-498.40
(24)	$C_{13}H_7^+ (12) \rightarrow C_{13}H_6^+ + H_5$	112.8 (4.89)	
(25)	$C_{13}H_7^+ (12) \rightarrow C_{13}H_6^+ + H_4$	113.1 (4.91)	
(26)	$C_{13}H_7^+ (12) \rightarrow C_{13}H_6^+ + H_3$	112.7 (4.89)	
(27)	$C_{13}H_7^+ (12) \rightarrow C_{13}H_6^+ + H_2$	114.4 (4.96)	
(28)	$C_{13}H_7^+ (12) \rightarrow C_{13}H_6^+ + H_1$	113.3 (4.91)	
(29)	$C_{13}H_7^+ (12) \rightarrow C_{13}H_6^+ + H_9$	117.0 (5.07)	

Table 3 – continued

Reaction		Bond Energy (kcal/mol (eV))	Energy of Precursor (Hartrees)
Fifth H loss (m/z 162 → 161)			
(30)	$\text{C}_{13}\text{H}_6^+ \text{ (23)} \rightarrow \text{C}_{13}\text{H}_5^+ + \text{H5}$	<b>99.8 (4.33)</b>	-497.73
(31)	$\text{C}_{13}\text{H}_6^+ \text{ (23)} \rightarrow \text{C}_{13}\text{H}_5^+ + \text{H9}$	135.1 (5.86)	
(32)	$\text{C}_{13}\text{H}_6^+ \text{ (23)} \rightarrow \text{C}_{13}\text{H}_5^+ + \text{H1}$	147.2 (6.38) <sup>a</sup>	
(33)	$\text{C}_{13}\text{H}_6^+ \text{ (23)} \rightarrow \text{C}_{13}\text{H}_5^+ + \text{H2}$	154.0 (6.67) <sup>a</sup>	
(34)	$\text{C}_{13}\text{H}_6^+ \text{ (23)} \rightarrow \text{C}_{13}\text{H}_5^+ + \text{H3}$	149.5 (6.48) <sup>a</sup>	
(35)	$\text{C}_{13}\text{H}_6^+ \text{ (23)} \rightarrow \text{C}_{13}\text{H}_5^+ + \text{H4}$	148.6 (6.44) <sup>a</sup>	
Sixth H loss (m/z 161 → 160)			
(36)	$\text{C}_{13}\text{H}_5^+ \text{ (30)} \rightarrow \text{C}_{13}\text{H}_4^+ + \text{H9}$	115.0 (4.98)	-497.07
(37)	$\text{C}_{13}\text{H}_5^+ \text{ (30)} \rightarrow \text{C}_{13}\text{H}_4^+ + \text{H1}$	113.0 (4.90)	
(38)	$\text{C}_{13}\text{H}_5^+ \text{ (30)} \rightarrow \text{C}_{13}\text{H}_4^+ + \text{H2}$	113.6 (4.93)	
(39)	$\text{C}_{13}\text{H}_5^+ \text{ (30)} \rightarrow \text{C}_{13}\text{H}_4^+ + \text{H3}$	112.7 (4.89)	
(40)	$\text{C}_{13}\text{H}_5^+ \text{ (30)} \rightarrow \text{C}_{13}\text{H}_4^+ + \text{H4}$	113.5 (4.92)	

<sup>a</sup> One negative frequency was found for the calculated product.

probable positions from which these hydrogens are lost. The following discussion refers extensively to Table 3 and Figure 37.

#### Loss of first hydrogen

The C-H bond energies were calculated by determining the total energy of the  $\text{C}_{13}\text{H}_{10}^+$  ion and subtracting this value from the total energy of the  $\text{H} + \text{C}_{13}\text{H}_9^+$  products. The C-H bond energies are listed in Table 3. Figure 37 shows the calculated lowest energy photoreaction pathways for sequential hydrogen loss. The C-H bonds (C-H9 and C-H9') on the five-membered ring are almost 50% weaker than the C-H bonds on the six-membered rings. This bond energy (60.9 kcal/mol) is similar to the value found by Bauschlicher for hydrogens bonded to the same carbon in the 1-hydronaphthalene cation (62.09 kcal/mol).<sup>146</sup>



Computation of the transition state (TS) involved in the abstraction of the H9' atom revealed a point on the potential surface at essentially the same energy as the dissociation limit of the C-H9' bond. This is not surprising since the optimized geometry of the TS shows that the H9' atom is 3.26 Å from the  $sp^3$  carbon and 2.12 Å from the H9 atom, indicating that H9' interacts only minimally with the rest of the ion. This situation is similar to the abstraction of the hydrogen from the 1-position of 1-hydronaphthalene cation, where a zero energy barrier was also found.<sup>146</sup>

#### Loss of second hydrogen

The most favorable route for the loss of the next hydrogen from  $C_{13}H_9^+$  with H9' removed) is the cleavage of the C-H6 (or equivalent C-H3) bond. (Since the fluorene molecule is symmetric, it was arbitrarily chosen to remove the hydrogens from carbons 5-8. The same results would apply to carbons 1-4.) This requires 4.88 eV, but this energy is only ca 3% lower than cleavage of the C-H9 bond, suggesting that the H6 loss channel (reaction (9) in Table 3) is only slightly more favorable than the channels in which the other hydrogens are removed.

#### Loss of the third hydrogen

There are several different ways to lose the third hydrogen depending on the configuration of the  $C_{13}H_8^+$  precursor ion. The preferred route uses the 164c form found in Figure 37. The calculated C-H bond energy for hydrogens on the same ring varied from 4.0 eV to 4.5 eV, while removing H9 required 5.8 eV.

If the first two hydrogens lost are H9 and H9', the C-H bond energies at the H5 – H8 positions range from 5.2 to 6.4 eV as shown in reactions (19) – (22) of Table 3. These energies are 30 and 59% higher, respectively, than the bond energies in the

preferred reaction (12), indicating their probable low yield. (They are therefore not displayed in Fig. 37.)

Abstraction of H8 from 164a, H7 from 164b, H6 from 164c and H5 from 164c (all not displayed) require 4.5 eV, 5.04 eV, 4.5 eV and 5.0 eV energy, respectively. These are significantly larger energies than those displayed for the third H loss in Fig. 37. They also are expected to be low-yield routes. Finally, removal of the third hydrogen from the same six-membered ring requires lower energies than removal from the other six-membered ring. As mentioned before, stripping hydrogen from the same ring requires 4.0 to 4.5 eV, while stripping from the other ring requires 50-66% more energy (cf. (15)-(18), Table 3).

In the third H loss step, only four forms (a, b, c, and d) of the  $m/z$  164 precursor were studied. Figure 37 shows eight energetically plausible reaction pathways starting from these four precursors. C-H bond energies range from 3.94 to 4.25 eV. Table 3 lists the energies of all the reactions that occur via reaction (7), involving only the  $m/z$  164 (form c) precursor.

#### Loss of fourth hydrogen

Eight routes are possible for the loss of the fourth hydrogen. In this, as well as in the second H loss step, the precursors are in their singlet ground states. The computed C-H bond energies are higher by 15-24% (4.6 to 4.9 eV versus 4.0 eV) than the energies in third and fifth H loss step, where the precursors are in doublet ground states. Again, abstraction of the fourth H from the other six-membered ring (i.e., H1-H4), or the abstraction of H9, require higher energies (between 6 to 9.3% more) than removing H5-H8 via the reactions displayed in Fig 37. This correlates well with the experimental data

collected for reaction rates in Table 2. The rates for the loss of the second and fourth hydrogen are much slower than for the loss of the other hydrogens.

#### Loss of fifth hydrogen

There are four reaction channels from four different  $C_{13}H_6^+$  isomers that are favored for the removal of the fifth hydrogen (cf. Figure 37). The removal of H from the same ring of the ion requires 4.1 to 4.3 eV. Removal of the fifth hydrogen from the other six-membered ring requires 35-47% more energy and is therefore much less likely (cf. (31)-(35), Table 3).

#### Loss of sixth hydrogen

The observed loss of only 5 hydrogens is understandable now, since the C-H bond energies calculated for the  $m/z$  161 ( $C_{13}H_5^+$ ) species (sixth H loss in Table 3) are high (over 4.89 eV). On the other hand, other photoproducts are observed which originate from the  $m/z$  161 species. These decomposition pathways, involving loss of neutral  $C_2H_2$ ,  $C_4H_2$ ,  $C_6H_2$ ,  $C_8H_2$ , species, are energetically more favorable than loss of another hydrogen. These products are discussed in the next section.

In summary, the bond energies listed in Table 3 and Figure 37 indicate that the first hydrogen removed from the fluorene cation is from the  $sp^3$  carbon on the five-membered ring, and the next four hydrogens come from one of the six-membered rings. Loss of the sixth hydrogen is not energetically feasible under the photolysis conditions used in the experiment.

#### Structural Integrity vs Ring Opening

Further photolysis of the dehydrogenated odd mass fluorene species ( $m/z$  161, 163, 165) has been observed to produce a number of low-mass fragments. These low-mass products cannot be satisfactorily understood starting from a fluorene-like

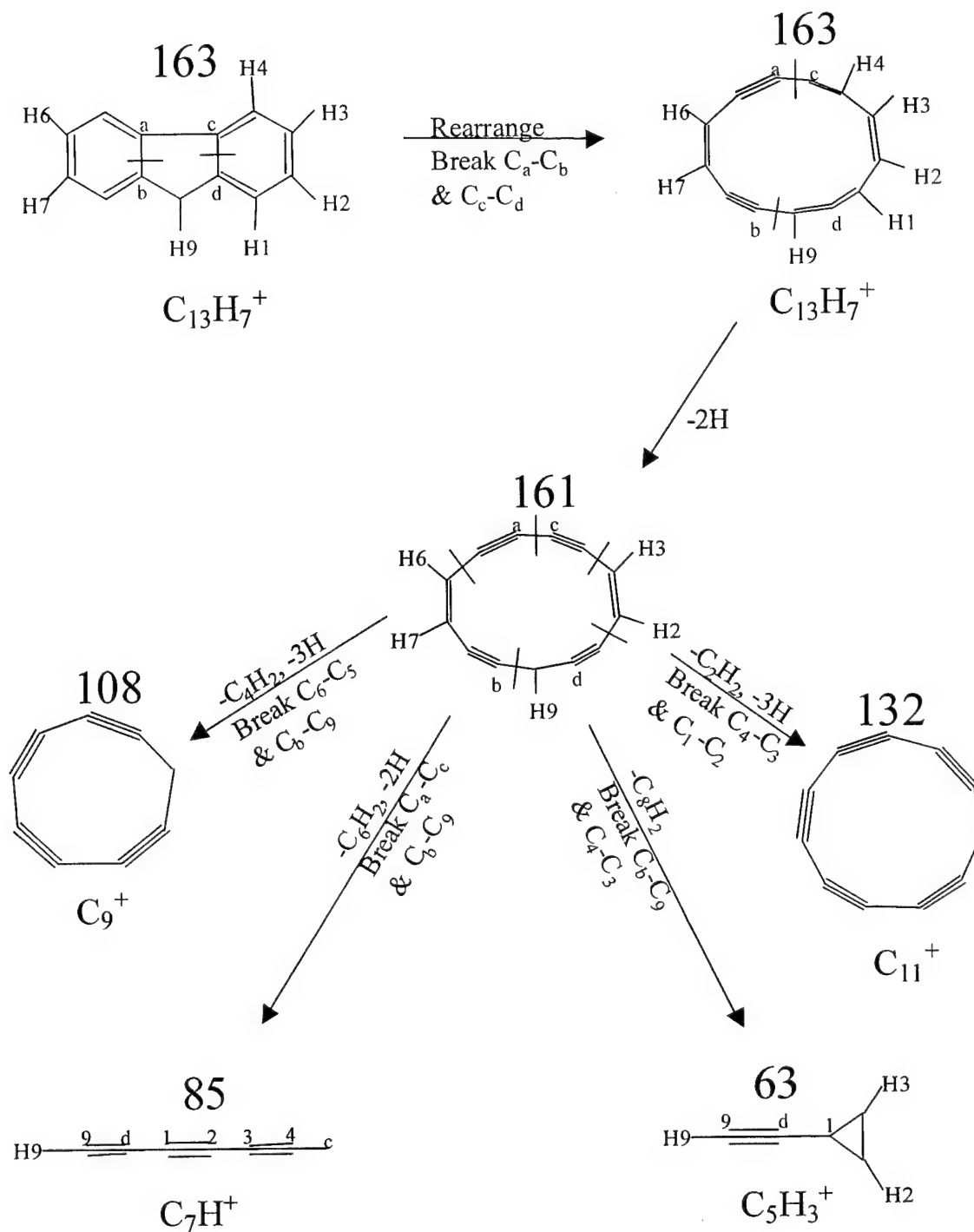


Figure 38. Formation of cyclic  $m/z$  163 ( $C_{13}H_7^+$ ) and  $m/z$  161 ( $C_{13}H_5^+$ ) ions by rupture of the  $C_a-C_b$  and  $C_c-C_d$  bonds in the proposed ring-opening mechanism. The final lowest energy photoproducts are formed via the opening of the specific bonds marked.

framework. Production of all the product fragments can, however, be explained in a consistent and plausible manner if one or more rings are assumed to open and  $C_2H_2$ ,  $C_2H_4$ , and/or  $C_2H_6$ , are ejected.

In the initial calculations, it was assumed that the  $m/z$  165 precursor retains its fluorene-like carbon framework. Then, the  $C_a-C_b$  bond (for labels, cf. Fig 38) in the  $C_{13}H_9^+$  ion was broken and the  $C_a-C_b$  distance increased stepwise. Single point total energy calculations were performed (B3LYP/4-31G) on the singlet potential surface for each step. A plot of total energy vs.  $R$  ( $C_a-C_b$ ) distances showed a local maximum at  $R_r$  ( $C_a-C_b$ ) = 1.93 Å with a relative energy of +5.85 eV. For  $R > R_r$ , total energies decreased with increasing distance, indicating that  $C_{13}H_9^+$  forms other, more stable structures that are not fluorene-like in structure. However, the energies calculated are not expected to be reliable, since geometries were not optimized at first. Calculations (B3LYP/4-31G) on energetically-relaxed cyclic structures with the  $C_a-C_b$  and  $C_c-C_d$  bonds open for  $C_{13}H_9^+$ ,  $C_{13}H_7^+$  and  $C_{13}H_5^+$  ions yielded total energies of +6.23 eV, +2.59 eV and -0.33 eV, respectively, relative to the closed-bond fluorene forms. This suggests that ring opening may occur in the  $C_{13}H_7^+$  and  $C_{13}H_5^+$  singlet state ions when exposed to 5.5 eV energy photons.<sup>147</sup> On the other hand, formation of monocyclic  $C_{13}H_5^+$  may also occur by the stripping of two hydrogens from cyclic  $C_{13}H_7^+$  (cf. Fig. 38). Thus, it appears possible that both fluorene-like and cyclic isomers of  $C_{13}H_7^+$  and  $C_{13}H_5^+$  could be generated in the FTICR/MS experiments.

#### Further Fragmentation

Although the earlier study<sup>114</sup> with short photolysis exposures found only dehydrogenated products, the present work has since determined that longer irradiation

leads to other, lower mass products. Isolation and further photolysis of each of the dehydrogenated product ions results in a set of unique lower mass products, as shown in Figure 32. To rationalize the formation of these products, the strategy adopted was to establish the lowest energy C-C bond-cleavage route that leads to the observed low-mass products without requiring repositioning of any hydrogen atoms. The possible pathways from each of the odd mass dehydrogenated precursors are discussed in turn below.

#### Photoproducts from the m/z 165 ion

Photolysis of the m/z 165 ion yields m/z 164, 163, 139 and 115 product ions directly (cf. Fig 32). Breaking a pair of C-C bonds in the  $C_{13}H_9^+$  species with ejection of  $C_2H_2$  and  $C_4H_2$  neutral fragments could lead to the observed m/z 139 ( $C_{11}H_7^+$ ) and m/z 115 ( $C_9H_7^+$ ) ions. Further ejection of two  $C_2H_2$  fragments from the m/z 115 ion could lead ultimately to the  $C_5H_3^+$  (m/z 63) ion. However, the m/z 63 ion could also be formed from the m/z 139 ion by ejection of  $C_2H_2$  and  $C_4H_2$  fragments. Isolation of the m/z 139 ion followed by further photolysis also produced the m/z 87 ( $C_7H_3^+$ ), 86 ( $C_7H_2^+$ ), and 85 ( $C_7H^+$ ) ions sequentially.

#### Photoproducts from the m/z 163 ion

Figure 32 also shows that photolysis of the m/z 163 ion produces m/z 162, 161, 89, and 87 product ions directly. They may result from ejection of H,  $H_2$ ,  $C_6H_2$ , and  $C_6H_4$ , neutral fragments. These products may be readily understood if one assumes that the m/z 163 ion initially exists in four isomeric fluorene-like forms. As an example, consider m/z 163c and 163d isomeric precursors. The first has the H5, H8 and H9' hydrogens removed, as shown in Figure 38. It may rearrange by breaking its internal  $C_a - C_b$  and  $C_c - C_d$  bonds, to form a monocyclic ring which, upon absorption of more energy, may break its  $C_4 - H_4$  and  $C_1 - H_1$  bonds to form cyclic m/z 161,  $C_{13}H_5^+$ .

Another photofragmentation scenario (Figure 39) is proposed for the  $m/z$  163d isomer. Since the placement of the hydrogens on the original fluorene-like framework is different in this isomer, it is now possible, after ring opening, to eject two different  $C_6H_4$  neutral fragments without any hydrogen relocations. This may occur by breaking either the  $C_5 - C_a$ ,  $C_d - C_1$  bond set or the  $C_6 - C_7$ ,  $C_2 - C_3$  bond set, both of which lead to a different  $m/z$  87 ( $C_7H_3^+$ ) ion. One of these may then rearrange to form the lower energy species having a “tadpole-like” shape (i.e., a three-membered ring attached to an acetylenic carbon chain tail). Further photolysis may produce a seven carbon linear chain with a terminal hydrogen.

A scheme for the  $m/z$  89 cation production directly from  $m/z$  163c precursor is sketched in Fig. 40. The most stable form for this product ion is a six-membered ring, formed by ring closure of the  $C_9$  carbon with the  $C_c$  and  $C_d$  carbons, fused into a three-membered ring. Further photolysis can form the  $m/z$  63 product.

#### Photoproducts from the $m/z$ 161 ion

Photolysis of the  $m/z$  161 ion produces the  $m/z$  135, 111, 87, and 63 products directly (cf. Fig 38). Both the  $m/z$  135 and 111 products lose three hydrogens sequentially to yield the  $m/z$  132 and 108 species, respectively. The  $m/z$  87 product loses two hydrogens to give the  $m/z$  85 ion. This fragmentation sequence is understandable via the scheme sketched in Fig. 39. The monocyclic ring form of the  $C_{13}H_7^+$  ( $m/z$  163) precursor initially loses two hydrogens (H1 and H4) to give  $C_{13}H_5^+$  ( $m/z$  161), which may then decompose in one of four ways, i.e., by ejecting one of the neutral fragments  $C_2H_2$ ,  $C_4H_2$ ,  $C_6H_2$ , or  $C_8H_2$ . Ejection of  $C_2H_2$  leads to  $C_{11}H_3^+$  ( $m/z$  135) which then sequentially photolyzes to cyclic  $C_{11}^+$  ( $m/z$  132). Ejection of  $C_4H_2$  yields  $C_9H_3^+$  ( $m/z$  111) and finally,

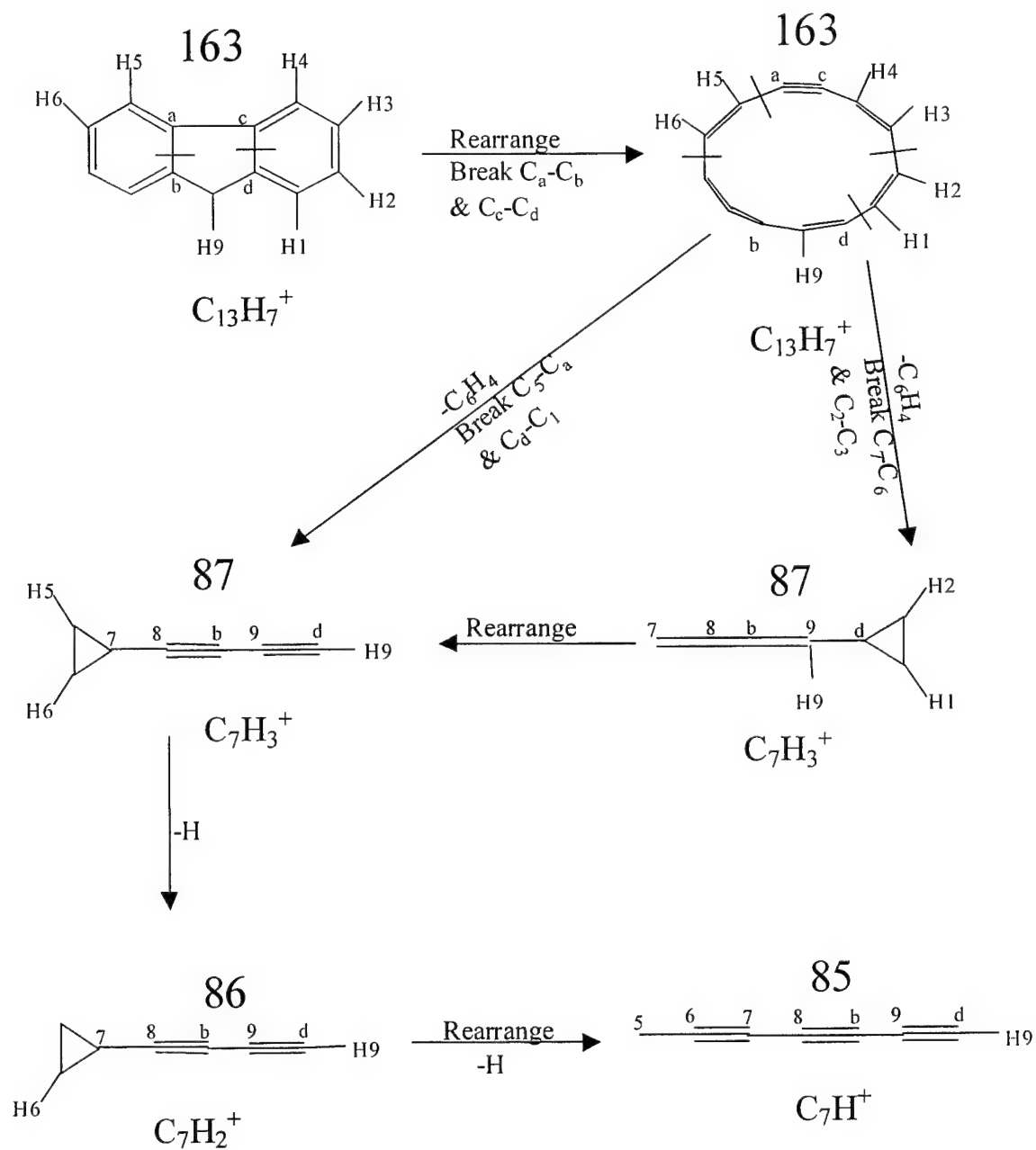


Figure 39. Formation of  $m/z$  87 ( $C_7H_3^+$ ) and  $m/z$  85 ( $C_7H^+$ ) from the  $m/z$  163 (Table 3, form 163d,  $C_{13}H_7^+$ ) isomer.



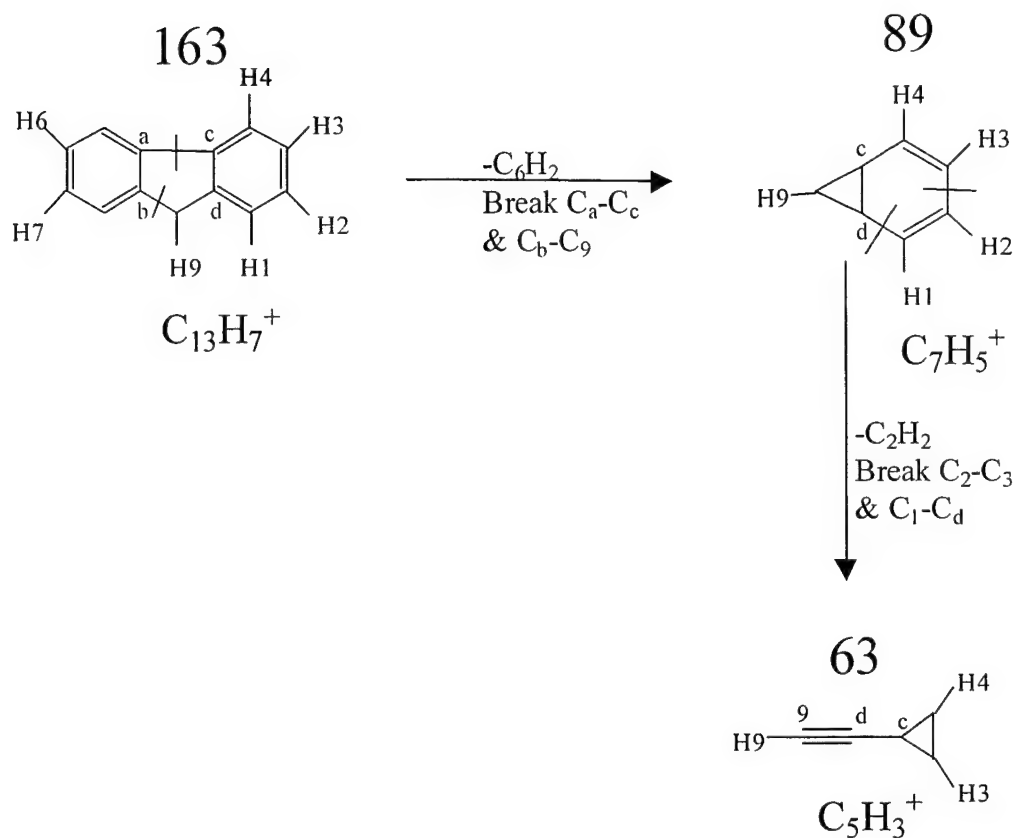


Figure 40. Formation of m/z 89 ( $C_7H_5^+$ ) directly from m/z 163 (Table 3, form 163c,  $C_{13}H_7^+$ ) isomer.

after the elimination of three hydrogens, to  $C_9^+$  (m/z 108). Removal of  $C_6H_2$  from  $C_{13}H_5^+$  leaves  $C_7H_3^+$  (m/z 87), which then further loses two hydrogens to give  $C_7H^+$  (m/z 85). Stripping of  $C_8H_2$  from  $C_{13}H_5^+$  leaves the  $C_5H_3^+$  (m/z 63) product.

The most stable geometries of the initial precursors (m/z 166, 165 and 161) and the final photodecomposition products have been calculated and are shown in Figures 41 and 42.  $C_5H_3^+$ , like its larger cousin,  $C_7H_3^+$ , has a tadpole-like structure, while  $C_7H^+$  prefers a linear acetylenic form with hydrogen at one end. The pure carbon products,  $C_9^+$  and  $C_{11}^+$ , have been studied previously by Giuffreda et al.<sup>148</sup> and Bowers and

coworkers.<sup>149, 150</sup> Different calculations (using B3LYP/cc-pVDZ, B3PW91/cc-pVDZ and CCSD(T)) indicate that both these species are probably monocyclic. However, a linear structure for  $C_9^+$  is not excluded, since its energy lies only 1.7 kcal/mol (B3LYP) or 13.1 kcal/mol (CCSD(T)) above the monocycle ( $C_{2v}$ ,  $^2B_1$ ) form.<sup>148</sup>

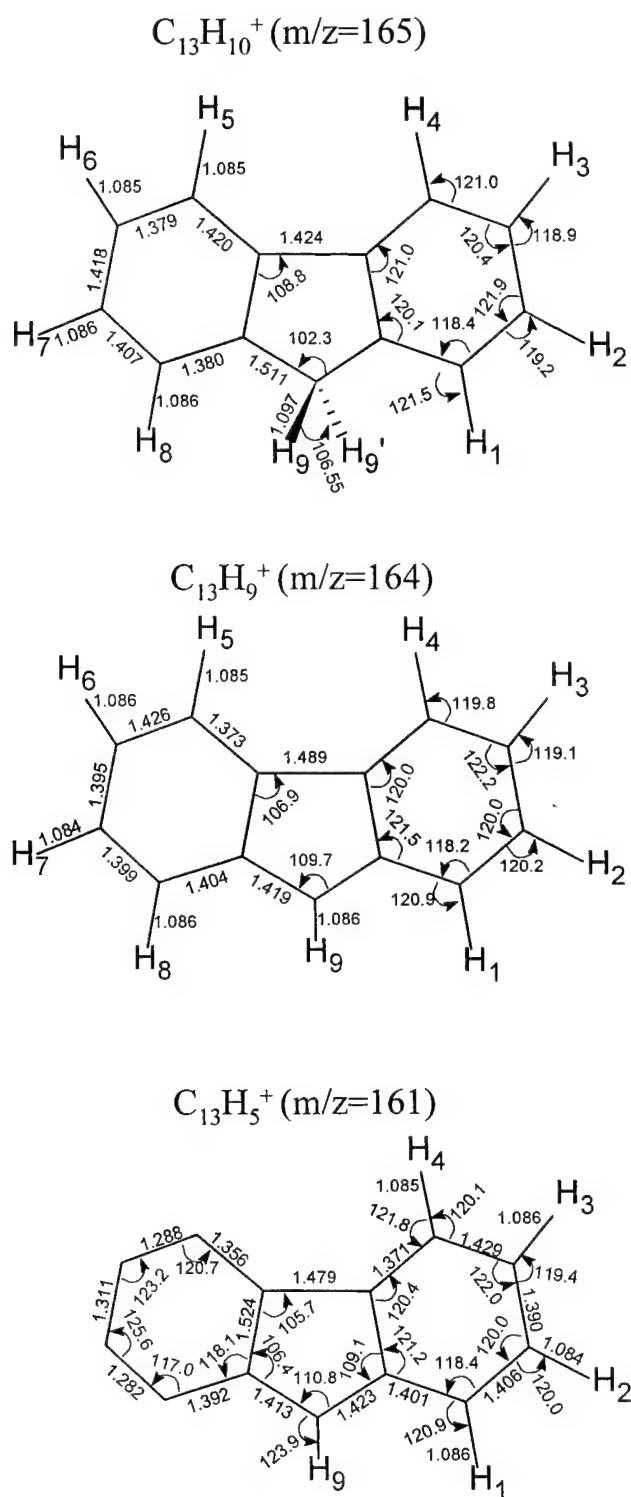


Figure 41. Optimized geometries for: (a) fluorene cation ( $\text{C}_{13}\text{H}_{10}^+$ ,  $m/z$  166), (b) fluorene cation fragment with  $\text{H}_{9'}$  loss ( $\text{C}_{13}\text{H}_9^+$ ,  $m/z$  165), (c) fluorene cation fragment with 5 H ( $\text{H}_{9'}$ ,  $\text{H}_8$ ,  $\text{H}_7$ ,  $\text{H}_6$  and  $\text{H}_5$ ) loss ( $\text{C}_{13}\text{H}_5^+$ ,  $m/z$  161).

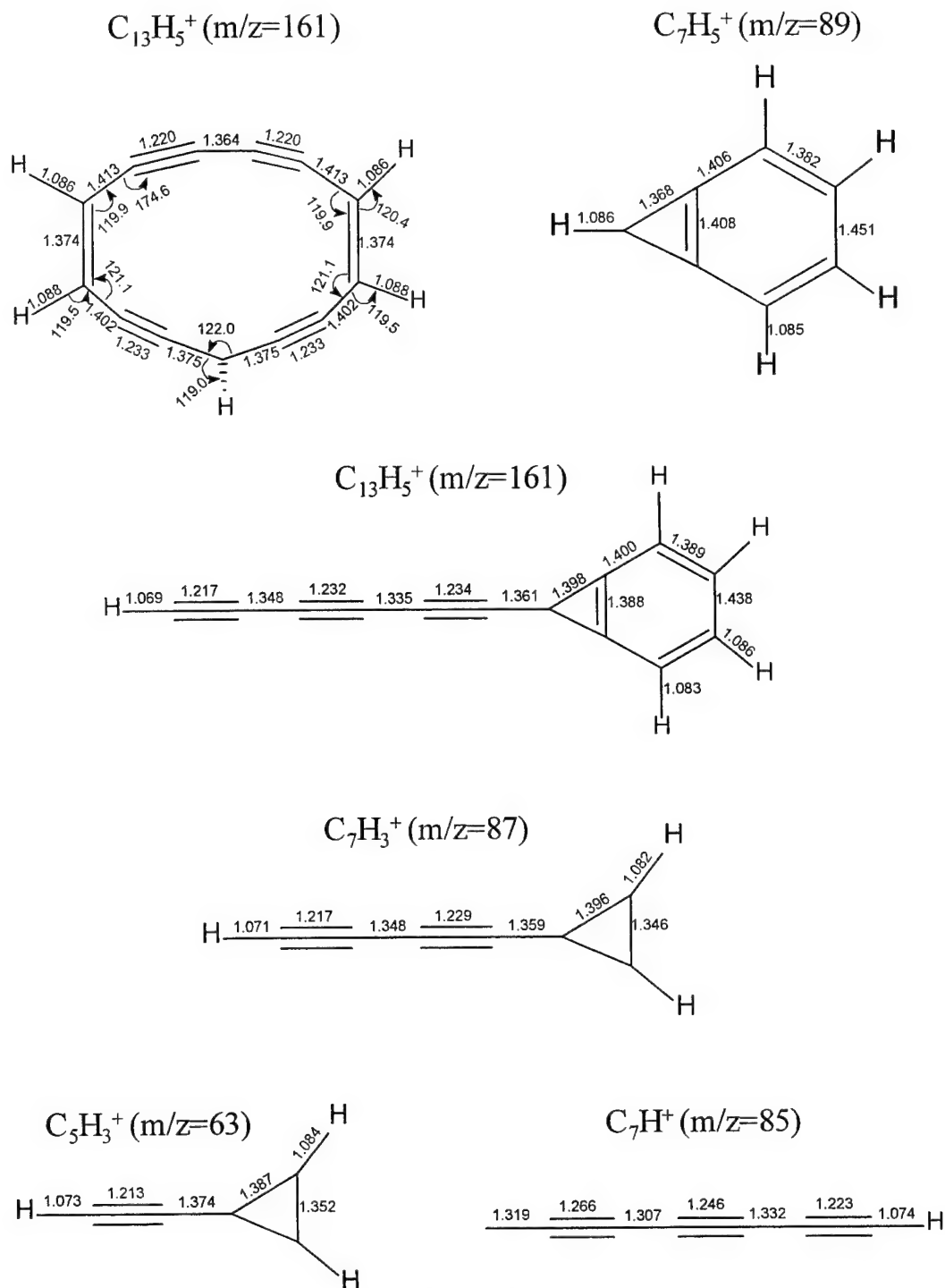


Figure 42. Optimized structures (B3LYP/6-31G(d, p) level) for the  $m/z$  63, 85, 87, 89, and two different  $m/z$  161 cations proposed as photolysis products of the fluorene cation. The bond lengths are in angstroms and angles in degrees. These are the lowest energy isomers found on the potential surface. The calculated energy of the  $m/z$  161 cyclic isomer is 0.698 eV above the chain-triangle-ring structure.

## CHAPTER 4

### ABSORPTION SPECTRA OF FLUORENE CATION

To identify the species responsible for the unidentified infrared absorption bands, IR emission spectra must be obtained in the gas phase at temperatures and conditions appropriate to the interstellar medium. While this is currently not possible in the laboratory, many approaches have been attempted. The principal one has been to isolate molecules (or ions) in rare-gas matrices such as argon or neon. Vala and coworkers have obtained many spectra of PAH cations such as naphthalene, anthracene, pyrene, perylene and coronene in argon matrices.<sup>151, 152</sup> Allamandola and coworkers have also undertaken a program to analyze PAHs in neon matrices and have recorded spectra for 23 neutral and 19 cationic species.<sup>21, 153, 154</sup>

One of the problems with spectra obtained in this manner is that no matter how “non-perturbing” the matrix is, it will still have an effect on the spectra compared to the gas-phase. Progress is being made in this direction however. Allamandola and coworkers obtained the gas phase spectrum of the naphthalene cation by cavity ring-down spectroscopy in a continuous supersonic slit jet coupled with an electronic discharge.<sup>94</sup> Brechignac and Pino have also obtained spectra of the phenanthrene cation in a supersonic pulsed jet.<sup>155</sup> Neither method is simple, however, and results may still be affected by inhomogeneous broadening.

### Action Spectrum of Fluorene Cation

The method employed in this study to obtain the absorption (action) spectrum of the fluorene cation involves monitoring the mass abundance of a dehydrogenated product ion while varying the irradiation wavelength. A small, fast monochromator (Farrand, 0.25 m) was used in conjunction with the xenon arc lamp. By scanning all wavelengths, an action spectrum may be generated. The original goal was to obtain spectra of all of the dehydrogenated fluorene ions, but the flux of the lamp after passing through the monochromator was too low.

Isolated  $m/z$  166 fluorene ions were trapped in the FTICR and irradiated by the output of the monochromator for periods of up to eight seconds. The monochromator wavelength was increased by 2.5 nm intervals between 250 and 700 nm (14000 to 40000  $\text{cm}^{-1}$ ). The results are shown in Figure 43. A broad peak is seen at ca. 617 nm along with another, more intense peak at 372 nm. This spectrum mimics reasonably well (cf. Figure 44) the electronic absorption spectrum in a rigid matrix reported previously by Shida.<sup>156</sup> The presence of two widely separated peaks suggests that excitation proceeds from a ground electronic state to two different excited electronic states. It can thus be concluded that excitation into either electronic state leads to dehydrogenation.

At 372 nm, the photon energy is 3.3 eV while at 617 nm it is only 2.0 eV. It was previously shown in Chapter 3 that the bond energy of the first hydrogen lost is 2.64 eV. This would indicate that the photons in the near-UV range could dissociate fluorene with a single photon while those in the red range would require multiple photons. This would explain the lower intensity and the loss of resolution of the absorption feature around 617 nm compared to Shida's spectra.

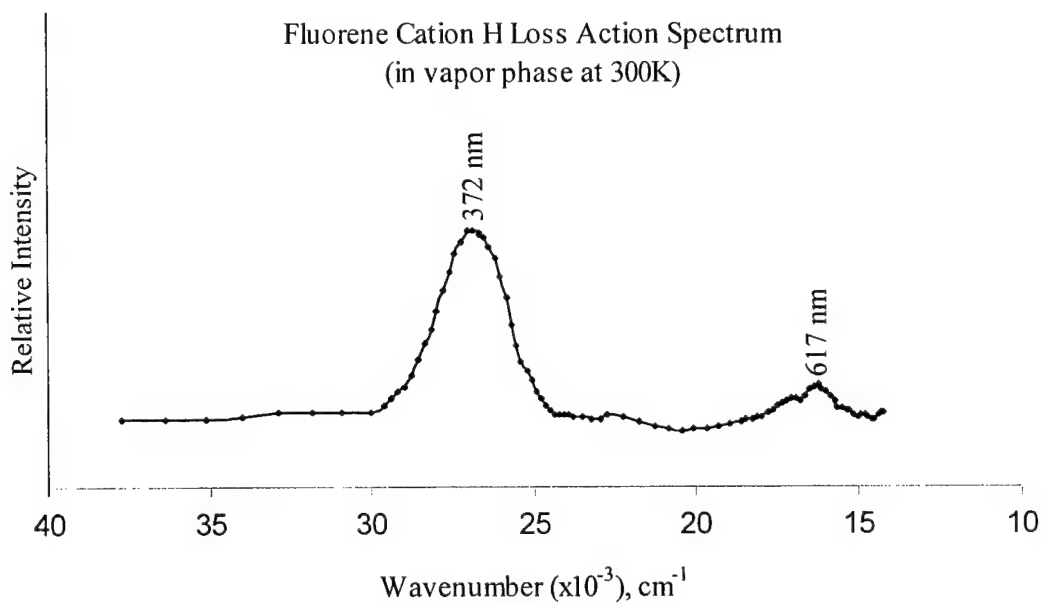


Figure 43. FTICR "action" spectrum obtained by monitoring the  $m/z$  165 ion mass peak and scanning the irradiation wavelength with a monochromator / Xe lamp combination.

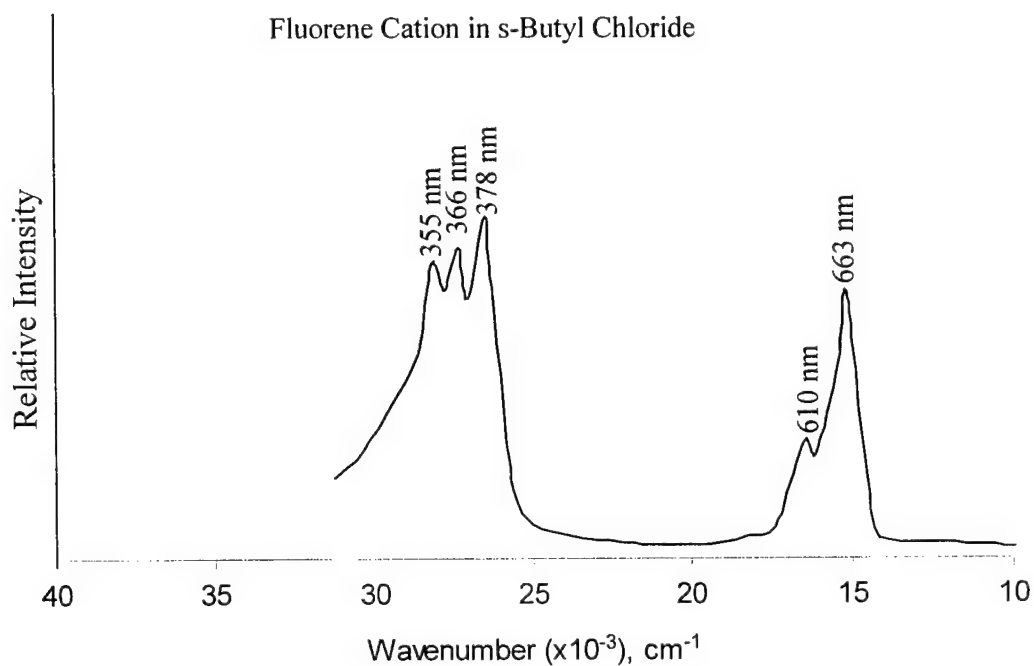


Figure 44. Absorption spectrum of the fluorene cation in a sec-butylchloride solid matrix at 77K. Adapted from Shida<sup>156</sup>.

### Laser Induced Action Spectrum

It was of interest to better resolve the absorption features in Figure 43. This was accomplished using a TDL50 Nd:YAG pumped dye laser (Quantel), using the dyes Rhodamine 590, 610, 640 and DCM.

The experimental sequence consisted of 1) an isolation pulse (to isolate the  $m/z$  166 ion and ensure that no  $m/z$  165 ions were present from electron ionization), 2) a laser trigger pulse (to fire the laser 10 times at a rate of 9 Hz) and 3) normal excitation and detection pulses.

The laser power (532 nm) was 325 mJ (pulse width approximately 10 ns), while the dye laser output was approximately 60-70 mJ. However, because of safety considerations, the laser output could not be directed in a straight line to the window of the FT-ICR. A series of four prisms was required to transfer the laser beam approximately 14 meters to the window of the FT-ICR mass spectrometer. This resulted in a severe degradation (to  $\sim 8$  mJ) of the dye laser power. This loss also degraded the useful wavelength range of the dyes to 10-15 nm. A power meter was used to measure the power of the laser pulse for each wavelength at the entrance to the FT-ICR instrument.

Since the power was not constant, it was important to ensure that the response of the system was linear at varying levels of power. Calibration curves were obtained for 1-10 laser pulses at the peak wavelength for several of the dyes (cf. Figure 45, 46). The calibration curve for a mixture of Rhodamine 610/640 at 600 nm at the normal operating pressure of  $3 \times 10^{-8}$  torr displays large scatter. By lowering the pressure to  $1.5 \times 10^{-8}$  torr, a calibration curve obtained at the same conditions produces a linear response (cf. Figure 46). All experiments were performed at this reduced pressure.



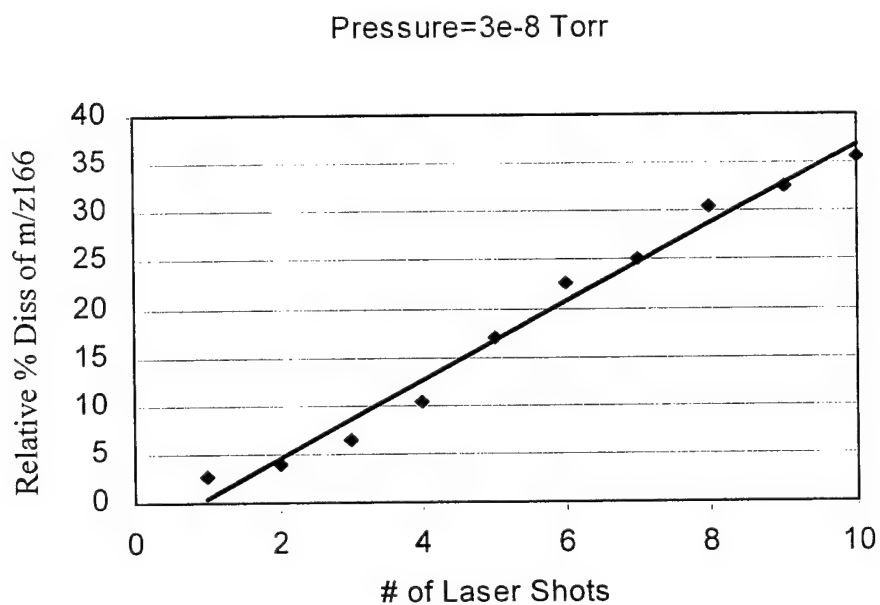


Figure 45. Calibration curve (% dissociation vs number of laser pulses) obtained at 600 nm at a pressure of  $3 \times 10^{-8}$  torr.

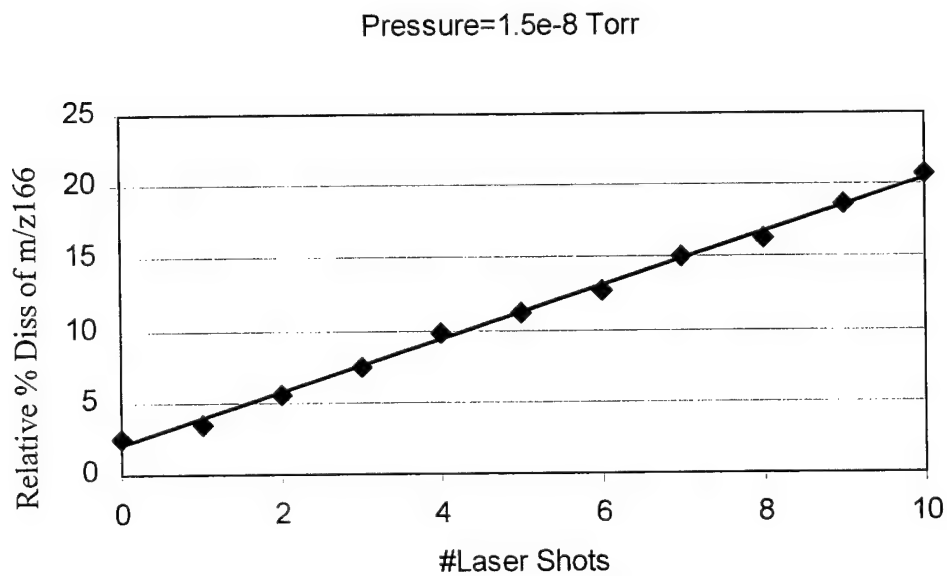


Figure 46. Calibration curve (% dissociation vs number of laser pulses) obtained at 600 nm at a pressure of  $1.5 \times 10^{-8}$  torr.

The useful ranges for each dye are shown in Table 4. Two different proportions of the R610/R640 mix were used to cover a broader range. The first mixture had a higher proportion of R610 compared to the second mixture.

Table 4. Laser dyes and their useful ranges.

Dye	Wavelength Range (nm)
R590	577-587
R590/R610	587-600
R610	593-599
R610/R640 #1	595-606
R610/R640 #2	607-615
R640	608-612
DCM	622-630

The percent dissociation was determined by dividing the  $m/z$  165 signal by the sum of the  $m/z$  165 and  $m/z$  166 signals. The result was then normalized by the measured power and the wavelength. The spectrum was scanned in one nm steps. Each section of the curve represents the use of a different dye and is the average of at least two different readings.

The results, in Figure 47, show two peaks, the first at  $\sim 602$  nm, and the second one is  $\sim 617$  nm. This does match well with the previous results using the monochromator and lamp.

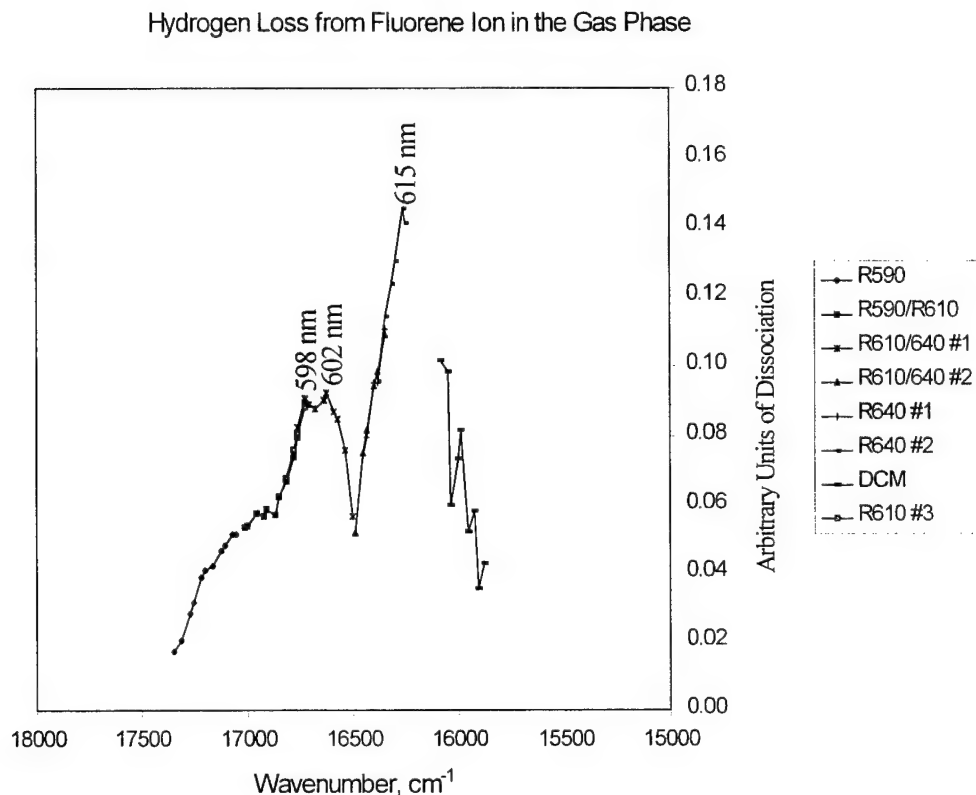


Figure 47. FTICR action spectrum obtained by monitoring the  $m/z$  165 ion mass peak and scanning the irradiation wavelength with the dye laser.

Experiments were also performed to determine the absorption spectra for the dehydrogenated fluorene ions. No dissociation was observed in the 577-630 nm range. This could be due to either the power being too low to effect dissociation or the absorption spectra being shifted for the dehydrogenated ions.

The spectra obtained with the monochromator/xenon arc lamp and the dye laser eliminate the perturbation effects seen in spectra obtained by isolation of ions in rare-gas matrices. Broad absorption peaks were observed at  $\sim 372$  nm and  $\sim 617$  nm with the monochromator, while the dye laser was able to resolve this upper peak into two peaks at

~600 and ~615 nm. Results with the dye laser could be improved dramatically if the use of prisms could be eliminated. The higher power would not only increase the amount of dissociation, it would also increase the usable range for each dye.

## CHAPTER 5 ION-MOLECULE REACTION PRODUCTS OF FLUORENE

### Aggregate Formation

Although detailed studies of ion-molecule reactions involving fluorene are rare, they may be of importance in the formation of larger PAHs in the interstellar medium. Kage<sup>142</sup> noted the presence of ion-molecule reaction products for fluorene but was unable to deduce the formation mechanisms.

Aggregates are observed from ion-neutral molecule reactions that take place when delay times are introduced after trapping of a particular ion in the FT-ICR cell. Masses of these aggregates of the fluorene ion and its dehydrogenated photoproducts range from  $m/z$  226 to  $m/z$  331 and form with apparently rather high efficiencies. Interaction rate constants of the order  $10^{-9} \text{ cm}^3/\text{s}$  (for reaction of the  $m/z$  166 ion with neutral fluorene) can be approximated.<sup>157,158</sup> At an operating pressure of  $4 \times 10^{-8}$  torr, this translates into 2.3 collisions per second. For typical delay times of four seconds, ca. nine collisions are thus expected. The ease with which aggregate product ions are observed (cf. Fig. 48) indicates a high reaction efficiency between neutral and ionic reactants.

In Figure 48 are shown the photo-degradation and photo-aggregation products obtained after four seconds irradiation of the parent  $m/z$  166 ion followed by a four second delay. Figure 49 is an expansion of Figure 48 showing the aggregation products. Specific groups of aggregates with differing (and usually even) numbers of carbon atoms and hydrogen atoms are easily discerned.

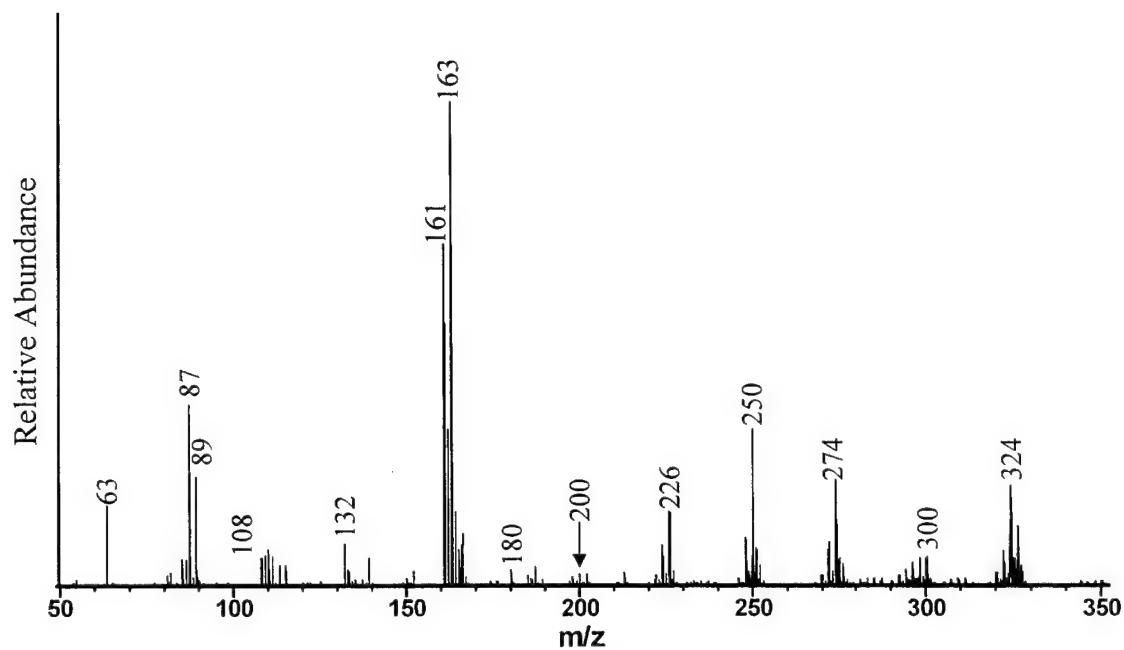


Figure 48. FTICR mass spectrum of photolysis products after a four second irradiation of the  $m/z$  166 ion and four second reaction delay.

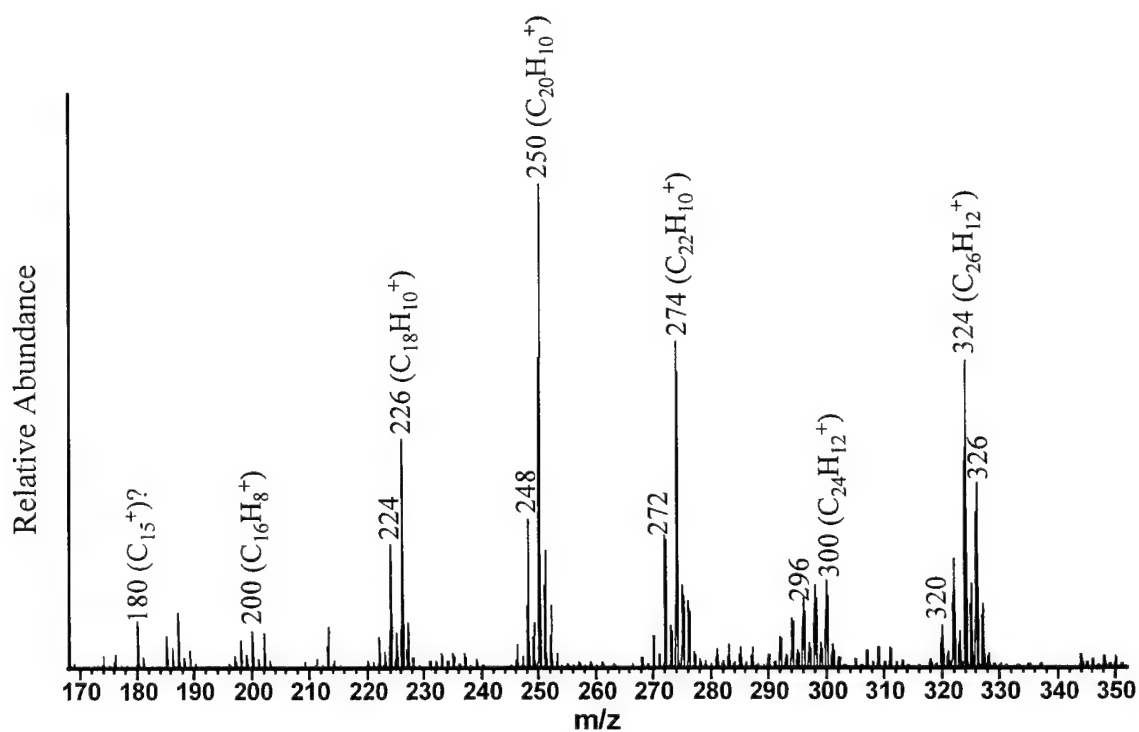


Figure 49. Expansion of Figure 48 showing aggregate products only.

Two mechanisms for the production of fluorene aggregates are possible. In the first, a dimer-like ion with  $m/z$  values in the range 327-332 could form from the reaction of one of the  $m/z$  161-166 precursor ions and neutral fluorene. Figure 50 illustrates the products of this reaction. Irradiation of these larger ions might then produce lower mass ions by ejecting  $C_2H_2$  or  $C_2$  fragments and various numbers of hydrogens. Figure 51, in which ions in the range  $m/z$  316-328 were isolated and further irradiated for four seconds, shows, however, that lower mass fragments are not produced. Only dehydrogenation occurs. The predominant peak is now  $m/z$  324, formed by a loss of three hydrogens from the  $m/z$  327 ion. All of these aggregates have the formula  $C_{26}H_n^+$ , where  $n=4$  to 16.

The lack of lower mass fragments points to a second possible mechanism. Aggregates may form from reactions of initial low-mass photoproducts and neutral fluorene. Figure 52 shows that this is indeed the case. The photolysis products between  $m/z$  50 and 159 were isolated and all others ejected. After a reaction delay of four seconds, all aggregate groups are now observed, except for  $m/z$  320-330. This latter group is not expected to form since the  $m/z$  161-166 ions were ejected and thus not available for reaction. The presence of the  $m/z$  166 ion is due to charge transfer. (It will be shown later that the  $m/z$  166 ion cannot react with neutral fluorene.)

#### Source Of Photoaggregates

In the experiment described above, in which a broad range of ionic fragments ( $m/z$  50 to 159) was selected and allowed to react, no specific information about which ion(s) led to what aggregates was obtained. To secure these data, each group of primary photolysis products was isolated in turn and allowed to react for four seconds before excitation and detection. Only groups with odd numbers of carbons were isolated, since

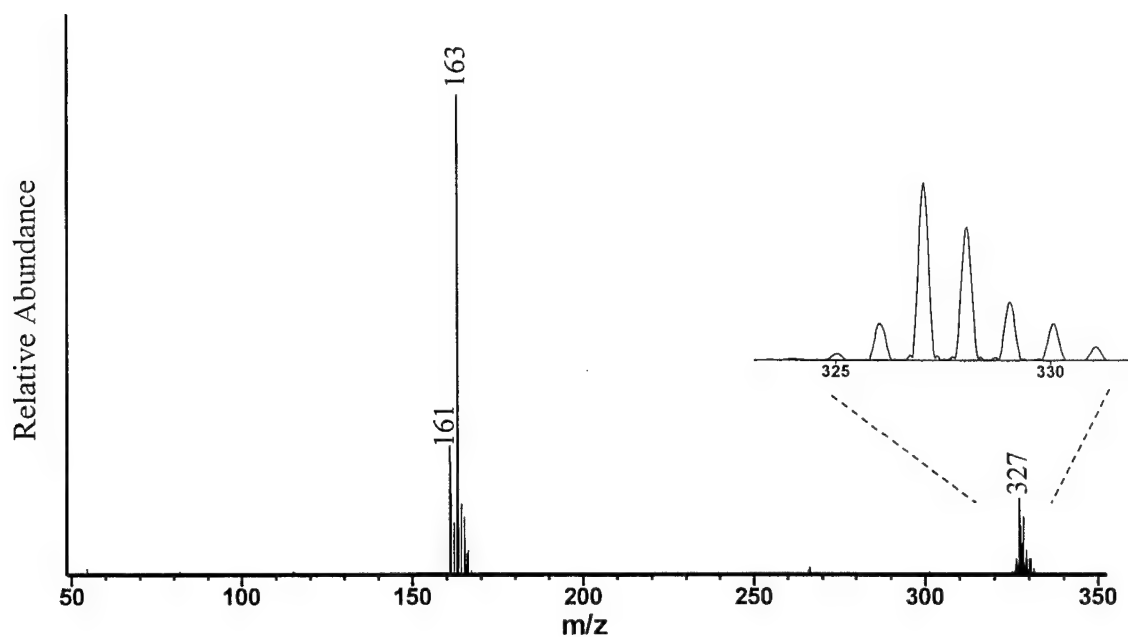


Figure 50. FTICR mass spectrum of the ion-molecule reaction products of isolated  $m/z$  161-166 after a four second reaction delay.

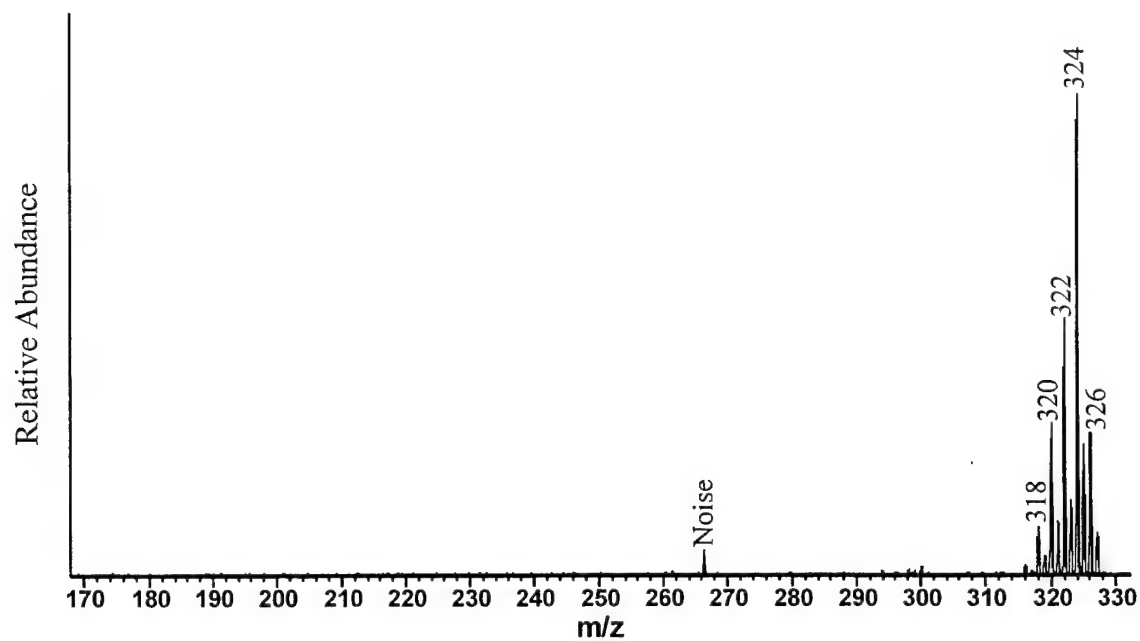


Figure 51. FTICR mass spectrum of photolysis products after four seconds of irradiation of isolated  $m/z$  316-328.



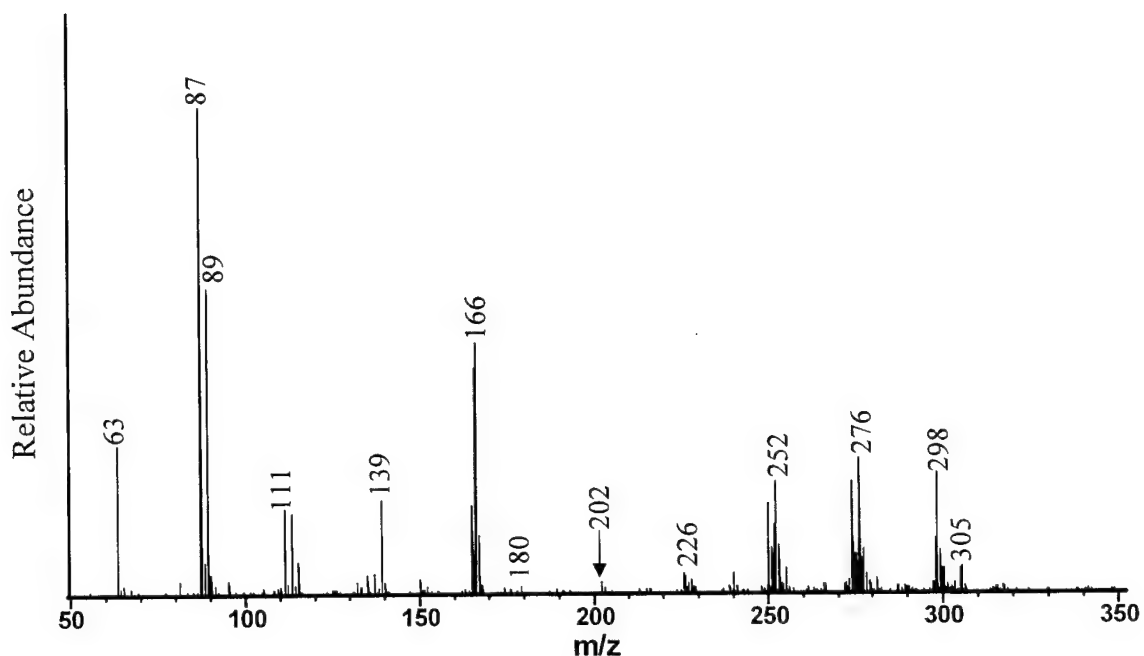


Figure 52. FTICR mass spectrum of the ion-molecule reaction products of isolated  $m/z$  50-159 after a four second reaction delay.

the abundance of groups with even numbers of carbons was too low to give meaningful results. In addition, the photostabilities of the aggregates were determined by isolation and photolysis (for four seconds) of each aggregate group in the  $m/z$  180 to 330 range. The results for each ion group will be discussed in turn below.

#### $C_5H_n^+$ Ions ( $m/z$ 62-68)

Although  $m/z$  63 ( $C_5H_3^+$ ) is the primary ion in this grouping, minor fragments at  $m/z$  64, 65, and 67 are also present. Figure 53 indicates an ion-neutral reaction taking place with  $m/z$  63 to form  $m/z$  226-230. The direct product is  $m/z$  229 ( $63+166=229$ ) with some  $m/z$  230 forming from a reaction with a fluorene neutral having a  $^{13}C$  isotope ( $63+167=230$ ). All of the fragment ions have been photolyzed from the mass-selected  $m/z$  166 parent fluorene ion so all contain only  $^{12}C$  isotopes. However, the neutrals have the normal isotopic distribution for carbon. Since fluorene has 13 carbons, 14% of them

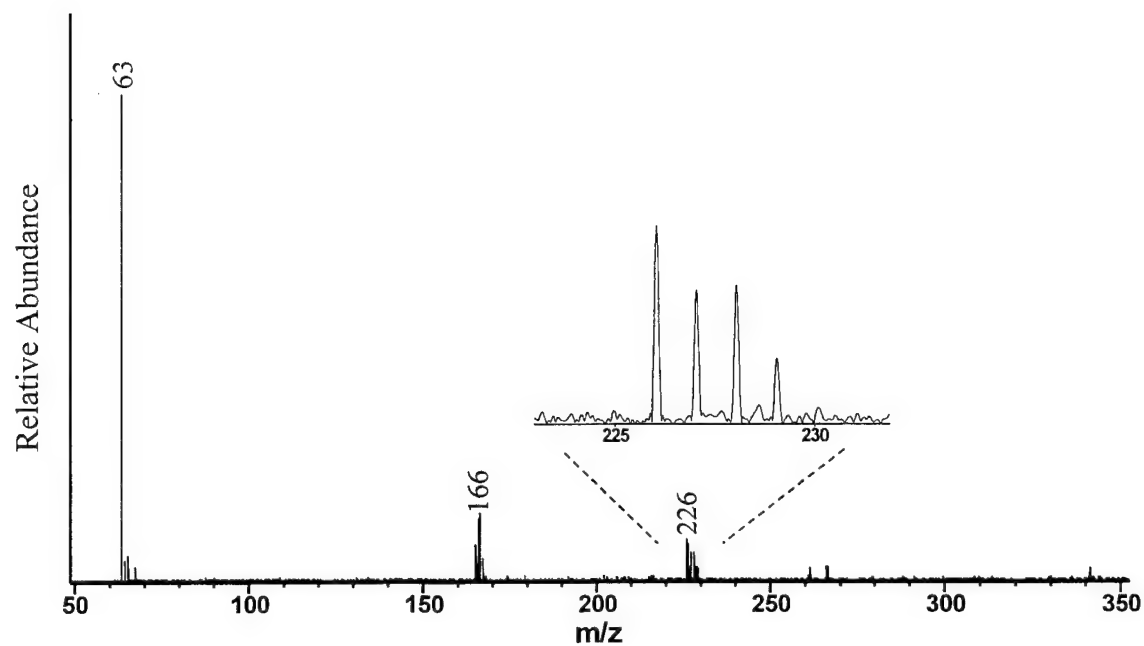


Figure 53. FTICR mass spectrum of the ion-molecule reaction products of isolated  $m/z$  52-68 after a four second reaction delay.

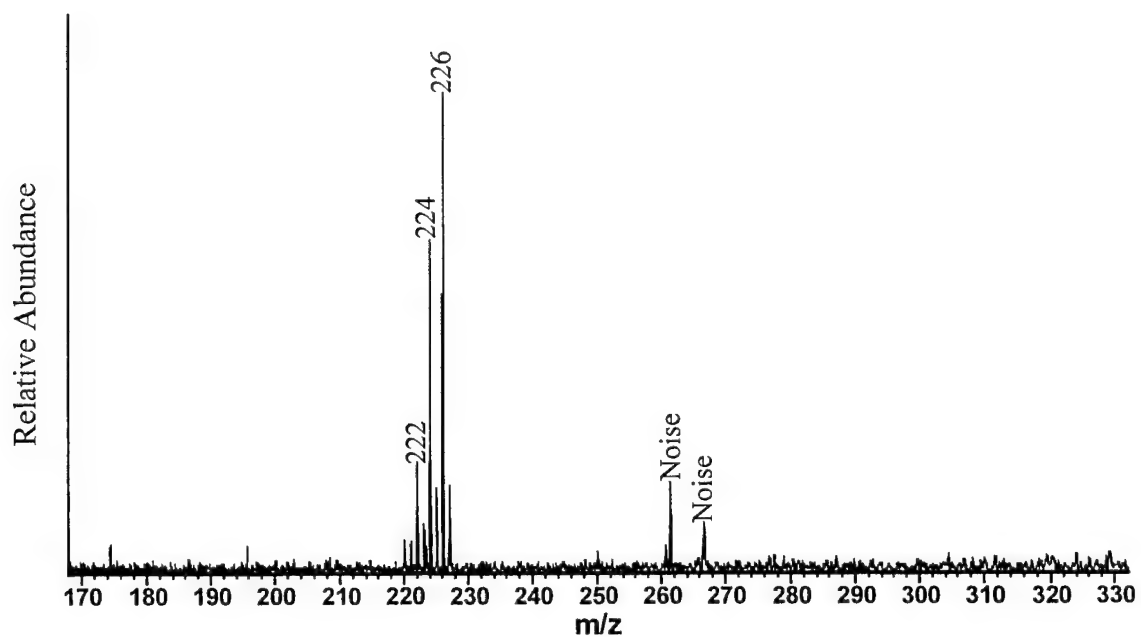


Figure 54. FTICR mass spectrum of photolysis products after four seconds of irradiation of isolated  $m/z$  219-230.

will have a mass of 167 while only 0.16% of them will have a mass of 168. The  $m/z$  229 ion may also eject three additional hydrogens during this reaction to form  $m/z$  226. The aggregates formed in this reaction have the formula  $C_{18}H_n^+$ , where  $n=12$  to 15.

Isolation and photolysis of the aggregates in the  $C_{18}H_n^+$  group resulted only in further dehydrogenation (cf. Figure 54). The primary peak is still at  $m/z$  226 ( $C_{18}H_{10}^+$ ), but the products range from  $C_{18}H_4^+$  to  $C_{18}H_{10}^+$ . The  $m/z$  227 peak is presumed to be due to a  $^{13}C$  isotope.

#### $C_7H_n^+$ ( $m/z$ 84-92)

Ions in the  $m/z$  84-92 range (where the primary ions are  $m/z$  87 and  $m/z$  89) reacted with fluorene to form aggregates in the  $m/z$  250 to  $m/z$  255 range (cf. Figure 55). The isolation of  $m/z$  87 with a four second reaction delay is shown in Figure 57. As expected,  $m/z$  253 is present ( $87+166=253$ ). It appears that one hydrogen is easily ejected during this process to also form the predominant peak at  $m/z$  252.

The  $m/z$  89 ion case is more interesting, as shown in Figure 58. The expected peak at  $m/z$  255 ( $89 + 166$ ) is observed, but the single-hydrogen-loss peak at  $m/z$  254 is absent. This contrasts with the reaction involving the  $m/z$  87 ion, whose aggregate product easily loses a hydrogen.

Figure 58 also shows a peak at  $m/z$  240, which was initially seen in Figure 52. This product ion is now known to result from the reaction of the  $m/z$  89 ion with neutral fluorene. During the aggregation process, a carbon and three hydrogens are ejected to form the  $C_{19}H_{12}^+$  ion. The  $m/z$  87 ion did not form this aggregate, giving a further indication that the  $m/z$  87 and  $m/z$  89 ions have different structures, as mentioned in Chapter 3. The aggregates formed in this reaction have the formula  $C_{20}H_n^+$ , where  $n=10$  to 15.

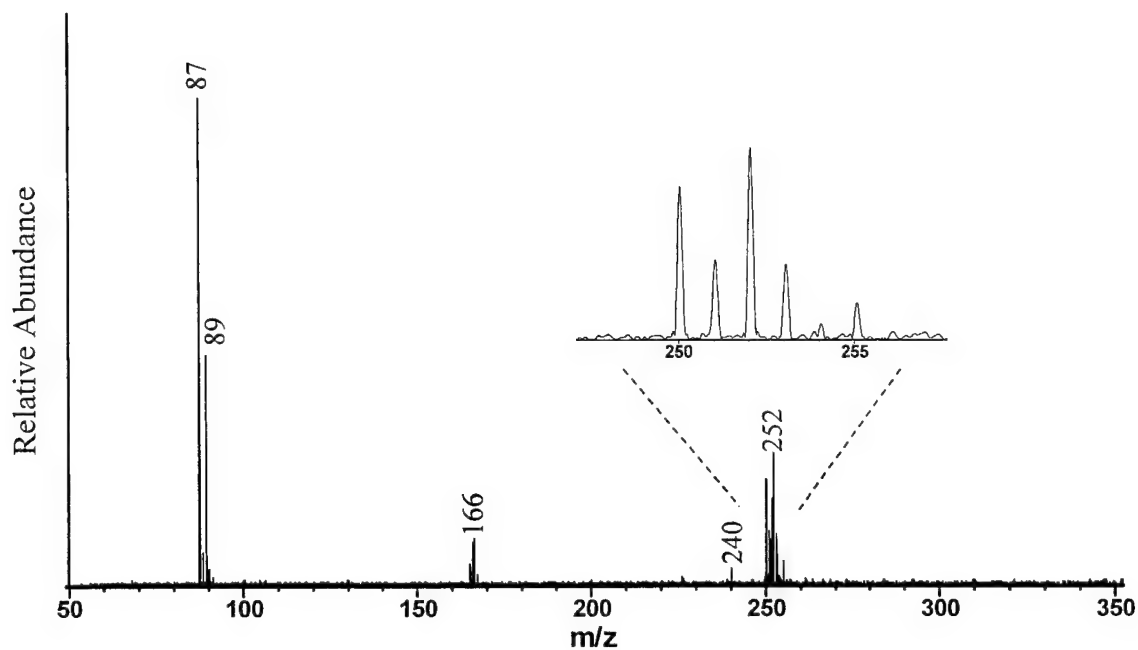


Figure 55. FTICR mass spectrum of the ion-molecule reaction products of isolated  $m/z$  82-92 after a four second reaction delay.

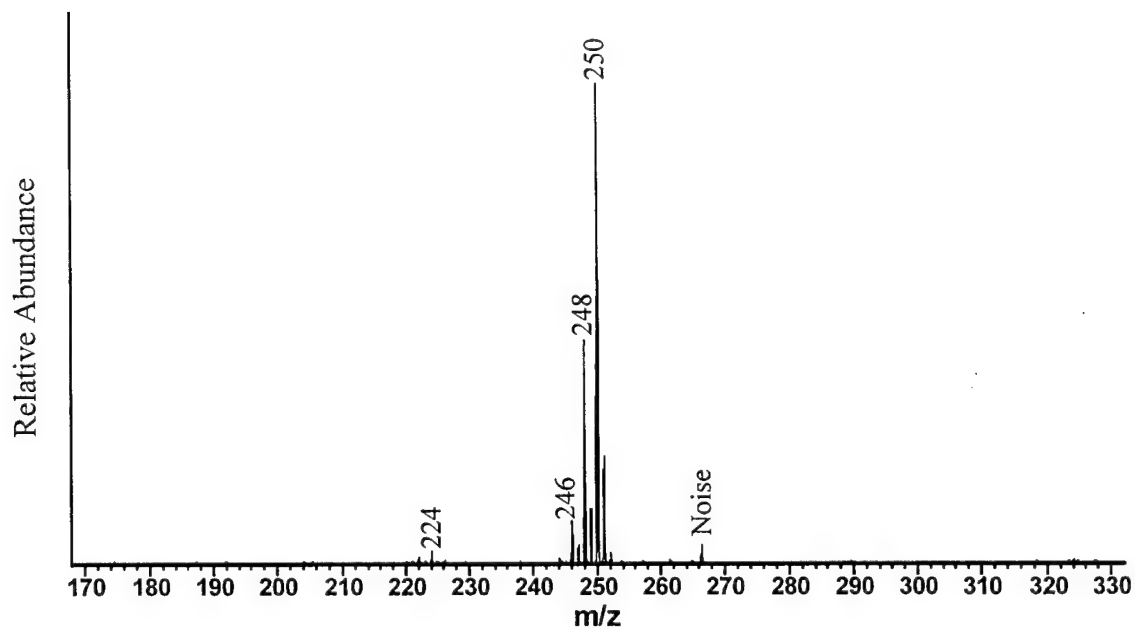


Figure 56. FTICR mass spectrum of photolysis products after four seconds of irradiation of isolated  $m/z$  244-253.

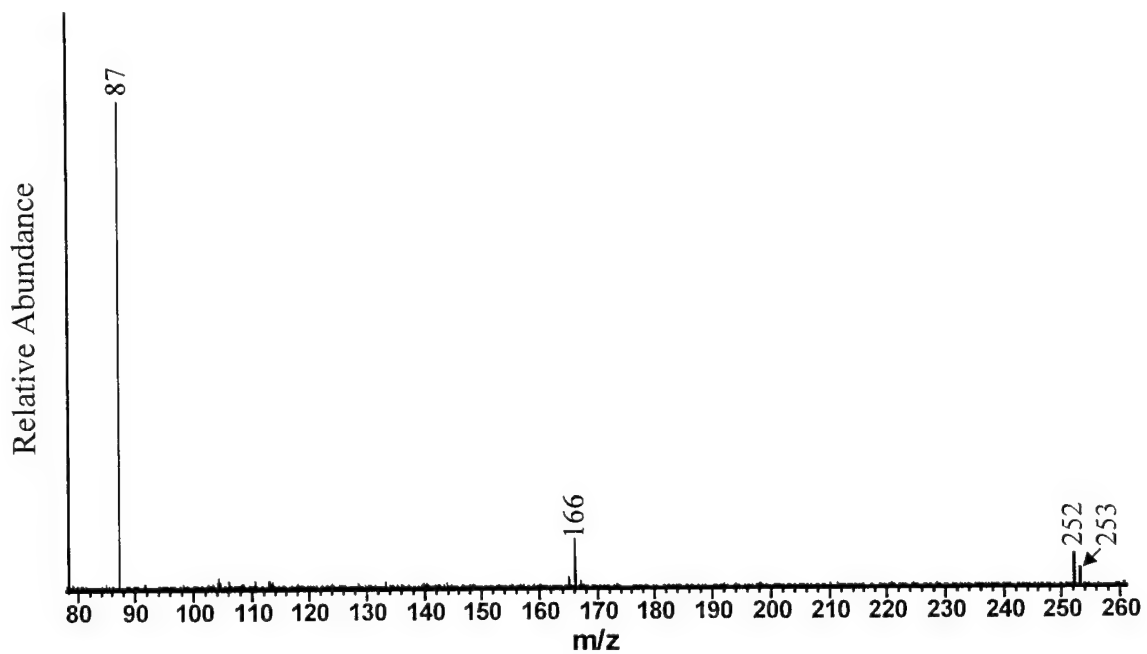


Figure 57. FTICR mass spectrum of the ion-molecule reaction products of isolated  $m/z$  87 after a four second reaction delay.

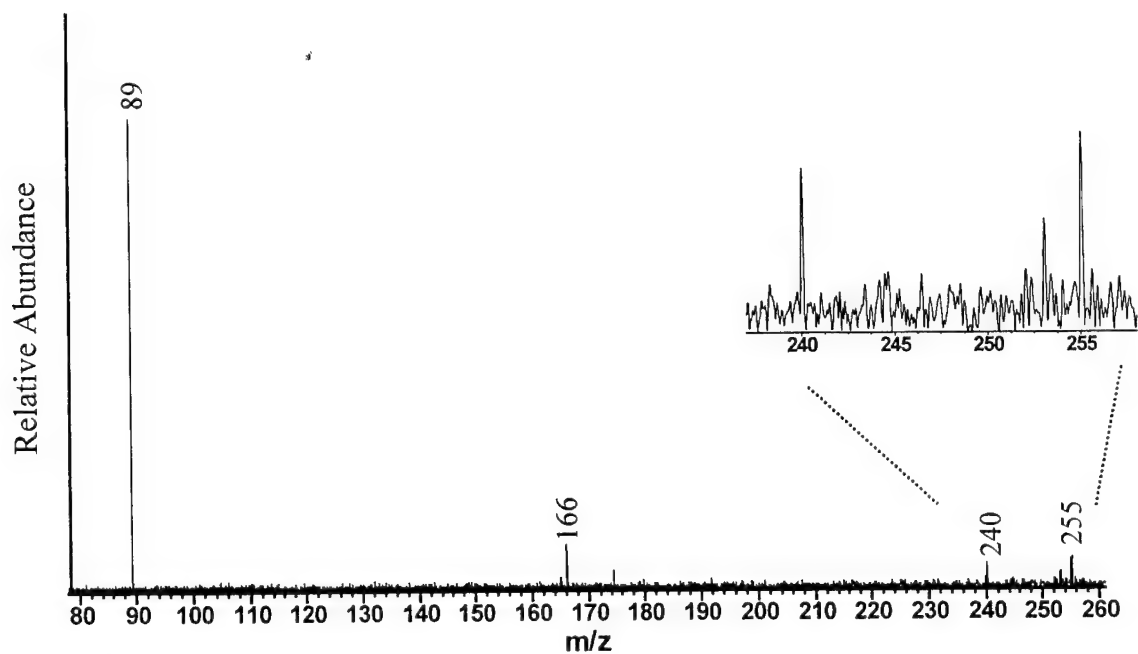


Figure 58. FTICR mass spectrum of the ion-molecule reaction products of isolated  $m/z$  89 after a four second reaction delay.

The isolation and further irradiation of m/z 244-253 aggregates is shown in Figure 56. Dehydrogenation is the primary process, with the most intense peak moving from m/z 252 to m/z 250. The smallest ion in this group is m/z 244,  $C_{20}H_4$ , with the largest ion at m/z 252,  $C_{20}H_{12}^+$ . A slight amount of m/z 220-226 is present, indicating  $C_2$  or  $C_2H_2$  fragment ejection.

#### $C_9H_n^+$ (m/z 108-115)

This group of ions contains nine carbons and up to seven hydrogens. It was shown in Chapter 3 that m/z 111 will dehydrogenate completely with irradiation to  $C_9^+$ . Figure 59 shows the primary ions are m/z 111, m/z 113, and m/z 115. After four seconds of reaction delay, ion-neutral reactions have formed ions at m/z 272 to m/z 281 with the most abundant at m/z 276. Independent experiments confirm that m/z 111 reacts to form m/z 276 and m/z 277 while m/z 113 is unreactive. Ions of m/z 115 react to produce primarily m/z 278, (an ion-neutral reaction ejecting three hydrogens), and a small amount of m/z 281. The aggregates formed have the formula  $C_{22}H_n^+$ , where n=8 to 17.

Figure 60 shows the photolysis products of the isolated m/z 267-277 ions. Significant dehydrogenation occurs, with an end product of m/z 266,  $C_{22}H_2^+$ . However, even greater fragmentation takes place for this group.  $C_2$  or  $C_2H_2$  fragments are ejected during irradiation to form m/z 246 and m/z 248 ions. Two rather unusual peaks are seen at m/z 216 and a smaller amount at m/z 217. These correspond to the  $C_{18}^+$  and  $C_{18}H^+$  ions. Since these were not observed in Figure 56 (photolysis of the  $C_{20}H_n^+$  ions), it is presumed they are formed by the ejection of a  $C_4H_x$  fragment.

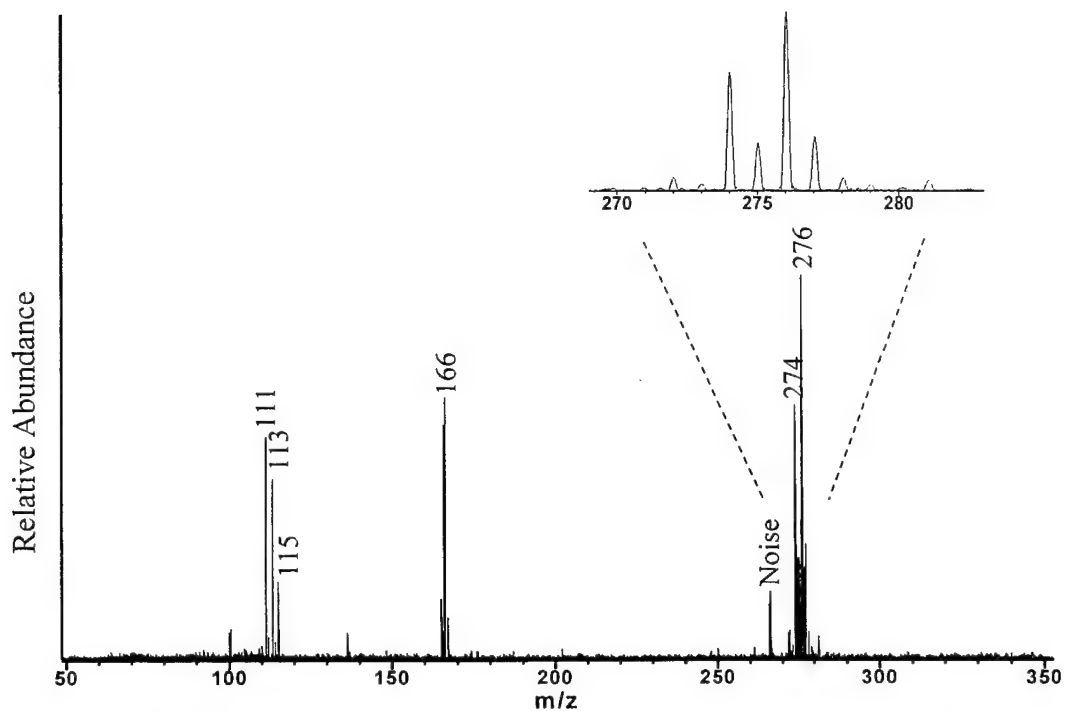


Figure 59. FTICR mass spectrum of the ion-molecule reaction products of isolated  $m/z$  108-115 after a four second reaction delay.

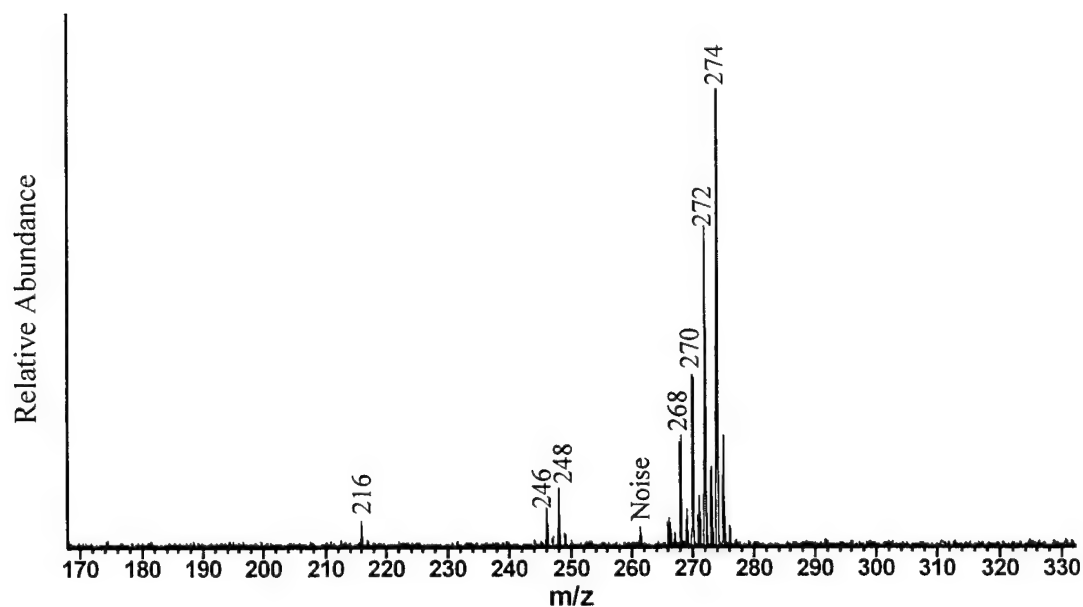


Figure 60. FTICR mass spectrum of photolysis products after four seconds of irradiation of isolated  $m/z$  267-277.

$C_{11}H_n^+$  (m/z 132-141)

The next set of ions is more diverse, including m/z 132, m/z 135, m/z 137 and m/z 139, all as major ions. After a four second reaction delay, aggregates with m/z 297-306 are formed (cf. Figure 61). The most intense peak is observed at m/z 298, which is the addition of neutral 166 to m/z 132. A slight peak at m/z 297 represents the loss of a single hydrogen. M/z 139 clearly reacts to form m/z 305. Although the abundance of the m/z 139 ion is the largest in this group, the abundance of its aggregate product, m/z 305, is much smaller. This may indicate a smaller reaction rate for the aggregation of m/z 139 compared to m/z 132. The aggregates formed in this reaction have the formula  $C_{124}H_n^+$ , where  $n=9$  to 18.

The interesting feature in the photolysis of the isolated aggregates is the large amount of dehydrogenation (Figure 62). Only m/z 286-302 ions were included in this isolation group. Because of significant dehydrogenation, two different groups overlap each other at the larger masses so that m/z 305 was actually included in the next higher group. For this isolation, the most intense peak is at m/z 300 ( $C_{24}H_{12}^+$ ), but full dehydrogenation down to m/z 288 ( $C_{24}^+$ ) is clearly visible. No  $C_2$  or  $C_2H_2$  ejection was observed.

 $C_{13}H_n^+$  (m/z 161-166)

For this group of ions, m/z 161-166 ions were isolated individually and allowed to react during a four second delay time. Figure 63 shows the reaction of m/z 161 to form m/z 326 and m/z 327. The 327 is a straight addition of neutral 166 ( $161 + 166 = 327$ ). The aggregation of m/z 162 is a little more interesting (cf. Figure 64). Straight addition of neutral fluorene should yield m/z 328, but its intensity is very small. The major



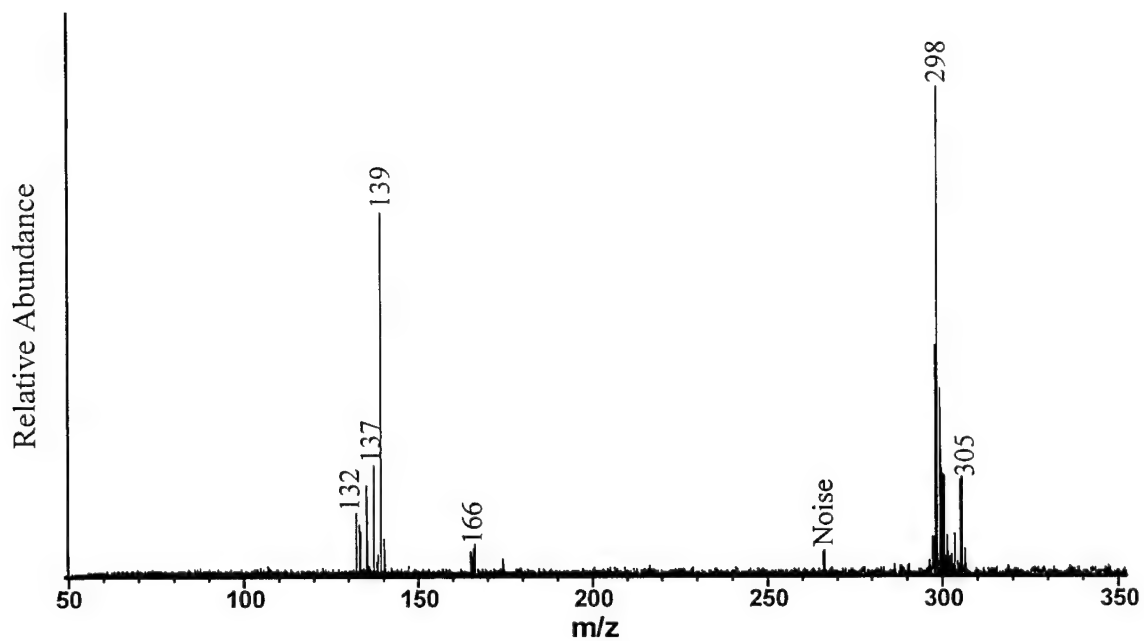


Figure 61. FTICR mass spectrum of the ion-molecule reaction products of isolated  $m/z$  131-141 after a four second reaction delay.

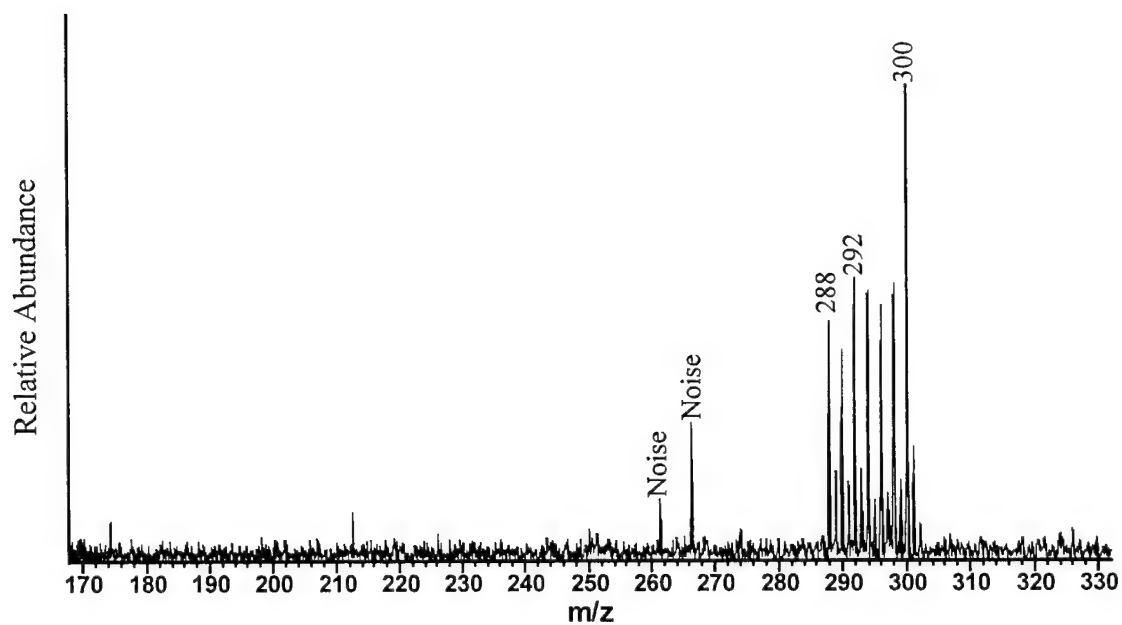


Figure 62. FTICR mass spectrum of photolysis products after four seconds of irradiation of isolated  $m/z$  286-302.

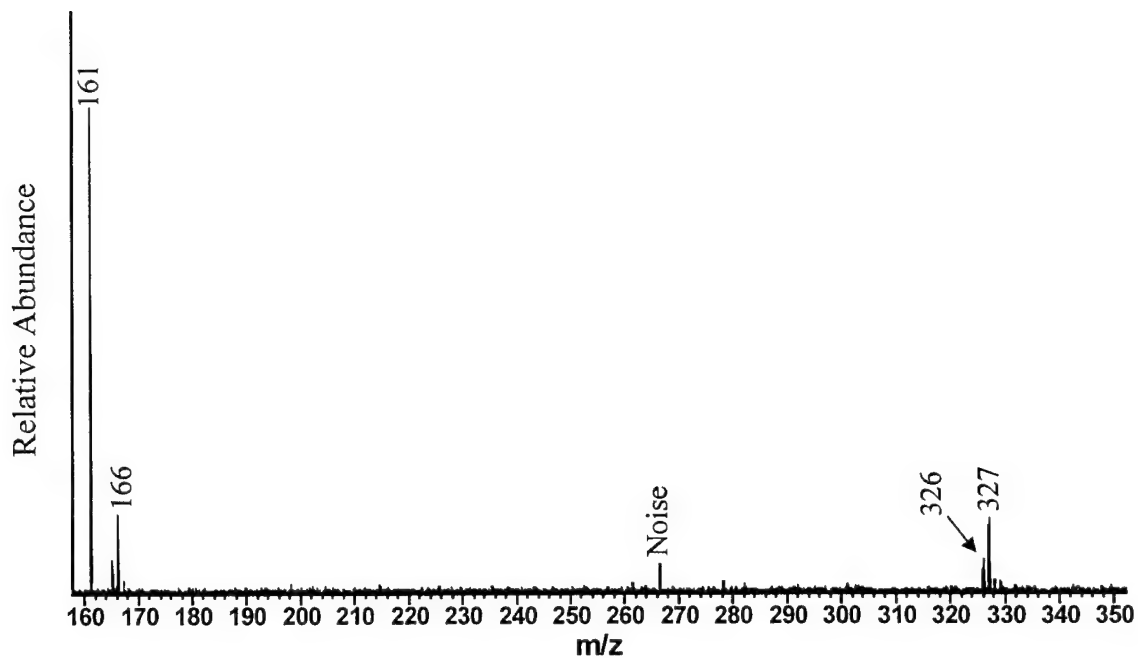


Figure 63. FTICR mass spectrum of the ion-molecule reaction products of isolated  $m/z$  161 after a four second reaction delay.

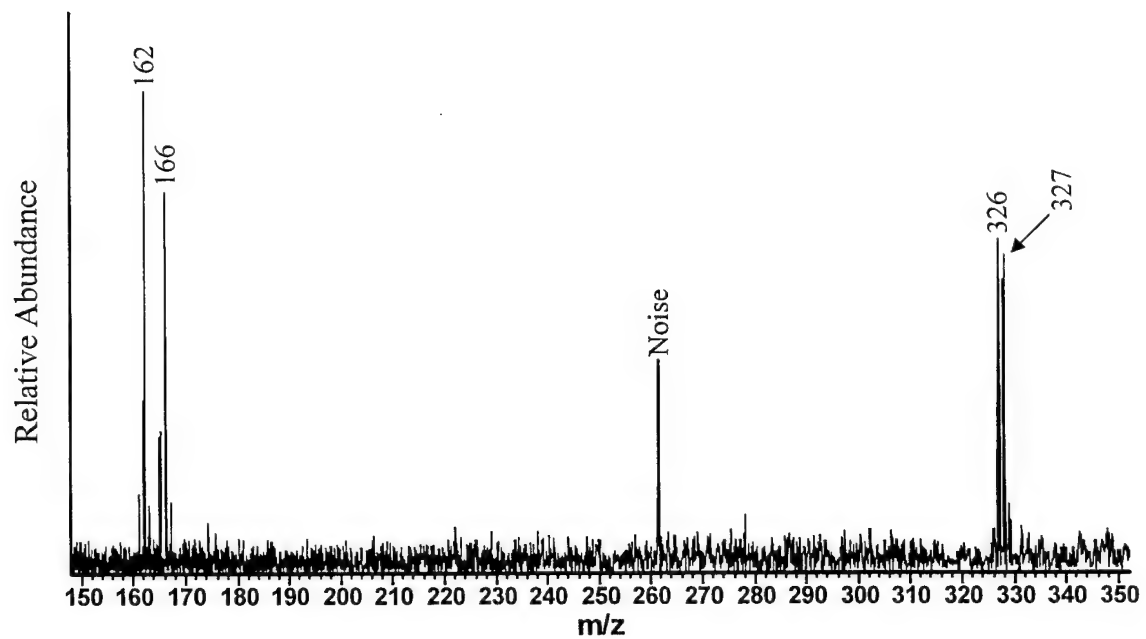


Figure 64. FTICR mass spectrum of the ion-molecule reaction products of isolated  $m/z$  162 after a four second reaction delay.

products are  $m/z$  326 and  $m/z$  327.  $M/z$  162 has three radical carbons on one ring along with one hydrogen. This lone hydrogen is probably ejected during the reaction to form  $m/z$  327. The  $m/z$  326 ion probably results from the loss of one hydrogen from the neutral species.

Figures 65 and 66 show the products of the reaction of  $m/z$  163 and  $m/z$  164, respectively. A peak with very small intensity appears at  $m/z$  329 for  $m/z$  163, which is a straight addition of fluorene neutral with no hydrogen loss.  $M/z$  164 also shows straight addition to form a small intensity peak at  $m/z$  330.

$M/z$  165 is relatively unreactive but a slight peak is observed at  $m/z$  331 as well as an even smaller intensity ion formed at  $m/z$  330 representing the loss of one hydrogen (cf. Figure 67). No aggregate ions are formed during the reaction of  $m/z$  166 with a neutral (cf. Figure 68).

The aggregation products and their photolysis products are summarized in Table 5. Key observations include:

1. All groups form aggregates by reacting with a fluorene neutral molecule.
2. All aggregate products exhibit significant dehydrogenation during irradiation.
3. The aggregate products from only two groups ( $C_7H_n^+$  and  $C_9H_n^+$ ) eject minor amounts of  $C_2$  or  $C_2H_2$  fragments during irradiation.
4. The aggregate formed from the  $C_9H_n^+$  group may eject a  $C_4H_n$ .
5. Only one ion,  $C_7H_5^+$ , ejects a carbon during aggregation.

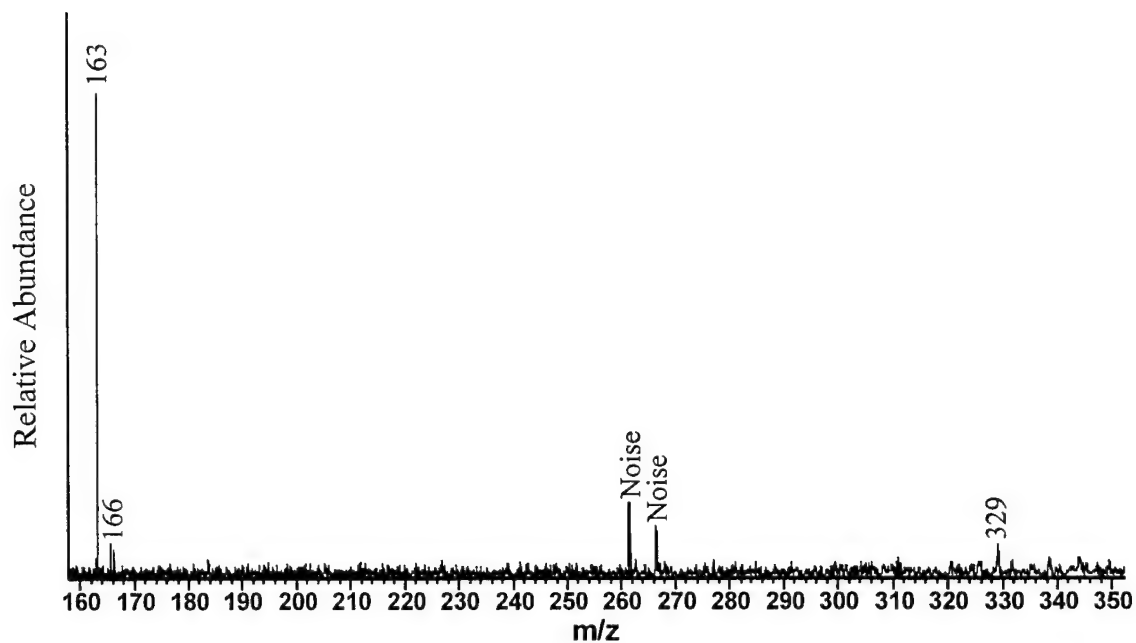


Figure 65. FTICR mass spectrum of the ion-molecule reaction products of isolated  $m/z$  163 after a four second reaction delay.

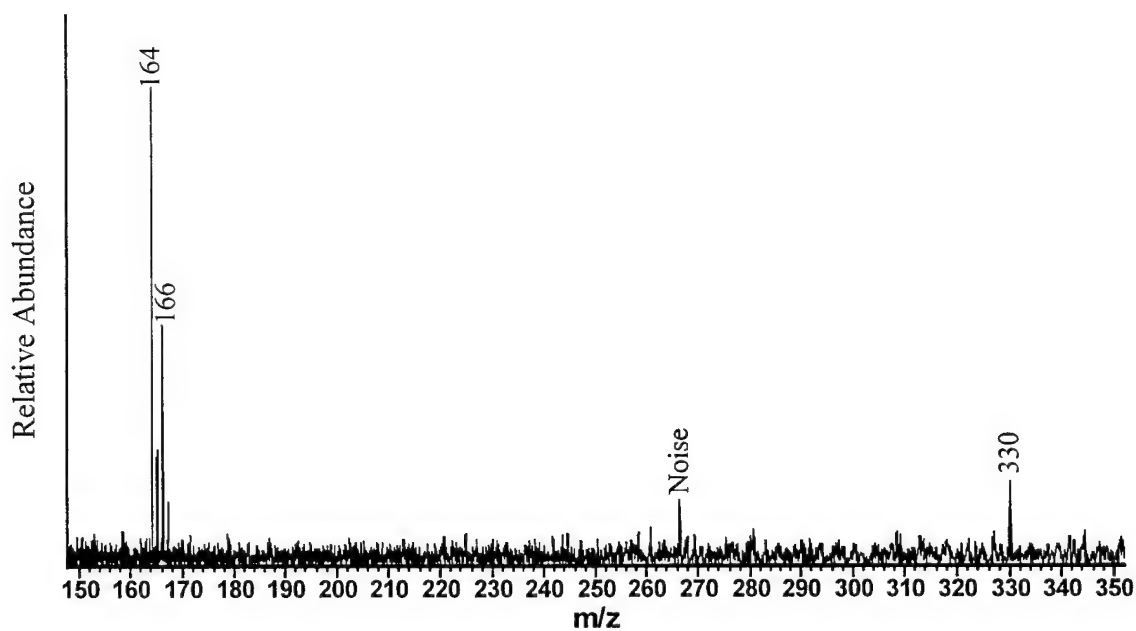


Figure 66. FTICR mass spectrum of the ion-molecule reaction products of isolated  $m/z$  164 after a four second reaction delay.

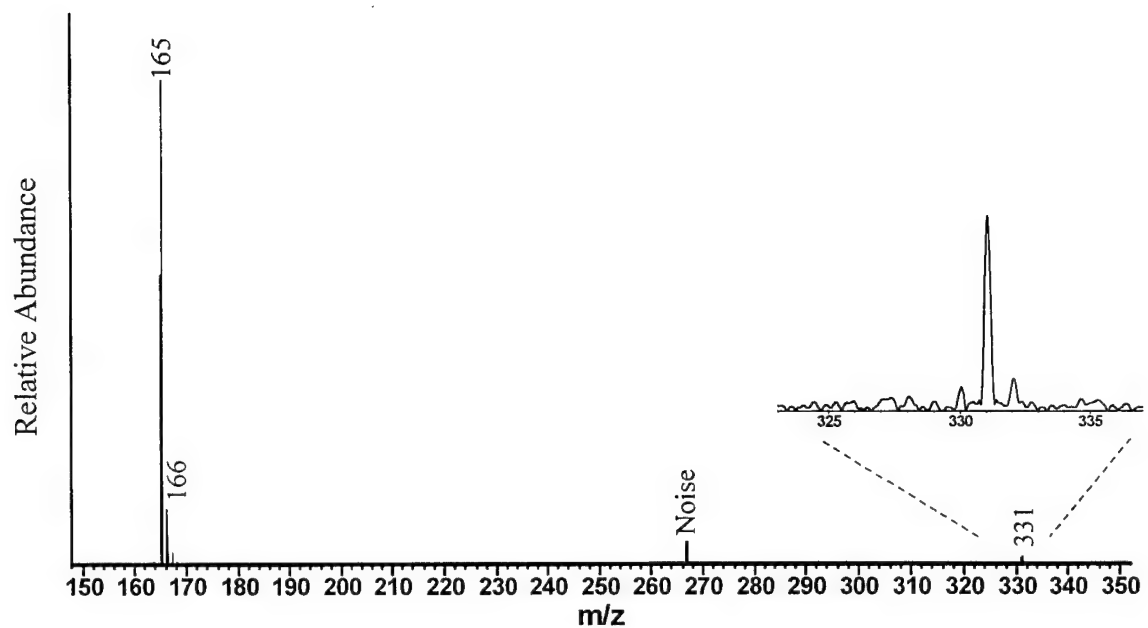


Figure 67. FTICR mass spectrum of the ion-molecule reaction products of isolated  $m/z$  165 after a four second reaction delay.

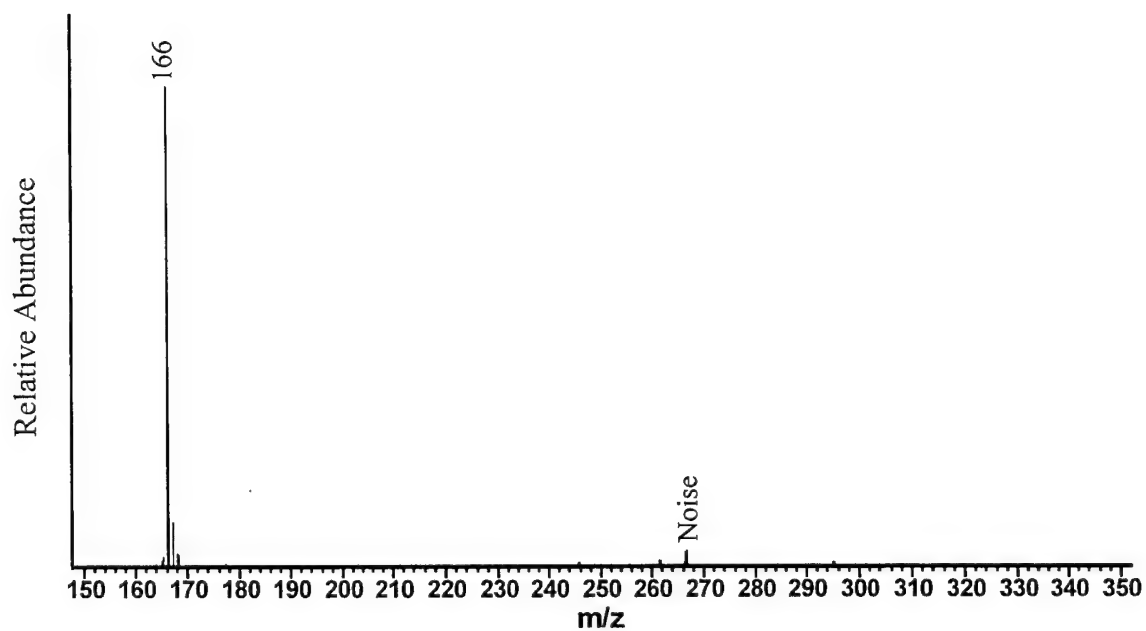


Figure 68. FTICR mass spectrum of the ion-molecule reaction products of isolated  $m/z$  166 after a four second reaction delay.

Table 5. Summary of the aggregates formed during a four second delay time (column 3) with their formulas. The last column lists the photolysis products of the isolated aggregates after four seconds of irradiation.

Isolation Group	Primary Ions	Aggregates (4s rxn delay)	Aggregate Formula	Aggregate photoproducts (4s of irradiation)
$C_5H_n^+$	63	226-230	$C_{18}H_n^+$ (n=12-15)	$C_{18}H_n^+$ (n=4-12)
$C_7H_n^+$	87, 89	250-255	$C_{20}H_n^+$ (n=10-15)	$C_{20}H_n^+$ (n=4-12)
		240	$C_{19}H_{12}^+$	$C_{18}H_n^+$ (n=4-10) --
$C_9H_n^+$	111, 113, 115	272-281	$C_{22}H_n^+$ (n=8-17)	$C_{22}H_n^+$ (n=2-12) $C_{20}H_n^+$ (n=6, 8) $C_{18}^+$ , $C_{18}H^+$
$C_{11}H_n^+$	132-140	297-306	$C_{24}H_n^+$ (n=9-18)	$C_{24}H_n^+$ (n=0-14)
$C_{13}H_5^+$	161	326, 327	$C_{26}H_n^+$ (n=14,15)	$C_{26}H_n^+$ (n=4-16)
$C_{13}H_6^+$	162	326-328	$C_{26}H_n^+$ (n=14-16)	
$C_{13}H_7^+$	163	329	$C_{26}H_{17}^+$	
$C_{13}H_8^+$	164	330	$C_{26}H_{18}^+$	
$C_{13}H_9^+$	165	330, 331	$C_{26}H_n^+$ (n=14,15)	
$C_{13}H_{10}^+$	166	None	None	

## CHAPTER 6

### PHOTOLYSIS OF NAPHTHALENE AND 1,2-BENZANTHRACENE

Many photolysis studies have been performed on naphthalene neutrals and ions (for its molecular structure cf. Figure 69). Most recently, Oomens et al.<sup>159</sup> determined the infrared spectra of gas-phase naphthalene cations by infrared photodissociation. Other studies include determination of the structure of the product ion formed after acetylene loss from the naphthalene cation,<sup>111</sup> photofragmentation in the energy range of 7-22 eV,<sup>103</sup> and the determination of C—H bond strength of the naphthalene cation.<sup>160</sup> However, very little work has been done on the photoaggregation of naphthalene. Two studies<sup>161, 162</sup> involving naphthalene aggregation have, however, been done in connection with the 2175 Å interstellar extinction feature. However, beyond recognizing that aggregates are formed, specific mechanisms were not identified.

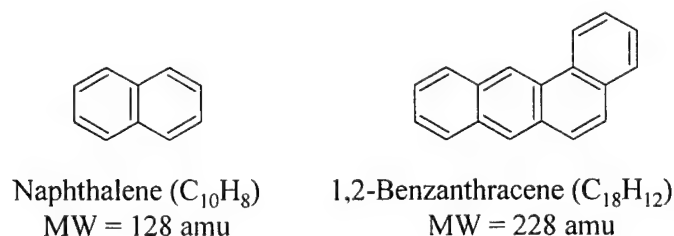


Figure 69. Molecular structures of naphthalene and 1,2-benzanthracene.

Studies on the photoaggregation of 1,2-benzanthracene (for its molecular structure cf. Figure 69) are even fewer. Using dehydrogenated 1,2-benzanthracene, Guo,

Grutzmacher and Nibbering<sup>163</sup> performed ion-molecule reactions with benzene. Ekern et al.<sup>114</sup> have investigated the fragmentation of 1,2-benzanthracene.

### Naphthalene

Figure 70 shows the mass spectrum of the parent naphthalene ion after irradiation with a xenon arc lamp (for 7s). Figures 71 and 72 are expanded views of the fragments and products of ion-molecule reactions, respectively. While Ekern et al.<sup>114</sup> found naphthalene to be totally destroyed by irradiation after only 0.5 seconds, these figures show a much softer photolysis with less fragmentation. This is probably due to different intensities of the xenon arc lamp. However, many of the same fragments are observed, including ions located at  $m/z$  102 and 76, which indicate the loss of one and two acetylene fragments ( $C_2H_2$ ), respectively. New fragments are found at  $m/z$  89, 91 and

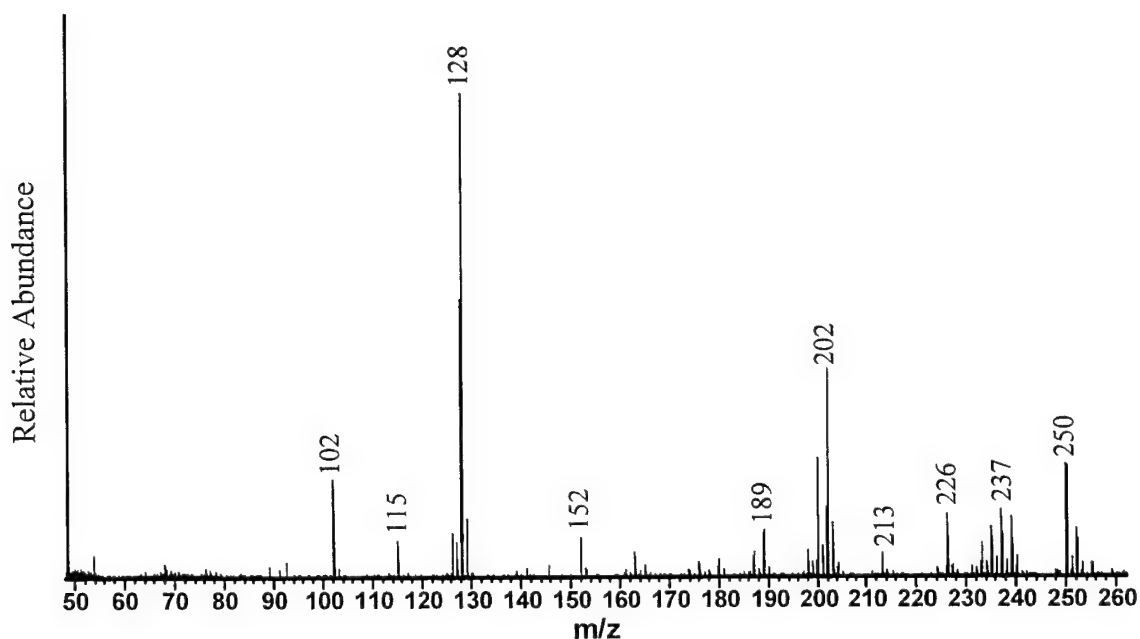


Figure 70. FTICR mass spectrum of photolysis products and ion-molecule reaction products after a seven second irradiation period of the  $m/z$  128 ion.



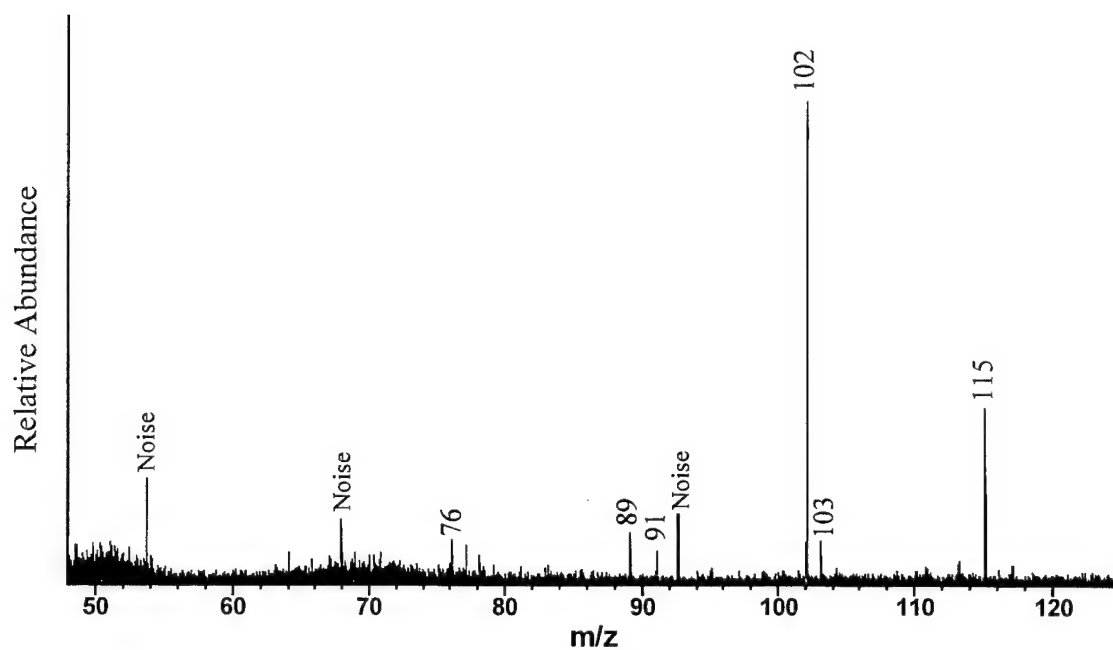


Figure 71. Expansion of the lower mass range of Figure 70 showing fragmentation products only.

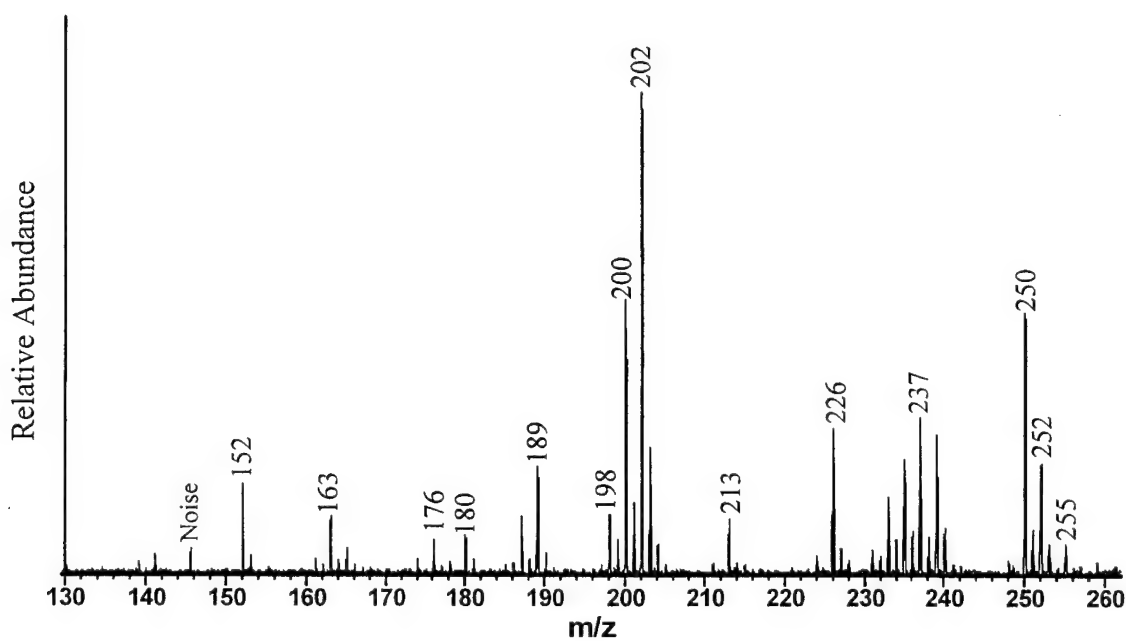


Figure 72. Expansion of the upper mass range of Figure 70 showing the aggregate products only.

115. A wealth of ion-molecule reaction products are found, ranging from  $C_{12}H_n$  up to the “dimer-like” ion at  $C_{20}H_n$ . Each of these groupings will be examined in turn.

$C_{10}H_n^+$  (m/z 126-129)

This group, which includes the parent naphthalene ion (m/z 128), contains 10 carbons. The naphthalene cation is seen to lose only two hydrogen atoms upon photolysis (cf. Figure 73), which is markedly different behavior from fluorene, which may lose up to five hydrogens. The ion at m/z 129 contains a  $^{13}C$  isotope. Each of the ions (m/z 128, m/z 127 and m/z 126) was studied individually and revealed interesting differences. After isolation and irradiation (for 3s), the first ion (m/z 128) shows fragments at m/z 115 (loss of CH), m/z 102 (loss of  $C_2H_2$ ) and m/z 76 (loss of two acetylenes) as shown in Figure 74. Additional experiments were performed to determine the origin of the m/z 76 ion. It was found that the m/z 76 ion forms directly from the m/z 102 species, signaling a sequential loss of acetylene from the parent.

In Figure 75, the isolated m/z 128 ion was subjected to a four second reaction delay to induce aggregate formation. However, none was observed. This result was not unexpected, since no aggregates were observed for ion-molecule reactions of the parent fluorene ion either.

The m/z 127 ion was isolated and irradiated for three seconds (cf. Figure 76). Lower mass fragments were observed at m/z 126 (H loss) and m/z 115 (C loss). The carbon that is fragmented is the most likely the same one that has already lost the hydrogen, since otherwise, a peak would be observed at m/z 114, representing the loss of CH. No acetylene loss occurs. Higher mass products are found after a reaction delay time of only two seconds (cf. Figure 77). The addition of the m/z 127 ion to neutral

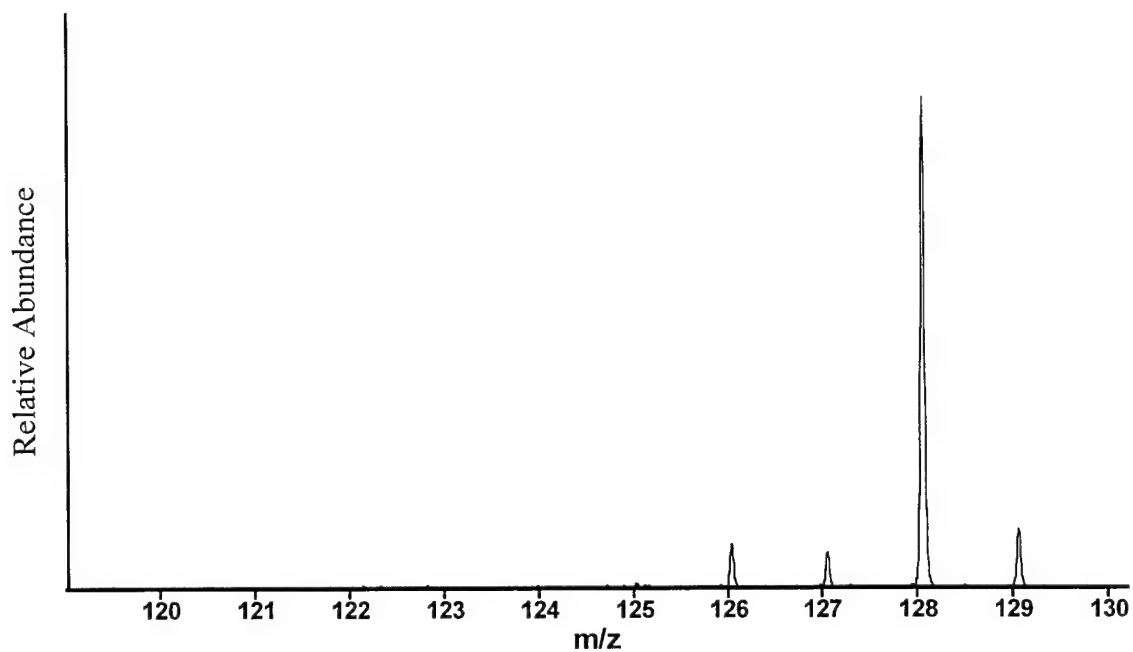


Figure 73. FTICR mass spectrum of photolysis products of  $m/z$  128 after seven seconds of irradiation, showing a maximum dehydrogenation of two.

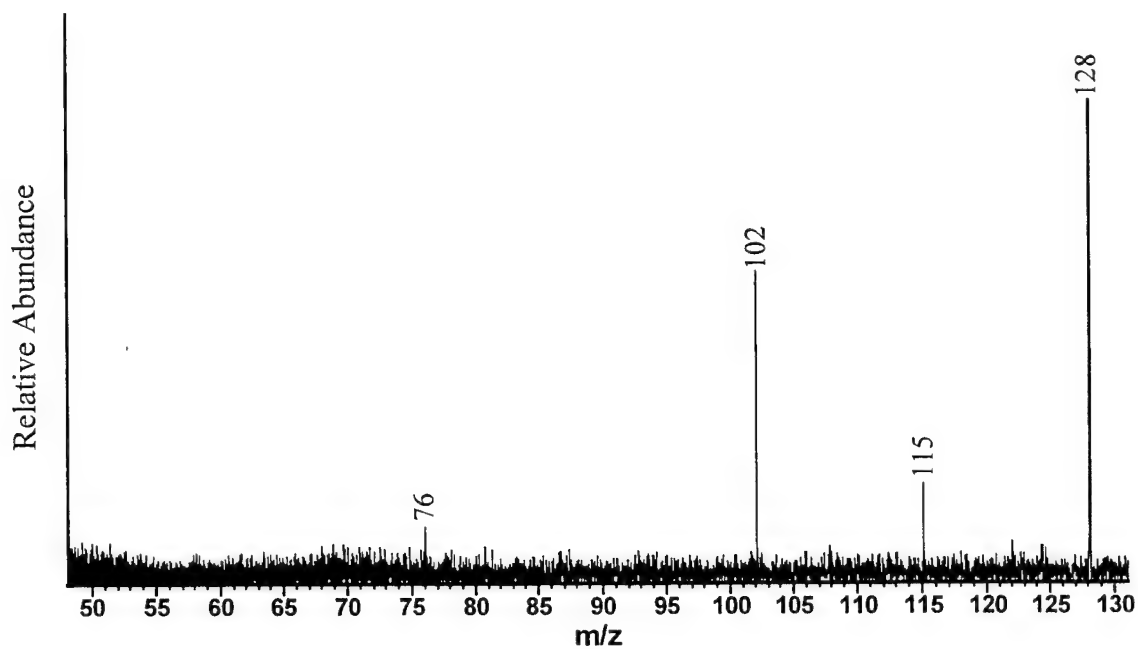


Figure 74. FTICR mass spectrum of photolysis products after three seconds of irradiation of the isolated  $m/z$  128 ion.

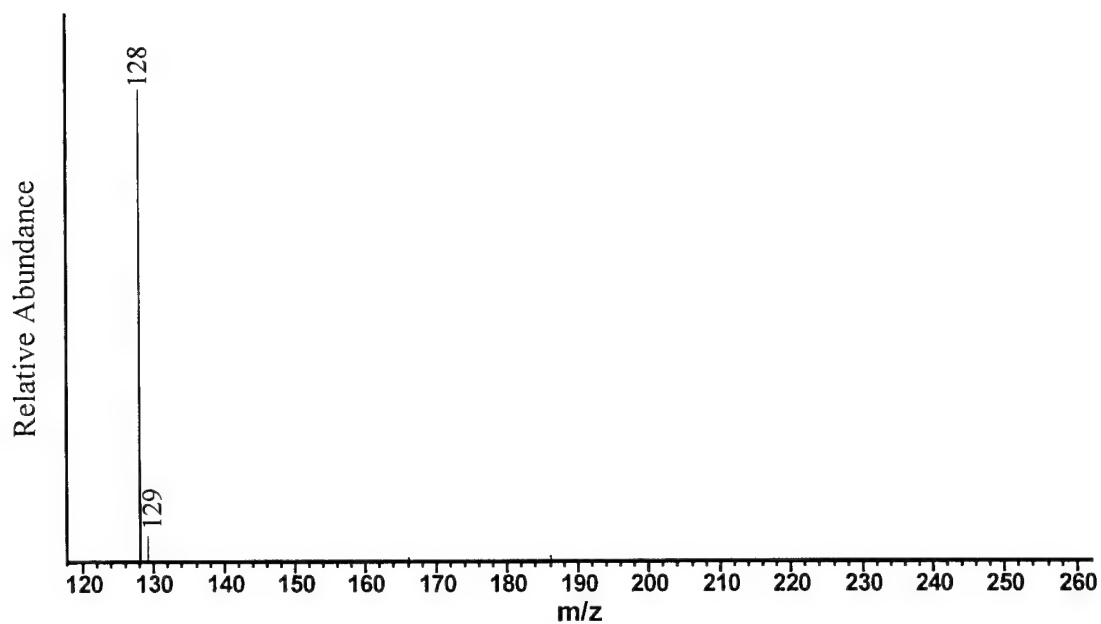


Figure 75. FTICR mass spectrum of the ion-molecule reaction products of isolated  $m/z$  128 after a four second reaction delay.

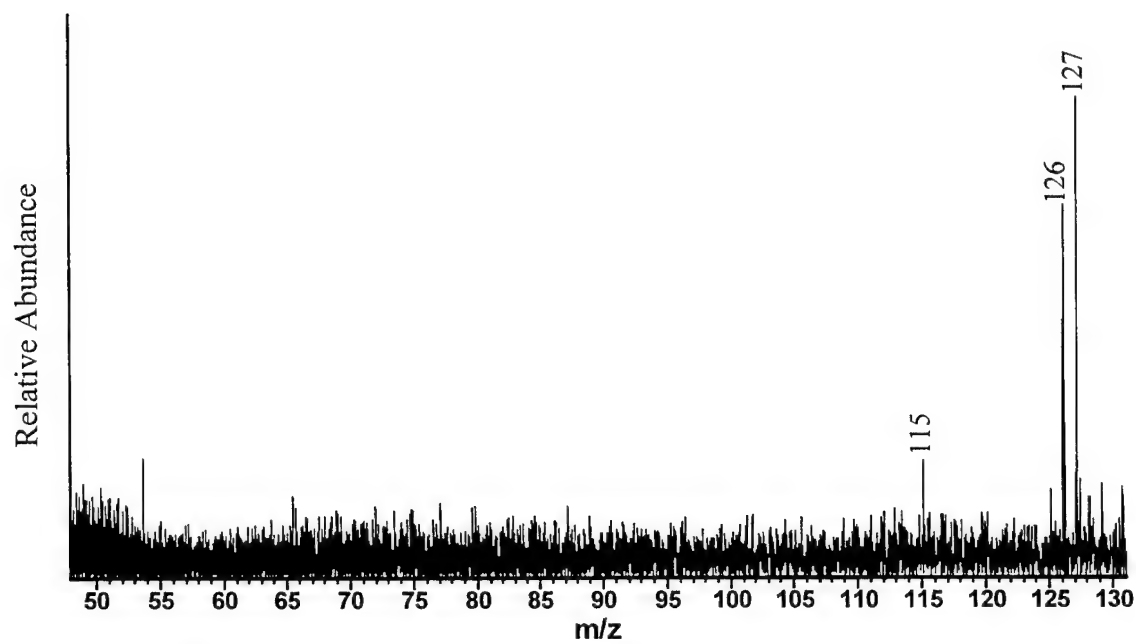


Figure 76. FTICR mass spectrum of photolysis products after a three second irradiation of the  $m/z$  127 ion.

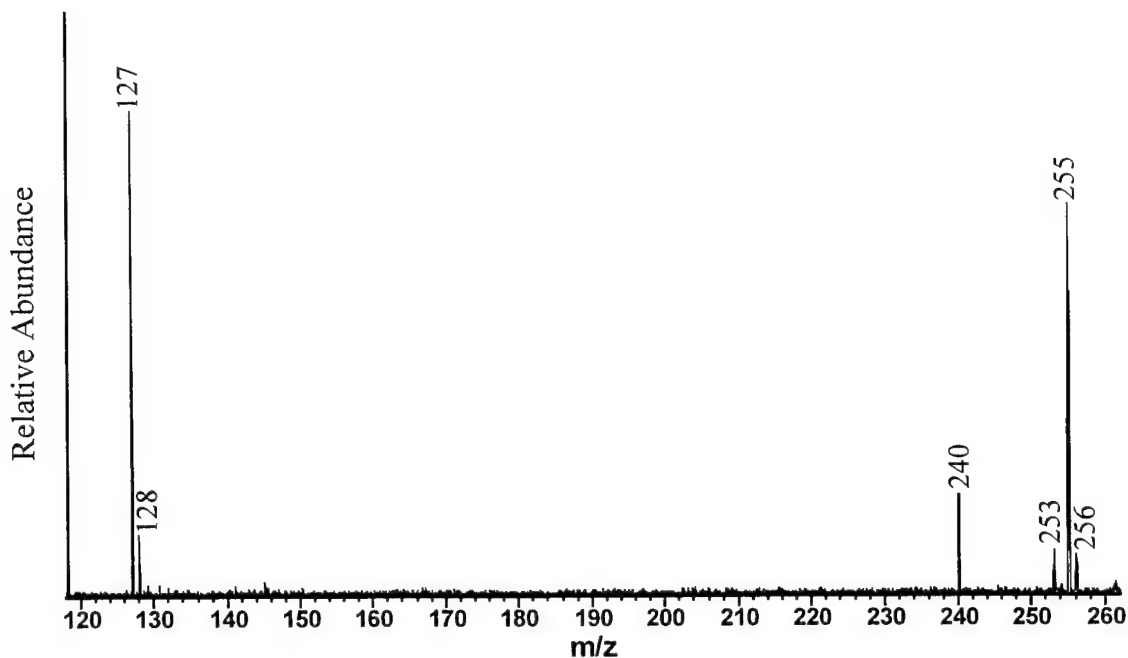


Figure 77. FTICR mass spectrum of the ion-molecule reaction products of isolated  $m/z$  127 after a two second reaction delay.

naphthalene yields an aggregate at  $m/z$  255 ( $m/z$  256 contains a  $^{13}\text{C}$  isotope of the neutral). Loss of two hydrogens from this aggregate also forms  $m/z$  253. A peak at  $m/z$  240 is the loss of  $\text{C} + 3\text{H}$  from  $m/z$  255 or  $\text{CH}$  from  $m/z$  253. (This is very similar to the ion-molecule reaction observed for the  $m/z$  89 fluorene fragment in Chapter 5. It also aggregated to form  $m/z$  255 and  $m/z$  240.) The dehydrogenated radical carbon must be fairly unstable if it is ejected during a simple ion-molecule reaction without any photolysis.

The isolated ion at  $m/z$  126 is very unreactive, as shown in Figures 78 and 79. Photolysis for three seconds does not form any fragments, while four seconds of reaction delay do not form any aggregates. Only charge transfer to form  $m/z$  128 is seen. This stability may be the result of triple bond formation between two adjacent carbons that

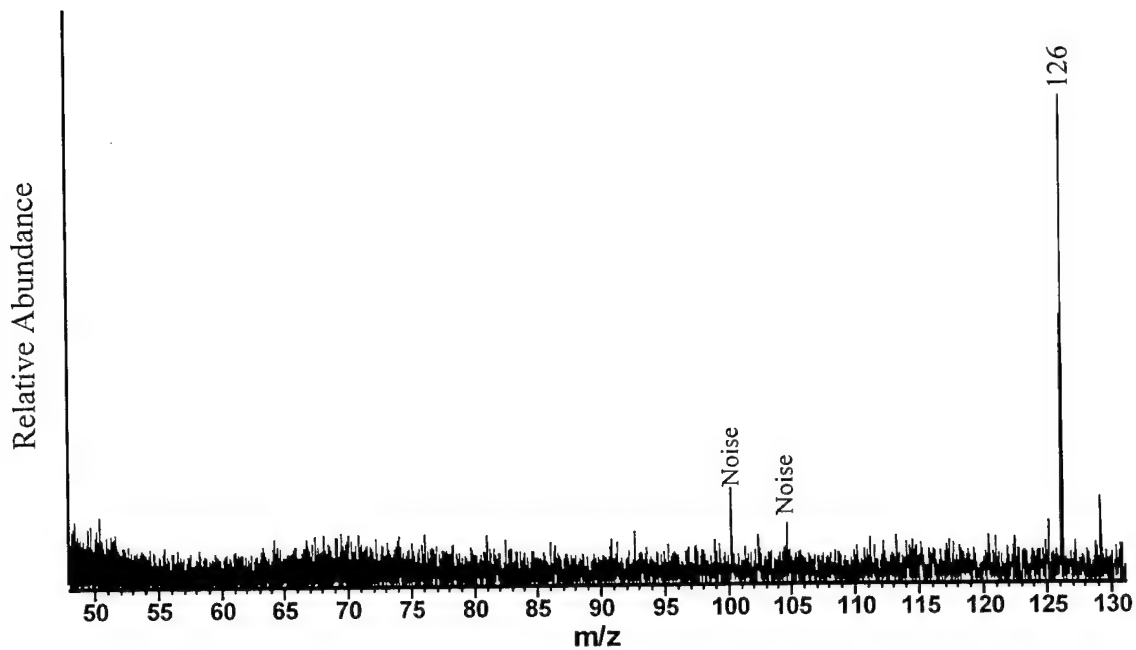


Figure 78. FTICR mass spectrum of photolysis products after a three second irradiation of the  $m/z$  126 ion.

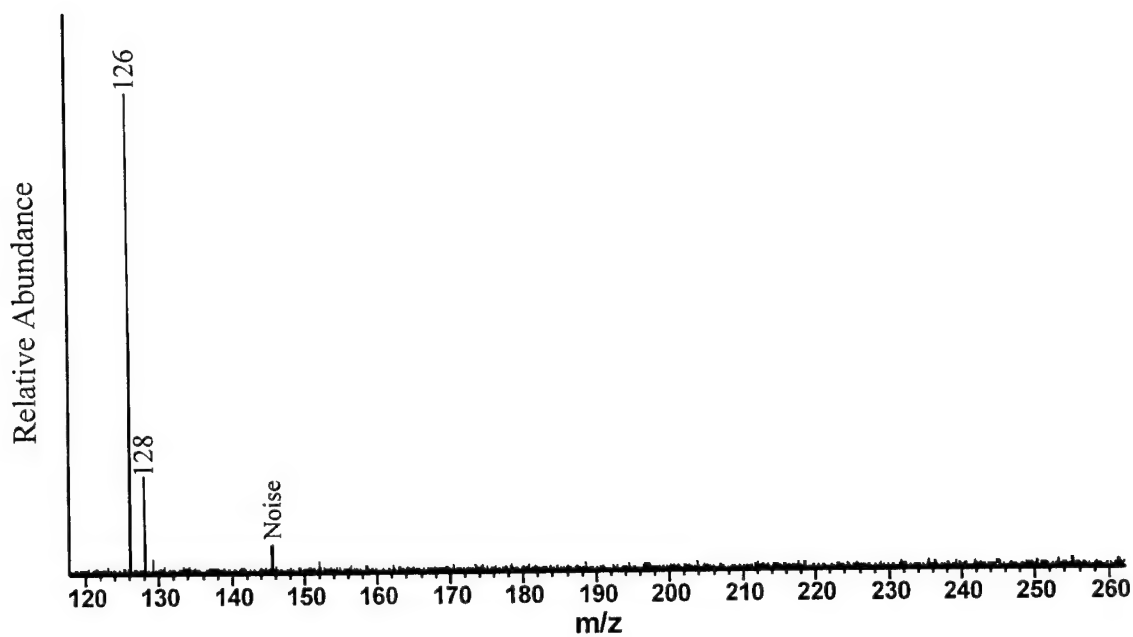


Figure 79. FTICR mass spectrum of the ion-molecule reaction products of isolated  $m/z$  126 after a four second reaction delay.

have lost hydrogens. Since there are no radical sites present on the naphthyne species, it would be expected to have the same reactivity as the parent naphthalene ion, i.e. no ion-molecule reactions. Although unverified at this time, ring opening may occur to relieve the strain of the triple bond.

#### $C_8H_6^+$ (m/z 102)

The next group consists of a single ion (m/z 102) that contains 8 carbons. Photolysis of this ion for three seconds (cf. Figure 80) reveals one product peak at m/z 76 (loss of  $C_2H_2$ ). No dehydrogenation occurs. This can be explained by the rearrangement of the molecule to form benzocyclobutadiene. Similar to the m/z 126 and m/z 128 ions, this molecule has no radical sites so no aggregate products would be expected. Figure 81 reveals this to be true. The only visible product is the m/z 128 ion, formed by charge transfer of the m/z 102 ion with naphthalene neutral. Without the postulated ring closure, aggregate products would be expected to form.

#### $C_6H_4^+$ (m/z 76)

Although the abundance of the m/z 76 ion is fairly low (cf. Figures 70 and 71), meaningful results were obtained by using carefully controlled ejections. As discussed in the previous section, the m/z 102 ion photolyzes to form the m/z 76, product but no aggregates. Figure 82 shows that irradiating the isolated m/z 102 ion while ejecting m/z 76 results in no fragments or aggregates. The results of photolysis of the isolated m/z 102 ion, without the ejection of the m/z 76 ion, are shown in Figure 83. Since m/z 102 is non-reactive for the formation of aggregates, any products formed must be due to m/z 76. A group of ions with high abundance in the range m/z 200 to m/z 204 is seen. The highest mass ion, m/z 204, results from the addition of neutral naphthalene (76 + 128), while m/z 202 and m/z 200 represent the loss of two and four hydrogens, respectively. An

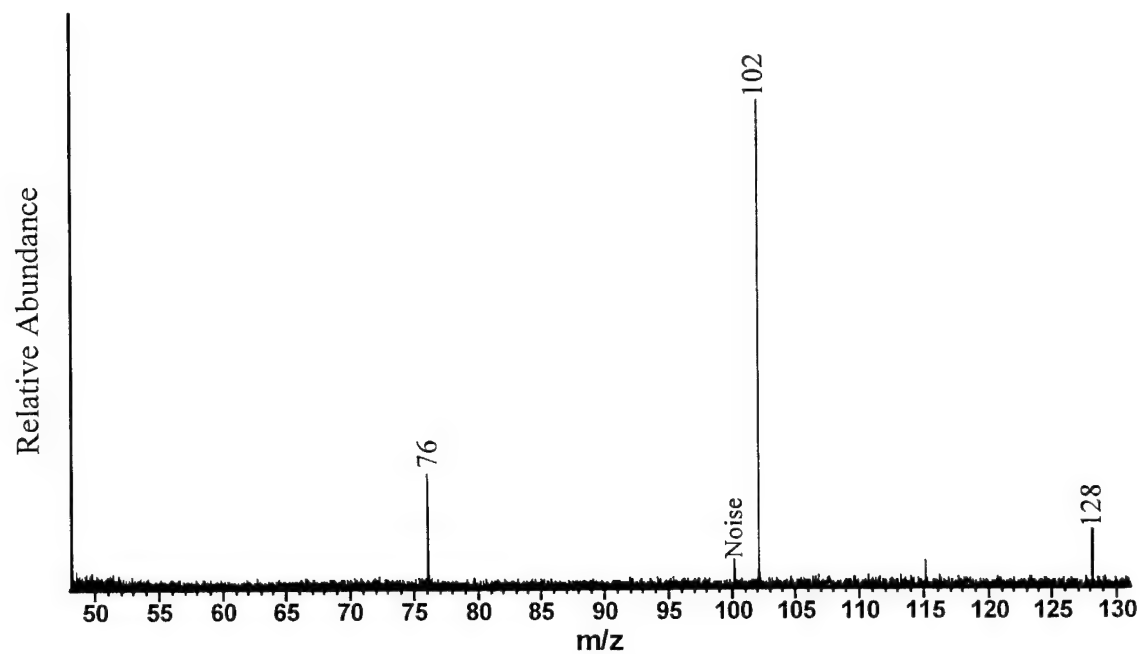


Figure 80. FTICR mass spectrum of photolysis products after a three second irradiation of the  $m/z$  102 ion.

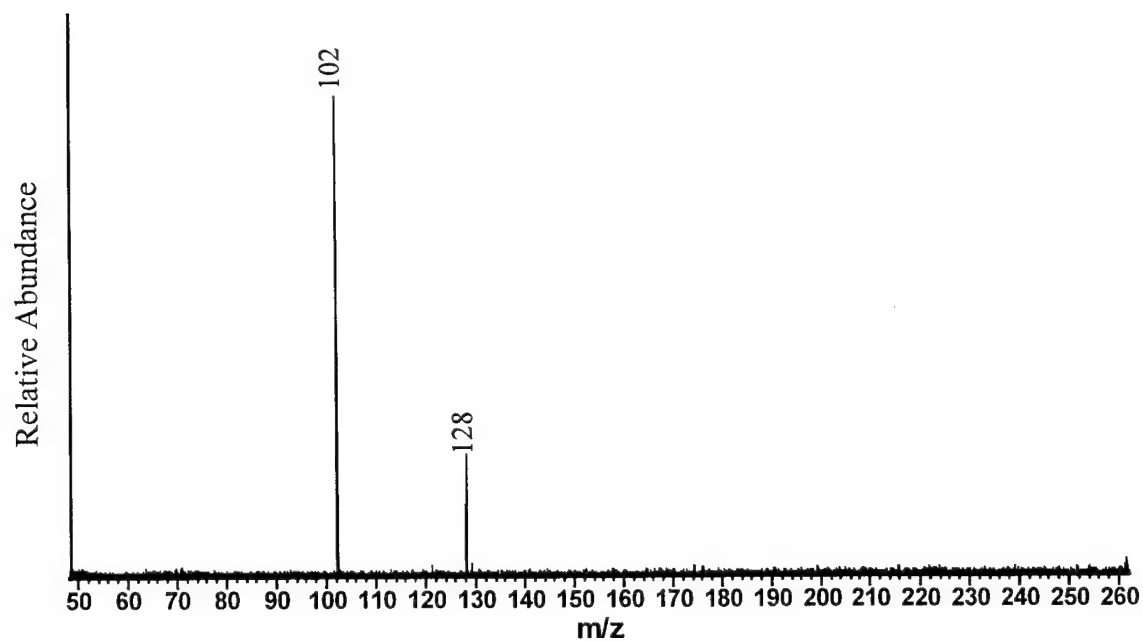


Figure 81. FTICR mass spectrum of the ion-molecule reaction products of isolated  $m/z$  102 after a four second reaction delay.



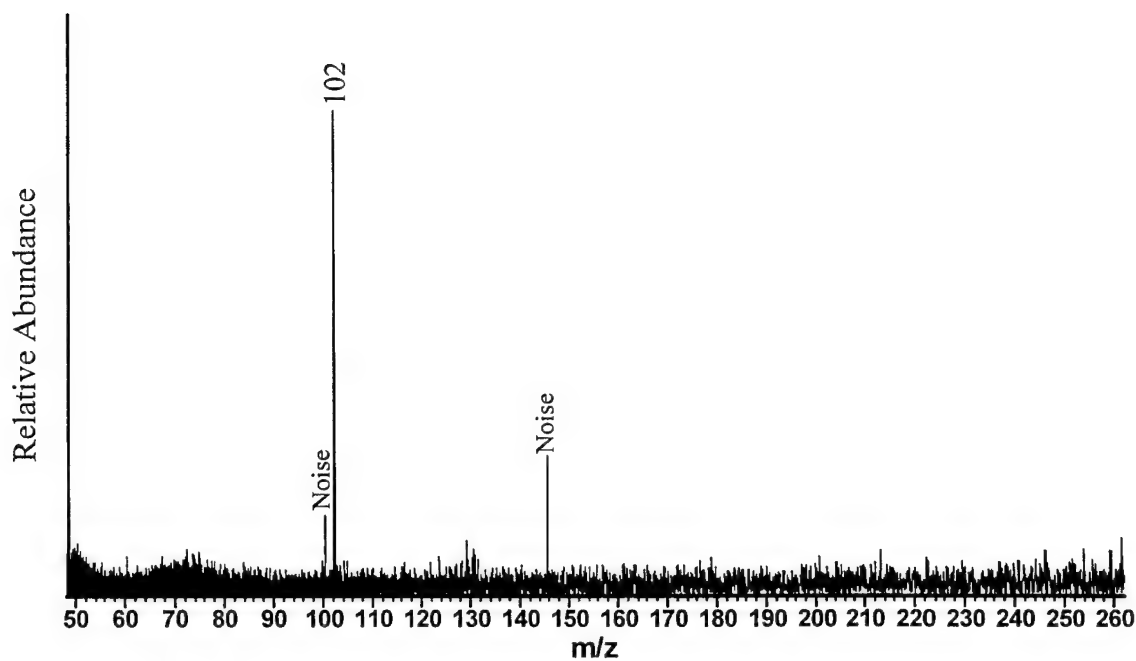


Figure 82. FTICR mass spectrum of photolysis products after a two second irradiation of the  $m/z$  102 ion while ejecting  $m/z$  76-78.

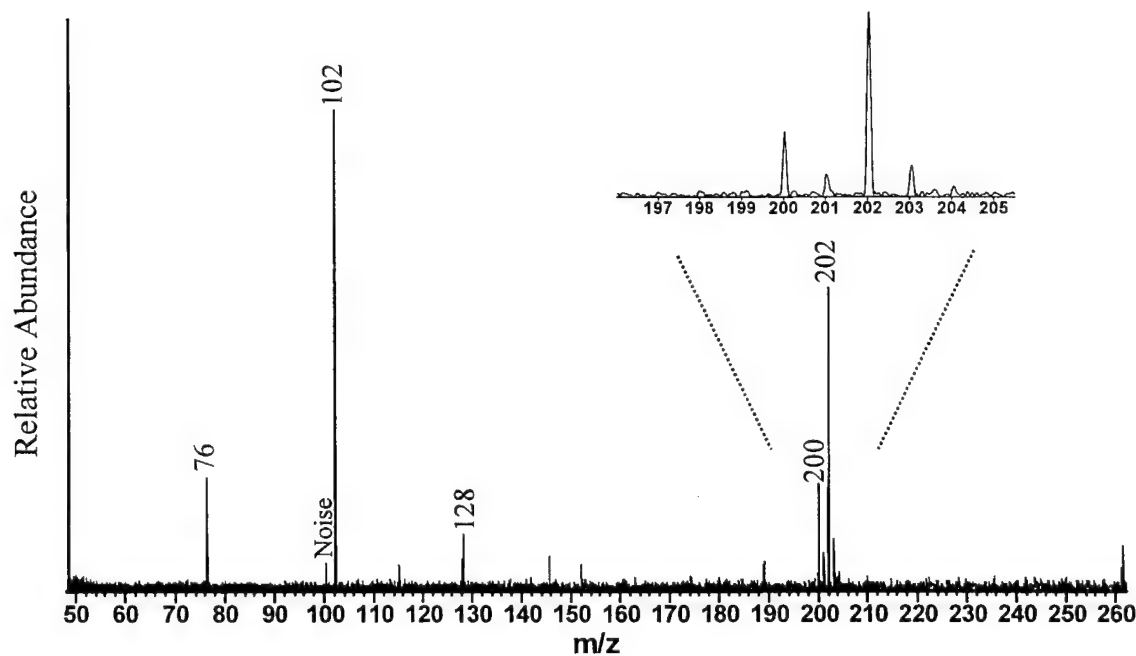


Figure 83. FTICR mass spectrum of photolysis products and ion-molecule reaction products after a three second irradiation of the  $m/z$  102 ion.

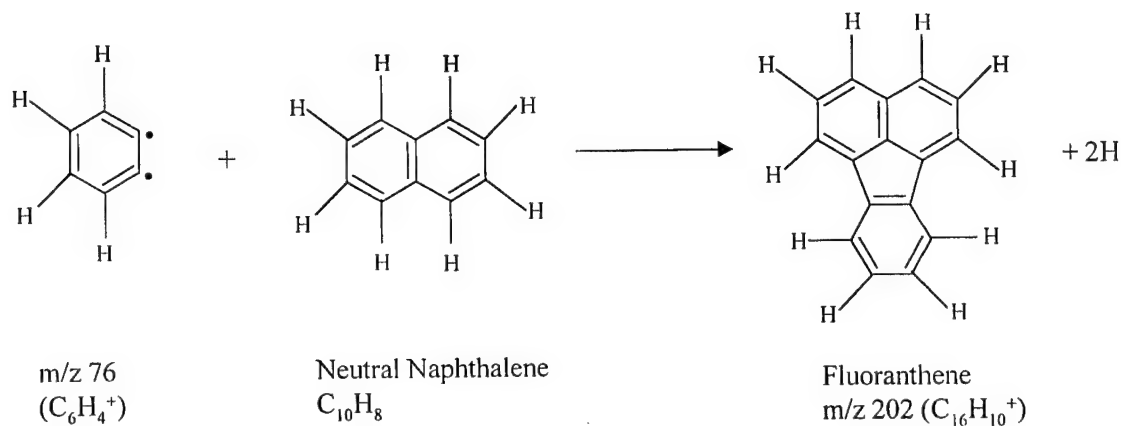


Figure 84. Proposed mechanism for the ion-molecule reaction of the  $m/z$  76 ion to form  $m/z$  202.

ion-molecule reaction between the  $m/z$  76 ion and neutral naphthalene could form fluoranthene ( $C_{16}H_{10}$ ) while ejecting two hydrogens (cf. Figure 84).

#### $C_{20}H_n^+$ ( $m/z$ 250-255)

The photostability of the aggregates was of particular interest. Although the  $m/z$  255 ion is the direct aggregate formed (127 ion + 128 neutral), it quickly dehydrogenates to  $m/z$  252 and  $m/z$  250 (cf. Figure 85). Single carbon loss is observed, along with dehydrogenation, to form ions at  $m/z$  237 and 239. A single peak at  $m/z$  226 is also observed, indicating acetylene loss from  $m/z$  252 or  $C_2$  loss from  $m/z$  250. Further experiments will be required to resolve these two possibilities.

#### $C_{19}H_n^+$ ( $m/z$ 231-243)

The relative abundance of this group is rather surprising since it has an odd number of carbons. For fluorene, the abundance of aggregates of this type was fairly low. The primary effect of irradiation on this group of ions (cf. Figure 86) is

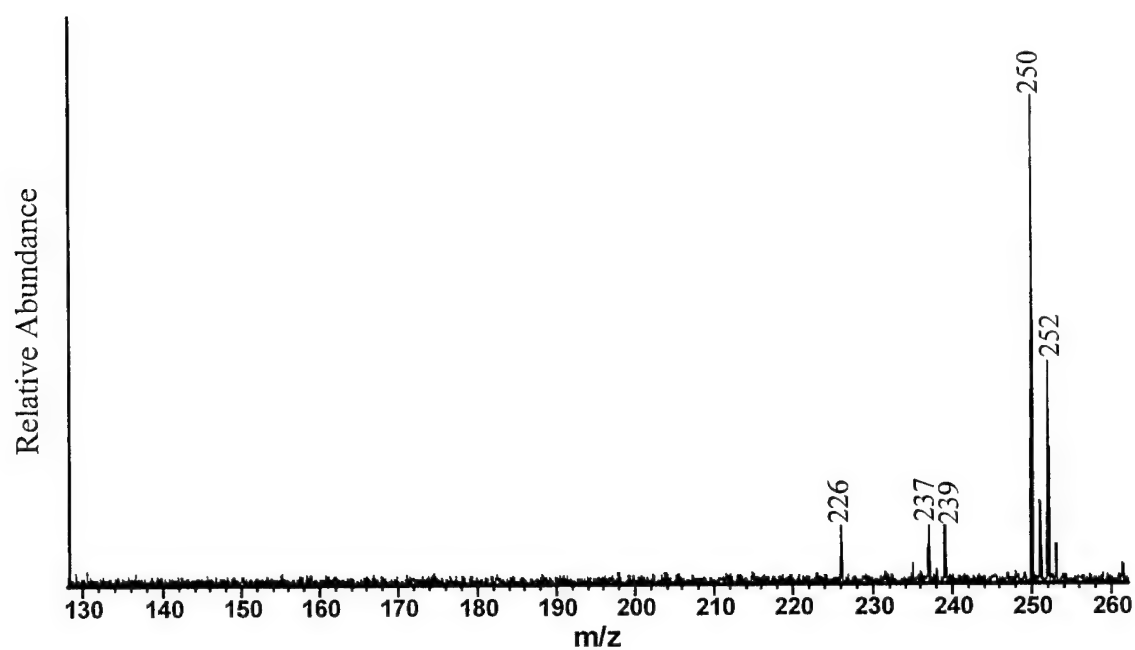


Figure 85. FTICR mass spectrum of photolysis products after two seconds of irradiation of isolated  $m/z$  249-256 ions.

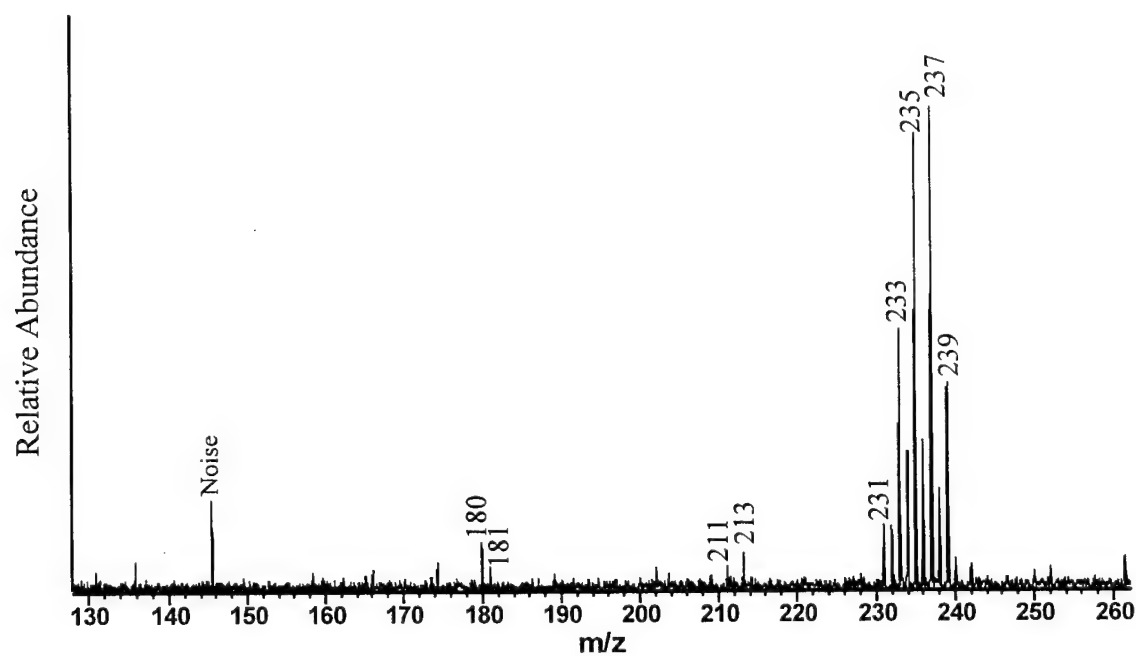


Figure 86. FTICR mass spectrum of photolysis products after three seconds of irradiation of the isolated  $m/z$  231-241 ions.

dehydrogenation to ions  $C_{19}H_n^+$ , where  $n=3$  to 12. Some acetylene loss is observed with peaks at  $m/z$  211 and 213. Interesting peaks are also observed at  $m/z$  180 ( $C_{15}^+$ ) and  $m/z$  181 ( $C_{15}H^+$ ). The loss of a  $C_4H_4$  fragment from  $m/z$  233 could form  $m/z$  181. This indicates that the lowest energy photofragmentation route is dehydrogenation until this mass is reached, after which  $C_4H_4$  can be ejected.

#### $C_{18}H_n^+$ ( $m/z$ 224-228)

The only source for this group of ions containing 18 carbons, is acetylene loss from the naphthalene “dimer” ion. Figure 87 shows this group to be very stable except for dehydrogenation. The most abundant ion is  $m/z$  226 ( $C_{18}H_{10}^+$ ) with a smaller peak at  $m/z$  224 ( $C_{18}H_8^+$ ). No acetylene fragmentation is observed.

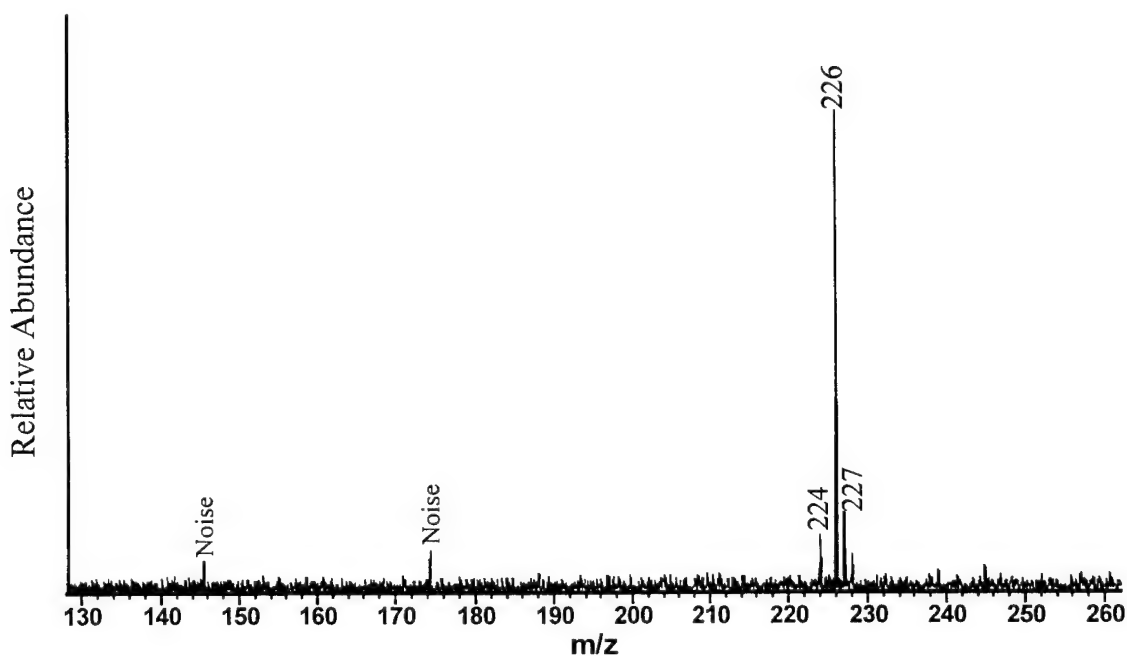


Figure 87. FTICR mass spectrum of photolysis products after three seconds of irradiation of the isolated  $m/z$  224-230 ions.

$C_{16}H_n^+$  (m/z 198-204)

This group of ions is only formed via an ion-molecule reaction from m/z 76. By comparing the relative abundances of m/z 76 and this group of ions (cf. Figure 70), it appears that this reaction occurs with great efficiency. The m/z 76 ion is not visible while m/z 202 is the most abundant ion, after the naphthalene parent (m/z 128). The largest aggregate that can be formed is m/z 204 (76 + 128) but this quickly dehydrogenates to m/z 202 (cf. Figure 88). Further dehydrogenation to m/z 200 and m/z 198 is also visible. A very small peak at m/z 176 is visible showing  $C_2$  or acetylene loss from m/z 200 or m/z 202, respectively.

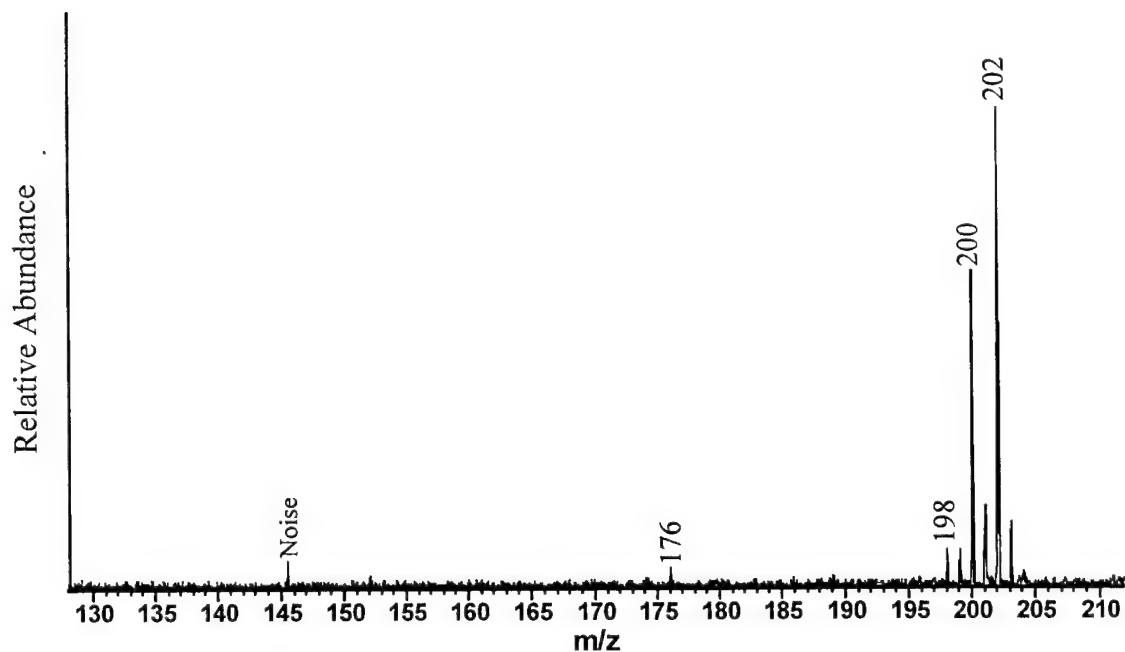


Figure 88. FTICR mass spectrum of photolysis products after four seconds of irradiation of the isolated m/z 198-206 ions.

### Naphthalene Summary

A flowchart with the observed reactions is shown in Figure 89. Compared to fluorene, it is relatively straightforward. Naphthalene will lose a maximum of two hydrogens. The  $m/z$  128 ion will photolyze to form  $m/z$  115 (CH loss) and  $m/z$  102 ( $C_2H_2$  loss) while the  $m/z$  127 ion will only fragment to form  $m/z$  115 (C loss). The  $m/z$  126 ion does not produce photo-fragments. This stability may be the result of the formation of a naphthyne species.

The  $m/z$  128 ion does not produce aggregates while the  $m/z$  127 ion produces several, including  $m/z$  255 and  $m/z$  253. A peak at  $m/z$  240 is the loss of C + 3H from  $m/z$  255 or CH from  $m/z$  253 during formation of the aggregate. The  $m/z$  126 ion does not form any aggregates. Again, this stability may be due to the formation of a triple bond, eliminating any radical sites on the ion.

The  $m/z$  102 ion will photodissociate to form the  $m/z$  76 ion ( $C_2H_2$  loss) but will not form aggregate products. No acetylene loss from the  $m/z$  76 ion was observed, but the  $m/z$  202 aggregate product, (possibly the formation of fluoranthene), was very abundant.

All aggregate products dehydrogenated to some extent when irradiated.  $C_{18}H_n^+$  was the only group that did not lose acetylene upon photolysis.  $C_{20}H_n^+$  was the only group that lost CH.

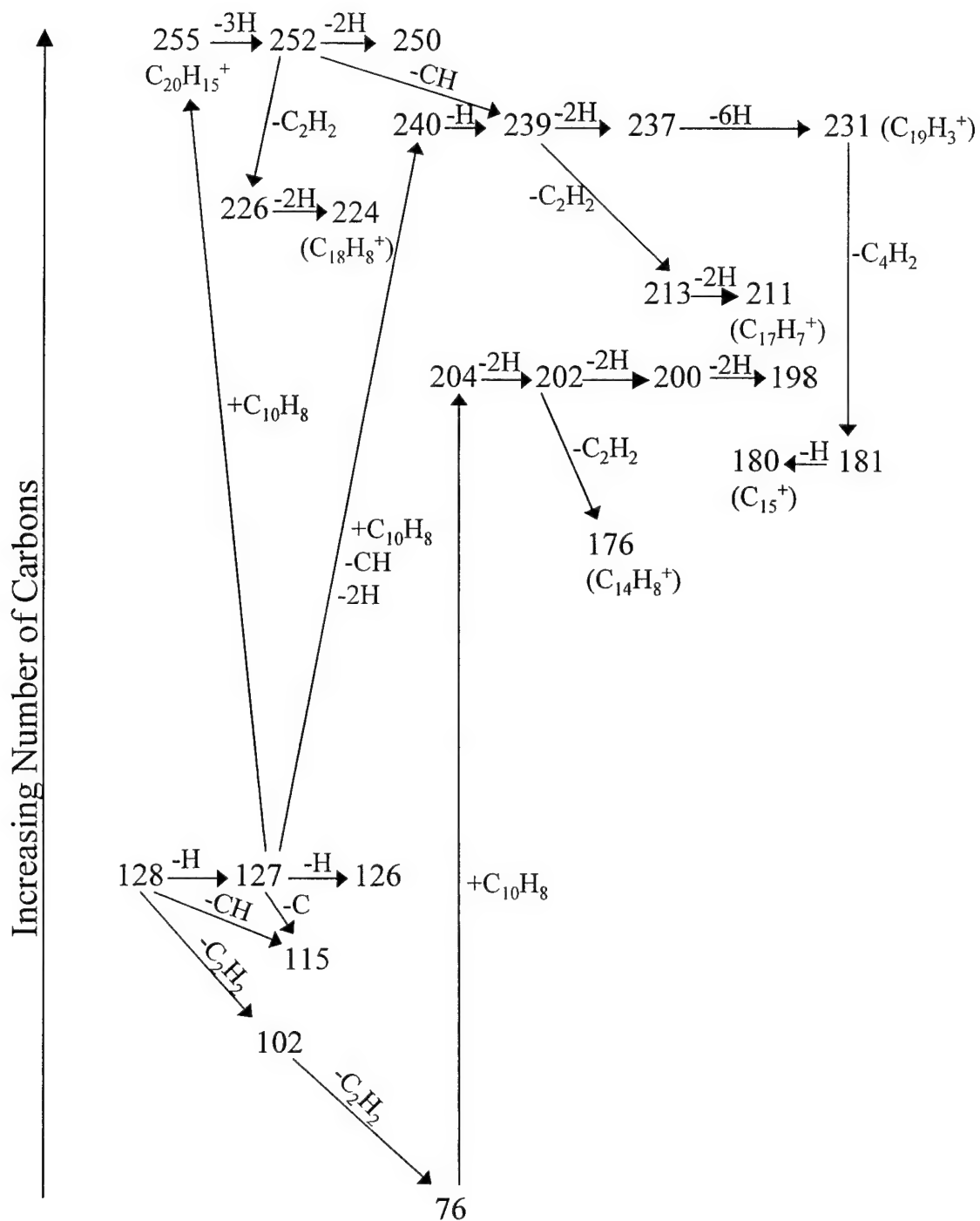


Figure 89. Proposed fragmentation and ion-molecule reaction pathways for naphthalene.

### 1,2-Benzanthracene

Previous work by Ekern et al.<sup>114</sup> found that upon irradiation, 1,2-benzanthracene dehydrogenated and lost one acetylene. Figure 90 shows the results of photolysis for nine seconds of the parent ion ( $m/z$  228). The Ekern results are confirmed in this figure. The 1,2-benzanthracene ion is much more stable than fluorene or naphthalene, as evidenced by the rather low abundance of lower mass fragment peaks after significantly longer irradiation. However, Figure 91, showing the expansion of the photolysis products from Figure 90, reveals more detail. Not only is acetylene loss visible ( $m/z$  202), but single carbon loss to  $m/z$  215, as well as the loss of three, four, five and six carbons, is clearly visible.

A time dependent study of the fragmentation of the  $m/z$  228 ion is shown in Figure 92. Ions with the same number of carbons were grouped together and tracked as a function of irradiation time. Steady-state is achieved after irradiation for only two seconds. The abundance of the parent  $C_{18}$  group is still 80%, indicating the relative stability of 1,2-benzanthracene. Figure 93 is an expansion of the smaller intensity groups shown in Figure 92. There is a slight decrease in the most abundant group,  $C_{16}$ , from nearly 12% down to 10%, but all others remain constant at abundances of 1-4%.

### Hydrogen Loss

1,2-benzanthracene dehydrogenates much more completely than either fluorene or naphthalene. Figure 94 shows that 8 of the 12 hydrogens may be lost due to photolysis, although the loss of only two hydrogens is dominant. The loss of hydrogen in pairs appears to be a stabilizing effect since the relative abundance of ions of even  $m/z$  is higher.



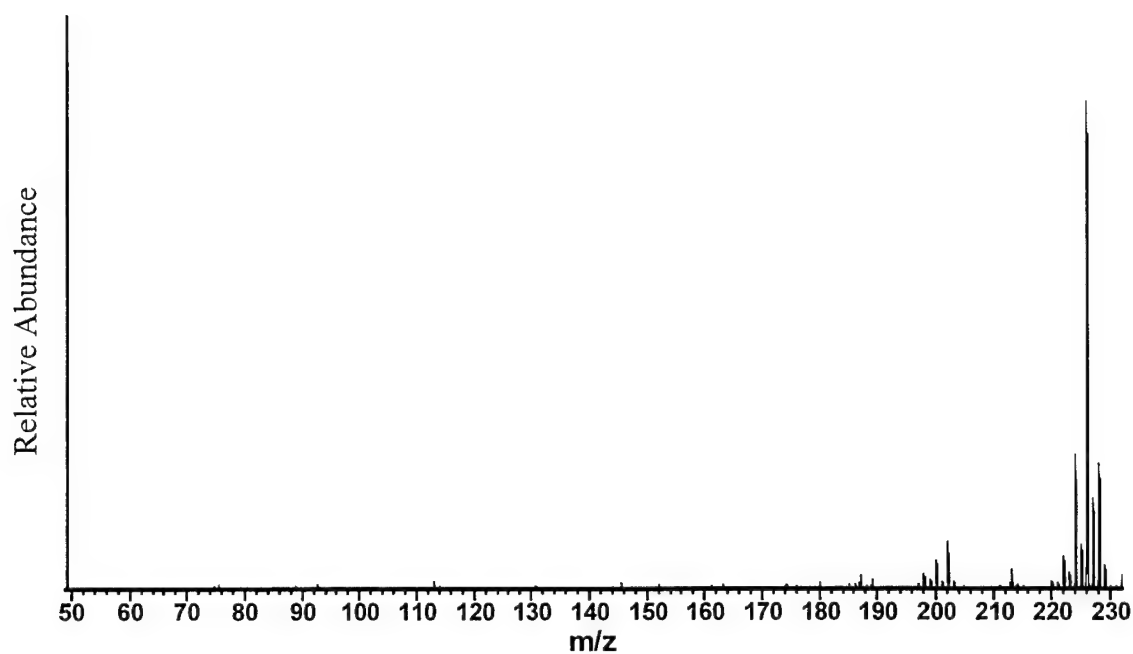


Figure 90. FTICR mass spectrum of the photolysis products after irradiation of the  $m/z$  228 ion (9s.).

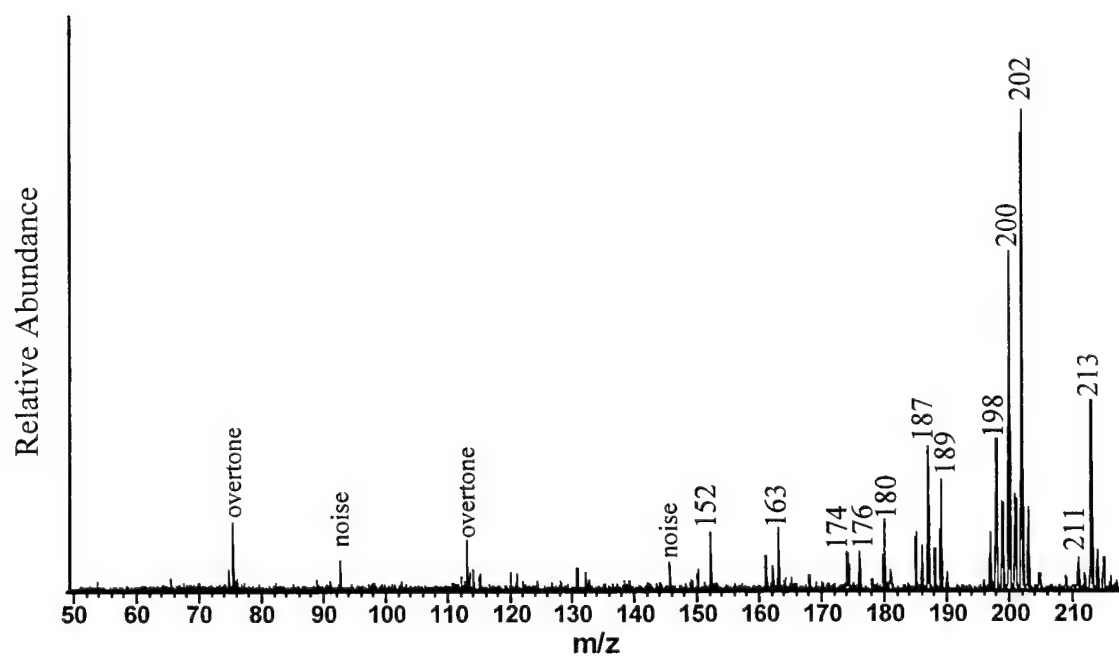


Figure 91. Expansion of the lower mass range of Figure 90 showing photolysis products only.

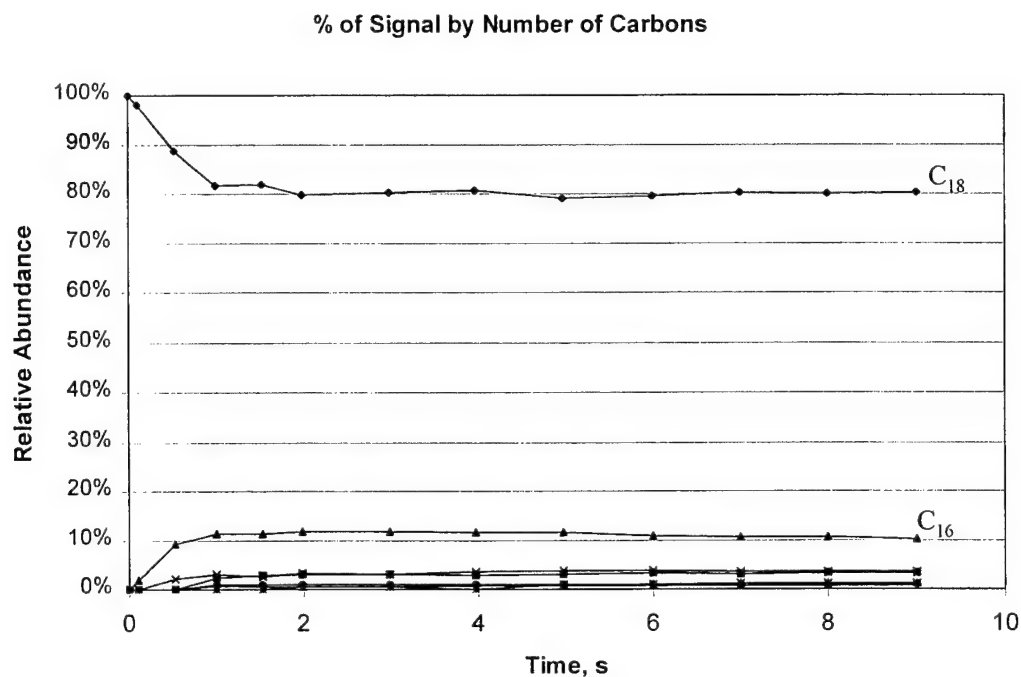


Figure 92. Time dependence of the abundance of photoproducts of the  $m/z$  228 ion, grouped by number of carbons.

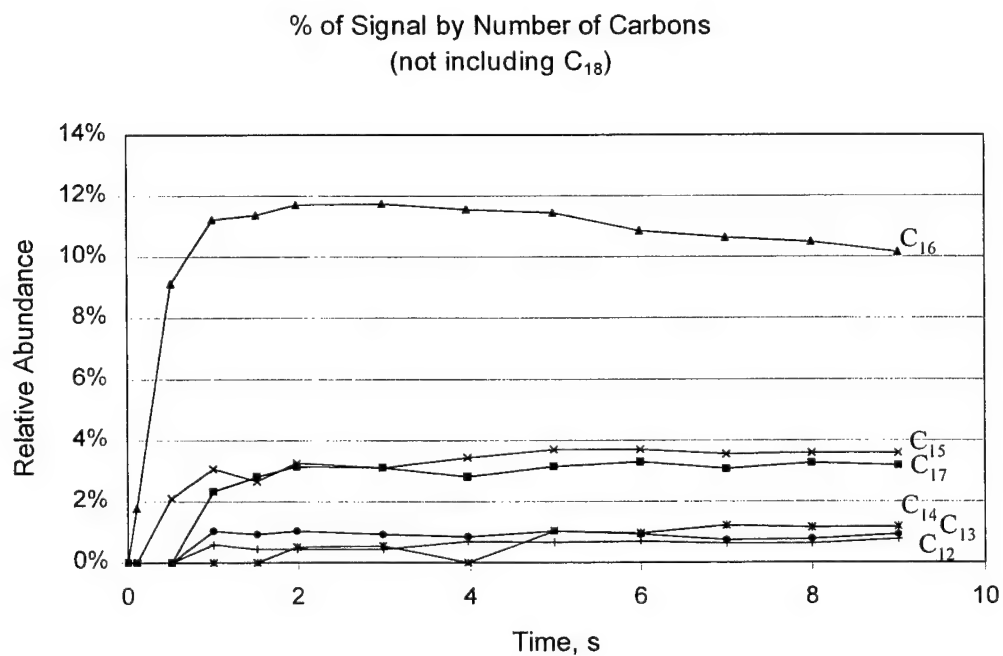


Figure 93. Expansion of Figure 92 without the parent group, C<sub>18</sub>.

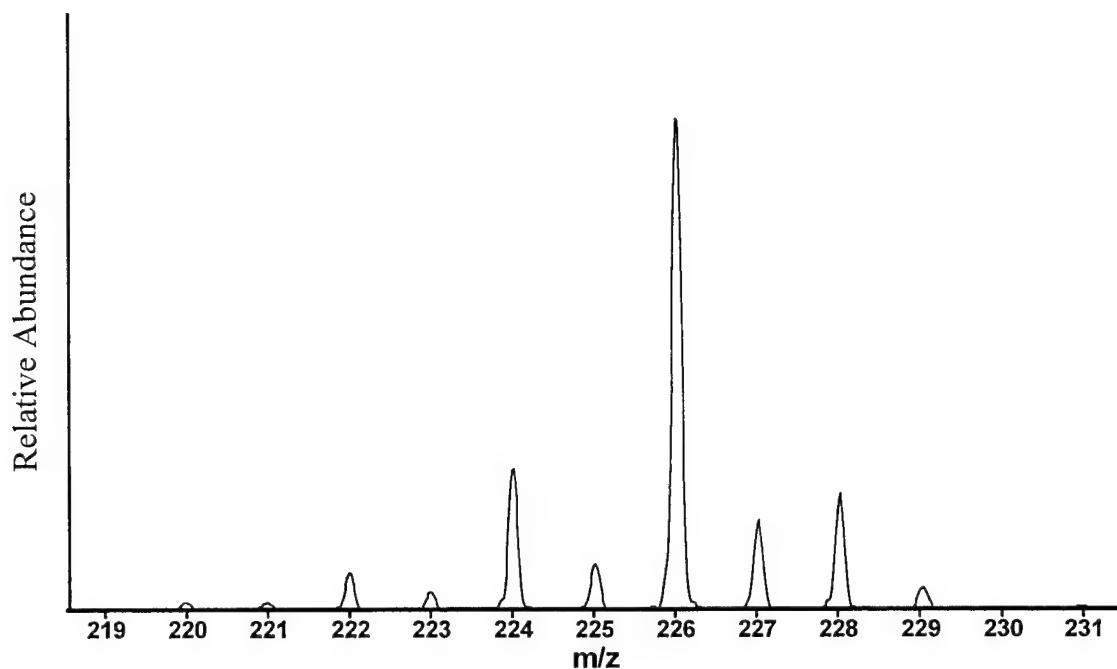


Figure 94. FTICR mass spectrum of photolysis products after 10 seconds of irradiation of the  $m/z$  228 ion.

To determine if the hydrogen is lost as atoms or molecules, single frequency ejection pulses were used during irradiation of the parent ion. Figure 95 shows the photolysis products after irradiation for 0.5 seconds and indicates a strong peak at  $m/z$  226. In Figure 96, the  $m/z$  227 ion is ejected during irradiation of the parent ion. If dehydrogenation were to occur only via single hydrogen loss, no  $m/z$  226 would be detected. However, Figure 96 clearly shows the presence of an ion at  $m/z$  226, indicating the loss of two hydrogens simultaneously or the loss of  $H_2$ .

To test for the loss of  $H_2$  fragments at lower masses, longer irradiation times were used. Figure 97 indicates the photolysis products after irradiation for three seconds. Using this as a comparison, Figure 98 shows the photolysis products while  $m/z$  226 is ejected. Since  $m/z$  227 has an odd number of hydrogens, the loss of  $H_2$  is not expected and Figure 99 confirms this result. No  $m/z$  225 ion is produced directly from  $m/z$  227.

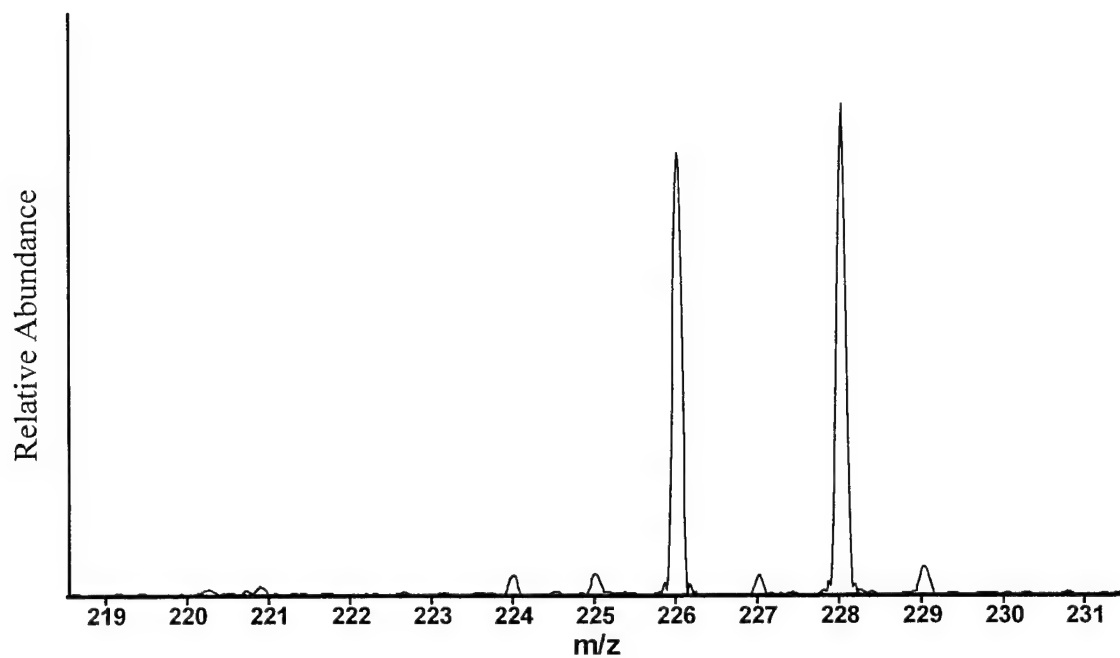


Figure 95. FTICR mass spectrum of photolysis products after 0.5 seconds of irradiation.

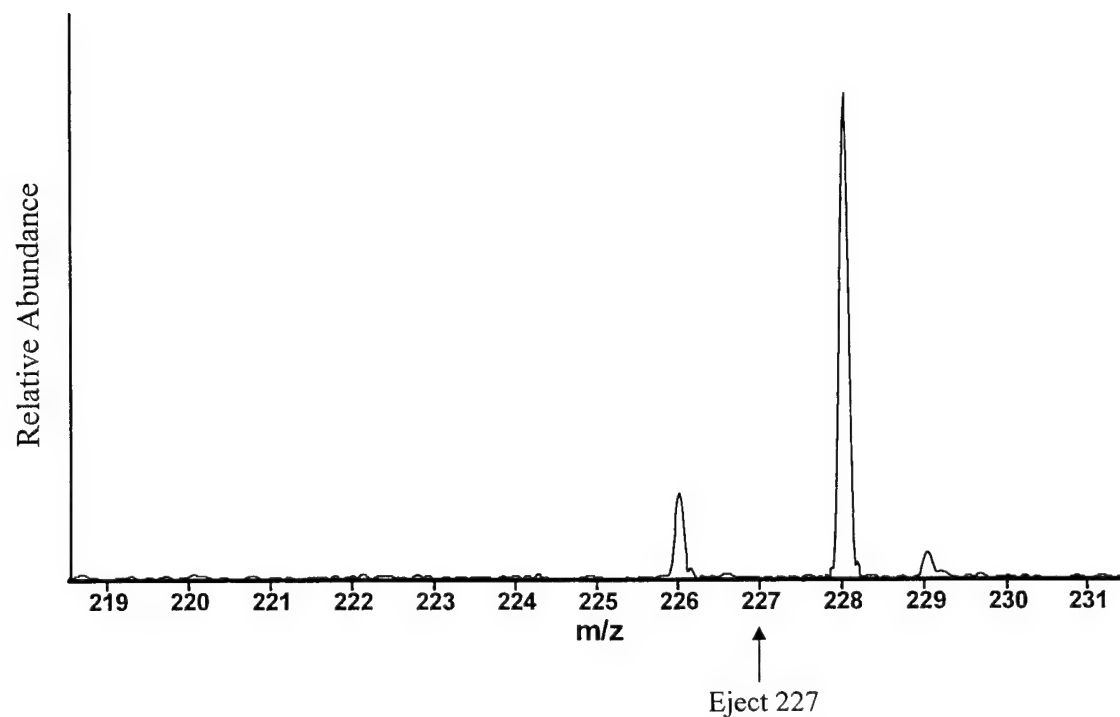


Figure 96. FTICR mass spectrum of photolysis products after 0.5 seconds of irradiation while  $m/z$  227 was ejected.

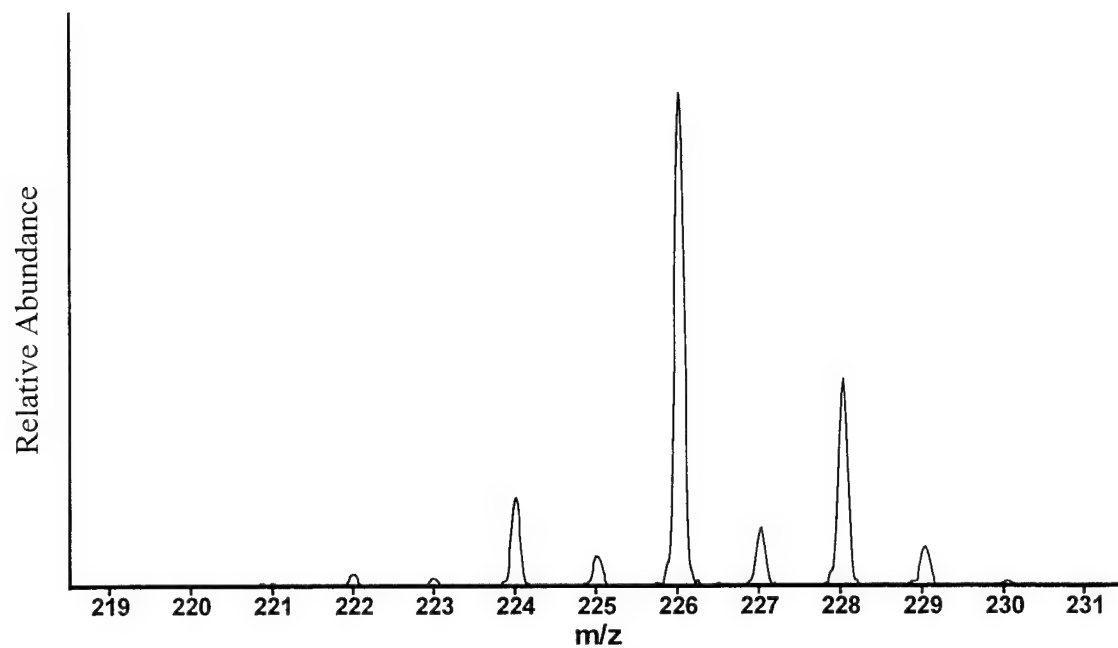


Figure 97. FTICR mass spectrum of photolysis products after three seconds of irradiation of the  $m/z$  228 ion.

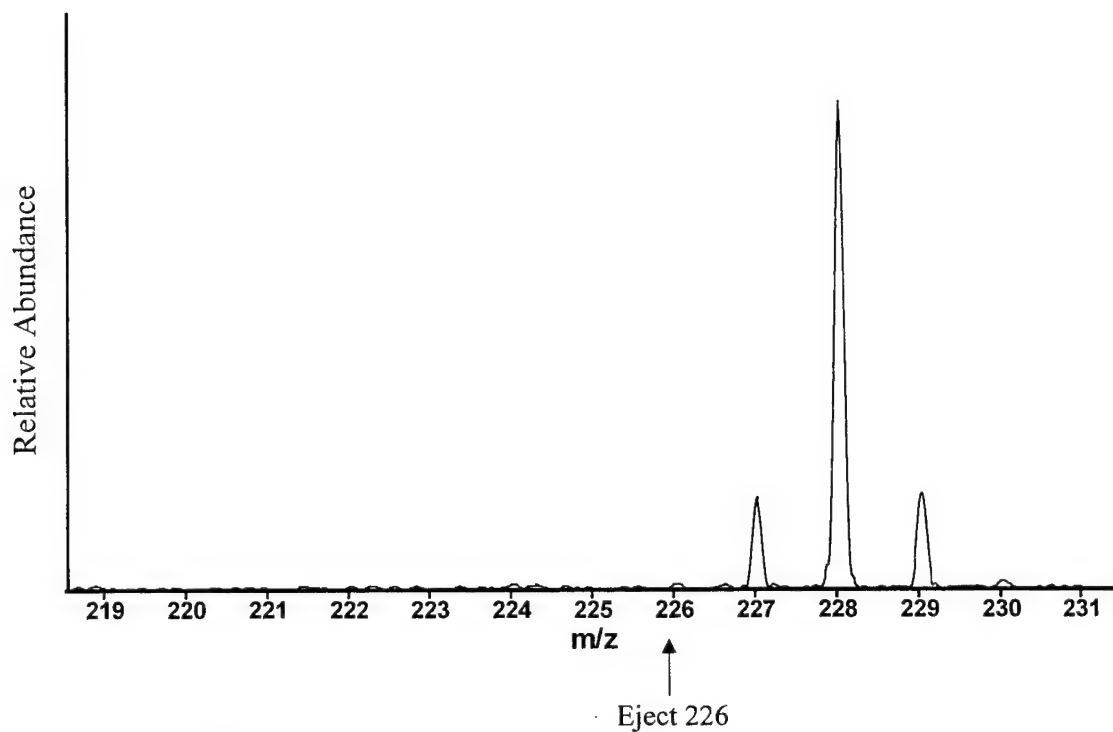


Figure 98. FTICR mass spectrum of photolysis products after three seconds of irradiation of the  $m/z$  228 ion while ejecting  $m/z$  226.

H<sub>2</sub> loss from m/z 226 was also examined. Figure 99 shows the results of irradiation of the m/z 228 ion for five seconds while Figure 100 includes the ejection of m/z 225 with the same irradiation. A very slight peak (<1% of m/z 226 abundance) at m/z 224 is visible. The appearance of this peak suggests that H<sub>2</sub> loss is possible but is a low probability dissociation pathway.

#### C<sub>18</sub>H<sub>n</sub><sup>+</sup> (m/z 226-228)

The major ions in this group, m/z 226-228, were isolated individually and irradiated for various amounts of time to determine their photolysis products. Figures 101, 102 and 103 are similar, all showing the same photoproducts. One difference to note is the reaction rate of the m/z 227 ion. Irradiation for only 0.25 seconds was required to form fragments in similar ratios as m/z 226 and m/z 228, which required four seconds and two seconds of irradiation, respectively. The m/z 227 ion also formed m/z 180, C<sub>15</sub><sup>+</sup>, which is not distinguishable from the background in the other two spectra.

#### C<sub>17</sub>H<sub>n</sub><sup>+</sup> (m/z 209-218)

The results of irradiation for three seconds of the group containing 17 carbons is shown in Figure 104. Loss of one carbon to form m/z 202 and acetylene loss to form m/z 187 and m/z 189 is shown. Although m/z 163 is also present, it is unclear if this is formed directly from the C<sub>17</sub> group or by sequential acetylene loss via m/z 189.

#### C<sub>16</sub>H<sub>n</sub><sup>+</sup> (m/z 197-204)

The group containing 16 carbons was irradiated for five seconds as shown in Figure 105. Dehydrogenation makes m/z 200 the predominant ion compared to m/z 202 as shown in Figure 91. Single carbon loss to produce m/z 187 and 189 is clear. An ion at m/z 163 is also present but is probably derived from acetylene fragmentation of the m/z 187 and m/z 189 ions.

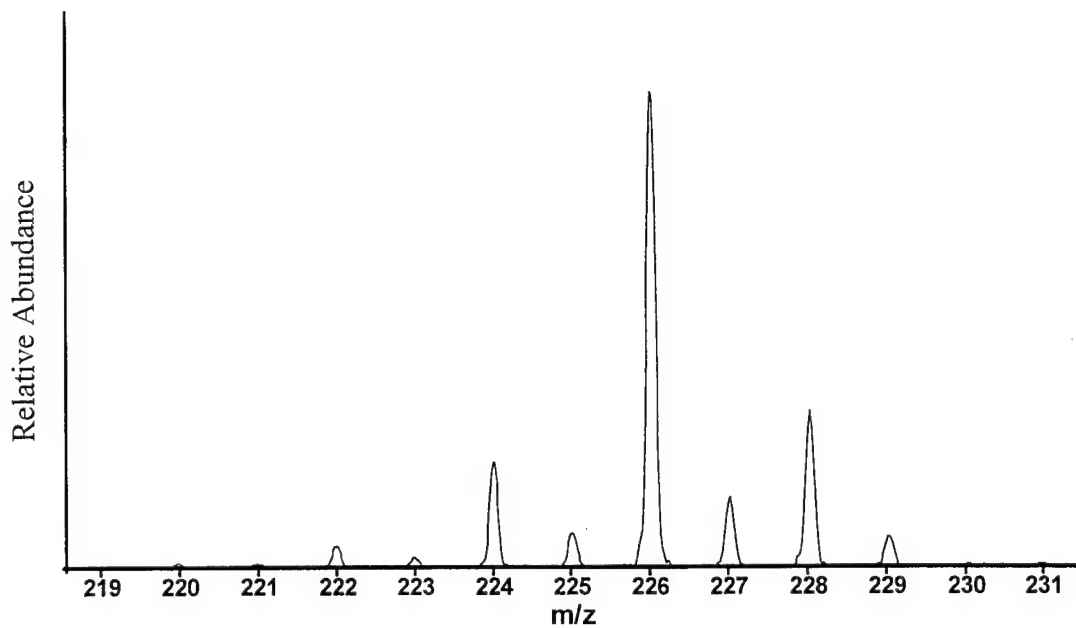


Figure 99. FTICR mass spectrum of photolysis products after five seconds of irradiation of the  $m/z$  228 ion.

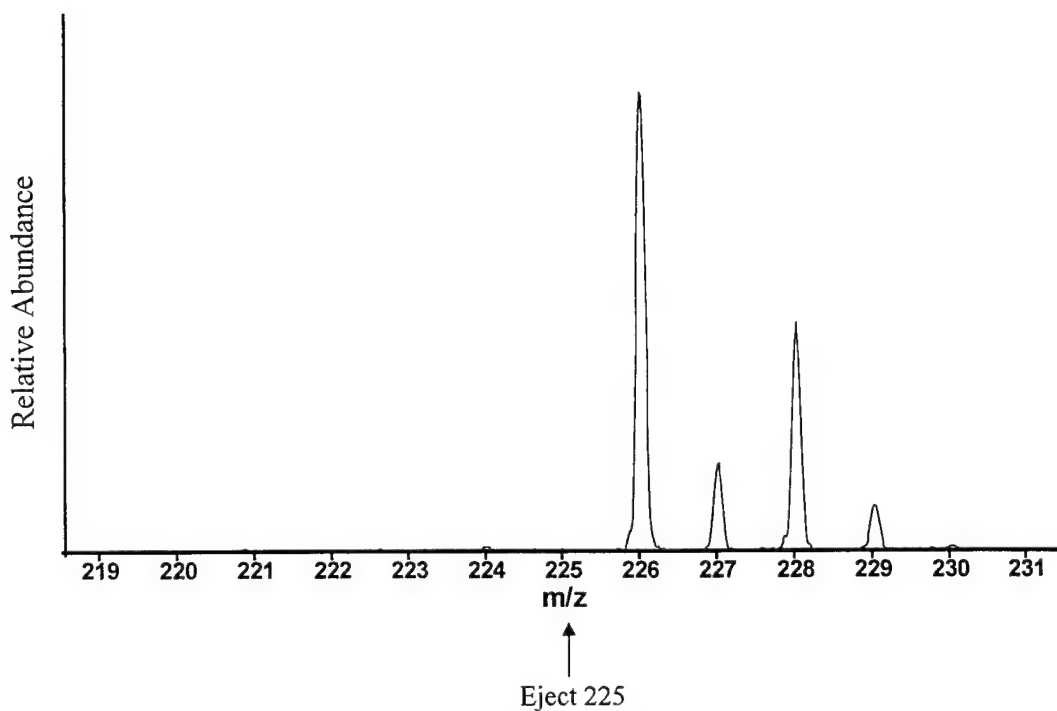


Figure 100. FTICR mass spectrum of photolysis products after five seconds of irradiation of the  $m/z$  228 ion while ejecting  $m/z$  225.

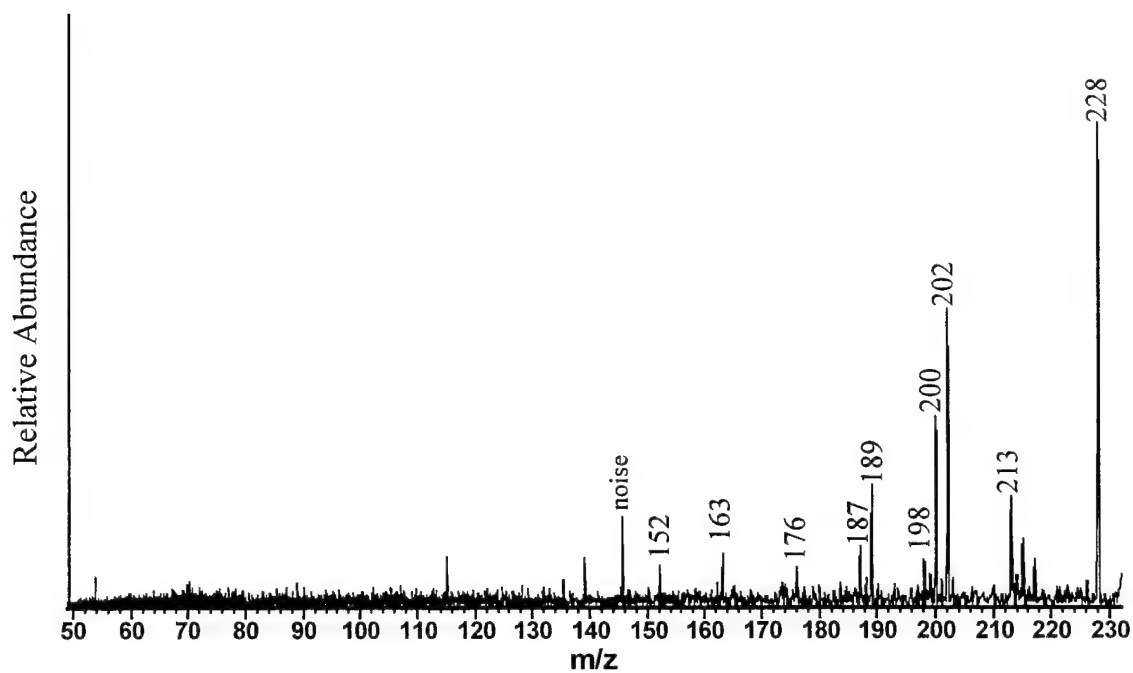


Figure 101. FTICR mass spectrum of photolysis products after two seconds of irradiation of the isolated  $m/z$  228 ion.

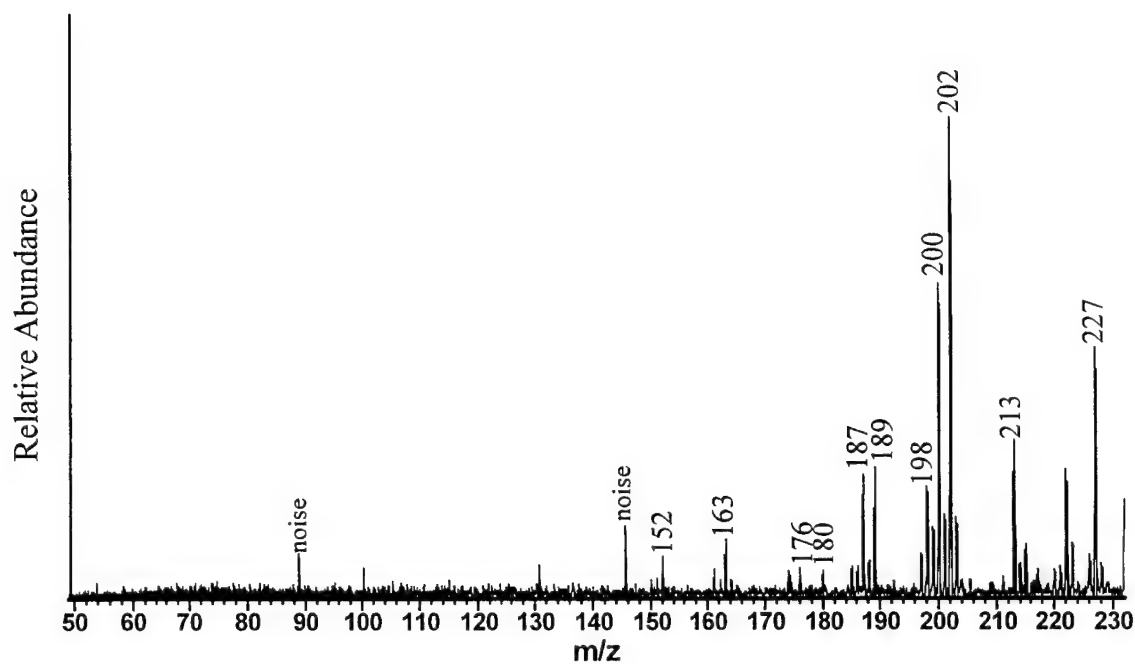


Figure 102. FTICR mass spectrum of photolysis products after 0.25 seconds of irradiation of the isolated  $m/z$  227 ion.



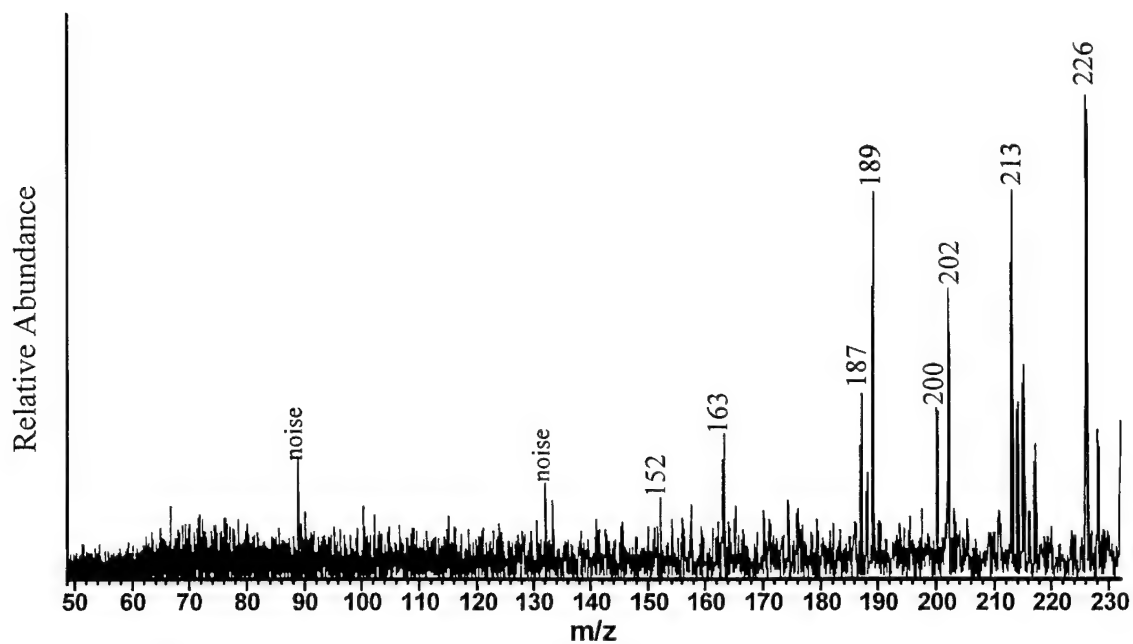


Figure 103. FTICR mass spectrum of photolysis products after four seconds of irradiation of the isolated  $m/z$  226 ion.

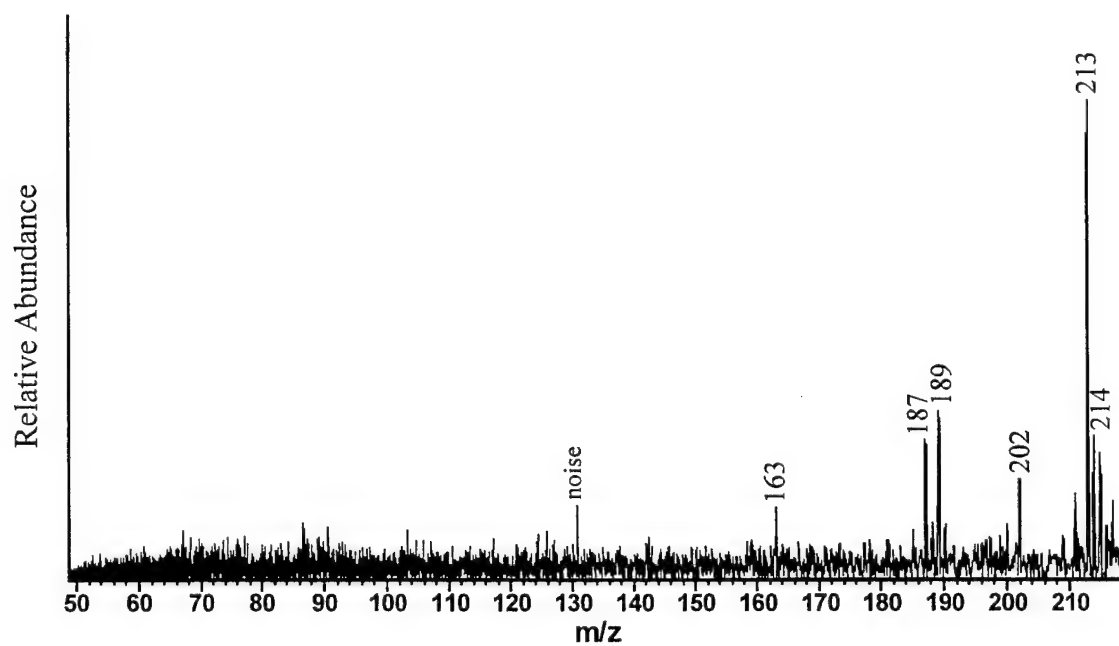


Figure 104. FTICR mass spectrum of photolysis products after three seconds of irradiation of the isolated  $m/z$  209-218 ions.

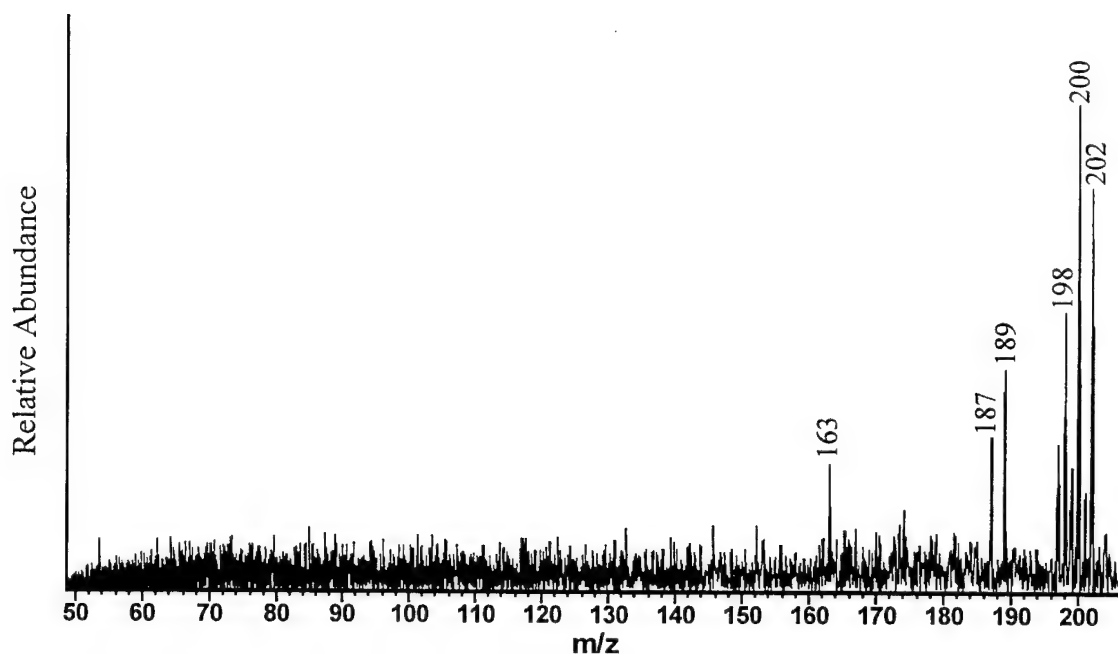


Figure 105. FTICR mass spectrum of photolysis products after five seconds of irradiation of the isolated  $m/z$  197-204 ions.

#### $C_{15}H_n^+$ ( $m/z$ 184-191)

Irradiation for three seconds of the group containing 15 carbons is shown in Figure 106. Loss of acetylene is observed to form the ion at  $m/z$  163. No other processes are observed.

#### Ion-molecule reactions

1,2-benzanthracene behaves differently from the other two molecules studied. Figure 107 shows the isolation of the parent ion and its dehydrogenated fragments. No dimer-like products are observed. This may be due to its nonlinear structure, although additional experiments (such as with tetracene) would be necessary to explore this hypothesis.

Some ions larger than the parent 1,2-benzanthracene are, however, visible in Figure 108, an expansion of the upper mass range of Figure 90. Although the source of

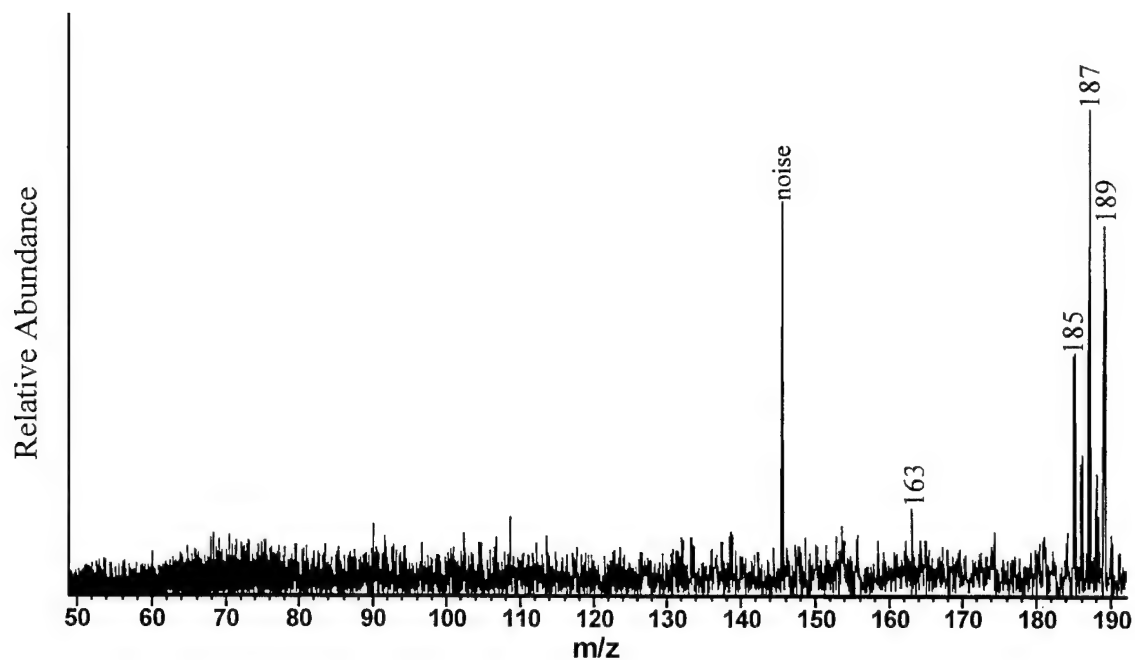


Figure 106. FTICR mass spectrum of photolysis products after irradiation (3 s.) of the isolated m/z 184-191 ions.

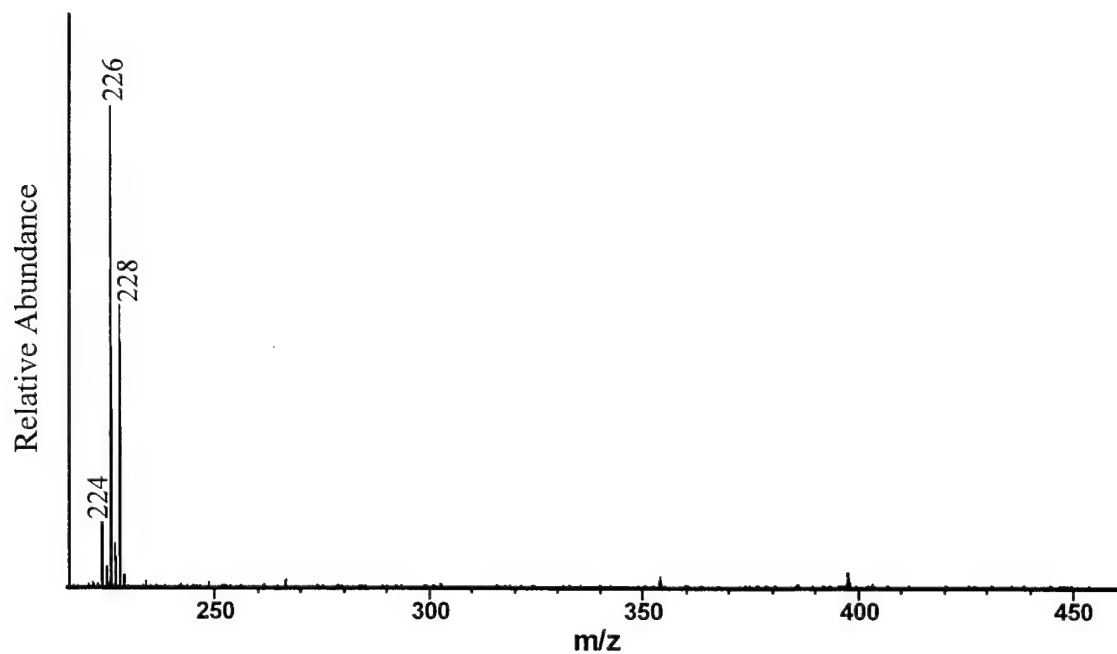


Figure 107. FTICR mass spectrum of the ion-molecule reaction products of isolated m/z 220-228 ions after a five second delay.

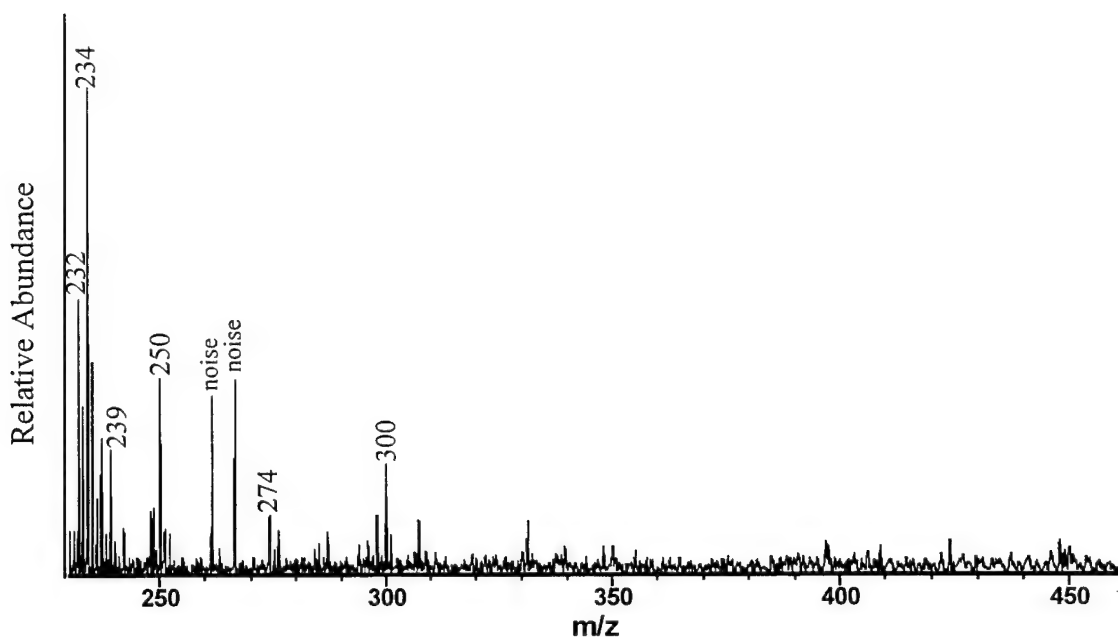


Figure 108. FTICR mass spectrum of possible ion-molecule reaction products formed after 9 seconds of irradiation.

these fragments could not be determined experimentally, it is possible to speculate about their origin. The ions between  $m/z$  232 to  $m/z$  240 contain one extra carbon while  $m/z$  250 has two extra carbons,  $m/z$  274 has four extra carbons and  $m/z$  300 has six extra carbons when compared to the parent ion. If the fragments created during the photolysis of the parent ion undergo ion-molecule reactions, they could form aggregates in this range. However, this assumes they are fragmenting as ions or forming ions during the aggregation process, which may not be very likely. Further experiments will be required to resolve this issue.

#### 1,2-Benzanthracene Summary

1,2-benzanthracene is more resistant to photofragmentation than either fluorene or naphthalene. It is capable of fragmenting to lose from one to eight carbons although the relative abundance of the photoproducts is only 20% compared to the parent ion. The ion

also dehydrogenates more completely, losing 8 of its 12 hydrogens. Similar to fluorene,  $\text{H}_2$  loss is evident from ions with an even mass, while only single hydrogen loss occurs from ions with an odd mass.

Irradiation of the parent ion ( $m/z$  228), produces similar photoproducts as the  $m/z$  227 and  $m/z$  226 ions. However, the reaction rate for  $m/z$  227 is much faster. Acetylene loss, as well as CH loss, was observed for the irradiation of  $\text{C}_{17}\text{H}_n$  and  $\text{C}_{16}\text{H}_n$  while only acetylene loss was observed from  $\text{C}_{15}\text{H}_n$ .

Although photoproducts with a mass greater than the parent ion were observed, their source could not be determined. The groups  $\text{C}_{15}\text{H}_n$  through  $\text{C}_{18}\text{H}_n$ , did not form aggregates.

## CHAPTER 7 CONCLUSIONS

FT-ICR mass spectrometry was used to determine the photolysis products of the ionized PAHs fluorene, naphthalene and 1,2-benzanthracene by irradiation with a xenon arc lamp. Products of ion-molecule reactions were also characterized for all three PAHs. An "action" spectrum for the absorption of fluorene was determined.

By a combination of isolations and ejections in the ICR cell, it is established that the H atom loss from fluorene is sequential with a loss of up to five H atoms observed. Only the odd mass species,  $m/z$  163 and 165, may also lose two hydrogens simultaneously (as  $2H$  or  $H_2$ ). The even mass species  $m/z$  162, 164 and 166 lose only single hydrogens.

Irradiation times longer than 2s lead to photofragments with smaller masses. Major products appear at  $m/z$  63, 87, 89, 111, 115, 116, 135, 139 and 140, plus the dehydrogenated species at  $m/z$  161-165. By isolating the parent and dehydrogenated precursor partners in turn and irradiating them further, the photoproducts originating from each have been found.

Rate constants and branching ratios for each of these decomposition pathways have been determined. Kinetic plots (mass abundance vs irradiation time) for each precursor and its products were fit by computer solution of a series of coupled differential equations. Sequential single H atom loss is shown to be the preferred decomposition pathway.

Density functional theory calculations have shown that the most probable positions for extraction of the five hydrogens are, first, from the  $sp^3$  carbon and, then, from the four positions on one of the six-membered rings. Removal of hydrogens on the other ring and removal of a sixth hydrogen require substantially higher energies.

Further fragmentation of the odd mass dehydrogenated products ( $m/z$  165, 163, and 161) has been explored theoretically and various monocyclic ring intermediates suggested which lead plausibly to the observed lower mass final products. Unusual geometries, such as a "tadpole" shape (three-membered ring attached to a linear carbon chain) for the  $C_5H_3^+$  species, a three-membered ring fused to a six-membered ring for the  $C_7H_5^+$  product and monocyclic rings for the all-carbon  $C_9^+$  and  $C_{11}^+$  product ions are computed to be the most stable for these observed products.

All isolated groups of photofragments form aggregates by reacting with a fluorene neutral molecule and these aggregate products exhibit significant dehydrogenation during irradiation.

Irradiation of the naphthalene ion for short times results in a maximum loss of two hydrogens. The  $m/z$  128 ion will photolyze to form  $m/z$  115 (CH loss) and  $m/z$  102 ( $C_2H_2$  loss) while the  $m/z$  127 ion will only fragment to form  $m/z$  115 (C loss). The  $m/z$  126 ion does not produce photo-fragments. This stability may be the result of the formation of a naphthyne species.

Only the  $m/z$  127 ion produces aggregates, including  $m/z$  255 and  $m/z$  253. A peak at  $m/z$  240 is the loss of C + 3H from  $m/z$  255 or CH from  $m/z$  253 during formation of the aggregate. The  $m/z$  128 and the  $m/z$  126 ions do not form any

aggregates. The stability of the  $m/z$  126 ion may be due to the formation of a triple bond, eliminating any radical sites on the ion.

The  $m/z$  102 ion will photodissociate to form the  $m/z$  76 ion ( $C_2H_2$  loss) but will not form aggregate products. The  $m/z$  76 ion did not photodissociate, but the  $m/z$  202 aggregate product, (possibly fluoranthene), was very abundant.

1,2-benzanthracene is more resistant to photofragmentation than either fluorene or naphthalene. It is capable of fragmenting to lose from one to six carbons although the relative abundance of the photoproducts is only 20% compared to the parent ion. The ion also dehydrogenates more completely than others studied, losing 8 of its 12 hydrogens. Similar to fluorene,  $H_2$  loss is evident from ions with an even mass, while only single hydrogen loss occurs from ions with an odd mass.

Irradiation of the parent ion ( $m/z$  228) produces similar photoproducts as the  $m/z$  227 and  $m/z$  226 ions. However, the reaction rate for  $m/z$  227 is much faster. Acetylene loss, as well as CH loss, was observed for the irradiation of  $C_{17}H_n$  and  $C_{16}H_n$  while only acetylene loss was observed from  $C_{15}H_n$ .

Although photoproducts with a mass greater than the parent ion were observed, their source could not be determined. The groups  $C_{15}H_n$  through  $C_{18}H_n$ , did not form aggregates.

The action spectrum of the  $m/z$  166  $\rightarrow$   $m/z$  165 decomposition of fluorene mimics closely the matrix spectrum of the fluorene cation recorded previously. The spectra obtained with the monochromator/xenon arc lamp and the dye laser eliminate the perturbation effects seen in spectra obtained by isolation of ions in rare-gas matrices. Broad absorption peaks were observed at  $\sim 372$  nm and  $\sim 617$  nm with the



monochromator, while the dye laser was able to resolve this upper peak into two peaks at ~600 and ~615 nm. Results with the dye laser could be improved dramatically if the use of prisms could be eliminated. The higher power would not only increase the amount of dissociation, it would also increase the usable range for each dye.

Possible studies for the future should include photolysis of anthracene and tetracene. The irradiation of anthracene, especially the aggregate products formed, can be contrasted to 1,2-benzanthracene. The study of tetracene could help to establish the pattern of lower fragmentation with larger structures.

## REFERENCES

1. National Radio Astronomy Observatory, *The 121 Reported Interstellar and Circumstellar Molecules*, [www.cv.nrao.edu/~awootten/allmols.html](http://www.cv.nrao.edu/~awootten/allmols.html), **27 Apr 2001**.
2. Kaiser, R. I.; Roessler, K. *Astrophys. J.*, **1997**, 475, 144.
3. Leger, A. and Puget, J.L., *Astron. and Astrophys.* **1984**, 137, L5.
4. Allamandola, L.J., Tielens, A.G.G.M., Barker, J.R., *Astrophys. J.* **1985**, 290, L25.
5. Russell, R., Soifer, B., Willner, W., *Astrophys. J.* **1977**, 217, L149; *ibid.*, **1978**, 220, 568.
6. Leger, A. and d'Hendecourt, L. *Astron. and Astrophys.* **1985**, 146, 81.
7. van der Zwet, G.P. and Allamandola, L.J. *Astron. and Astrophys.* **1985**, 146, 76.
8. Omont, A., *Astron. and Astrophys.* **1986**, 164, 159.
9. Tielens, A.G.G.M., Allamandola, L.H.J., Barker, J. R., Cohen, M. In *Polycyclic Aromatic Hydrocarbons and Astrophysics*, Leger, A., d'Hendecourt, L., Boccarra, N., Eds.; Reidel: Dordrecht, 1987, p 273.
10. Allamandola, L.J., Tielens, A.G.G.M., Barker, J.R., *Astrophys. J. Suppl.* **1989**, 71, 733.
11. Geballe, T.R., Tielens, A.G.G.M., Allamandola, L.J., Moorhouse, A., Brand, P.W. *Astrophys. J.* **1989**, 341, 278.
12. Leger, A., Boissel, P., Desert, F.X., d'Hendecourt, L.J. *Astron. and Astrophys.* **1989**, 213, 351.
13. Leger, A., d'Hendecourt, L.J., Defourneau, D. *Astron. and Astrophys.* **1989**, 216, 148.
14. Verstraete, L., Leger, A., d'Hendecourt, L.J., Dutuit, O., Defourneau, D., *Astron. and Astrophys.* **1990**, 237, 436.
15. Allamandola, L. J.; Tielens, A. G. G. M.; Barker, J. R. *Astrophys. J.* **1989**, 345, L59.
16. Crawford, M. K.; Tielens, A. G. G. M.; Allamandola, L. J. *Astrophys. J.* **1985**, 293, L45.

17. Salama, F.; Bakes, E. L. O.; Allamandola, L. J.; Tielens, A. G. G. M. *Astrophys. J.*, **1996**, 458, 621.
18. Salama, F.; Galazutdinov, G. A.; Krelowski, J.; Allamandola, L. J.; Musaev, F. A. *Astrophys. J.* **1999**, 526, 265.
19. *The Diffuse Interstellar Bands*, Tielens, A. G. G. M.; Snow, T. P. Eds.; Kluwer Academic Publishers: Dordrecht, 1995.
20. Salama, F.; Allamandola, L. J. *Astrophys. J.* **1992**, 395, 301.
21. Salama, F.; Allamandola, L. J. *Nature*, **1992**, 358, 42.
22. Léger, A.; d'Hendecourt, L.; Défourneau, D. *Astron. Astrophys.* **1995**, 293, L53.
23. Jenniskens, P.; Désert, F. X. In *The Diffuse Interstellar Bands*; Tielens, A. G. G. M.; Snow, T. P., Eds.; Kluwer Academic Publishers: Dordrecht, 1995; p 39.
24. Szczepanski, J.; Vala, M. *Nature*, **1993**, 363, 699.
25. Joblin, C.; Tielens, A. G. G. M.; Geballe, T. R.; Wooden, D. H. *Astrophys. J.* **1996**, 460, L119.
26. Snow, T. P.; Page, V. L.; Keheyan, Y.; Bierbaum, V. *Nature* **1998**, 392, 259.
27. Siegmann, K.; Satler, K. *J. Chem. Phys.* **2000**, 112, 698, and references therein.
28. Senkan, S.; Castaldi, M. *Flame* **1996**, 107, 10.
29. Ciajolo, A.; D'Anna, A.; Barbella, R. *Combust. Sci. Technol.* **1994**, 100, 271.
30. Hepp, H.; Siegmann, K.; Sattler, K. *Chem. Phys. Lett.* **1995**, 233, 16.
31. Feitelberg, A. S.; Longwell, J. P.; Sarofim, A. F. *Combust. Flame* **1993**, 92, 13.
32. Wang, H.; Frenklach, M. *Combust. Flame* **1997**, 110, 49.
33. Marinov, N. M.; Pitz, W. J.; Westbrook, C. K.; Castaldi, M. J.; Senkan, S. M. *Combust. Sci. Technol.* **1996**, 116, 77.
34. Marr, J. A.; Giovane, L. M.; Longwell, J. P.; Howard, J. B.; Lafleur, A. L. *Combust. Sci. Technol.* **1994**, 101, 301.
35. Stein, S.; Fahr, A. *J. Phys. Chem.* **1985**, 89, 3714.
36. Pope, C. J.; Howard, M. B. *Aerosol. Sci. Technol.* **1997**, 27, 22.
37. Ikegami, M.; Yoshihara, Y.; Li, X. H. *JSME* **1986**, 29, 4256.

38. Kaiser, R. I.; Lee, Y. T.; Bettinger, H. F.; von Schleyer, P. R.; Schreiner, P. R.; Schaefer, H. F. *Abstr. Pap. Am. Chem. Soc.* **1998**, 215, 303-PHYS.
39. Herbst, E.; Dunbar, R. C. *Mon. Not. R. Astr. Soc.* **1991**, 253, 341.
40. Martin, P. G.; Rogers, C. *Astrophys. J.* **1987**, 322, 374.
41. Bittner, J. D.; Howard, J. B. In *18<sup>th</sup> Symp. (Int.) on Combustion*, The Combustion Institute: Pittsburgh, **1981**, p 1105.
42. Frenklach, M.; Clary, D. W.; Gardiner, W. C.; Stein, S. E. In *20<sup>th</sup> Symp. (Int.) on Combustion*, The Combustion Institute: Pittsburgh, **1984**, p 887.
43. Gail, H. P.; Sedlmayr, E. In *Physical Processes in Interstellar Clouds*, Morfill, G. E., Scholer, M., Eds.; Reidel: Dordrecht, The Netherlands, **1987**, p 275.
44. Keller, R. In *Polycyclic Aromatic Hydrocarbons and Astrophysics*, Léger, A.; d'Hendecourt, L. B.; Boccara, N., Eds.; Reidel: Dordrecht, The Netherlands, **1987**, p 387.
45. Frenklach, M.; Feigelson, E. D. *Astrophys. J.*, **1989**, 341, 372.
46. Tielens, A. G. G. M. In *Carbon in the Galaxy: Studies from Earth and Space*, Tarter, J., Ed.; NASA CP-3061, **1990**, p 59.
47. Ellinger, Y.; Pauzat, F.; Lengsfeld, B. H. *J. Mol. Struct. Theoch.* **1999**, 458, 203.
48. Winnewisser, G. *J. Mol. Struc.*, **1997**, 408-409, 1.
49. Henning, Th.; Salama, F. *Science* **1998**, 282, 2204.
50. Bohme, D. K. In *Rate Coefficients in Astrochemistry*; Millar, T. J., Williams, D. A., Eds.; Kluwer: Dordrecht, The Netherlands, **1988**, p 117.
51. Scott, A.; Duley, W. W.; Pinho, G. P. *Astrophys. J.* **1997**, 489, L193.
52. Herbst, E.; Leung, C. M. *Astrophys. J. Suppl.* **1989**, 69, 271.
53. Dalgarno, A.; Black, J. H. *Rep. Prog. Phys.* **1976**, 39, 573.
54. van Dishoeck, E. F. In *The Molecular Astrophysics of Stars and Galaxies*, Hartquist, T. W.; Williams, D. A. Eds.; Oxford: New York **1998**, p 53.
55. Dunbar, R. C. *Int. J. Mass Spectrom. Ion Processes* **1997**, 160, 1.
56. Cherchneff, I.; Barker, J. R.; Tielens, A. G. G. M. *Astrophys. J.* **1992**, 401, 269.
57. Helling, C.; Jørgensen, U. G.; Plez, B.; Johnson, H. R. *Astron. Astrophys.* **1996**, 315, 194.

58. Allain, T.; Sedlmayr, E.; Leach, S. *Astron. Astrophys.*, **1997**, 323, 163.
59. Tielens, A. G. G. M. *Astrophys. Space Sci.* **1997**, 251, 1.
60. Hucknall, D. J. *Chemistry of Hydrocarbon Combustion* Chapman and Hall: New York, **1985**.
61. Barnard, J. A.; Bradley, J. N. *Flame and Combustion* Chapman and Hall: New York, **1985**.
62. Smyth, K. C.; Miller, J. H. *Science*, **1987**, 236, 1540.
63. Curl, R. F.; Smalley, R. E. *Science*, **1988**, 242, 1017.
64. Starukhina, L. V.; Shkuratov, Y. G. *Icarus*, **1995**, 113, 442.
65. Cherchneff, I. In *The Molecular Astrophysics of Stars and Galaxies*, Hartquist, T. W.; Williams, D. A. Eds.: Oxford: New York **1998**, p 265.
66. Mimura, K. *Geochimica et Cosmochimica Acta* **1995**, 59, 579.
67. Scott, A.; Duley, W. W. *Astrophys. J.* **1996**, 472, L123.
68. Duley, W. W. *Astrophys. J.* **2000**, 528, 841.
69. Gillett, F. C.; Forrest, W. J.; Merrill, K. M. *Astrophys. J.*, **1973**, 183, 87.
70. Russell, R. W.; Soifer, B. T.; Willner, S. P. *Astrophys. J.*, **1977**, 217, L149.
71. Aitken, D. K. In *Infrared Astronomy*, Wynn-Williams, C. G., Cruikshank, C. P., Eds.; Reidel: Dordrecht, 1981, p 201.
72. Willner, S. P. In *Galactic and Extragalactic Infrared Spectroscopy*, Kessler, M. F., Phillips, J. P., Eds.; Reidel: Dordrecht, 1984, p 37.
73. Phillips, M. M.; Aitken, D. K.; Roche, P. F. *MNRAS*, **1984**, 207, 25.
74. Geballe, T. R.; Tielens, A. G. G. M.; Kwok, S.; Hrivnak, V. J. *Astrophys. J.*, **1992**, 387, L89.
75. Roelfsma, P. R., et al. *Astron. and Astrophys.* **1996**, 315, L289.
76. Laureijs, R. J., et al. *Astron. and Astrophys.* **1996**, 315, L313.
77. Onaka, R.; Yamamura, I.; Tanabe, R.; Roellig, T. L.; Yuen, L. *PASJ*, **1996**, 48, L59.
78. Matilla, K. et al. *Astron. and Astrophys.* **1996**, 315, L353.

79. Sloan, G. C.; Bregman, J. D.; Geballe, R. R.; Allamandola, L. J.; Woodward, C. E. *Astrophys. J.*, **1997**, 474, 735.
80. Heger, M. L. *Lick Obs. Bull.* **1922**, 10, 146.
81. Leach, S. J. *Electron Spectrosc. Rel. Phen.*, **1986**, 41, 427.
82. Leach, S. In *Polycyclic Aromatic Hydrocarbons and Astrophysics*, Léger, A., d'Hendecourt, L., Boccaro, N., Eds.; Reidel: Dordrecht, 1987, p 99.
83. Sellgren, K. *Astrophys. J.*, **1984**, 277, 623.
84. Merrill, P. W. *Publ. Astron. Soc. Pac.*, **1934**, 46, 206.
85. Merrill, P. W. *Publ. Astron. Soc. Pac.*, **1936**, 48, 179.
86. Merrill, P. W.; Wilson, O. C. *Astrophys. J.*, **1938**, 87, 9.
87. Herbig, G. H. *Astrophys. J.*, **1975**, 196, 129.
88. Weselak, T.; Schmidt, M.; Krelowski, J. *Astron. Astrophys. Suppl. Ser.*, **2000**, 142, 239.
89. Herbig, G. G. *Annu. Rev. Astrophys.* **1995**, 33, 19.
90. Cami, J.; Sonnentrucker, P.; Ehrenfreund, P.; Foing, B. H. *Astron. Astrophys.*, **1997**, 326, 822.
91. Moutou, C.; Krelowski, J.; d'Hendecourt, L.; Jamroszczak, J. *Astron. Astrophys.*, **1999**, 351, 680.
92. Krelowski, J.; Schmidt, M. Snow, T. P. *PASP*, **1997**, 109, 1135.
93. Heckman, T. M.; Lehnert, M. D. *Astrophys. J.*, **2000**, 537, 690.
94. Romanini, D.; Biennier, L.; Salama, F.; Kachanov, A. Allamandola, L. J.; Stoeckel, F. *Chem. Phys. Letters*, **1999**, 303, 165.
95. Puget, J. L.; Léger, A. *ARA&A* **1989**, 27, 161.
96. Allamandola, L.J., Hudgins, D. M., And Sandford, S.A., *Astrophys. J.* **1999**, 511, L125.
97. Jochims, H. W.; Baumgärtel, H.; Leach, S. *Astrophys. J.* **1999**, 512, 500.
98. Snow, T.P. and Witt, A. N., *Science* **1995**, 270, 1455.
99. Pachuta, S. J.; Kenttämaa, J. I.; Sack, T. M.; Cerny, R. L.; Tomer, K. B.; Gross, M. L.; Pachuta, R. R.; Cooks, R. G. *J. Am. Chem. Soc.*, **1988**, 110, 657.

100. Boissel, P.; Lefèvre, G.; Thiébot, Ph. In *Conf. Proc. No. 312 Molecules and Grains in Space*; Nenner, I., Ed.; Am. Inst. of Phys.: New York, 1994, p 667.
101. Boissel, P.; de Parseval, P.; Marty, P.; Lefèvre, G.; *J. Chem. Phys.* **1997**, *106*, 4973.
102. Allain, T.; Leach, S.; Sedlmayr, E. *Astron. Astrophys.* **1996**, *305*, 602, 616.
103. Jochims, H. W.; Rasekh, J.; Rühl, E.; Baumgärtel, H.; Leach, S. *Chem. Phys.*, **1992**, *168*, 159.
104. Lifshitz, C. *Int. Rev. Phys. Chem.* **1997**, *16*, 113.
105. Dunbar, R. D., *Mass Spectrom. Rev.* **1992**, *11*, 309.
106. Ho, Y.; Yang, Y.; Klippenstein, S. J.; Dunbar, R. C. *J. Phys. Chem.* **1995**, *99*, 12115.
107. Gauthier, J.W.; Trautman, D.B.; Jacobson, D.B. *Anal. Chim. Acta*, **1991**, *246*, 211.
108. Guo, X.; Sievers, H. L.; Grützmacher, H. F. *Int. J. Mass Spectrom.*, **1999**, *185*, 1.
109. Granucci, G.; Ellinger, Y.; Boissel, P. *Chem. Phys.* **1995**, *191*, 165.
110. Ling, Y., Martin, J.M.L., Lifshitz, C. *J. Phys. Chem.* **1997**, *101*, 219.
111. Schroeter, K.; Schröder, D.; Schwarz, H. *J. Phys. Chem.* **1999**, *103*, 4174.
112. Joblin, C.; Masselon, C.; Boissel, P.; de Parseval, P.; Martinovic, S.; Muller, J. *Rapid Commun. Mass Spectrom.* **1997**, *11*, 1619.
113. Ekern, S. P.; Marshall, A. G.; Szczepanski, J.; Vala, M. *Astrophys. J.* **1997**, *488*, L39.
114. Ekern, S. P.; Marshall, A. G.; Szczepanski, J.; Vala, M. *J. Phys. Chem.* **1998**, *102*, 3498.
115. Marshall, A. G. *Int. J. Mass Spectrom.* **2000**, *200*, 331.
116. Lawrence, E. O.; Livingston, M. S. *Phys. Rev.* **1932**, *40*, 19.
117. Sommer, H.; Thomas, J. A.; Hipple, J. A. *Phys. Rev.* **1951**, *47*, 697.
118. A. G. Marshall, in D.M. Grant, R.K. Harris (Eds.), *Encyclopedia of Nuclear Magnetic Resonance*, Vol. 1, Wiley, London, 1996, 486.
119. Wobschall D. *Rev. Sci. Instrum.* **1965**, *36*, 466.
120. Llewellyn, P. M. *U.S.A. Patent No. 3,390,265*, issued 25 June, 1969.

121. Baldeschwieler, J. D. *Science* **1968**, 159, 263.
122. Beauchamp, J. L. *Annu. Rev. Phys. Chem.* **1971**, 22, 527.
123. Comisarow, M. B.; Marshall, A. G. *Chem. Phys. Lett.* **1974**, 25, 282.
124. Comisarow, M. B.; Marshall, A. G. *Chem. Phys. Lett.* **1974**, 26, 489.
125. Marshall, A. G.; Verdun, F. R. *Fourier Transforms in NMR, Optical, and Mass spectrometry: A User's Handbook*; Elsevier: Amsterdam, 1990.
126. Marshall, A. G.; Hendrickson, C. L.; Jackson, G. S. *Mass Spectrom. Rev.* **1998**, 17, 1.
127. McIver, R. T., Jr. *Rev. Sci. Instrum.* **1970**, 41, 555.
128. Amster, I. J. *J. Mass Spectrom.* **1996**, 31, 1325.
129. Comisarow, M. B.; Marshall, A. G. *Chem. Phys. Lett.* **1974**, 25, 282.
130. Ghaderi, S.; Kulkarni, P. S.; Ledford, E. B., Jr.; Wilkins, C. L.; Gross, M. L. *Anal. Chem.* **1981**, 53, 428.
131. White, R. L.; Wilkins, C. L. *Anal. Chem.* **1982**, 54, 2443.
132. Sack, T. M.; Gross, M. L. *Anal. Chem.* **1983**, 55, 2419.
133. Laude, D. A. J.; Pentoney, S. L. J.; Griffiths, P. R.; Wilins, C. L. *Anal. Chem.* **1987**, 59, 2283.
134. Stockton, G. W.; Meek, J. T.; Millen, W. G.; Wayne, R. S. in B. Asamoto(Eds.), *FT-ICR/MS: Analytical Applications of Fourier transform Ion Cyclotron Resonance Mass Spectrometry*, Vol. VCH, New York, 1991, p. 235.
135. Stacey, C. C.; Kruppa, G. H.; Watson, C. H.; Wronka, J.; Laukien, F. H.; Bancks, J. F.; Whitehouse, C. M. *Rapid Comm. Mass Spectrom* **1994**, 8, 513.
136. Loo, J. A.; Quinn, J. P.; Ryu, S. I.; Henry, K. D.; Senko, M. W.; McLafferty, F. W. *Proc. Natl. Acad. Sci.* **1992**, 89, 286.
137. Winger, B. E.; Hofstadler, S. A.; Bruce, J. E.; Udseth, H. R.; Smith, R. D. *J. Am. Soc. Mass Spectrom.* **1993**, 4, 566.
138. Comisarow, M. B.; Marshall, A. G. *Chem. Phys. Lett.*, **1974**, 26, 489.
139. Guan, S.; Marshall, A. G. *Int. J. Mass Spectrom. Ion Processes*, **1996**, 157/158, 5.
140. Marshall, A. G.; Wang, T.-C. L.; Ricca, R. L. *J. Am. Chem. Soc.*, **1985**, 107, 7893.



141. Senko, M. W.; Canterbury, J. D.; Guan, S.; Marshall, A. G. *Rapid Comm. Mass Spectrom.*, **1996**, *10*, 1839.
142. Kage, D. *Fourier Transform Ion Cyclotron Resonance Mass Spectrometry Investigation of Gas-Phase Ions*, Dissertation, University of Florida, 1999.
143. Boissel, P.; de Parseval, P.; Marty, P.; Lefèvre, G.; *J. Chem. Phys.* **1997**, *106*, 4973.
144. Richardson, D. E., *Kinetics Simulation & Fitting Program Download Page*, [www.chem.ufl.edu/~der/chm6621.htm](http://www.chem.ufl.edu/~der/chm6621.htm), **15 Jun 2000**.
145. Frisch, J. J.; Trucks, G. W.; Schlegel, H. B.; Scuseria, G. E.; Robb, M. A.; Cheeseman, J. R.; Zakrzewski, V. G.; Montgomery, Jr., J. A.; Stratmann, R. E.; Burant, J. C.; Dapprich, S.; Millam, J. M.; Daniels, A. D.; Kudin, K. N.; Strain, M. C.; Farkas, O.; Tomasi, J.; Barone, V.; Cossi, M.; Cammi, R.; Mennucci, B.; Pomelli, C.; Adamo, C.; Clifford, S.; Ochterski, J.; Petersson, G. A.; Ayala, P. Y.; Cui, Q.; Morokuma, K.; Malick, D. K.; Rabuck, A. D.; Raghavachari, K.; Foresman, J. B.; Cioslowski, J.; Ortiz, J. V.; Stefanov, B. B.; Liu, G.; Liashenko, A.; Piskorz, P.; Komaromi, I.; Gomperts, R.; Martin, R. L.; Fox, D. J.; Keith, T.; Al-Laham, M. A.; Peng, C. Y.; Nanayakkara, A.; Gonzalez, C.; Challacombe, M.; Gill, P. M. W.; Johnson, B.; Chen, W.; Wong, M. W.; Andres, J. L.; Gonzalez, C.; Head-Gordon, M.; Replogle, E. S.; Pople, J. A. Gaussian98®, Revision A.3 Gaussian, Inc., Pittsburgh PA, **1998**.
146. Bauschlicher, Jr., C. W. *Astrophys. J.*, **1998**, *507*, L125-L127 and references therein.
147. Dibben, M. J.; Kage, D.; Szczepanski, J.; Eyler, J. R.; Vala, M. *J. Phys. Chem.* **2001**, accepted.
148. Giuffreda, M. G.; Deleuze, M. S.; Francois, J. P. *J. Phys. Chem. A* **1999**, *103*, 5137.
149. von Helden, G.; Hsu, M. T.; Kemper, P. R.; Bowers, M. T. *J. Chem. Phys.* **1991**, *95*, 3835.
150. von Helden, G.; Gotts, N. G.; Bowers, M. T. *J. Am. Chem. Soc.* **1993**, *115*, 4363.
151. Szczepanski, J.; Vala, M. *Astrophys. J.* **1993**, *414*, 646.
152. Szczepanski, J.; Roser, D.; Personette, W.; Eyring, M.; Pellow, R.; Vala, M. *J. Phys. Chem.* **1992**, *96*, 7876.
153. Salama, F.; Joblin, C.; Allamandola, L. J. *J. Chem. Phys.* **1995**, *101*, 10252.
154. Ehrenfreund, P.; Foing, B. H.; d'Hendecourt, L.; Jenniskens, P.; Désert, X. *Astron. Astrophys.* **1995**, *299*, 213.
155. Bréchignac, P.; Pino, T. *Astron. Astrophys.* **1999**, *343*, L49.

156. Shida, T. *Electronic Absorption Spectra of Radical Ions*, Elsevier, Amsterdam, 1988.
157. McDaniel, E. W. *Collision Phenomena in Ionized Gases*; John Wiley and Sons, Inc.: New York, 1964.
158. Table of Dielectric Constants and Electric Dipole Moments of Substances I the Gaseous State, Maryott, A. A.; Buckley, F. National Bureau of Standards Circular 537, June 25, 1953.
159. Oomens, J.; van Roij, A. J. A.; Meijer, G.; von Helden, G. *Astrophys. J.*, **2000**, 542, 404.
160. Ho, Y-P.; Dunbar, R. C.; Lifshitz, C. *J. Am. Chem. Soc.*, **1995**, 117, 6504.
161. Arnoult, K. M.; Wdowiak, T. J. *Astrophys. J.*, **2000**, 535, 815.
162. Beegle, L. W.; Wdowiak, T. J.; Robinson, M. S.; Cronin, J. R.; McGehee, M. D.; Celmett, S. J.; Gillette, S. *Astrophys. J.*, **1997**, 487, 976.
163. Guo, X. H.; Grutzmacher, H. F.; Nibbering, N. M. M. *Eur. J. Mass Spect.*, **2000**, 6, 357.

## BIOGRAPHICAL SKETCH

Mark Dibben was born April 26, 1963, in Junction City, Kansas. He grew up in Junction City and graduated from Junction City High School in 1981. Accepting an Air Force ROTC scholarship, he attended the University of Kansas, majoring in chemical engineering. After graduating in 1985, he was commissioned as a second lieutenant in the Air Force.

His first assignment was at the Occupational and Environmental Health Laboratory at Brooks AFB, San Antonio, Texas. He was responsible for analyzing air, water and soil samples for contaminants. He was then selected to attend the Air Force Institute of Technology at Wright-Patterson AFB, Dayton, Ohio, where he obtained his M. S. degree in nuclear engineering. His thesis, "Thermal Analysis of an Annular Fuel Core in a Space Nuclear Reactor," involved modeling the thermal and hydrodynamics of nuclear reactors.

He was then transferred to Kirtland AFB, Albuquerque, New Mexico, to perform thermal analysis on the recently acquired Russian TOPAZ II space nuclear reactor. After two years, he transitioned into plans and programs where he was responsible for coordinating research efforts in the development of satellites among the Air Force, Army, Navy and Ballistic Missile Defense Office.

His next assignment took him to the United States Air Force Academy where he discovered his joy of teaching. To continue teaching at the Academy, a PhD was

required which brought him to the University of Florida. His obvious interest in space coincided with Dr. Martin Vala's research efforts in identifying molecules in space.

He is married to the former Lynn Sanchez and has three children, Jason, Luis and Amanda, and three step-children, Anthony, Annette and Angela.